OPTICAL VORTICES: GENERATION AND DETECTION

EDITED BY: Junjie Yu, Pei Zhang, Gianluca Ruffato and Di Lin
PUBLISHED IN: Frontiers in Physics

frontiers Research Topics

ISSN 1664-8714
ISBN 978-2-83250-495-6
DOI 10.3389/978-2-83250-495-6

About Frontiers

Frontiers is more than just an open-access publisher of scholarly articles: it is a pioneering approach to the world of academia, radically improving the way scholarly research is managed. The grand vision of Frontiers is a world where all people have an equal opportunity to seek, share and generate knowledge. Frontiers provides immediate and permanent online open access to all its publications, but this alone is not enough to realize our grand goals.

Frontiers Journal Series

The Frontiers Journal Series is a multi-tier and interdisciplinary set of open-access, online journals, promising a paradigm shift from the current review, selection and dissemination processes in academic publishing. All Frontiers journals are driven by researchers for researchers; therefore, they constitute a service to the scholarly community. At the same time, the Frontiers Journal Series operates on a revolutionary invention, the tiered publishing system, initially addressing specific communities of scholars, and gradually climbing up to broader public understanding, thus serving the interests of the lay society, too.

Dedication to Quality

Each Frontiers article is a landmark of the highest quality, thanks to genuinely collaborative interactions between authors and review editors, who include some of the world's best academicians. Research must be certified by peers before entering a stream of knowledge that may eventually reach the public - and shape society; therefore, Frontiers only applies the most rigorous and unbiased reviews.
Frontiers revolutionizes research publishing by freely delivering the most outstanding research, evaluated with no bias from both the academic and social point of view. By applying the most advanced information technologies, Frontiers is catapulting scholarly publishing into a new generation.

What are Frontiers Research Topics?

Frontiers Research Topics are very popular trademarks of the Frontiers Journals Series: they are collections of at least ten articles, all centered on a particular subject. With their unique mix of varied contributions from Original Research to Review Articles, Frontiers Research Topics unify the most influential researchers, the latest key findings and historical advances in a hot research area! Find out more on how to host your own Frontiers Research Topic or contribute to one as an author by contacting the Frontiers Editorial Office: frontiersin.org/about/contact

OPTICAL VORTICES: GENERATION AND DETECTION

Topic Editors:
Junjie Yu, Shanghai Institute of Optics and Fine Mechanics, Chinese Academy of Sciences (CAS), China
Pei Zhang, Xi'an Jiaotong University, China
Gianluca Ruffato, University of Padua, Italy
Di Lin, University of Southampton, United Kingdom

Citation: Yu, J., Zhang, P., Ruffato, G., Lin, D., eds. (2022). Optical Vortices: Generation and Detection. Lausanne: Frontiers Media SA.
doi: 10.3389/978-2-83250-495-6

Table of Contents

frontiers | Frontiers in Physics

TYPE Editorial
PUBLISHED 29 September 2022
DOI 10.3389/fphy.2022.1026004

OPEN ACCESS

EDITED AND REVIEWED BY
Lorenzo Pavesi,
University of Trento, Italy

*CORRESPONDENCE
Junjie Yu,
junjiey@siom.ac.cn
Pei Zhang,
zhangpei@mail.ustc.edu.cn
Gianluca Ruffato,
gianluca.ruffato@unipd.it
Di Lin,
dilin@gdut.edu.cn

SPECIALTY SECTION
This article was submitted to Optics and Photonics,
a section of the journal
Frontiers in Physics

RECEIVED 23 August 2022
ACCEPTED 12 September 2022
PUBLISHED 29 September 2022

CITATION
Yu J, Zhang P, Ruffato G and Lin D (2022), Editorial: Optical vortices: Generation and detection.
Front. Phys. 10:1026004.
doi: 10.3389/fphy.2022.1026004

Editorial: Optical vortices: Generation and detection

Junjie Yu[1]*, Pei Zhang[2]*, Gianluca Ruffato[3]* and Di Lin*[,4,5,6]

[1]Laboratory of Information Optics and Optoelectronics Techniques, Shanghai Institute of Optics and Fine Mechanics, Academia Sinica, Shanghai, China, [2]MOE Key Laboratory for Nonequilibrium Synthesis and Modulation of Condensed Matter, School of Physics, Xi'an Jiaotong University, Xi'an, China, [3]Department of Physics and Astronomy "G. Galilei", University of Padova, Padova, Italy, [4]Advanced Institute of Photonics Technology, School of Information Engineering, Guangdong University of Technology, Guangzhou, Guangdong, China, [5]Guangdong Provincial Key Laboratory of Photonics Information Technology, Guangdong University of Technology, Guangzhou, Guangdong, China, [6]Optoelectronics Research Centre, University of Southampton, Southampton, United Kingdom

KEYWORDS

vortices, orbital angular momentum (OAM), singularity, OAM-multiplexing, rotational doppler effect (RDE)

Editorial on the Research Topic
Optical vortices: Generation and detection

Vortices are typically characterized by singularities and represent an interesting phenomenon that occurs widely in nature, such as tornadoes, fluid eddies, spiral galaxies and even in black holes, etc. Like other types of vortices, optical vortices share the property of carrying orbital angular momentum (OAM), as proved by the seminal paper of Allen and coworkers in 1992 [1], which ignited the flourishing research field of structured light. As one of the most prominent candidates for structured light, optical vortices are arousing ever-increasing interest among both scientific and engineering communities due to their disruptive applications in an amazing variety of realms, ranging from stimulated emission depletion (STED) nanoscopy [2, 3] to both quantum and classical OAM-multiplexed optical communications [4–6] and more recently high-intensity vortex physics [7, 8]. In this Research Topic, different schemes and techniques, including complex reconstruction, metasurfaces, integrated log-polar mode sorters, etc., were proposed for the generation, modulation, and detection of various vortex fields. Also, some novel vortex fields, such as asymmetric vortex beams, perfect vortex beams, and anomalous vortex beams, etc., were also demonstrated. In addition, more exciting and promising applications were explored further, including OAM-based optical communications, optical manipulation, and remote sensing of rotating objects, etc.

Although vortex beams have been intensively studied during the past decades, a full knowledge of the basic physical mechanism, especially clear spatial and temporal dynamics, is still missing to some extent. By using the ray-tracing method based on geometric optics, Cai et al. analyzed and established an intuitive mathematical model for giving an explanation of the physical picture underlying the propagation and evolution of the dark fields of focused vortices. The results are helpful to intuitively understand the

propagation behaviour of this special vortex beam. In addition, the method can be extended to other specific vortex beams.

Among different families of beams carrying OAM, perfect optical vortices [9] have gained increasing interest during the last decade due to the independence of their ring-like intensity profile from the carried amount of OAM. Jiang et al. reported a novel multi-foci integration method to overcome the critical limits of standard techniques for perfect vortices generation and produce beams without focus deviation, showing controllable spot arrays with custom phase distributions for intriguing applications in optical trapping and manipulation.

The paraxial local topological charge of anomalous vortex beam varies with propagation, which provides an additional degree of freedom. Therefore, the beams have potential applications in fields such as quantum information and laser shaping. However, the lack of optical devices to efficiently generate those beams hinders their applications. Huang et al. proposed a phase-only device called spiral axicons to efficiently generate anomalous vortex beams. The relationship between the spiral axicon parameters and the topological charge of anomalous vortex beams is given theoretically and experimentally. This will promote the application of anomalous vortex beams. Zhang et al. proposed a theoretical model of the partially coherent power exponential phase vortex beam, which enriches the variety of vortex beams. This work opens up opportunities for applications in beam shaping, optical trapping, and particle manipulation because of the asymmetric vortex beam. In addition, partially coherent beams have some unique advantages in applications.

Metasurfaces [10] represent the latest evolution of optical elements in terms of design and materials [11], and suggest new optical architectures and techniques for the advanced generation of optical vortices. Vogliardi et al. reported the design and simulation of new silicon metaoptics for the spin-controlled generation and focusing of beams carrying OAM. The combined control of dynamic and geometric phases *via* rotated nanopillars with different cross-sections allows encoding different functionalities on the two orthogonal circular polarizations, enabling the focusing of beams carrying different values of OAM at distinct points in space. Song et al. demonstrated an evolution of the previous metasurfaces with further engineered meta-atoms for generating achromatic focused optical vortex beams through a single germanium metasurface in the longwave infrared with high efficiency and high mode purity, where the chromatic aberration and polarization sensitivity are eliminated by superimposing a polarization-insensitive geometric phase and a dispersion-engineered dynamic phase. It has been shown that the longwave infrared corresponds to an atmospheric transparent window, which makes it an ideal range for optical wireless communications. Thus, this work makes a great significance for promoting the application of chip-level optical communications in infrared range based on OAM-multiplexing.

It has been well known that vortex beams, which are endowed with OAM, can be used as information carriers to increase the information capacity of optical communication channels at the same frequency, which requires mode sorters that can effectively distinguish among different vortex beam patterns. However, none of the currently known solutions can provide direct integration to other optical elements, or provide simple lithography procedures for various functionalities. Lightman et al. proposed a fabrication method that can provide high-quality and integrated log-polar mode sorters. This lays the foundation for construction of an optical fiber-based communication system. Conformal transformations represent an efficient and versatile method for the compact manipulation of OAM beams by using a cascade of two confocal phase elements [12, 13]. Li et al. presented a numerical study on the generation of OAM beams by using the so-called log-polar transformation [14] to wrap a rectangular intensity profile with a linear phase into a ring of light carrying an azimuthal phase gradient, proving the efficient generation and also mode detection of integer and fractional OAM beams with continuous tunability.

Since the seminal paper of Bozinovic et al. in 2013 [6], the stable propagation of OAM modes has been widely exploited both in commercial and special optical fibers. The review of Ma et al. summarizes the state-of-the-art in the generation, transmission, and exploitation of guided OAM beams, considering several types of optical fibers, as photonic crystal fibers, ring core fibers, fiber gratings and other all-fiber systems supporting OAM, and giving a final outlook on applications of OAM in cutting-edge disciplines, such as nonlinear optics, optical communication, particle manipulation and imaging. Zhao et al. proposed a method to reconstruct both the amplitude and phase profiles of OAM beams by collecting their interference patterns with two reference waves of different phases in a coherent detection scheme, proving the feasibility of the technique both numerically and experimentally and its robustness even under the presence of atmospheric turbulence.

In addition, vortex light had been utilized for remote sensing of rotating objects, both microscopic particles and macroscopic objects, based on the rotational Doppler effect (RDE). Qiu et al. presented an overview on the technical progress in measuring the rotating Doppler effect associated with OAM, giving the basic mechanism of RDE, the recent developments in rotational speed measurement ranging from macro-objects and molecular motion to quantum optical realms, and a summary of challenges and prospects. Recent years have witnessed a growing interest in vector vortex beams [15, 16]. Qiu et al. reported a flexible and robust scheme to generate the symmetric and asymmetric vector structured beams instead of conventional interferometer configuration, and they further demonstrated the spectrum observation of the rotational Doppler effect based on the coherent interaction between atoms and structured light in an atomic vapor.

In summary, vortex beams bring new degrees of freedom for photons due to their carried OAM and also complex spatial mode profiles. Also, various novel vortex fields and advanced control over vortex fields with more degrees of flexibility are explored. Furthermore, more and more exciting applications are expected in the future, with the advance of compact and integrated devices. This Research Topic collects the works of the large community working in those fields, showing the prominent role played by optical vortices and the still vivid and inspiring action of OAM beams 30 years later.

Author contributions

JY initiated this project, and JY, PZ, and GR wrote the draft. All authors contributed to reading, modification and final approval of the manuscript and also the whole project.

Conflict of interest

The authors declare that the research was conducted in the absence of any commercial or financial relationships that could be construed as a potential conflict of interest.

Publisher's note

References

1. Allen L, Beijersbergen MW, Spreeuw RJC, Woerdman JP. Orbital angular momentum of light and the transformation of laguerre-Gaussian laser modes. *Phys Rev A* (1992) 45:8185–9. doi:10.1103/physreva.45.8185

2. Hell SW, Wichmann J. Breaking the diffraction resolution limit by stimulated emission: Stimulated-emission-depletion fluorescence microscopy. *Opt Lett* (1994) 19:780–2. doi:10.1364/OL.19.000780

3. Kamper M, Ta H, Jensen NA, Hell SW, Jakobs S. Near-infrared STED nanoscopy with an engineered bacterial phytochrome. *Nat Commun* (2018) 9: 4762. doi:10.1038/s41467-018-07246-2

4. Sit A, Bouchard F, Fickler R, Gagnon-Bischoff J, Larocque H, Heshami K, et al. High-dimensional intracity quantum cryptography with structured photons. *Optica* (2017) 4(9):1006–10. doi:10.1364/optica.4.001006

5. Willner AE, Huang H, Yan Y, Ren Y, Ahmed N, Xie G, et al. Optical communications using orbital angular momentum beams. *Adv Opt Photon* (2015) 7:66–106. doi:10.1364/AOP.7.000066

6. Bozinovic N, Yue Y, Ren Y, Tur M, Kristensen P, Huang H, et al. Terabit-scale orbital angular momentum mode division multiplexing in fibers. *Science* (2013) 340:1545–8. doi:10.1126/science.1237861

7. Zhang X, Shen B, Shi Y, Wang X, Zhang L, Wang W, et al. Generation of intense high-order vortex harmonics. *Phys Rev Lett* (2015) 114(17):173901. doi:10.1103/PhysRevLett.114.173901

8. Wang W, Jiang C, Dong H, Lu X, Li J, Xu R, et al. Hollow plasma acceleration driven by a relativistic reflected hollow laser. *Phys Rev Lett* (2020) 125(3):034801. doi:10.1103/PhysRevLett.125.034801

9. Ostrovsky AS, Rickenstorff-Parrao C, Arrizón V. Generation of the "perfect" optical vortex using a liquid-crystal spatial light modulator. *Opt Lett* (2013) 38(4): 534–6. doi:10.1364/ol.38.000534

10. Capasso F. The future and promise of flat optics: A personal perspective. *Nanophotonics* (2018) 7(6):953–7. doi:10.1515/nanoph-2018-0004

11. Genevet P, Capasso F, Aieta F, KhorasaninejadDevlin MR. Recent advances in planar optics: From plasmonic to dielectric metasurfaces. *Optica* (2017) 4:139–52. doi:10.1364/optica.4.000139

12. Hossack WJ, Darling AM, Dahdouh A. Coordinate transformations with multiple computer-generated optical elements. *J Mod Opt* (1987) 34:1235–50. doi:10.1080/09500348714551121

13. Ruffato G, Rotunno E, Giberti LMC, Grillo V. Arbitrary conformal transformations of wave functions. *Phys Rev Appl* (2021) 15(5):054028. doi:10.1103/PhysRevApplied.15.054028

14. Berkhout GCG, Lavery MPJ, Courtial J, Beijersbergen MW, Padgett MJ. Efficient sorting of orbital angular momentum states of light. *Phys Rev Lett* (2010) 105:153601. doi:10.1103/PhysRevLett.105.153601

15. Rosales-Guzman C, Ndagano B, Forbes A. A review of complex vector light fields and their applications. *J Opt* (2018) 20(12):123001. doi:10.1088/2040-8986/aaeb7d

16. Nape I, Singh K, Klug A, Buono W, Rosales-Guzman C, McWilliam A, et al. Revealing the invariance of vectorial structured light in complex media. *Nat Photon* (2022) 16:538–46. doi:10.1038/s41566-022-01023-w

frontiers in Physics

ORIGINAL RESEARCH
published: 23 November 2021
doi: 10.3389/fphy.2021.781688

Generation and Propagation of Partially Coherent Power-Exponent-Phase Vortex Beam

Hao Zhang[1], Xingyuan Lu[1], Zhuoyi Wang[1], A. P. Konijnenberg[2], Haiyun Wang[1], Chengliang Zhao[1] and Yangjian Cai[1,3,4]**

[1]School of Physical Science and Technology, Soochow University, Suzhou, China, [2]Eindhoven University of Technology, Eindhoven, Netherlands, [3]School of Physics and Electronics, Shandong Normal University, Jinan, China, [4]Shandong Provincial Engineering and Technical Center of Light Manipulation & Shandong Provincial Key Laboratory of Optics and Photonic Devices, School of Physics and Electronics, Shandong Normal University, Jinan, China

We report on a partially coherent power-exponent-phase vortex beam (PC-PEPV), whose spatial coherence is controllable and the initial phase exhibits a periodic power exponential change. The PC-PEPV beam was generated experimentally with various spatial coherence widths, and its propagation properties were studied both numerically and experimentally. By modulating the topological charge (TC) and power order of the PC-PEPV beam, the structure of the vortex beam can be adjusted from circular to elliptic, triangular, quadrangle, and pentagon. When the power order is odd, the PC-PEPV beam with a negative TC can be generated, and the profiles of the PC-PEPV beam can be precisely controlled *via* adjusting the value of the power order. For the case of high spatial coherence width, the number of the dark cores in the polygonal intensity array of the PC-PEPV beam equals the magnitude of the TC. However, when decreasing the spatial coherence width, the dark cores vanish and the intensity gradually transforms into a polygonal light spot. Fortunately, from the modulus and phase distributions of the cross-spectral density (CSD), both the magnitude and sign of the TC can be determined. In the experiment, the modulus and phase distribution of the CSD are verified by the phase perturbation method. This study has potential applications in beam shaping, micro-particle trapping, and optical tweezers.

Keywords: singular optics, vortex beam, partially coherent, power-exponent-phase, beam shaping

OPEN ACCESS

Edited by:
Pei Zhang,
Xi'an Jiaotong University, China

Reviewed by:
Zhi-Han Zhu,
Harbin University of Science and Technology, China
Xinzhong LI,
Henan University of Science and Technology, China

****Correspondence:***
Chengliang Zhao
zhaochengliang@suda.edu.cn
Yangjian Cai
yangjiancai@suda.edu.cn

Specialty section:
This article was submitted to Optics and Photonics, a section of the journal Frontiers in Physics

Received: *23 September 2021*
Accepted: *25 October 2021*
Published: *23 November 2021*

Citation:
Zhang H, Lu X, Wang Z, Konijnenberg AP, Wang H, Zhao C and Cai Y (2021) Generation and Propagation of Partially Coherent Power-Exponent-Phase Vortex Beam. Front. Phys. 9:781688. doi: 10.3389/fphy.2021.781688

INTRODUCTION

Since it was verified that the optical vortex can carry orbital angular momentum (OAM) [1], it became a research hot spot in the field of light manipulation. It is well known that the optical vortex possesses a helical phase term of $\exp(im\theta)$, where m is the topological charge (TC) and θ is the azimuthal angle. At the center of the optical vortex, the phase is undetermined and the intensity is zero. Optical vortices are widely investigated in many fields, such as micro-particle manipulation [2–5], free-space optical communications [6–8], optical measurements [9, 10], and super-resolution imaging [11].

The conventional optical vortex has a circular intensity profile, which limits its applications. To address this problem, various asymmetric and non-canonical models for optical vortices are proposed, providing higher freedom of control, for example, the optical vortex with a 3D free-style structure [12], the asymmetric Bessel beam [13], remainder-phase optical vortex [14],

anomalous optical vortex [15], and power-exponent-phase vortex (PEPV) [16]. It is worth noting that, compared with the classical vortex, the PEPV beam has a non-uniform phase and a spiral-shaped intensity distribution. Specifically, the phase on a closed path around the center point will increase exponentially. Soon afterward, the propagation properties of the PEPV beam was investigated [17], and this kind of vortex shows more advantages in particle manipulation [18–20]. Recently, a new kind of PEPV (NPEPV) beam was proposed, where each part of the spiral phase increases from 0 to 2π, showing exponential growth [21]. In addition, the phase and intensity patterns both show rotational symmetry. However, these excellent studies are only focused on the field of fully coherent light.

Coherence is one of the most important characteristics of the laser beam. Compared with the fully coherent beam, the partially coherent beam [22, 23] is more ubiquitous and has some unique advantages in practical applications. For instance, the partially coherent beam can increase the transfer efficiency in the process of non-linear optics [24], enhance the signal to noise ratio [25], decrease the bit error ratio [26], and realize particle trapping [27, 28] and ghost imaging [29, 30]. The partially coherent vortex beam was first proposed by Gori et.al., which is expressed by the incoherent superposition of a series of coherent Laguerre–Gaussian modes [31]. Subsequently, the study of the vortex beam has expanded from fully coherent to partially coherent and attracted enormous attention during the past decades [32–38]. The partially coherent vortex beam has several advantages over the fully coherent vortex beam. For instance, it is less disturbed when propagating through a turbulent atmosphere [39] as high-freedom beam shaping is possible [40], and it has remarkable self-reconstruction properties [41]. Different from fully coherent vortex beam with dark hollow intensity distribution, the central dark core in the partially coherent vortex beam will gradually vanish as the spatial coherence width decreases [42]. To describe the singularity of the partially coherent vortex beam, the concept of a coherence vortex, named as coherence singularity, is proposed. It reveals that the singularity of the partially coherent vortex will be hidden in the distribution of the cross-spectral density (CSD), instead of intensity [43, 44]. Meanwhile, the TC of the partially coherent beam can be determined by measuring the modulus and phase of the CSD function [45, 46]. However, the aforementioned conventional partially coherent vortex beams only carry the common helical phase term $\exp(\mathrm{i}m\theta)$, where the structure of the beams can only be reshaped from a doughnut-like intensity pattern to a circular intensity spot, limiting its practical applications. It inspires us to explore a special partially coherent vortex beam with a controllable structure.

To address this problem, in this study, we propose the theoretical model of a partially coherent power-exponent-phase vortex (PC-PEPV) beam, and its propagation properties are studied by numerical simulations. Different from the conventional partially coherent vortex beam, the PC-PEPV beam can realize a polygonal-structured intensity distribution and be shaped freely and precisely *via* varying the initial spatial coherence width, power order, and topological charge. In addition, we experimentally generated the PC-PEPV beam and measured the modulus and phase distributions of its CSD function *via* the phase perturbation method. The coherence singularities are observed in the phase distributions, which helps the determination of magnitude and sign of the TC. Compared with the partially coherent conventional vortex beam, our study enriches the mode distributions and realizes a controllable beam shaping, which have potential applications in particle manipulation.

METHODS

Principle of Generating the PC-PEPV Beam

Compared with a conventional vortex beam with a uniformly varying phase, that is, $\exp(\mathrm{i}m\theta)$, the electric field of a NPEPV beam with Gaussian-distributed amplitude in the source plane ($z = 0$) can be written as [21]:

$$E(r,\theta) = \exp\left(-\frac{r^2}{w_0^2}\right)\exp\left(\mathrm{i}2\pi\left[\frac{\mathrm{rem}(m\theta,2\pi)}{2\pi}\right]^n\right), \quad (1)$$

where (r, θ) denotes the polar coordinates in the source plane, r is the radial coordinate, θ is the azimuthal coordinate, w_0 is the beam width, rem(.) means the remainder function [14], m is the TC number, and n represents the power order of the spiral phase. Note that the power order n can be an integer or a fraction. It should be noted that the NPEPV beam will reduce to the conventional vortex beam if the parameters are $n = 1$.

To distinguish the difference between the conventional vortex beam and NPEPV beam, according to **Eq. 1**, the initial phases of them are depicted in **Figure 1**. Here, the value of TC is fixed as $m = 3$. As shown in **Figures 1A,B**, the initial phases with power order $n = 1$ and 2 can be regard as the initial phase of conventional vortex and NPEPV beam, respectively. Furthermore, the relationship between the initial phases and azimuth of the two phases is shown in **Figure 1C**. In contrast to the initial phase of the conventional vortex beam, which has a linear variation from 0 to 2π, the initial phase of the NPEPV beam shows a periodic power exponential change. However, the **Eq.1** is only suitable for perfectly coherent cases which neglected the significance of coherence of the light. Hence, in the following study, we extend this fully coherent NPEPV beam to a partially coherent field.

For a partially coherent beam, the CSD function in the space–frequency domain [23, 47] can be used to express its statistical characteristics as follows:

$$W(r_1,\theta_1,r_2,\theta_2,\omega) = \langle E^*(r_1,\theta_1,\omega)E(r_2,\theta_2,\omega)\rangle, \quad (2)$$

where (r_1, θ_1) and (r_2, θ_2) represent the coordinates of two random points in the source plane, denotes the ensemble average, and * represents the complex conjugate. In the

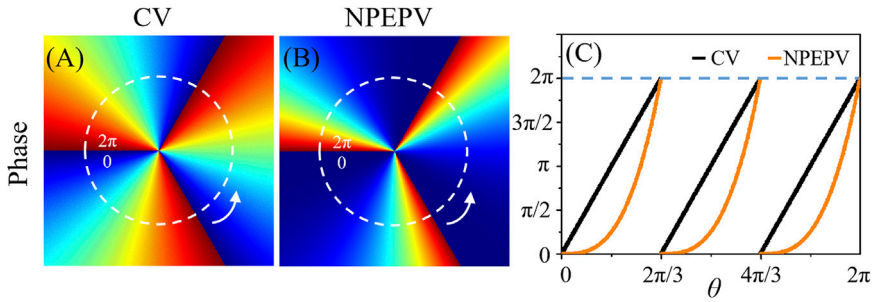

FIGURE 1 | Numerical simulation initial phases of the conventional vortex (CV) and NPEPV. **(A)** is the initial phase of the conventional vortex beam with TC $m = 3$, and power order $n = 1$, **(B)** is the initial phase of the NPEPV beam with TC $m = 3$ and power order $n = 3$, and **(C)** is the relationship between the initial phases and azimuth in a closed path marked by the white circular dashed line in **Figure 1A**; **Figure 1B**.

following derivation, for brevity, we only consider a monochromatic beam and omit the frequency ω [42, 48]. By substituting **Eq. 1** into **Eq. 2**, we find that for a Schell model PC-PEPV beam carrying the distinct power-exponent-phase shown in **Figure 1B**, the CSD function can be written as follows (see **Supplementary Material**):

$$W(r_1,\theta_1,r_2,\theta_2) = \exp\left(-\frac{r_1^2+r_2^2}{w_0^2}\right)\times\exp\left[-\frac{r_1^2-2r_1r_2\cos(\theta_1-\theta_2)+r_2^2}{2\sigma^2}\right]\times\exp\left(\mathrm{i}2\pi\left\{\left[\frac{\mathrm{rem}(m\theta_1,2\pi)}{2\pi}\right]^n-\left[\frac{\mathrm{rem}(m\theta_2,2\pi)}{2\pi}\right]^n\right\}\right), \tag{3}$$

where σ denotes the initial spatial coherence width of the beam. Generally, the propagation properties through a paraxial ABCD optical system can be studied *via* the generalized Collins formula. The CSD function in the observation plane can be written as follows:

$$W(\rho_1,\varphi_1,\rho_2,\varphi_2,z) = \left(\frac{1}{\lambda|B|}\right)^2\int_0^\infty\int_0^\infty\int_0^{2\pi}\int_0^{2\pi} r_1r_2\mathrm{d}r_1\mathrm{d}r_2\mathrm{d}\theta_1\mathrm{d}\theta_2 W(r_1,\theta_1,r_2,\theta_2)\times\exp\left\{-\frac{\mathrm{i}k}{2B^*}\left[A^*r_1^2-2r_1\rho_1\cos(\theta_1-\varphi_1)+D^*\rho_1^2\right]\right\}\times\exp\left\{\frac{\mathrm{i}k}{2B}\left[\mathrm{A}r_2^2-2r_2\rho_2\cos(\theta_2-\varphi_2)+D\rho_2^2\right]\right\}. \tag{4}$$

Here, ρ and φ are the radial and azimuthal coordinates of the observation plane, respectively. A, B, C, and D are the transfer matrix elements of the optical system. For a focused optical system, we can set $A = 0$, $B = f$, $C = -1/f$, and $D = 1$, where f is the focal length of the lens.

OAM Spectrum of the PC-PEPV Beam

Due to the introduction of the power order, the characteristics of the PC-PEPV beam differ from the conventional partially coherent vortex, which is closely related to the OAM spectrum. In **Figure 2**, we calculated the OAM spectrum of the PC-PEPV beam with different initial spatial coherence and power order in the source plane. Here, TC $m = 3$ and $w_0 = 1$ mm. Any vortex beam can be expressed as an orthogonal superposition of a series of integer OAM beams [49, 50]. Hence, the **Eq. 1** can be rewritten as follows:

$$E(r,\theta) = \frac{1}{\sqrt{2\pi}}\sum_{l=-\infty}^{\infty} a_l(r)\exp(\mathrm{i}l\theta), \tag{5}$$

where l is an integer and the mode coefficients are given by:

$$a_l(r) = \frac{1}{\sqrt{2\pi}}\int_0^{2\pi} E(r,\theta)\exp(-\mathrm{i}l\theta)\mathrm{d}\theta, \tag{6}$$

and the power weight is defined as $|a_l(r)|^2$. Likewise, the power weight of the PC-PEPV beam can be written as follows:

$$\langle|a_l(r)|^2\rangle = \frac{1}{2\pi}\exp\left[-\frac{2r^2}{w_0^2}\right]\int_0^{2\pi}\int_0^{2\pi}\exp\left[\mathrm{i}2\pi\left(\frac{\mathrm{rem}(m\theta_1,2\pi)}{2\pi}\right)^n\right]\times\exp\left[-i2\pi\left(\frac{\mathrm{rem}(m\theta_2,2\pi)}{2\pi}\right)^n\right]\times\exp[-il(\theta_1-\theta_2)]\times\exp\left[-\frac{r^2}{\sigma^2}(1-\cos(\theta_1-\theta_2))\right]\mathrm{d}\theta_1\mathrm{d}\theta_2. \tag{7}$$

Here, the normalized power weight for each OAM mode can then be defined as follows:

$$P_l = \frac{\int_0^\infty\langle|a_l(r)|^2\rangle r\mathrm{d}r}{\sum_l\int_0^\infty\langle|a_l(r)|^2\rangle r\mathrm{d}r}. \tag{8}$$

As depicted in **Figures 2A–C**, the power order $n = 1$, which corresponds to a conventional vortex beam. Clearly, the OAM spectrum of the conventional vortex beam with high spatial coherence is shown in **Figure 2A** and features a unique peak at $l = 3$. When the spatial coherence decreases, the OAM spectrum tends to a Gaussian distribution, and the main peak

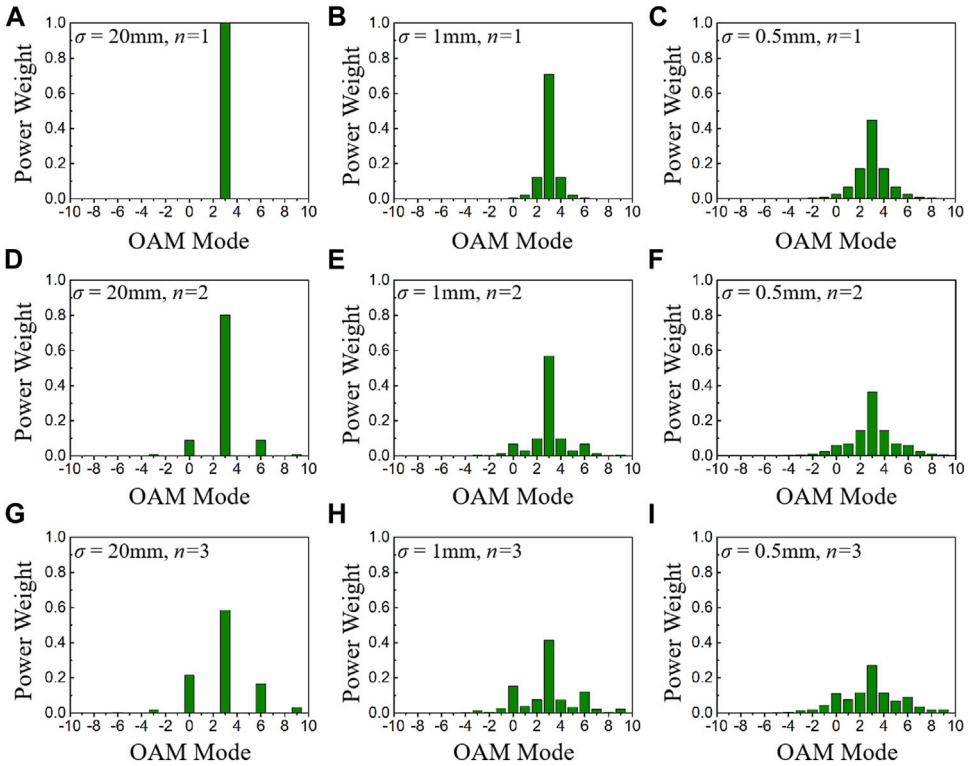

FIGURE 2 | OAM spectrum of the PC-PEPV beam with beam waist $w_0 = 1$ mm and TC $m = 3$, under different spatial coherence σ and power order n. **(A–C)** $\sigma = 20$, 1, 0.5 mm, and power order $n = 1$; **(D–F)** $\sigma = 20$, 1, 0.5 mm, and power order $n = 2$; and **(G–I)** $\sigma = 20$, 1, 0.5 mm, and power order $n = 3$.

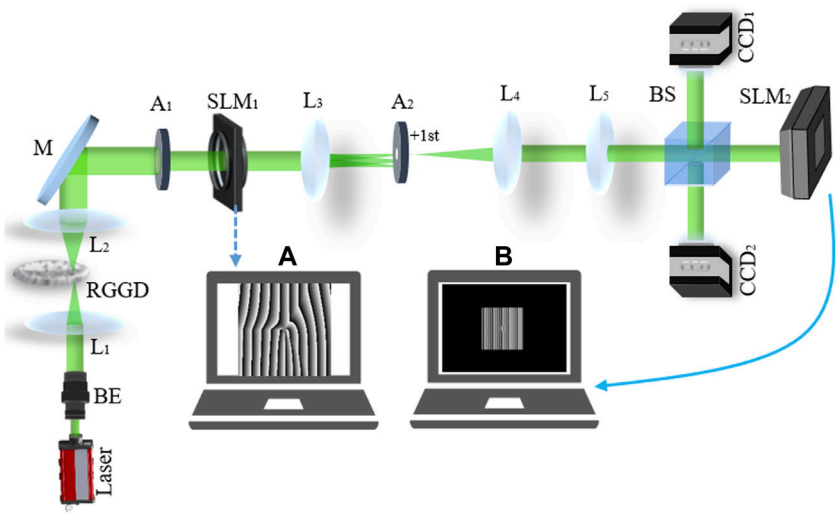

FIGURE 3 | Experimental setup for generating a PC-PEPV beam and measuring the amplitude and phase distribution of its CSD. **(A)** Fork grating written into SLM_1 and **(B)** phase mask written into SLM_2. BE, beam expander; L_1–L_5, lenses; RGGD, rotating ground-glass disk; M, mirror; A_1, A_2, apertures; SLM_1, SLM_2, spatial light modulators; BS, beam splitter; and CCD_1, CCD_2, charge-coupled device.

is located at $l = 3$. As the power order increases, that is, $n = 2$ and 3, the conventional vortex beam transforms into the PC-PEPV beam, and the OAM spectra with high spatial coherence are depicted in **Figures 2D,G**, respectively. By contrast, the OAM spectrum increases at $l = 0$ and 6 but decreases at $l = 3$ due to the power order in the spiral phase. Similarly, the OAM spectrum tends to a Gaussian distribution as the spatial coherence decreases.

Experimental Setup

The schematic of the experimental setup is depicted in **Figure 3**, which is used for generating a PC-PEPV beam and measuring the modulus and phase distribution of its CSD function. The coherent laser beam with a wavelength of $\lambda = 532$ nm is emitted from a solid-state laser and then expanded by the beam expander. The expanded beam is focused on the rotating ground-glass disk (with 400 Grit and 20 Hz rotational frequency) by the lens L_1 ($f_1 = 100$ mm), and then collimated by the lens L_2 ($f_2 = 100$ mm) to get a partially coherent Gaussian Schell model beam with controllable spatial coherence. The initial spatial coherence width can be controlled *via* adjusting the focused beam spot size on the rotating ground-glass disk [47]. The aperture A_1 is used to get the central area of the partially coherent Gaussian Schell model beam. Then it is reflected to the first spatial light modulator (SLM_1) *via* a mirror M. As shown in **Figure 3A**, the fork grating loaded on SLM_1 is designed *via* the method of computer-generated holograms [10]. Then the lenses L_3 and L_4 and aperture A_2 are used to form a 4-*f* system and filter the +1 order of the output beam, named as the PC-PEPV beam. The PC-PEPV beam is focused by the lens L_5. One path is reflected *via* the beam splitter, and the intensity is recorded by the charge-coupled device (CCD_1), which is located at the focal plane of L_5. To verify the CSD distribution and measure the coherence singularities of the PC-PEPV beam, the other path is transmitted through the beam splitter and focused onto SLM_2. The phase written into SLM_2 is shown in **Figure 3B**, containing a central square window with displacement grating, spherical wave phase for focusing, and an additional central phase perturbation [51, 52]. Note that the focused input PC-PEPV beam and the center of SLM_2 need to be aligned. Finally, the output beam from SLM_2 is reflected by the beam splitter and recorded by the CCD_2 located at the Fourier plane.

Method to Measure the CSD Function of the PC-PEPV Beam

The Fourier transformation intensity recorded by the CCD_2 with no additional phase perturbation can be written as follows:

$$I_0(\mathbf{k}) = \int\int W(\boldsymbol{\rho}_1, \boldsymbol{\rho}_2) \exp[-i2\pi\mathbf{k}(\boldsymbol{\rho}_1 - \boldsymbol{\rho}_2)]\mathrm{d}\boldsymbol{\rho}_1\mathrm{d}\boldsymbol{\rho}_2, \quad (9)$$

where $W(\boldsymbol{\rho}_1, \boldsymbol{\rho}_2)$ is the CSD function of the PC-PEPV beam on the plane of SLM_2 and $\mathbf{k}$ represents the coordinate vector in the plane of CCD_2. Then we introduce an on-axis phase perturbation at $\boldsymbol{\rho}_2 = \boldsymbol{\rho}_0 = (0, 0)$ of SLM_2. The complex-valued phase perturbation can be expressed as $C = [\exp(\mathrm{i}\varphi) - 1]\delta(\boldsymbol{\rho} - \boldsymbol{\rho}_0)$, where $\delta(\boldsymbol{\rho})$ represents the Dirac function. Thus, the perturbed Fourier transformation intensity will change as follows:

$$I(\mathbf{k}) = I_0(\mathbf{k}) + CC^*W(\boldsymbol{\rho}_0, \boldsymbol{\rho}_0) + C\int W(\boldsymbol{\rho}_1, \boldsymbol{\rho}_0) \exp[-\mathrm{i}2\pi\mathbf{k}(\boldsymbol{\rho}_1 - \boldsymbol{\rho}_0)]\mathrm{d}\boldsymbol{\rho}_1 + C^*\int W(\boldsymbol{\rho}_0, \boldsymbol{\rho}_2) \exp[-\mathrm{i}2\pi\mathbf{k}(\boldsymbol{\rho}_0 - \boldsymbol{\rho}_2)]\mathrm{d}\boldsymbol{\rho}_2. \quad (10)$$

Performing an inverse Fourier transform of this intensity gives the following equation:

$$FT^{-1}[I(\mathbf{k})](\boldsymbol{\rho}) = FT^{-1}[I_0(\mathbf{k})](\boldsymbol{\rho}) + CC^*W(\boldsymbol{\rho}_0, \boldsymbol{\rho}_0)\delta(\boldsymbol{\rho}) + CW(\boldsymbol{\rho}_0 + \boldsymbol{\rho}, \boldsymbol{\rho}_0) + C^*W(\boldsymbol{\rho}_0, \boldsymbol{\rho}_0 - \boldsymbol{\rho}). \quad (11)$$

To measure the CSD function of the PC-PEPV beam, the phase assignments φ need to be assigned three times to get three equations, and the CSD function can be calculated *via* the following equation:

$$W(\boldsymbol{\rho}, 0) = FT^{-1}\left\{\frac{(C_3 - C_1)[I_2 - I_1] - (C_2 - C_1)[I_3 - I_1]}{(C_3 - C_1)(C_2^* - C_1^*) - (C_3^* - C_1^*)(C_2 - C_1)}\right\}. \quad (12)$$

Here, C_1, C_2, and C_3 represent three different phase perturbations with φ equal to φ_1, φ_2, and φ_3, which should be chosen as far away as possible within 2π (i.e., phase working range of SLM_2 with wavelength equal to 532 nm). It can help obtain three intensities with maximum difference and enhance the signal to noise ratio of the retrieval. Here, we set $\varphi_1 = 0$, $\varphi_2 = -2\pi/3$, and $\varphi_3 = 2\pi/3$.

RESULTS AND DISCUSSION

Numerical Simulation Results With Different Coherence Width and TC

In this section, we investigate the properties of the PC-PEPV beam focused by a thin Fourier lens *via* numerical calculation based on the complex random screen decomposition [53–55]. **Figure 4** illustrates the initial phase patterns of PC-PEPV beams on the source plane and the simulated distributions of PC-PEPV beams on the focal plane with high initial spatial coherence width ($\sigma = 20$ mm), including the intensity, and the modulus and phase of the CSD function with on-axis reference ($r_2 = 0$, $\theta_2 = 0$). The initial spatial coherence width means the transverse width between the maximum value to the point with $e^{-1/2}$ the maximum value of the modulus of the degree of coherence [23]. Here, $\lambda = 532$ nm, $w_0 = 1$ mm, $f = 300$ mm, power order $n = 2$, and TCs $m = 2$, 3, 4, and 5. The simulated initial phase patterns and intensity patterns are shown in the first and second rows of **Figure 4**, respectively. It is observed that the initial phase exhibits a periodic power exponential change and the polygonal optical vortex arrays are generated, respectively. The number of the dark cores are $N = 2$, 3, 4, and 5, which are equal to the absolute value of the TC. Note that each dark core is a unit vortex with TC = +1 so that they are separated imperfect doughnut-like dark core. Moreover, the geometry of the generated PC-PEPV beam are elliptic, triangular, quadrangle, and pentagon, respectively, which is specific compared with the conventional vortex beam that has a "doughnut-like" profile. In this case where we have a high initial spatial coherence width, the number of vortices and the geometry of the PC-PEPV beam can be freely modulated *via* adjusting the values of the TC.

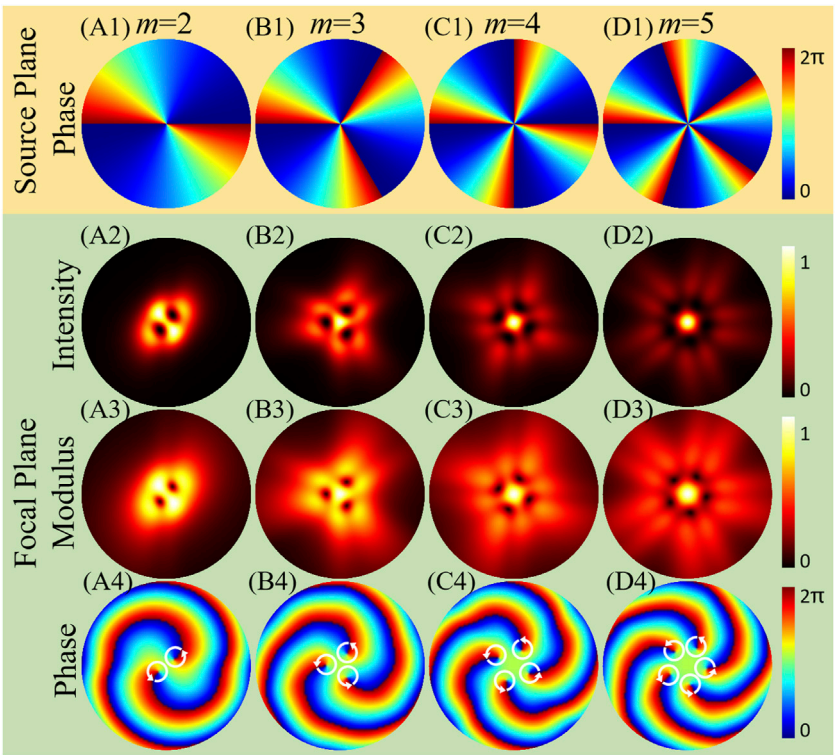

FIGURE 4 | Numerical simulation initial phases, intensities, and CSD distributions of the PC-PEPV with high spatial coherence (σ = 20 mm) and power order n = 2. **(A1–D1)** are the initial phases on the source plane, **(A2–D2)** are the intensity patterns, **(A3–D3)** are the modulus of the CSD function, and **(A4–D4)** are the phase patterns of the CSD function. All results are calculated on the focal plane, except the initial phase. White circular arrows represent the anticlockwise direction of the phase winding which indicates the positive TC.

However, as the TC increases, the intensity becomes higher for the central spot and lower for the outer region. The reason is that radius of a vortex beam will increase with the TC increase, which causes the total energy to disperse in the outer region. As a consequence, the dark cores in the intensity gradually become indistinguishable and the value of the TC becomes difficult to determine. To solve this problem, we calculated the modulus and the phase of the CSD function, as shown in the third and bottom rows of **Figure 4**, respectively. The structure of the modulus is similar to the intensity pattern when the initial spatial coherence width σ is much larger than the beam waist w_0. Furthermore, the number of the dark cores in the modulus of the CSD function also equals the magnitude of the TC. To verify the sign of the vortex, the corresponding phase patterns are shown in **Figures 4A4–D4**. The phase rotation of coherence singularities is marked by the white circular arrow. Anticlockwise corresponds to a positive sign of TC and clockwise indicates that the TC is negative [56]. The locations of these phase singularities correspond to those of the dark cores in the modulus of the CSD function. Furthermore, it can be seen from the phases that a light spot appeared in the center of intensity owing to the split of the singularities.

Then we studied the characteristic of the PC-PEPV beam with a medium spatial coherence width, which is equal to the beam waist (σ = 1 mm). The intensity patterns of the PC-PEPV beam are depicted in **Figures 5A1–D1**, which show that the focusing properties are very different between the PC-PEPV beam with different spatial coherence widths. The dark cores in the PC-PEPV beam at the focal plane disappear gradually as the coherence width σ decreases. When the TC is equal to 2 and 3, the zero-intensity dark cores in the high coherence case become low-intensity cores, as shown in **Figures 5A1,B1**. As the TC became larger, as shown in **Figures 5C1,D1**, the dark cores nearly disappeared, and the geometric structure of the vortex array disappeared at the same time. In this case, we could not determine the magnitude of the TC from its intensity. However, the modulus of the CSD function distribution in **Figures 5A2–D2** remains the same as that in **Figure 4** for high coherence case. Even for TC equals 5, one can also clearly tell that the number of the dark cores is equal to the number of the TC. Meanwhile, the magnitude and sign of the TC also can be determined *via* the phase distribution, as depicted in the bottom row of **Figure 5**.

In **Figure 6**, we consider a low spatial coherence (σ = 0.5 mm) to investigate the properties of the PC-PEPV beam. The dark cores in the intensity have completely vanished due to the modes overlapping for the partially coherent beam with lower coherence width [37]. The intensity is Gaussian distributed, and the geometry of the PC-PEPV beam becomes elliptic, triangular, quadrangle, and pentagon light spots which is specific compared with the conventional partially coherent vortex beam (show a circular intensity spot with Gaussian distribution) [32]. If the coherence width decreases further, the

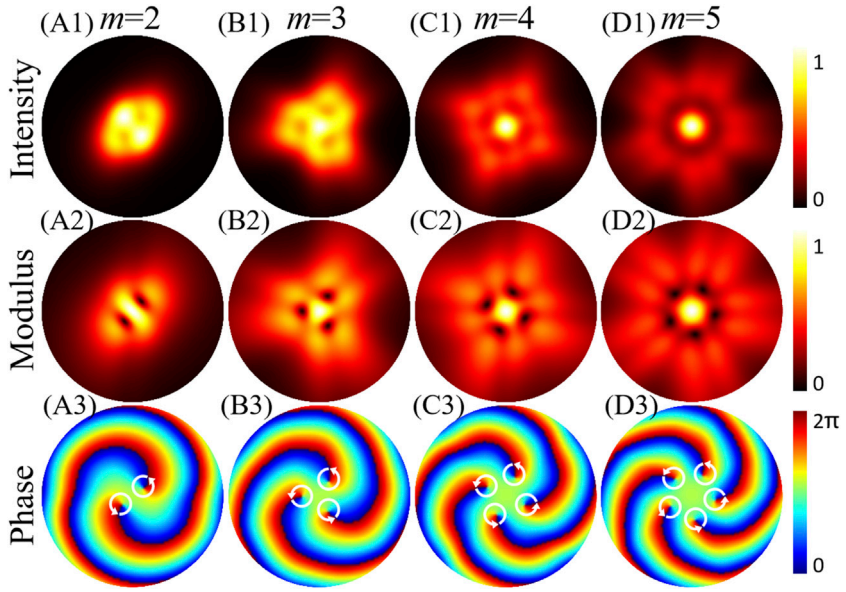

FIGURE 5 | Numerical simulation intensities and CSD distributions of the PC-PEPV beams on the focal plane with medium spatial coherence equal to the beam waist (σ = 1 mm) and power order n = 2. **(A1–D1)** are the intensity patterns, **(A2–D2)** are the modulus of the CSD function, and **(A3–D3)** are the phase patterns of the CSD function. White circular arrows represent the anticlockwise direction of the phase winding which indicates the positive TC.

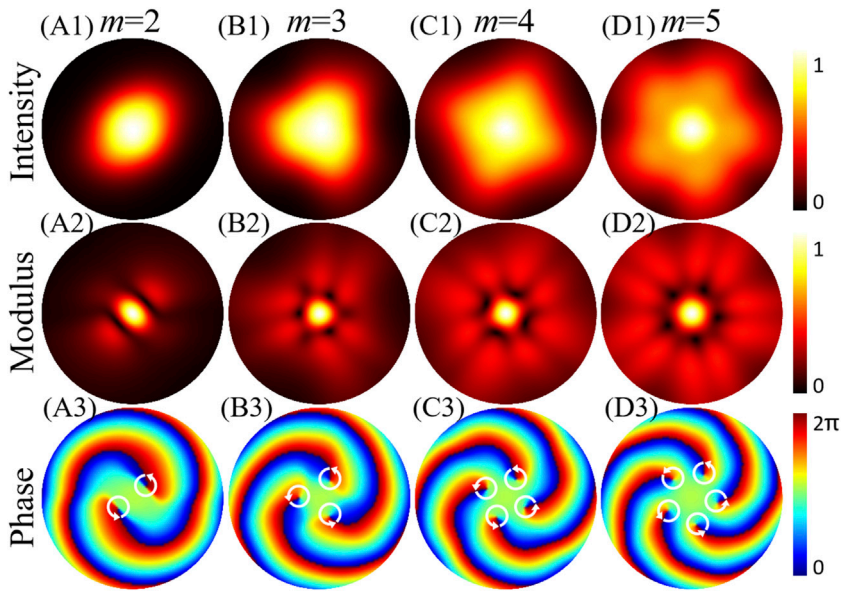

FIGURE 6 | Numerical simulation intensities and CSD distributions of the PC-PEPV beams on the focal plane with low spatial coherence (σ = 0.5 mm) and power order n = 2. **(A1–D1)** are the intensity patterns, **(A2–D2)** are the modulus of the CSD function, and **(A3–D3)** are the phase patterns of the CSD function. White circular arrows represent the anticlockwise direction of the phase winding which indicates the positive TC.

PC-PEPV beam will degenerate to a circularly symmetric Gaussian distribution [57]. From the low coherence intensity patterns, we could not find any information about the TC. However, we can still find the magnitude and sign of the TC from the modulus and phase of the CSD function, as shown in the middle and bottom rows of **Figure 6**.

Regulation Characteristics of the Power Order

As well known, the TC can be negative. In the aforementioned discussion of **Figures 4–6**, the sign of the TC m must be positive due to the power order n = 2. However, with the power order n = 3, the TC of the PC-PEPV beam can be both

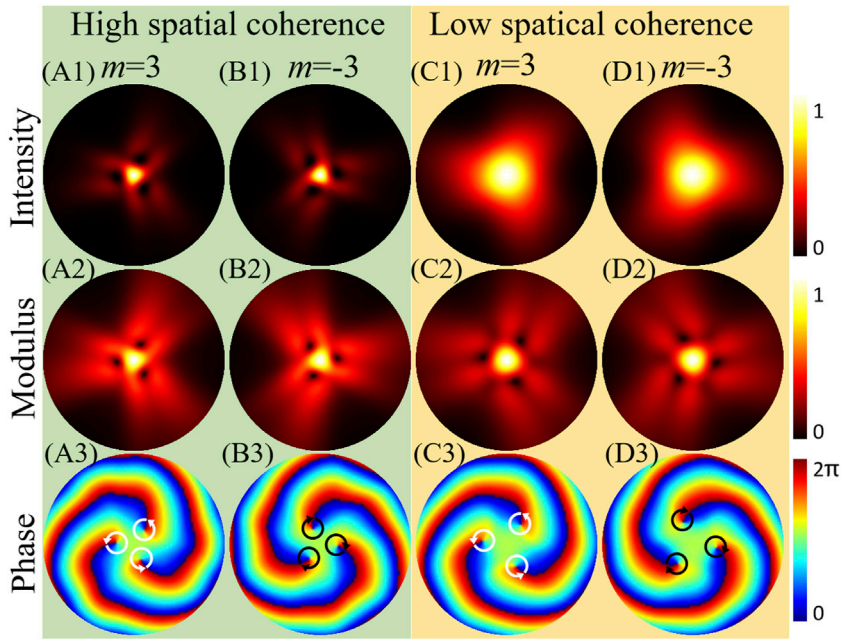

FIGURE 7 | Numerical simulation intensities and CSD distributions of the PC-PEPV beams on the focal plane with positive and negative TCs and power order $n = 3$ under high and low spatial coherence ($\sigma = 20$ and 0.5 mm). **(A1–D1)** are the intensity patterns, **(A2–D2)** are the modulus of the CSD function, and **(A3–D3)** are the phase patterns of the CSD function. White circular arrows represent the anticlockwise direction of the phase winding which indicates the positive TC.

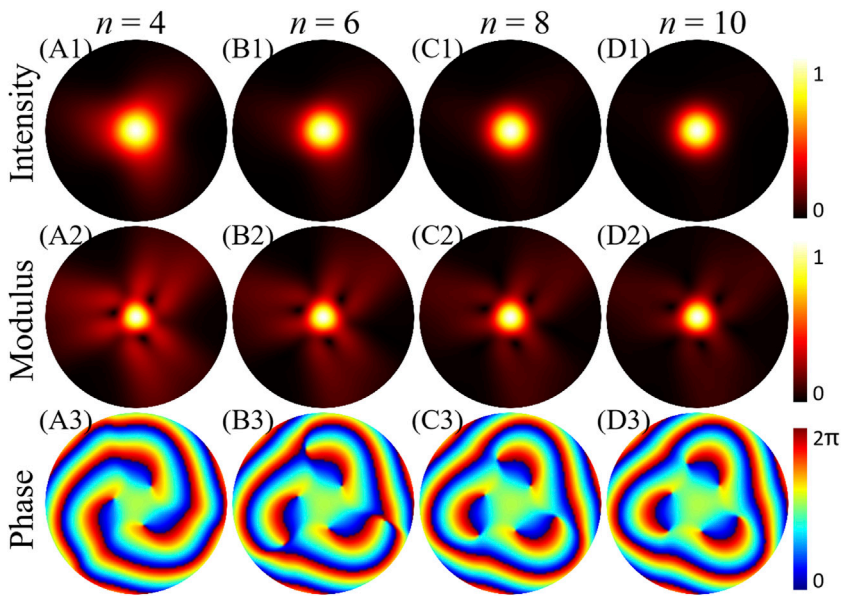

FIGURE 8 | Numerical simulation of intensities and CSD distributions of the PC-PEPV beams on the focal plane with TC $m = 3$ and low spatial coherence ($\sigma =$ 0.5 mm). **(A1–D1)** are the intensity patterns, **(A2–D2)** are the modulus of the CSD function, and **(A3–D3)** are the phase patterns of the CSD function.

positive and negative, as shown in **Figure 7**. The intensity, modulus, and phase of the CSD function of the PC-PEPV beam with high coherence width ($\sigma = 20$ mm) and TC ($m = 3$ and -3) are depicted in **Figures 7A1–A3**; **Figures 7B1–B3**, respectively. Meanwhile, the PC-PEPV beam with low coherence width ($\sigma =$ 0.5 mm) and TC ($m = 3$ and -3) are demonstrated in **Figures 7C1–C3** and **Figures 7D1–D3**, respectively. Compared with $n = 2$, the intensity of the central light spot increases and the intensities of the dark cores decrease. This is because the larger power order value makes the zeroth component of the spiral phase higher [21]. In

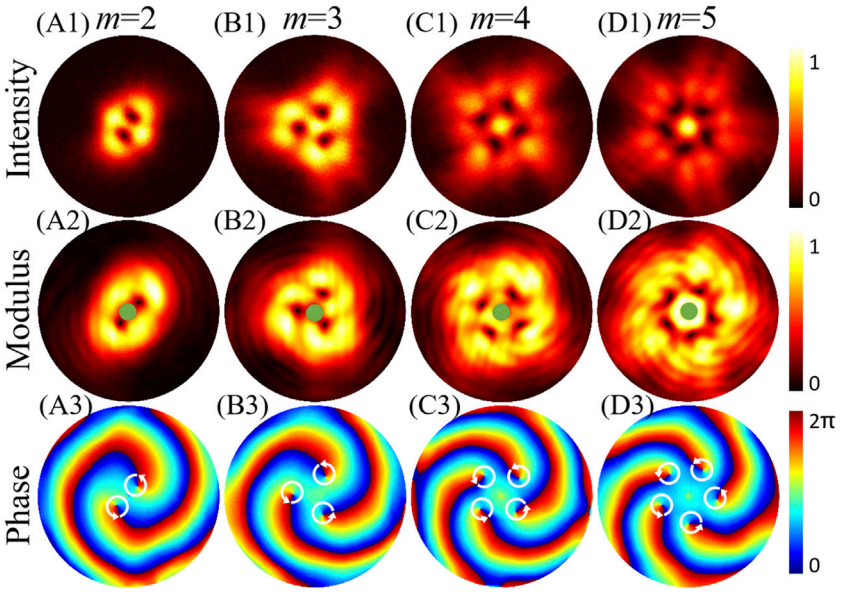

FIGURE 9 | Experimental intensity on CCD_1 and CSD distributions of the PC-PEPV beam with high spatial coherence width (σ = 20 mm). **(A1–D1)** are intensity patterns, **(A2–D2)** are modulus of the CSD function, and **(A3–D3)** are phase patterns of the CSD function.

addition, the magnitude and sign of the TC can be determined by the modulus and phase of the CSD function patterns. As depicted in **Figures 7A3–D3**, the anticlockwise phase winding (positive TC) and clockwise phase winding (negative TC) of coherence singularities are marked by the white and black circle arrows, respectively. The positive and negative of TC is relative, which is based on the theoretical model of the vortex phase, that is, **Equation 1**.

To further study the influence of the power order n, the numerical simulation intensities and CSD distributions of the PC-PEPV beam with power order n increase from 4 to 10 with step 2 are shown in **Figure 8**. Here, the TC m equals 3 and low spatial coherence σ is equal to 0.5 mm. In contrast to the aforementioned PC-PEPV beam with small power order n, the intensity transforms from triangular to approximately a Gaussian form with the increase of power order n, as shown in **Figures 8A1–D1** The reason is that the initial phase of the PC-PEPV beam is approaching to a constant with an increase power order n [21]. In addition, as shown in **Figures 8A2–D2** the modulus of the CSD function remains the same structure but decreases intensity in the outer region. It is interesting to note that the three positive singularities split to three positive and negative singularity pairs, which cause the total TC approach to 0 owing to annihilate between the singularity pairs, as depicted in **Figures 8A3–D3**.

Corresponding Experimental Results of the PC-PEPV Beam

Figure 9 shows the experimental measurements of the PC-PEPV beam with high coherence width (σ = 20 mm), and the other parameters are the same as that in **Figure 4**. The first row of **Figure 9** depicts the experimental intensity patterns of the PC-PEPV beam captured with CCD_1, which agree well with the numerical simulation results in **Figure 4**. The middle row demonstrates the experimental modulus of the CSD function of the PC-PEPV beam. The green spots represent the perturbation point located in the center. For TC equals 2, 3, 4, and 5, we can observe 2, 3, 4, 5 dark cores in the modulus of the CSD function, respectively, whose location correspond to the intensity dark cores. The number of the dark cores in the intensity and modulus of the CSD function both indicate the magnitude of the TC. Furthermore, based on **Eq. 12**, we can also get the phase distributions of CSD function of the PC-PEPV beam, as shown in **Figures 9A3–D3**. When TC is positive, the phase winding is anticlockwise and consistent for all the coherence singularities. The number of coherence singularities indicates the magnitude of TC and the orientation reveals the sign of the TC.

Figures 10, **11** show the experimental results of the PC-PEPV beam with medium (σ = 1 mm in **Figure 10**) and low spatial coherences (σ = 0.5 mm in **Figure 11**). The other parameters are the same as those in **Figures 5**, **6**, respectively. As shown in the first row of **Figures 10**, **11**, the dark cores in the intensity patterns fade away when the coherence width decreases, and the magnitude of the TC can no longer be determined from the intensity distributions. However, we can also obtain the magnitude of the TC from its retrieved modulus of the CSD function, as shown in the middle row of **Figures 10**, **11**. Similarly, both the sign and magnitude of the TC can be determined from the phase patterns, as shown in the bottom row of **Figures 10**, **11**. In the case with low coherence, the PC-PEPV beam with elliptic, triangular, quadrangle, and pentagon structures can be generated experimentally. The results may be useful in the field of beam shaping and optical trapping.

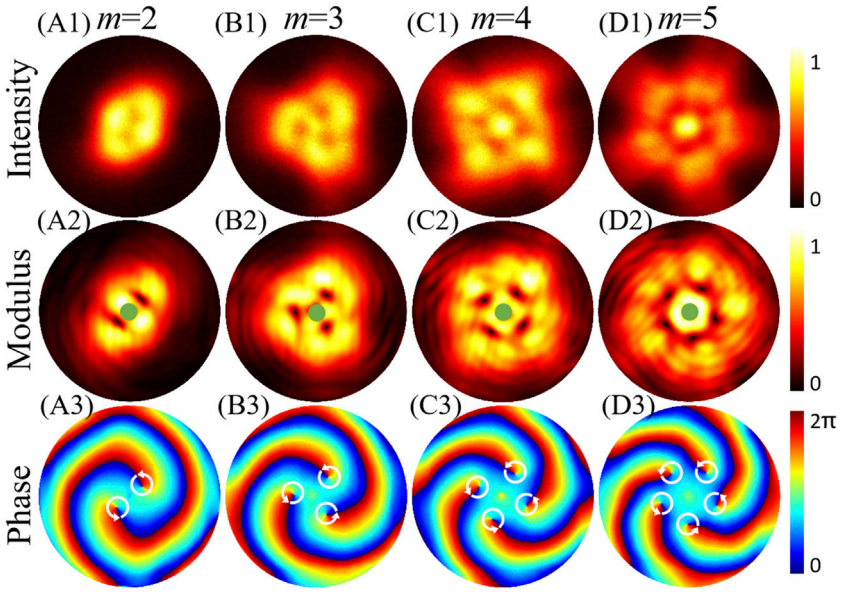

FIGURE 10 | Experimental intensity on CCD_1 and CSD distributions of the PC-PEPV beam with medium spatial coherence width (σ = 1 mm). **(A1–D1)** are intensity patterns, **(A2–D2)** are modulus of the CSD function, and **(A3–D3)** are phase patterns of the CSD function.

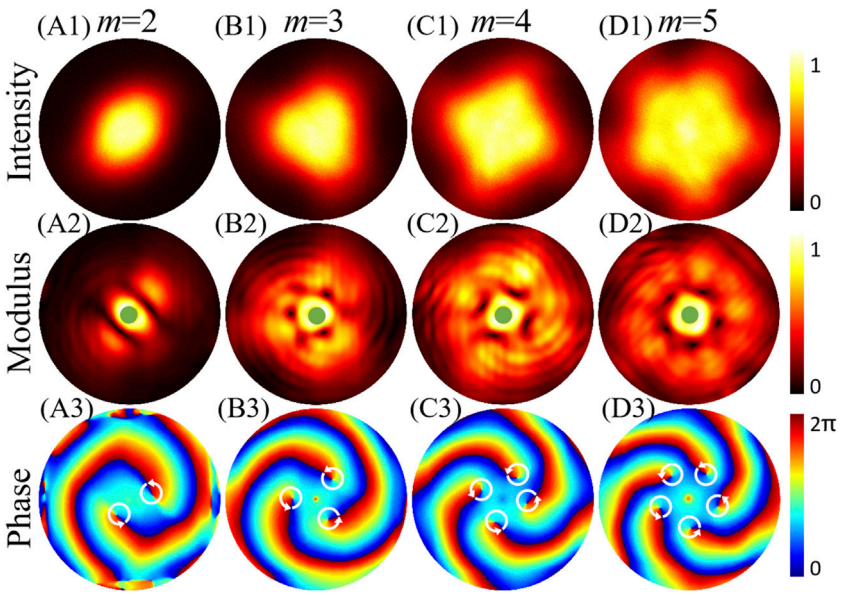

FIGURE 11 | Experimental intensity on CCD_1 and CSD distributions of the PC-PEPV beam with low spatial coherence width (σ = 0.5 mm). **(A1–D1)** are intensity patterns, **(A2–D2)** are modulus of the CSD function, and **(A3-D3)** are phase patterns of the CSD function.

In addition, with odd power order (n = 3), the PC-PEPV beam with positive and negative TC are generated experimentally, as depicted in **Figure 12**. All parameters of the PC-PEPV beam are same as those in **Figure 7**. The intensity and the modulus and phase of the CSD function are in agreement with the simulation results in **Figure 7**. Based on the aforementioned discussion, we know that the TC can adjust the polygonal structure of the PC-PEPV beam. Furthermore, the power order can also help realize a precise manipulation of the structure from circle to polygonal. The details of the numerical simulations and experimental intensities of the PC-PEPV beam (m = 3) with high and low spatial coherence are shown in Videos 1 and 2 (mmc 1 mmc 2 of the Supplementary Material), respectively, where the power order n increase from 1 to 3 with step 0.1.

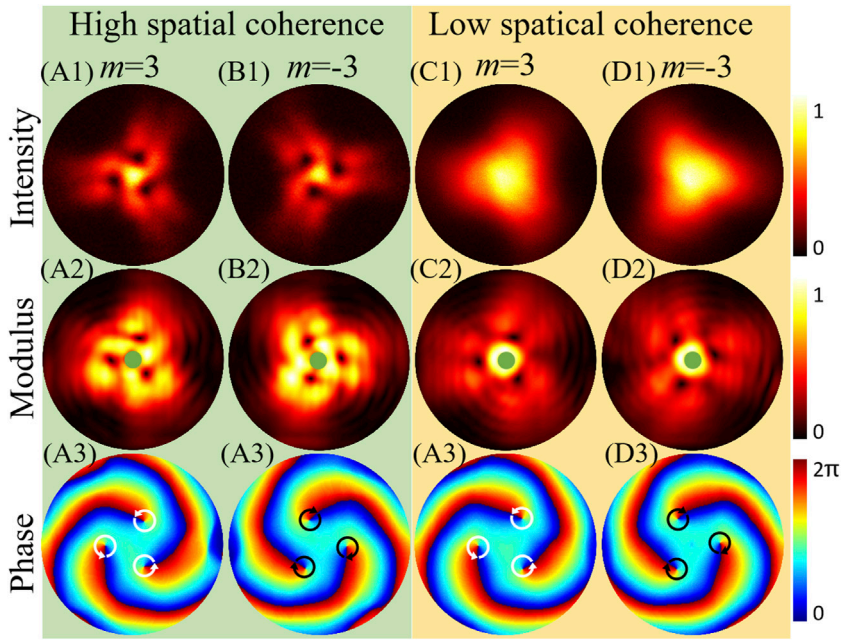

FIGURE 12 | Experimental intensity on CCD_1 and CSD distributions of the PC-PEPV beam with odd power order $n = 3$ and positive and negative TCs under high (σ = 20 mm) and low spatial coherence width (σ = 0.5 mm). **(A1–D1)** are intensity patterns, **(A2–D2)** are modulus of the CSD function, and **(A3–D3)** are phase patterns of the CSD function.

CONCLUSION

In conclusion, we have introduced the theoretical model of a PC-PEPV beam and studied its propagation properties numerically and experimentally. Different from the conventional partially coherent vortex beam where only a circular intensity distribution remains, the polygonal-structured intensity distribution of the PC-PEPV beam is manipulated by the value of the TC, and the polygonal vortex array is transformed into a polygonal light spot by decreasing the spatial coherence width. Furthermore, the value of the power order is used to control the details of the structure. For a PC-PEPV beam, the magnitude and sign of the TC can be determined by the coherence singularities in modulus and phase of CSD function, even when the optical array structure in the intensity fades away as the spatial coherence decreases. Moreover, when the power order is even, the sign of the TC is always positive. Our experimental results agree well with the numerical simulation results. We believe that the results will be useful for beam shaping and optical trapping.

DATA AVAILABILITY STATEMENT

The original contributions presented in the study are included in the article/**Supplementary Material**, further inquiries can be directed to the corresponding authors.

AUTHOR CONTRIBUTIONS

HZ proposed the idea. HZ and XL wrote the original manuscript. HZ and ZW performed the experiment. AK, HW, and CZ gave suggestions in numerical simulations. CZ and YC supervised the project. All authors contributed to the revision of the manuscript and approved the final version.

FUNDING

This work was supported by the National Key Research and Development Program of China (2019YFA0705000), National Natural Science Foundation of China (12174280, 11774250, 11974218, and 91750201), Innovation Group of Jinan (2018GXRC010), Priority Academic Program Development of Jiangsu Higher Education Institutions, China Scholarship Council (201906920048), and Tang Scholar, Local Science and Technology Development Project of the Central Government (YDZX20203700001766).

SUPPLEMENTARY MATERIAL

The Supplementary Material for this article can be found online at: https://www.frontiersin.org/articles/10.3389/fphy.2021.781688/full#supplementary-material

REFERENCES

1. Allen L, Beijersbergen MW, Spreeuw RJC, Woerdman JP. Orbital Angular Momentum of Light and the Transformation of Laguerre-Gaussian Laser Modes. *Phys Rev A* (1992) 45:8185–9. doi:10.1103/PhysRevA.45.8185
2. Grier DG. A Revolution in Optical Manipulation. *Nature* (2003) 424:810–6. doi:10.1038/nature01935
3. Padgett M, Bowman R. Tweezers with a Twist. *Nat Photon* (2011) 5:343–8. doi:10.1038/NPHOTON.2011.81
4. Li X, Zhou Y, Cai Y, Zhang Y, Yan S, Li M, et al. Generation of Hybrid Optical Trap Array by Holographic Optical Tweezers. *Front Phys* (2021) 9:591747. doi:10.3389/fphy.2021.591747
5. Zhang H, Li X, Ma H, Tang M, Li H, Tang J, et al. Grafted Optical Vortex with Controllable Orbital Angular Momentum Distribution. *Opt Express* (2019) 27: 22930–8. doi:10.1364/OE.27.022930
6. Wang J, Yang J-Y, Fazal IM, Ahmed N, Yan Y, Huang H, et al. Terabit Free-Space Data Transmission Employing Orbital Angular Momentum Multiplexing. *Nat Photon* (2012) 6:488–96. doi:10.1038/NPHOTON.2012.138
7. McLaren M, Agnew M, Leach J, Roux FS, Padgett MJ, Boyd RW, et al. Entangled Bessel-Gaussian Beams. *Opt Express* (2012) 20:23589–97. doi:10.1364/OE.20.023589
8. Bozinovic N, Yue Y, Ren Y, Tur M, Kristensen P, Huang H, et al. Terabit-scale Orbital Angular Momentum Mode Division Multiplexing in Fibers. *Science* (2013) 340:1545–8. doi:10.1126/science.1237861
9. Lavery MPJ, Speirits FC, Barnett SM, Padgett MJ. Detection of a Spinning Object Using Light's Orbital Angular Momentum. *Science* (2013) 341:537–40. doi:10.1126/science.1239936
10. Forbes A, Dudley A, McLaren M. Creation and Detection of Optical Modes with Spatial Light Modulators. *Adv Opt Photon* (2016) 8:200–27. doi:10.1364/AOP.8.000200
11. Tamburini F, Anzolin G, Umbriaco G, Bianchini A, Barbieri C. Overcoming the Rayleigh Criterion Limit with Optical Vortices. *Phys Rev Lett* (2006) 97: 163903. doi:10.1103/PhysRevLett.97.163903
12. Rodrigo JA, Alieva T. Freestyle 3D Laser Traps: Tools for Studying Light-Driven Particle Dynamics and beyond. *Optica* (2015) 2:812–5. doi:10.1364/OPTICA.2.000812
13. Kotlyar VV, Kovalev AA, Soifer VA. Asymmetric Bessel Modes. *Opt Lett* (2014) 39:2395–8. doi:10.1364/OL.39.002395
14. Ma H, Li X, Zhang H, Tang J, Li H, Tang M, et al. Optical Vortex Shaping via a Phase Jump Factor. *Opt Lett* (2019) 44:1379–82. doi:10.1364/OL.44.001379
15. Yang Y, Zhu X, Zeng J, Lu X, Zhao C, Cai Y. Anomalous Bessel Vortex Beam: Modulating Orbital Angular Momentum with Propagation. *Nanophotonics* (2018) 7:677–82. doi:10.1515/nanoph-2017-0078
16. Li P, Liu S, Peng T, Xie G, Gan X, Zhao J. Spiral Autofocusing Airy Beams Carrying Power-exponent-phase Vortices. *Opt Express* (2014) 22:7598–606. doi:10.1364/OE.22.007598
17. Lao G, Zhang Z, Zhao D. Propagation of the Power-exponent-phase Vortex Beam in Paraxial ABCD System. *Opt Express* (2016) 24:18082–94. doi:10.1364/OE.24.018082
18. Cheng S, Xia T, Liu M, Jin Y, Zhang G, Xiong Y, et al. Power-exponent Helico-Conical Optical Beams. *Opt Laser Techn* (2019) 117:288–92. doi:10.1016/j.optlastec.2019.04.041
19. Wang H, Tang L, Ma J, Hao H, Zheng X, Song D, et al. Optical Clearing and Shielding with Fan-Shaped Vortex Beams. *APL Photon* (2020) 5:016102. doi:10.1063/1.5133100
20. Pei Z, Huang S, Chen Y, Yan C. Comparison of Microparticle Manipulating Characteristics of Canonical Vortex Beam and Power-exponent-phase Vortex Beam. *J Mod Opt* (2021) 68:224–32. doi:10.1080/09500340.2021.1889060
21. Shen D, Wang K, Zhao D. Generation and Propagation of a New Kind of Power-exponent-phase Vortex Beam. *Opt Express* (2019) 27:24642–53. doi:10.1364/OE.27.024642
22. Wolf E. Optics in Terms of Observable Quantities. *Nuovo Cim* (1954) 12: 884–8. doi:10.1007/BF02781855
23. Mandel L, Wolf E. *Optical Coherence and Quantum Optics*. Cambridge: Cambridge University Press (1995).
24. Cai Y, Peschel U. Second-harmonic Generation by an Astigmatic Partially Coherent Beam. *Opt Express* (2007) 15:15480–92. doi:10.1364/OE.15.015480
25. Ricklin JC, Davidson FM. Atmospheric Optical Communication with a Gaussian Schell Beam. *J Opt Soc Am A* (2003) 20:856–66. doi:10.1364/JOSAA.20.000856
26. Ricklin JC, Davidson FM. Atmospheric Turbulence Effects on a Partially Coherent Gaussian Beam: Implications for Free-Space Laser Communication. *J Opt Soc Am A* (2002) 19:1794–802. doi:10.1364/JOSAA.19.001794
27. Zhao C, Cai Y, Lu X, Eyyuboğlu HT. Radiation Force of Coherent and Partially Coherent Flat-Topped Beams on a Rayleigh Particle. *Opt Express* (2009) 17: 1753–65. doi:10.1364/OE.17.001753
28. Zhang J-F, Wang Z-Y, Cheng B, Wang Q-Y, Wu B, Shen X-X, et al. Atom Cooling by Partially Spatially Coherent Lasers. *Phys Rev A* (2013) 88:023416. doi:10.1103/PhysRevA.88.023416
29. Cai Y, Zhu S-Y. Ghost Interference with Partially Coherent Radiation. *Opt Lett* (2004) 29:2716–8. doi:10.1364/OL.29.002716
30. Liu X, Wang F, Zhang M, Cai Y. Experimental Demonstration of Ghost Imaging with an Electromagnetic Gaussian Schell-Model Beam. *J Opt Soc Am A* (2015) 32:910–20. doi:10.1364/JOSAA.32.000910
31. Gori F, Santarsiero M, Borghi R, Vicalvi S. Partially Coherent Sources with Helicoidal Modes. *J Mod Opt* (1998) 45:539–54. doi:10.1080/09500349808231913
32. Wang F, Cai Y, Korotkova O. Partially Coherent Standard and Elegant Laguerre-Gaussian Beams of All Orders. *Opt Express* (2009) 17:22366–79. doi:10.1364/OE.17.022366
33. Li J, Zhang H, Lü B. Partially Coherent Vortex Beams Propagating through Slant Atmospheric Turbulence and Coherence Vortex Evolution. *Opt Laser Techn* (2010) 42:428–33. doi:10.1016/j.optlastec.2009.08.019
34. Raburn WS, Gbur G. Singularities of Partially Polarized Vortex Beams. *Front Phys* (2020) 8:168. doi:10.3389/fphy.2020.00168
35. Zeng J, Liu X, Wang F, Zhao C, Cai Y. Partially Coherent Fractional Vortex Beam. *Opt Express* (2018) 26:26830–44. doi:10.1364/OE.26.026830
36. Ostrovsky AS, García-García J, Rickenstorff-Parrao C, Olvera-Santamaría MA. Partially Coherent Diffraction-free Vortex Beams with a Bessel-Mode Structure. *Opt Lett* (2017) 42:5182–5. doi:10.1364/OL.42.005182
37. Dong M, Zhao C, Cai Y, Yang Y. Partially Coherent Vortex Beams: Fundamentals and Applications. *Sci China Phys Mech Astron* (2021) 64: 224201. doi:10.1007/s11433-020-1579-9
38. Liu R, Wang F, Chen D, Wang Y, Zhou Y, Gao H, et al. Measuring Mode Indices of a Partially Coherent Vortex Beam with Hanbury Brown and Twiss Type experiment. *Appl Phys Lett* (2016) 108:051107. doi:10.1063/1.4941422
39. Gallo K, Assanto G. All-optical Diode Based on Second-Harmonic Generation in an Asymmetric Waveguide. *J Opt Soc Am B* (1999) 16:267–9. doi:10.1364/JOSAB.16.000267
40. Masters BR. Three-dimensional Microscopic Tomographic Imaging of the Cataract in a Human Lens *In Vivo*. *Opt Express* (1998) 3:332–8. doi:10.1364/OE.3.000332
41. Yelin D, Oron D, Thiberge S, Moses E, Silberberg Y. Multiphoton Plasmon-Resonance Microscopy. *Opt Express* (2003) 11:1385–91. doi:10.1364/OE.11.001385
42. Gbur G, Visser TD. Coherence Vortices in Partially Coherent Beams. *Opt Commun* (2003) 222:117–25. doi:10.1016/S0030-4018(03)01606-7
43. Gbur G, Visser TD, Wolf E. Hidden Singularities in Partially Coherent Wavefields. *J Opt A: Pure Appl Opt* (2004) 6:S239–S242. doi:10.1088/1464-4258/6/5/017
44. Cai Y, Chen C. Paraxial Propagation of a Partially Coherent Hermite-Gaussian Beam through Aligned and Misaligned ABCD Optical Systems. *J Opt Soc Am A* (2007) 24:2394–401. doi:10.1364/JOSAA.24.002394
45. Zeng J, Lu X, Liu L, Zhu X, Zhao C, Cai Y. Simultaneous Measurement of the Radial and Azimuthal Mode Indices of a Higher-Order Partially Coherent Vortex Beam Based on Phase Detection. *Opt Lett* (2019) 44:3881–4. doi:10.1364/OL.44.003881
46. Liu X, Shen Y, Liu L, Wang F, Cai Y. Experimental Demonstration of Vortex Phase-Induced Reduction in Scintillation of a Partially Coherent Beam. *Opt Lett* (2013) 38:5323–6. doi:10.1364/OL.38.005323
47. Cai Y, Chen Y, Yu J, Liu X, Liu L. Generation of Partially Coherent Beams. *Prog Opt* (2017) 62:157–223. doi:10.1016/bs.po.2016.11.001
48. Palacios DM, Maleev ID, Marathay AS, Swartzlander GA. Spatial Correlation Singularity of a Vortex Field. *Phys Rev Lett* (2004) 92:143905. doi:10.1103/PhysRevLett.92.143905

49. Zeng J, Liu X, Zhao C, Wang F, Gbur G, Cai Y. Spiral Spectrum of a Laguerre-Gaussian Beam Propagating in Anisotropic Non-kolmogorov Turbulent Atmosphere along Horizontal Path. *Opt Express* (2019) 27:25342–56. doi:10.1364/OE.27.025342
50. Pinnell J, Nape I, Sephton B, Cox MA, Rodríguez-Fajardo V, Forbes A. Modal Analysis of Structured Light with Spatial Light Modulators: a Practical Tutorial. *J Opt Soc Am A* (2020) 37:C146–C160. doi:10.1364/JOSAA.398712
51. Shao Y, Lu X, Konijnenberg S, Zhao C, Cai Y, Urbach HP. Spatial Coherence Measurement and Partially Coherent Diffractive Imaging Using Self-Referencing Holography. *Opt Express* (2018) 26:4479–90. doi:10.1364/OE.26.004479
52. Lu X, Shao Y, Zhao C, Konijnenberg S, Zhu X, Tang Y, et al. Noniterative Spatially Partially Coherent Diffractive Imaging Using Pinhole Array Mask. *Adv Photon* (2019) 1:1. doi:10.1117/1.AP.1.1.016005
53. Xiao X, Voelz D. Wave Optics Simulation Approach for Partial Spatially Coherent Beams. *Opt Express* (2006) 14:6986–92. doi:10.1364/OE.14.006986
54. Voelz D, Xiao X, Korotkova O. Numerical Modeling of Schell-Model Beams with Arbitrary Far-Field Patterns. *Opt Lett* (2015) 40:352–5. doi:10.1364/OL.40.000352
55. Tong R, Dong Z, Chen Y, Wang F, Cai Y, Setälä T. Fast Calculation of Tightly Focused Random Electromagnetic Beams: Controlling the Focal Field by Spatial Coherence. *Opt Express* (2020) 28:9713–27. doi:10.1364/OE.386187
56. Li X, Zhang H. Anomalous Ring-Connected Optical Vortex Array. *Opt Express* (2020) 28:13775–85. doi:10.1364/OE.390985
57. Zhao C, Wang F, Dong Y, Han Y, Cai Y. Effect of Spatial Coherence on Determining the Topological Charge of a Vortex Beam. *Appl Phys Lett* (2012) 101:261104. doi:10.1063/1.4773236

Conflict of Interest: The authors declare that the research was conducted in the absence of any commercial or financial relationships that could be construed as a potential conflict of interest.

Publisher's Note: All claims expressed in this article are solely those of the authors and do not necessarily represent those of their affiliated organizations, or those of the publisher, the editors, and the reviewers. Any product that may be evaluated in this article, or claim that may be made by its manufacturer, is not guaranteed or endorsed by the publisher.

frontiers in Physics

REVIEW
published: 29 November 2021
doi: 10.3389/fphy.2021.773505

Generation, Transmission and Application of Orbital Angular Momentum in Optical Fiber: A Review

Minghao Ma[1,2], *Yudong Lian*[1,2]*, *Yulei Wang*[1,2] *and Zhiwei Lu*[1,2]

[1]Center for Advanced Laser Technology, Hebei University of Technology, Tianjin, China, [2]Hebei Key Laboratory of Advanced Laser Technology and Equiment, Tianjin, China

Optical orbital angular momentum (OAM) has become a hot research topic because of its unique properties due to its spiral distribution of phases. The production and transmission of OAM has also become a necessary condition for effective use of OAM. As an optical waveguide with good propagation properties, optical fibers are used in optical systems supporting OAM. This paper introduces the OAM generation and transmission system based on fiber, summarizes the current photonic crystal fiber, ring core fiber, fiber grating and other all-fiber systems that can support OAM modes, and explains some experimental principles. Finally, an outlook on OAM generation or transmission devices for all-fiber systems is presented, providing a useful reference for future related research.

OPEN ACCESS

Editors by:
Gianluca Ruffato,
University of Padua, Italy

Reviewed by:
Tingyun Wang,
Shanghai University, China
Zhenkun Wu,
Henan University, China.

***Correspondence:**
Yudong Lian
ydlian@hebut.edu.cn

Specialty section:
This article was submitted to Soft Matter Physics, a section of the journal Frontiers in Physics

Received: 10 September 2021
Accepted: 08 November 2021
Published: 29 November 2021

Citation:
Ma M, Lian Y, Wang Y and Lu Z (2021) Generation, Transmission and Application of Orbital Angular Momentum in Optical Fiber: A Review. Front. Phys. 9:773505. doi: 10.3389/fphy.2021.773505

Keywords: orbital angular momentum, photonic crystal fiber, ring core fiber, fiber grating, mode selective coupler

INTRODUCTION

Since Allen et al. [1] discovered the orbital angular momentum (OAM) contained in the vortex beam, OAM has been widely used. Because the vortex beam has a phase factor of $e^{il\varphi}$, its phase distribution presents a spiral shape. Due to the unique properties, OAM beams have a wide range of applications in microscopy [2, 3], micromanipulation [4, 5], optical tweezers [6, 7], nonlinear optics [8, 9], quantum communication [10, 11], and so on. In the traditional optical communication, the multiplexing technology improves the communication capacity by multiplexing the optical wave from the aspects of wavelength, frequency and space, but the communication capacity is close to the Shannon limit [12]. OAM has a spirally distributed phase, and different OAM modes are orthogonal to each other. Theoretically, it provides an infinite set of orthogonal bases, which provides a new research direction for optical communication and information transmission [13–15]. Among them, the OAM-based modular multiplexing communication technology has received widespread attention. mode-division multiplexing (MDM) technology increases the efficiency of data transmission by simultaneously transmitting beams of different modes in the same transmission channel. The orthogonal property of OAM provides a degree of freedom for the multiplexing technique, increasing the capacity of the transmitted data. Moreover, the experiments of multiple-input multiple-output (MIMO) communication system based on OAM multiplexing technology are also gradually improved [16, 17]. In addition, OAM is also considered as a potential communication method of 6G technology [18].

The effective use of the OAM beam cannot be achieved without the generation and stable transmission of OAM. At present, OAM beam can be generated and propagated by optical fiber or spatial optical device. Commonly used spatial optical devices include cylindrical lens [19], spatial light modulator [20], Q plate [21], etc. Compared with spatial optical devices, optical fiber provides a binding transmission medium for OAM transmission, which can reduce external interference and

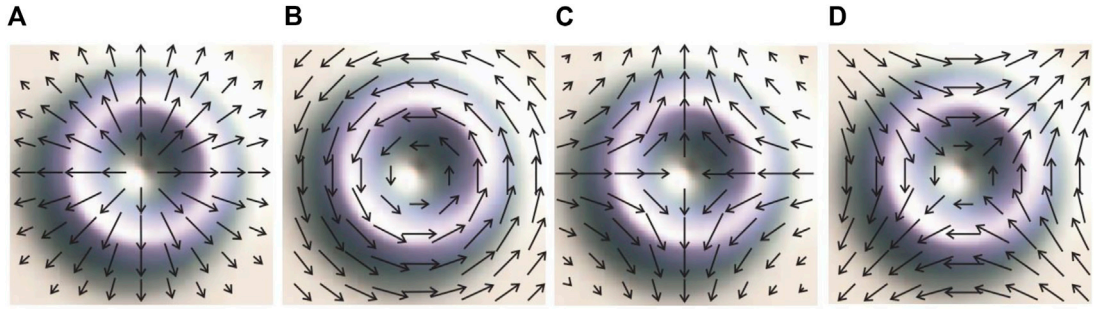

FIGURE 1 | Polarization and light intensity of the four basis vectors **(A)** TM mode **(B)** TE mode **(C)** HE_{21}^{even} mode **(D)** HE_{21}^{odd} mode [29].

increase transmission distance and efficiency [22]. In recent years, ring core fiber (RCF) and photonic crystal fiber (PCF) have become the main optical fibers for transmitting OAM. At present, the use of optical fiber transmission can achieve the stable propagation of thousands of OAM modes [23]. In addition, as the eigensolution of the optical fiber, OAM mode is formed by the coupling of the vector mode or scalar mode of the optical fiber, so the phase purity of OAM generated by the optical fiber is higher and the optical path complexity is lower. When OAM beam is generated in optical fiber, the vector mode or scalar mode of optical fiber is usually obtained first, and then the mode coupling is carried out with stress action or polarization controller (PC), etc. Therefore, fiber gratings and fiber mode selective couplers (MSCs) have attracted attention in the generation of OAM [24, 25]. The all-fiber OAM generation and transmission system provides a good carrier for OAM, which also provides a necessary condition for the effective use of OAM beam.

This review article discusses the principle, transmission, generation in optical fiber comprehensively, and introduces application of OAM. It's expected to be of great significance for OAM fiber design and application.

THE PRINCIPLE OF OAM GENERATION

Vortex Beam

Optical vortex is divided into polarization vortex and phase vortex. The former corresponds to the cylindrical vector beam (CVB) with polarization vortex characteristics, and the latter corresponds to the optical orbital angular momentum (OAM) with phase vortex characteristics [26].

Polarization Vortex

CVB corresponds to the polarization characteristics of vortex light. Polarized vortex light is generated by polarization singularities, and is also called vector beam [27], which is the solution of vector Maxwell's equations. For general linearly polarized light, circularly polarized light, and elliptically polarized light, the polarization state is the same everywhere in the cross section of the beam propagation, but for CVB, the polarization state of the light changes as the azimuth angle [28]. For CVB, there are two mutually orthogonal modes, namely radial polarization and angular polarization, which correspond exactly to the TM mode and TE mode in the fiber vector mode. In addtion, the two CVBs mentioned above live in a four dimensional space spanned by the basis formed by the Cartesian product of the mode bases and the polarization vectors, this also means that in addition to the TM and TE modes, there are two bases with different dimensions. By applying a unitary transformation to TM and TE modes, we can obtain two other basis vectors. These two basis vectors correspond exactly to the odd and even modes of HE_{21} in the fiber vector mode [29]. The intensity and polarization of these four basis vectors are shown schematically in **Figure 1**.

Phase Vortex

Since the OAM has a phase factor of $e^{il\varphi}$, the phase distribution of the OAM is also related to the azimuth angle. l represents the topological charge carried by the photon, the value is an integer, and each photon carries the OAM of $l\hbar$. The positive and negative values of l will affect the vortex direction and phase distribution of OAM beam respectively. According to the direction of the vortex, the OAM beam is divided into left-handed vortex light (l is positive) and right-handed vortex light (l is negative), and the phase change of one circle is $2l\pi$ on the cross section of the beam propagation.

The Coupling Theory of OAM

The OAM beam can be formed by the coupling of the vector mode or the scalar mode in the optical fiber. The OAM formed by the two coupling methods contains different spin angular momentum, so the polarization characteristics of the OAM formed by the different coupling methods are different.

For OAM beam formed by vector mode coupling, its coupling principle is as follows:

$$\begin{pmatrix} \sigma^{+}OAM_{+l} \\ \sigma^{-}OAM_{-l} \\ \sigma^{-}OAM_{+l} \\ \sigma^{+}OAM_{-l} \end{pmatrix} = F_{l,m} \begin{pmatrix} 1 & i & 0 & 0 \\ 1 & -i & 0 & 0 \\ 0 & 0 & 1 & i \\ 0 & 0 & 1 & -i \end{pmatrix} \begin{pmatrix} HE_{l+1,1}^{even} \\ HE_{l+1,1}^{odd} \\ EH_{l-1,1}^{even} \\ EH_{l-1,1}^{odd} \end{pmatrix} \quad (1)$$

Among them, $F_{l,m}$ represents the radial amplitude distribution, *even* and *odd* represent even mode and odd

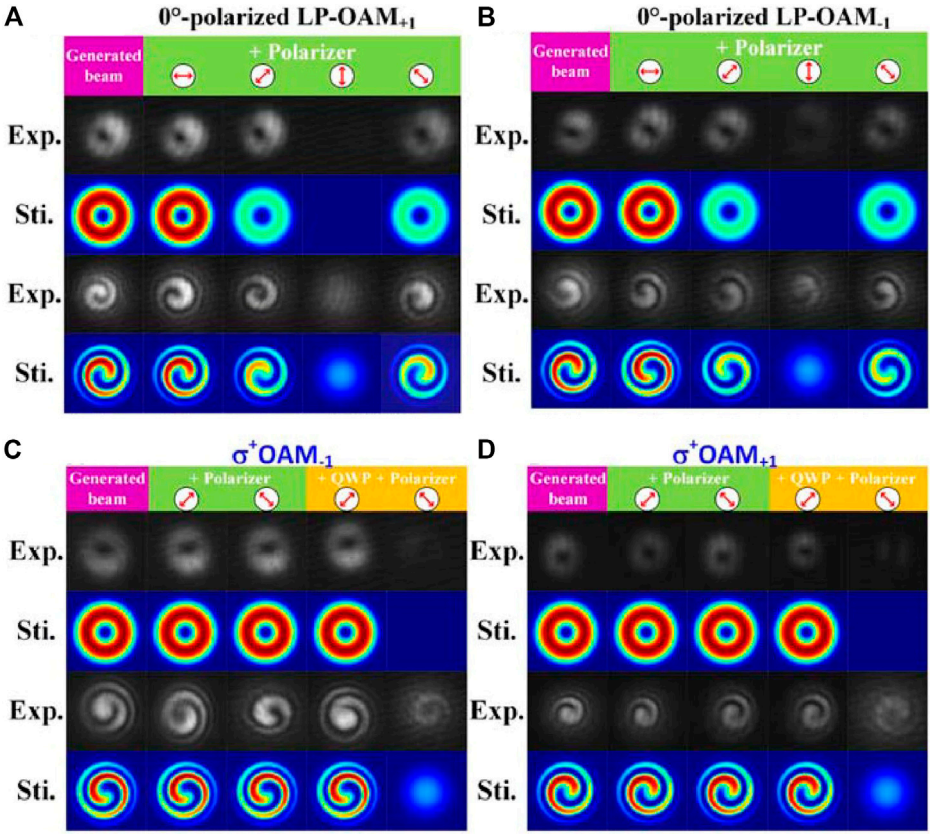

FIGURE 2 | (A) (B) Schematic diagram of the phenomenon of LP-OAM passing through the polarizer **(C) (D)** Schematic diagram of the phenomenon of CP-OAM passing through the polarizer [31].

mode. The positive and negative signs of σ indicate left-hand and right-hand spin, correspondingly. l represents topological charge. The spin of a photon is related to circular polarization, and the OAM formed by vector mode coupling has spin angular momentum, so it exhibits the characteristics of circular polarization.

For the OAM beam formed by scalar mode coupling, the corresponding relationship is [30]:

$$\begin{Bmatrix} \hat{x}L_{\pm l,m} \\ \hat{y}L_{\pm l,m} \end{Bmatrix} = \begin{Bmatrix} LP_{l,m}^{c,x} \pm iLP_{l,m}^{s,x} \\ LP_{l,m}^{c,y} \pm iLP_{l,m}^{s,y} \end{Bmatrix} = F_{l,m}(r) \begin{Bmatrix} \hat{x}e^{\pm il\varphi} \\ \hat{y}e^{\pm il\varphi} \end{Bmatrix}, (l \geq 1) \quad (2)$$

Among them, c and s represent the phase form of cosine or sine contained in the scalar mode, and $\hat{x}$ 、 $\hat{y}$ represent the polarization direction. At this time, the spin angular momentum of the generated OAM is 0, and the beam exhibits linear polarization.

For OAM with different polarization states, they can be judged by the phenomenon after the beam passes through the optical element, as shown in **Figure 2**. A linearly polarized orbital angular momentum (LP-OAM) can only pass through a polarizer in the same direction as the light vector polarization. However, when the circularly polarized orbital angular momentum beam (CP-OAM) passes through the waveplate, it can pass through any angle of polarization because of the oscillating electromagnetic field at any angle of polarization, and the intensity distribution of transmitted light is still circular. When CP-OAM passes through the quarter-wave plate (QWP), it becomes linear polarization mode, and when it passes through the polarizer orthogonal to the light polarization direction, the beam cannot pass through.

It is worth noting that both CP-OAM and LP-OAM are formed by coupling after generating a phase difference of $\pi/2$ between the corresponding vector modes or between the scalar modes. This also requires the system to be able to generate or provide a suitable phase difference to form or support OAM.

OAM TRANSMISSION IN OPTICAL FIBER

The long-distance transmission of OAM and optical communication multiplexing technology are inseparable from the stable transmission of OAM. As an excellent optical waveguide supporting beam transmission, optical fiber has become a research hotspot for effective transmission of OAM, but ordinary optical fiber is not suitable for OAM transmission [32]. Optical fibers that can transmit OAM stably, such as PCFs

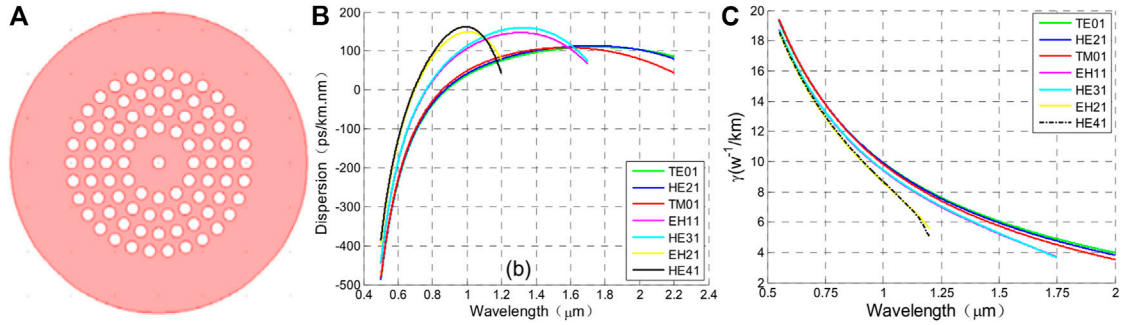

FIGURE 3 | (A) Structure diagram of circular photonic crystal fiber made of silica material **(B)** Dispersion curve **(C)** Variation of the nonlinear coefficient with wavelength [40].

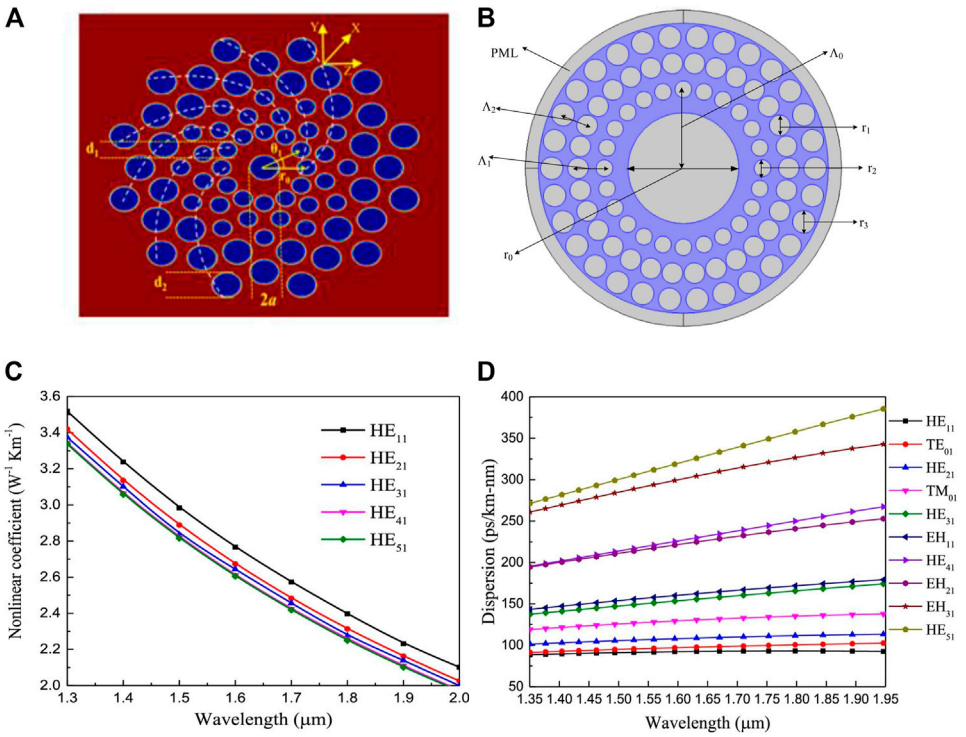

FIGURE 4 | (A) and **(B)**: Schematic diagram of some PCFs **(A)** Schematic diagram of spiral air pore arrangement [46] **(B)** Structure diagram of PCF with air holes of different sizes [41] **(C)** and **(D)**: Characteristic parameters of PCF with spiral air hole arrangement [46] **(C)** Nonlinear coefficients with wavelength **(D)** Dispersion curves.

[33], RCFs [34], and microstructure fibers (MSFs) [35, 36], have received widespread attention.

Photonic Crystal Fiber

The PCF has attracted widespread attention due to its non-stop single-mode transmission, large mode area, and adjustable dispersion characteristics [37]. In 1996, Knight prepared the world's first photonic crystal fiber (PCF) and achieved the property of having a single robust low-loss guiding mode over a wide spectrum [38]. Yang et al. [39] first proposed the use of PCF to transmit OAM. The proposed PCF supports two OAM modes, but there are problems include a small number of supported modes and large loss. Later, different structures of PCFs, such as circular air holes PCF [40–48], rectangular air holes PCF [49], and hybrid air hole PCF [50, 51], were proposed in some studies, and the performance of the fiber was optimized by changing the position and size of the air holes.

Circle Air-Hole Photonic Crystal Fiber

In 2015, Zhang et al. [40] proposed a four-ring cladding silicon dioxide circular photonic crystal fiber (C-PCF). The fiber supports 12 OAM modes. The cross-section structure, dispersion curve and nonlinear coefficient of proposed fiber are shown in **Figure 3**. It indicates the dispersion increases

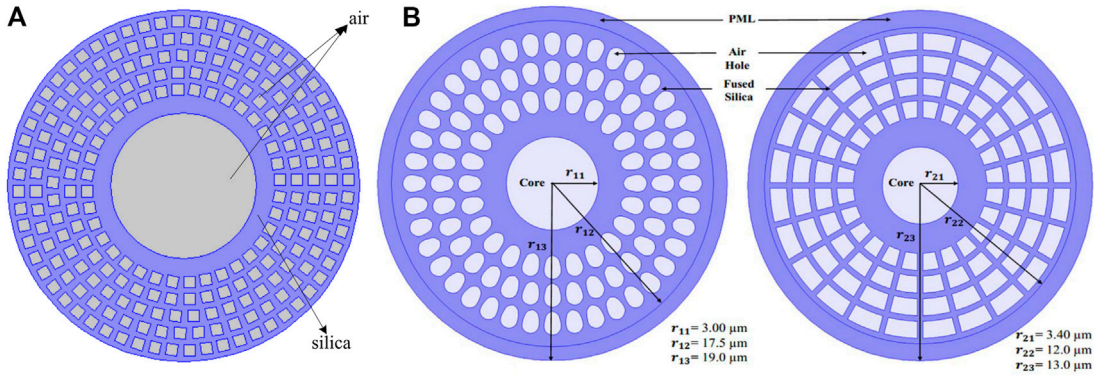

FIGURE 5 | (A) Schematic diagram of PCF structure with rectangular air holes [49] **(B)** Schematic diagram of PCF structures with Bessel polygon air holes [53].

TABLE 1 | OAM transmission characteristics of several PCFs.

Type	Number of OAM modes	Pulse width	Nonlinear coefficient	Confinement loss (at 1550 nm)	Refs
Rectangular air holes	46	1.2~2 μm	<2.58 $km^{-1} \cdot w^{-1}$	10^{-10}~10^{-8}dB/m	[49]
Circle air holes	30	1.5–1.6 μm	<0.71 $km^{-1} \cdot w^{-1}$	10^{-12}~10^{-10}dB/m	[43]
Mixed shape air holes	50	1.15–2.0 μm	0.6–1.5 $km^{-1} \cdot w^{-1}$	10^{-11}~10^{-9}dB/m	[51]
Polygon shaped air holes	38	0.8–1.2 μm	1.0444–4.3984 $km^{-1} \cdot w^{-1}$	10^{-8}~10^{-6}dB/m	[53]
Polygon shaped air holes	42	0.8–1.2 μm	1.5401–5.4390 $km^{-1} \cdot w^{-1}$	10^{-9}~10^{-6}dB/m	[53]
Circle air holes	50 + 30	1.52–1.58 μm	<2.65 $km^{-1} \cdot w^{-1}$	$<3 \times 10^{-8}$dB/m	[54]
Circle air holes	30	1.25–1.9 μm	<4.144 $km^{-1} \cdot w^{-1}$	10^{-11}~10^{-8}dB/m	[45]
Circle air holes	38	1.25~2 μm	250–600 $km^{-1} \cdot w^{-1}$	1×10^{-9}~3×10^{-9}dB/m	[41]

firstly and then decreases as wavelength, and the nonlinear coefficient is too high. None of these features are conducive to OAM lossless transmission.

In some studies, the properties of the circular air hole PCF were changed by changing the position and size of holes [42–44], as shown in **Figures 4A,B**. Nandam et al. [46] proposed a PCF with spiral-shaped air holes and could support 14 OAM modes. Some transmission characteristics are shown in **Figures 4C,D**. It shows that the dispersion change is relatively gentle, and the nonlinear coefficient is reduced by nearly one order of magnitude compared with the C-PCF designed by Zhang et al. mentioned above. Jia et al. [41] proposed a PCF with large round air holes, whose diameter gradually increased. The fiber can transmit 38 OAM modes and has low confinement loss.

Non-circular Air-Hole Photonic Crystal Fiber

In recent years, with the improvement of optical fiber fabrication technology, the design of PCF's holes is not limited to be circular. Several non-circular air-hole PCF are shown in **Figure 5**. Bai et al. [49] proposed the PCF of rectangular air holes, which can support up to 46 OAM modes, and the effective refractive index difference (ERID) between vector modes is all above 10^{-4}. **Figure 5B** shows two kinds of air hole whose shapes are Bessel polygon [52, 53], which have very low confinement loss in the order of 10^{-10} dB/m.

Now some studies have proposed some PCF combining air holes of different shapes [50, 51], which can support more OAM modes and have excellent characteristics. **Table 1** summarizes the OAM transmission characteristics of several PCFs. Compared to PCF with circular air holes, PCFs with new shaped air holes are more complicated, but they provide a new direction for the study of PCF.

In order to make the PCF more suitable for transferring OAM, the central air hole of the PCF is usually designed to be larger, which allows the ring-shaped OAM to be transmitted outside the central air hole. If the central air hole is too small, the number of OAMs that PCF can support will decrease. In addition, the outer air holes also need to be able to effectively restrict the light beam. Too few air holes will cause beam leakage, resulting in higher loss.

At present, there are many research directions of OAM propagation using PCF. Based on space division multiplexing, some studies aim to improve the number of OAM mode in PCF [54–56]. In terms of filling materials for PCF, Tao He [57] filled the magnetic fluid into the large air hole of PCF. By changing the intensity of the applied magnetic field, the refractive index of the magnetic fluid changes correspondingly, and the nonlinear coefficient of the PCF is also reduced compared to that with no magnetic fluid.

Ring Core Fiber

In 2009, Ramachandran et al [58] demonstrated that the ERID is maximum when there is a mirror relationship between the refractive index distribution of the fiber and the intensity distribution of the propagation mode. The high ERID between modes will reduces the coupling, and different OAM mode

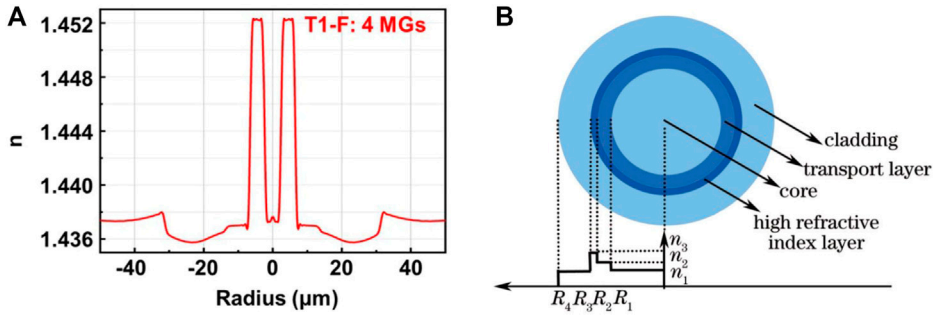

FIGURE 6 | (A) Refractive index distribution of SI-RCF [65] **(B)** Refractive index distribution of modified SI-RCF [66].

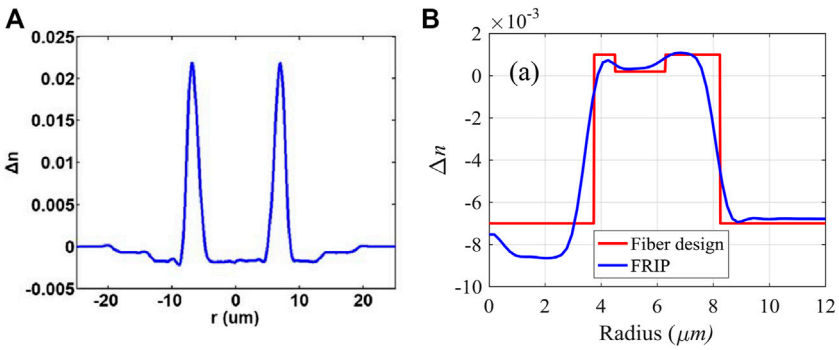

FIGURE 7 | (A) Refractive index distribution of GI-RCF [69] **(B)** Refractive index distribution of RIPM-RCF [70].

groups (MGs) can achieve good transmission. The ring structure with high refractive index distribution restricts the OAM transmission within the ring, and the fabrication process of the RCF is simpler than that of other OAM fibers. By changing the refractive index distribution and composition materials of the fiber, the RCF can have different OAM transmission properties. Typical RCF such as step-index ring core fibers (SI-RCF) [59], graded index-ring core fiber (GI-RCF) [60], refractive-index-profile-modulated RCF (RIPM-RCF) [61], air core fiber(ACF) [62] are more widely used.

Step Index Ring Core Fiber

In 2014, Brunet et al. [63] conducted a theoretical analysis of the vector and scalar modes of SI-RCF, and gave an analytical expression for the cut-off conditions of SI-RCF. Based on this theory, they designed a set of SI-RCFs [64]. The effective index separation of the vector mode reaches above 10^{-4} and has a lower dispersion parameter. The refractive index distribution of the SI-RCF is shown in **Figure 6**. Wang et al. [65] has designed two SI-RCF supporting $|l| = 3$ and $|l| = 5$ respectively. The ERID between different modes reaches 10^{-3} magnitude, which reduces cross-talk between groups. At the same time, the transmission loss of the fiber is below 0.25 dB/km, which has excellent transmission characteristics.

However, in the actual propagation process, high refractive index materials will increase the transmission loss of the propagation process [67], so it is particularly important to balance the problem of mode degeneration and high refractive index transmission loss. Huang et al. [66] improved the SI-RCF by introducing a high refractive index material between the cladding and the transmission layer. Since the high refractive index material does not transmit OAM, the RCF can transmit the OAM more effectively.

Graded Index Ring Core Fiber

In order to prevent the high loss caused by high refractive index materials, it is effective to change the distribution pattern of refractive index to enhance the transmission properties of OAM. The graded index distribution of GI-RCF presents a gradual change, as shown in **Figure 7A**. The GI-RCF designed by Zhu et al. [68] supports 5 MGs with low coupling, and the average attenuation any mode is about 1 dB/km. Zhu et al. [69] proposed the GI-RCF, which suppressed the radial high-order mode effectively. The ERID between the fourth and fifth order OAM modes is 3.9×10^{-3}, which greatly separates the high-order OAM modes.

Refractive-Index-Profile-Modulated RCF

In the real multiplexing system of OAM, the coupling between MGs can cause interference. In order to reduce the reference, Tan et al. designed RIPM-RCF [70]. Its refractive index distribution is shown in **Figure 7B**. The top of the ring core forms a numerical

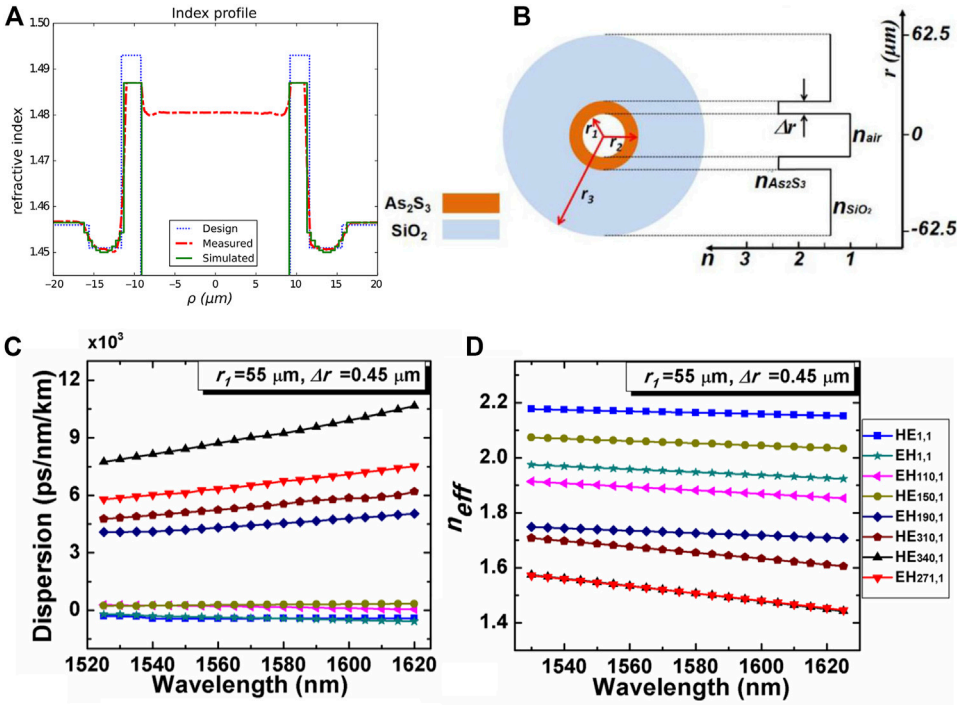

FIGURE 8 | (A) and **(B)**: Refractive index distribution of several ACFs [23, 74] **(C)** and **(D)**: Characteristic parameters of ACF proposed by Wang et al. [23] **(C)** dispersion curve **(D)** effective refractive index variation curve with wavelength.

gap of effective refractive index. The optical fiber supports four low-order MGs, and the ERID between the MGs is more than 0.8×10^{-3}. Moreover, due to the large ERID between the mode and the cladding and the presence of notch modulation, the mode coupling from the guiding mode to the leaky cladding mode is effectively suppressed with low fiber attenuation about 0.2 dB/km. The RIPM-RCF proposed by Zhang et al. [71] can support four low-order MGs, and the ERID between the second and third-order modules is 2.5×10^{-3}. Group crosstalk is less than −36 dB/km.

Air Core Fiber

Some studies proposed ACF, one of which is shown in **Figures 8A,B**. Due to the huge ERID between air and the annular transmission layer, OAM can be confined to the transmission layer, so ACF has received extensive attention [23, 72–76]. The ACF proposed by Gregg et al. [72] can support up to three high-order MGs ($|l| = 7, 8, 9$), and a large ERID is produced between different OAM modes. To a certain extent, the multi-path interference is reduced, and the purity of the transmission OAM is improved. Brunet et al [73, 74] added a low refractive index layer to the conventional ACF to increase the number of supported OAM modes, which can support up to 28 OAM modes for transmission.

Wang et al. [23, 76] used As_2S_3 as the material of the ring transmission layer in ACF, and the ERID between the transmission ring and the air hole was higher than that of the traditional ACF. Proposed fiber can support 1004 OAM modes in all O, E, S, C and L bands. The transmission characteristics of this fiber is shown in **Figures 8C,D**. The ERIDs of high-order vector modes keep is about 10^{-3} and the dispersion of the fiber changes smoothly. By adjusting the radius of the air hole, a double-frequency supercontinuum of 1,560–6,250 nm can be generated for the $OAM_{17,1}$ mode in the designed fiber.

In general, there are two design ideas that enable RCF to be more suitable for transmitting OAM. One is to add a high refractive index layer, and the other is to modulate the refractive index. For the first idea, the higher the refractive index and the smaller the width of the transmission layer added to the fiber, the greater the number of OAMs supported by the fiber. But this will cause higher losses. For the second idea, modulating the refractive index of the fiber according to the transmission characteristics can make the fiber obtain better transmission properties. The next experiment can combine idea one and idea two to modulate the refractive index of the fiber doped with a high refractive index layer.

Other Vortex Fiber

By changing the refractive index distribution in the fiber, some articles have also proposed other OAM fibers with good transmission performance.

B. Ung [77] proposed the inverse-parabolic graded-index fiber (IPGIF), and its refractive index profile is shown in **Figure 9A**. An ERID of 2.1×10^{-4} is provided between the first-order mode, and the propagation of the first-order OAM mode can reach 1.1 km. Chen Yun [78] added a low refractive index layer between the core and the cladding to increase the ERID. The refractive index

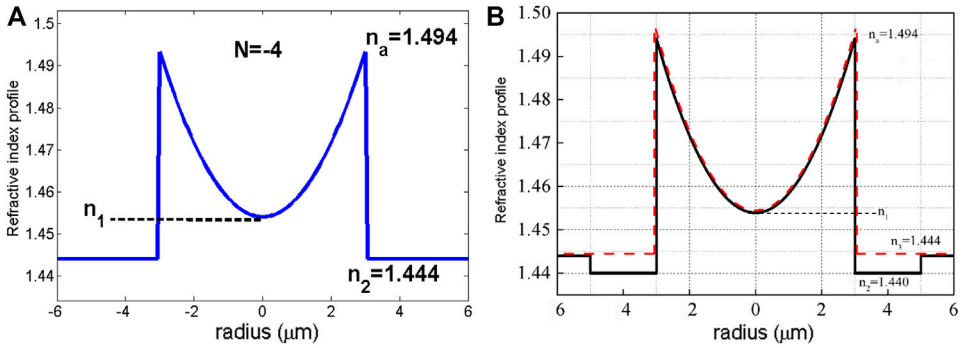

FIGURE 9 | (A) Refractive index distribution of IPGIF [77] **(B)** Refractive index distribution of modified IPGIF [78].

distribution is shown in **Figure 9B**. The simulation proves that the improved fiber can support the highest third-order OAM mode for effective transmission. Zhang et al. [79] performed a rotational twist on the designed IPGIF. Simulations show that the twisted IPGIF requires an order of magnitude less twist than the twisted air hole fiber. The twisted optical fiber can support 22 OAM modes in the entire C-band, and has excellent transmission characteristics with a small nonlinear coefficient.

The fibers mentioned above have different transmission properties due to differences in fiber structure and refractive index distribution. Taking into account the requirements of existing fabrication technology, RCF and PCF are more suitable for widespread production and use. From the perspective of optical communications, Optical fiber needs to meet the characteristics of low loss, large number of supported OAMs, and easy production. Therefore, the RCF with multiple transmission rings is more suitable for optical communications. The PCF is more suitable for transmitting OAM with special properties, such as adjustable dispersion and large mode field area. For the OAM fiber with a high refractive layer, although the number of supported OAMs is greatly increased, the loss is large. So this type of fiber is suitable for fiber lasers that generate high-order OAM. In addition to RCF and PCF, the manufacturing of some special structure optical fibers is limited by the technological level, but they exhibit excellent transmission characteristics, which provide a useful reference for the design of special fibers transmitting OAM.

THE GENERATION OF OAM IN FIBER

OAM beam can be generated by spatial optical devices and optical fibers. Among them, OAM generated by spatial optical devices can be generated by helical phase plate [85], spatial light modulator [86], Q plate [87], etc. However, generating OAM through a spatial optical device will increase the complexity of the optical path. The vortex beam itself is an intrinsic solution of the fiber, so the generation of the OAM mode in the fiber will simplify the optical path and improve the phase purity of OAM [88]. The main optical fibers used to generate OAM modes in optical fibers are fiber gratings [89, 90], fiber MSCs [91], and helically twisted PCF (HT-PCF) [92–94].

Fiber Grating

Fiber gratings are divided into long-period fiber gratings and short-period fiber gratings (Bragg gratings) according to the length of their period. The fiber grating has a periodic distribution of refractive index. When the input meets the phase matching condition, mode coupling can be performed.

Long Period Fiber Grating

Long period fiber grating (LPFG) is a transmission grating [95]. The relationship between wavelength and grating period is [96]:

$$\lambda = \left(n_{eff_1} - n_{eff_2}\right)\Lambda \tag{3}$$

Among them, n_{eff_1} and n_{eff_2} are the effective indices of the two coupled modes, respectively. λ represents the resonant wavelength, and Λ represents the period of the fiber grating. Due to the coupling and transmission characteristis of LPFG, Modes that satisfy the coupling conditions can be coupled to form LP modes or vector modes, thus further forming OAM. The experimental device in Ref. [97] contains a fiber grating for mode coupling, a vortex fiber for beam propagation, and a PC for forming OAM. The positive and negative conversion of the topological charge can be achieved by adjusting the *p*C. The schematic diagram is shown in **Figure 10**. Mode coupling of the input fundamental mode occurs within the fiber grating and generate a high-order mode. However, since the effective refractive index of the same order modes is approximately equal, the distribution of the same order modes generated at the same time is random and uneven. Therefore, PC or stress is usually added to adjust the amplitude and phase distribution of the same order mode, so the pure state vector mode or OAM mode can be output [98, 99].

Zhao et al. [100] designed a tilted LPFG (T-LPFG). In the T-LPFG, wave vector of the grating planes are tilted by angle θ with the *Z* axis. Compared with uniform LPFG, the grating period Λ_T of T-LPFG is related to the tilt angle θ, and $\Lambda_T = \Lambda \times \cos\theta$ is the actual grating period. By changing θ, the grating period can be changed, and it can be seen from **Eq. 4** that the resonant wavelength is related to the grating period, so the resonant wavelength and other parameters of TLPFG are adjustable. In the experiment, Zhao realized the mode coupling between LP_{01}

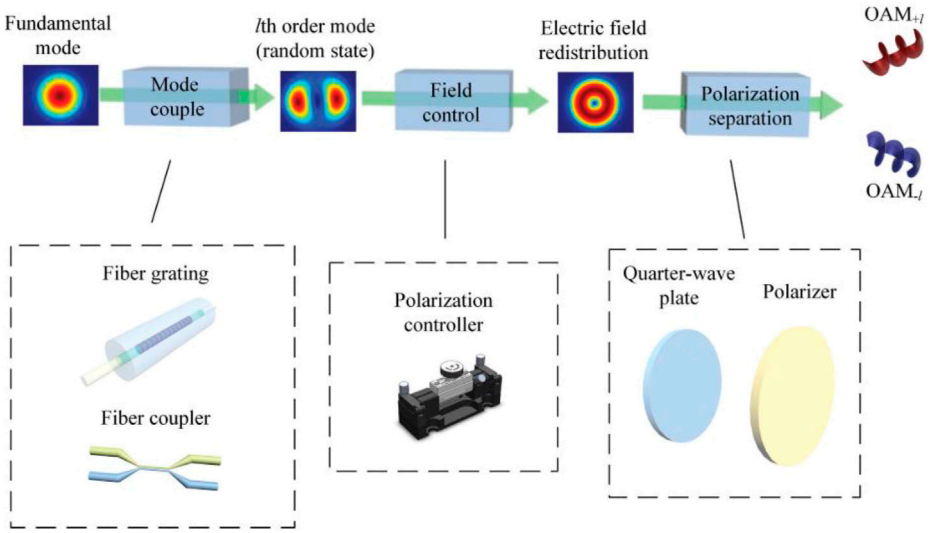

FIGURE 10 | Schematic diagram of the coupling process [98].

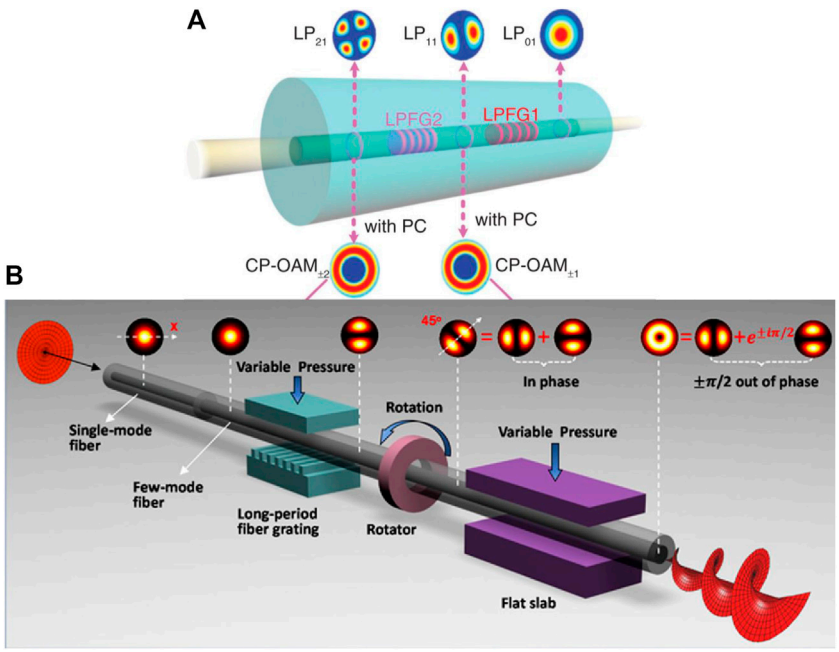

FIGURE 11 | (A) Schematic diagram of two-stage long-period grating cascade structure [102] **(B)** Schematic diagram of the LP mode formation process [103].

and LP_{11} by calculating the relationship between the effective refractive index and the period of LP mode, and the coupling efficiency was greater than 99%. After that, a first-order OAM beam was generated by adjusting the PC in the optical path.

On the basis of the pattern coupling between LP_{01} and LP_{11}, some studies realized the pattern coupling between LP_{01} and LP_{21} by cascading two LPFGs with different cycles [101, 102], as shown in **Figure 11A**. Through calculation, the designed two-stage LPFG meets the phase matching conditions of LP_{01} and LP_{11}, LP_{11} and LP_{21} respectively, and the mode coupling is carried out. At the output end of the second-order LPFG, by adjusting PC, the vector mode of LP mode is degenerated and recombined to generate the second-order OAM beam.

It is worth noting that the generation of OAM based on LPFG above is all formed through the combination of vector modes. Some studies use LPFG system to synthesize OAM through LP mode. Li et al. [103] used mechanical LPFG to couple the input LP_{01} into LP_{11}, and made the output of LP_{11} at an angle of 45° with the *X*-axis of

optical fiber cross section by rotation. LP_{11} was decomposed into two orthogonal LP_{11}, and then the phase difference was generated through the pressure action of the plate to form OAM, as shown in **Figure 11B**. Wu et al. [104] used a four mode fiber-LPFG system such that LP_{01} is coupled to form LP_{21} directly. Then, by rotating LPFG, a phase difference of $\pi/2$ was generated between the odd and even modes of LP_{21} to produce a second-order OAM. Since the phase difference of $\pi/2$ is difficult to achieve in some cases, Li et al. [105] proposed a scalar mode synthesis method and obtained OAM by synthesizing multiple LP modes with phase differences much smaller than $\pi/2$. By distorting the few-mode fiber-LFPG (FMF-LFPG), a series of LP_{11} modes with slight phase difference are generated, and the mode conversion is finally achieved with a power loss of 0.66 dB and a mode purity of 99%.

Both vector mode and LP mode coupling to OAM are based on the idea of mode coupling. Some studies have shown that it is possible to generate OAM patterns from a single CVB. Han et al. [106] firstly coupled the input beam into a single first-order CVB through the LPFG in tow mode fiber (TMF). After passing through QWP and the polarizer, the first-order OAM beam is generated by setting the angle of the polarizer. Compared to OAM synthesized from beams of two modes, a single CVB generates OAM with improved stability because it does not require a specific phase relationship between the two modes.

Considering the helical phase properties of OAM beams, helical long-period fiber gratings (HLPFG) are proposed [107–109]. Due to the special structure of HLPFG, the vortex phase can be directly excited without generating OAM beams through PC, stress and other operations. Moreover, the resonant wavelength of OAM can be adjusted when the HLPFG is twisted. The introduction of HLPFG can reduce the complexity of optical path, but the fabrication of grating is relatively complicated.

Fiber Bragg Grating

The fiber Bragg grating (FBG) is a reflective grating [95], and the relationship between the Bragg wavelength and the grating period is [96]:

$$\lambda = \left(n_{eff_1} + n_{eff_2}\right)\Lambda \tag{4}$$

Similar to LPFG, the research on FBG mainly focuses on uniform period Bragg grating, tilted Bragg grating, and spiral Bragg grating.

Wang et al. [110] used FBG to characterize OAM transmitted in optical fibers. When the wavelength meets **formula (4)**, the OAM beam is reflected by the grating. Topological charge reversal and circular polarization reversal can be observed. Wang et al. also showed that the Bragg grating could be applied to all fiber systems generating OAM.

Like TLPFG, the wavelength and period of the tilted FBG are also related to the cosine of the tilt angle. By adjusting the tilt angle, the resonant wavelength of the FBG can also be changed. The FMF-TFBG designed by Zhao et al. [111] realized the conversion of LP_{01} mode to LP_{11}, LP_{21}, LP_{02}, LP_{31} mode, and the conversion efficiency reached 90%. Then by controlling the PC, a phase difference of $\pi/2$ is generated between the vector modes to form the corresponding OAM mode. Yang [112] et al. designed a ring-shaped FMF system containing TFBG. The ERID of the vector mode is very small, and this method can form a stable LP-OAM ($|l| = 1, 2, 3$) mode. When the four degenerate vector modes are reflected, by adjusting the PC at the output end, the relative amplitude and phase between the degenerate modes are changed to generate a pure OAM mode.

The spiral FBG has the characteristic that the refractive index of the spiral can be modulated, and the refractive index in the lateral x direction and y direction has a phase shift of $\pi/2$. Lin et al. [113] fabricated a spiral FBG using a phase mask. Among them, helical FBG is used for generating OAM beam, ytterbium-doped fiber is used for beam gain amplification, and two FM-FBGs are used to filter LP beams which cannot generate OAM mode. Huang [114] believe that the mode propagation in ordinary fiber will be degenerate, so they use RCF for transmission, which improves the ERID of the vector modes and makes the transmission of OAM more stable.

Mode Selective Coupler

The MSC is formed by splicing two kinds of fibers. The principle is that the modes are coupled through the evanescent wave between the fibers, and the fundamental mode is transmitted in the single-mode fiber through the MSC. High-order modes are coupled in the FMF. Similar to the fiber grating, the fiber MSC also couples the low-order mode to the high-order mode.

Due to the existence of degeneracy, at the output of some mode selection couplers, PC or stress is usually added to change the amplitude and phase relationship between high-order degenerate modes to generate OAM beams [31, 115, 116].

The SMF-FMF mode selection coupler designed by Wang et al. [115] realizes the coupling of LP_{01}, LP_{11}, and LP_{21}, and the principle is shown in **Figure 12A**. Based on this mode selector, Wang et al. designed an all-fiber mode-locked fiber femtosecond vortex beam laser, as shown in **Figure 12B**. Zhang et al [31] demonstrated theoretically that the system combined by SMF-FMF and squeezed PC can generate OAM in arbitrary polarization states. They passed the resulting beam through QWP and polarizing plates, demonstrating that the system can selectively produce LP-OAM and CP-OAM. There are other studies [116] that produced pure-state vector beams by controlling the PC at the output of the SMF-FMF. The pure-state vector beam was then passed through the QWP with the polarizer and the OAM beam was output. Changing the direction of the polarizer can obtain OAM with opposite vortex direction.

There are also some studies that replace the FMF in the mode selection coupler with other fibers which can generate the first-order OAM directly at the output, such as SMF-ACF [117], SMF-RCF [118], SMF-GIFMF [119] etc. The unique refractive index distribution that these fibers have provides a high ERID. Therefore it is possible to design MSCs so that the base mode is coupled to generate OAM modes directly. The high-order mode coupled out of the fundamental mode can be steadily propagated in the fiber, and a higher purity OAM can be produced without adding a PC at the output end.

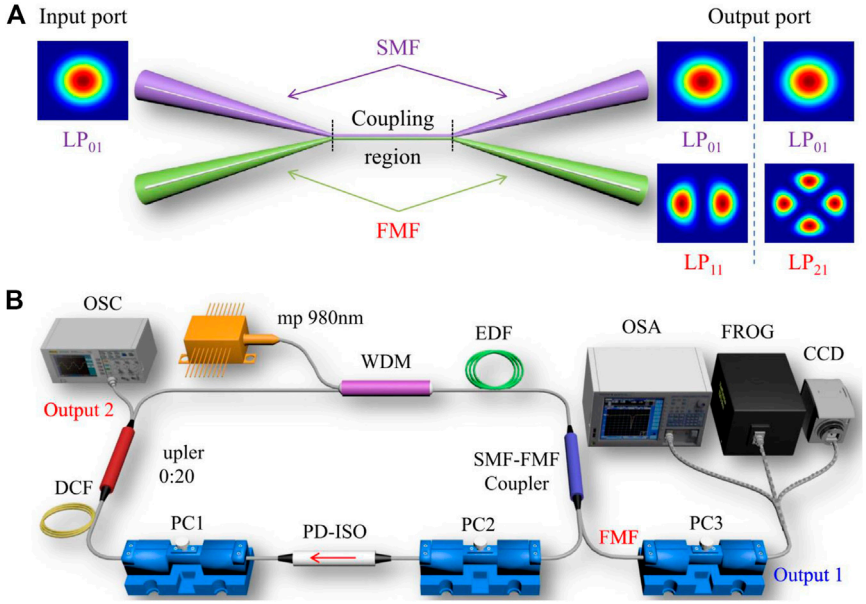

FIGURE 12 | (A) Schematic diagram of the LP mode coupling performed by MSC **(B)** The vortex beam laser designed by wang et al. [115].

In terms of fiber splicing, there is also a different method from the fiber splicing of the traditional mode selection coupler. Jin et al. [120] used SMF spliced with lateral offset to excite the HE_{21} mode in the RCF, and discussed the relationship between the offset distance and the purity of the mode. This method enables the first-order OAM beam to be generated in a wide wavelength range of 1,540 nm–1580 nm. Li et al. [121] spliced SMF to TMF with a specific offset and tilt angle, and realized high-order fiber mode conversion through fundamental mode coupling. However, the coupling efficiency of this splicing method is only about 34%, and the structure needs to be optimized.

Helically Twisted PCF

Based on the three-dimensional structure of PCF, in 2012 Wong et al. [122] proved for the first time that HT-PCF can excite OAM. Due to the special structure of the helical twist, the loss, dispersion and polarization state of the fiber can be controlled by changing the twist rate and other parameters.

The HT-PCF designed by Fu et al. [93] stimulated OAM modes with topological charges of +5 and +6 in the experiment. They found that the leakage orbit resonance in the cladding is closely related to the twist rate and length of the spiral PCF. The fiber produced a high-quality OAM_{+6} at the resonant wavelength with a coupling efficiency of −22.27 dB.

Yan et al. [123] designed HT-PCF for filtering. When the distortion ratio reaches a certain value, the difference of transmission loss between positive and negative OAM beams will increase significantly. HT-PCF has the property of transmitting vortex beams with the same chirality as the hollow channels', but dissipating vortex beams with opposite chirality. They also implemented the filtering of OAMs with different chirality in the experiment.

Acoustic-Induced Method

In 2006, Dashti et al. [124] studied the acousto-optic interaction in optical fibers from the perspective of optical vortices and acoustic vortices. The conversion of acoustic vortices and optical vortices is:

$$AV_{np} + CV^{s}_{l-n,k} \Leftrightarrow CV^{s}_{lm} \tag{5}$$

Among them, AV represents the OAM of the sound vortex. s indicates the spin of the photon. l denotes the order of the photon's OAM. n indicates the order of the phonon's OAM. p,k and m indicate the radial mode order of the phonon or photon. Based on this theory, Dashti conducted experiments to generate $AV_{\mp 1,0}$ by controlling the relative amplitude and phase of the radio frequency. When the fundamental mode passes through the acoustical driven generated AIFG, the fundamental mode will couple into the first-order OAM mode under acousto-optical conversion. However, due to the limitation of the acoustic resonance frequency under the acousto-optic phase matching, the device cannot generate high-order OAM modes. Zhang et al. [125] completed the coupling of the fundamental mode to the second-order OAM mode through the cascaded sound drive method, as shown in **Figure 13**. Two different frequencies of RF were used to induce two AIFGs simultaneously in the fiber. when the fundamental mode passed through, first-order and second-order OAM coupling occurred in the first- and second-order AIFGs, respectively.

By changing the radio frequency, the mode conversion after acousto-optic driving also shows wavelength tunability. Zhang et al. [126] realized the generation of the first-order vortex beam by means of acoustic drive in TMF, and achieved tunable wavelength in the 1,540 nm–1560 nm wavelength range by changing the radio frequency. In the entire wavelength tuning range, the mode conversion efficiency is maintained at about 95%.

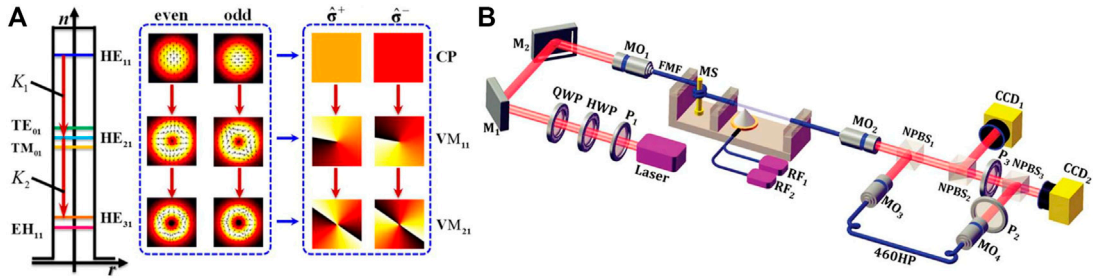

FIGURE 13 | (A) Schematic diagram of the principle of the secondary acoustic drive cascade **(B)** Schematic diagram of the experimental setup by Zhang et al. [125].

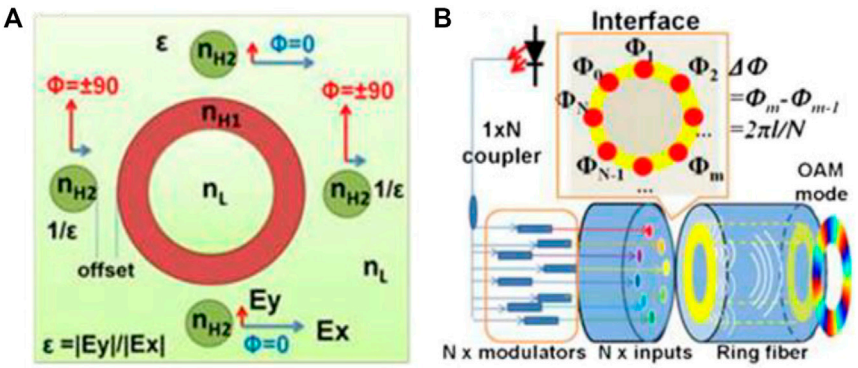

FIGURE 14 | (A) Structure of the fiber coupler and the phase and polarization state of the input lights [127] **(B)** Generation of OAM modes of charge number *l* in a ring fiber with N coherent Gaussian inputs [128].

Multi-Coherent Beam Synthesis

Yan et al. [127, 128] proposed a method of synthesizing OAM using input multiple coherent optical transmissions. As shown in **Figure 14A**, the fiber coupler consists of a central ring and four outer cores. The four coherent input lights pass through the four outer cores and are coupled into OAM beams, and the four coherent lights need to meet a certain phase difference. When the size of outer core changes, the OAM mode will also change. The purity of the OAM mode obtained by this coupling method is above 99%.

In the other way, multiple coherent Gaussian fundamental modes are input to form OAM mode coupling, as shown in **Figure 14B**. Yan et al. found that controlling the phase relationship of multiple inputs can selectively generate OAM modes of different states. Theoretically, it is proved that there is a discrete Fourier transform relationship between the input Gaussian mode channel and the output OAM channel, which is suitable for OAM mode division multiplexing system. However, this method of coherent optical coupling into OAM mode requires high coherence for external light sources and needs to meet the phase difference, so the practicality is less.

In addition to the methods mentioned above, there are some other methods such as using a square-hole fiber to couple the input fundamental mode into OAM [129], using a system composed of a spiral symmetric fiber and a normal fiber to generate OAM [130], and other special structured fibers. However, the fabrication of these fibers is relatively complicated, and therefore most of them are in the simulation stage. Optical elements such as fiber gratings and MSCs can be effective in generating OAM, and different studies have also improved the ability of the system to generate OAM by changing the properties of these optical elements. The existing industrial level can manufacture fiber gratings and MSCs, and both belong to fiber components, so they can be used to construct fiber lasers for OAM. Besides, the acoustic-induced method excites vortex light from the perspective of acousto-optical interaction. The next experiment can start from the perspective of acousto-optic conversion, cascading multiple acoustic drivers to generate high-order OAM. In addition, special optical fibers generating OAM usually has strict requirements on fiber preparation and external light sources. Although it is difficult to achieve, it provides a new idea for the generation of OAM.

APPLICATION OF OAM

OAM has the characteristics of infinite orthogonal basis and circular distribution of light intensity, which is different from

Gaussian beam. These characteristics make the OAM beam closely related to cutting-edge disciplines, such as nonlinear optics [131], optical communication [132, 133], particle manipulation [134] and microscopic imaging [135].

Nonlinear Optics

The wavelength range of the OAM beam can be increased by nonlinear frequency conversion, shifting the OAM carried by fundamental frequency light to harmonics. In this process, both the frequency and topological charge of the new OAM may change [136]. Zhang et al. [8] proposed a method to generate a high-order OAM vortex beam using relativistic harmonics on a solid surface. And the first-order OAM beam was used to irradiate and generate a high-intensity ninth-order vortex beam. Wu [137] demonstrated theoretically and experimentally that the OAM transformation is modulated by a phase-matching mechanism for nonlinear effect. Fang et al [138] demonstrated that the phase-matching conditions of the OAM mode can be changed by varying the relative group velocity, and proposed a new vortex fiber that can manipulate the nonlinearity of the OAM beam.

In addition, Yang [139] proposed a novel OAM coding technique. He used computational holography for the design of nonlinear multiplexed holograms, which solved the multi-channel multiplexing problem in nonlinear holography.

Optical Communication

The orthogonal basis contained in the OAM provides an additional degree of freedom for communication coding, so MIMO systems provide a suitable method for practical information transmission. Based on MIMO, the transmission capacity of OAM can be greatly increased by using multiplexing methods such as space-division multiplexing (SDM) and wave-division multiplexing (WDM).

During the transmission of SDM, inter-ring crosstalk affects the transmission characteristics. Li et al. [140] designed an optical fiber suitable for SDM transmission. This fiber consists of seven uniformly arranged transmission rings, and each ring supports 18 OAM modes. The rings have high contrast ring structure, which can not only improve the number of OAM support, but also well limit the transmission of OAM crosstalk. The crosstalk between rings is small to −30 dB through 100 km. Subsequently, Li et al. [67] used a high contrast refractive index loop and groove design to integrate 19 transmission rings in a single fiber and each ring supports 18 OAM modes. The 100 km inter-ring crosstalk is less than −45 dB. As with normal RCF, the high contrast refractive index structure increases the ERID and constrains crosstalk, but increases transmission loss.

During the MDM transmission process, inter-mode crosstalk will occur, which will hinder the transmission of multi-mode OAM. Using MIMO technology can solve the problem of inter-mode crosstalk effectively [141]. By increasing the ERID between mode groups, the cross-talk between modes and complexity of MIMO technology can both be reduced. However, the use of MIMO will further increase the complexity of the system. Therefore, multiplexing systems without MIMO have become a hot spot. By using optical fibers, the transmission of MDM systems without MIMO can be realized, which simplifies the complexity of the system [69, 142, 143].

Particle Manipulation

With a deeper understanding of the microscopic world, the research on microorganism, single cell and other microscopic levels requires the control technology of particles. The trapping manipulation methods for particles include the traditional mechanical tweezers and the modern optical tweezers. Compared with mechanical tweezers, optical tweezers use non-contact operation, and has the characteristics of small damage to life and high repeatability. Gahagan et al. [144] used vortex beams to trap and manipulate particles in a low refractive index environment. Compared with traditional Gaussian beams, vortex beams can support more kinds of particles to be trapped and manipulated.

In the area of particle manipulation, there is also the optical wrench technology that enables the rotation of particles. The principle of conventional optical wrenches is to rotate the particles by using the interactions that occur when the particles absorb and reflect light and other processes. In contrast, the OAM optical wrenches transfer spin angular momentum and OAM to the captured particle directly, enabling three-dimensional translation and one-dimensional rotation of the particle [145]. Therefore, the OAM optical tweezers are convenient to operate and suitable for more particles. Gao et al. [146] realized the capture, translation and rotation of particles using OAM beams. Lehmuskero et al. [147] used a vortex beam to irradiate plasma gold particles, which rotated rapidly along a circular orbit. It was measured that there was a relationship between the particle rotation frequency and OAM, and a transfer of both occurred during the action.

In addition, OAM exhibit unique quantum entanglement properties due to the infinite dimensional Hilbert space constituted by the orthogonal basis of the OAM. Therefore OAM also has a wide range of applications in the quantum field [148, 149]. OAM has an important role in the field of optical microscopy because of its spiral phase feature that enhances the imaging of objects and its unique interference fringes [150, 151].

CONCLUSION

There are many research directions of fiber-based OAM transmission and generation systems, and some researches continue to make changes in fiber structure and optical devices to make the all-fiber system better support OAM mode. At present, PCF and RCF have become the hotspots of OAM fiber optic transmission system because of their good transmission characteristics. The number of modes, transmission efficiency and transmission distance of OAM need to be further improved to meet the needs of the information society.

For OAM fiber generation system, there are some generation systems with high requirements for fiber structure and external light source, which are not practical due to insufficient preparation process. Therefore, the use of

fiber grating, MSC and other fiber structures with relatively mature preparation process is a hot research topic. The current all-fiber OAM generation system still has some problems for generating multiple OAM modes. A complete system for generating multiple high-purity OAM modes is also necessary to implement multiplexing technologies such as MDM and SDM.

Overall, there is a lot of room for improvement in fiber-based OAM transmission and generation systems. At the same time, the fiber system has great potential for OAM mode support [80–84].

AUTHOR CONTRIBUTIONS

MM analyzed the data and wrote the manuscript, LY revised the manuscript, WY and LZ proposed the idea.

FUNDING

The authors gratefully acknowledge financial support from the National Natural Science Foundation of China (61905062, 62070506 and 61927815), China Postdoctoral Science Foundation (2020M670613), Hebei Postdoctoral Scholarship Project (B2020003026). Thanks for the support of the Key Laboratory of all Optical Networks and Advanced Communications Networks of Ministry of Education (Beijing Jiaotong University) (AON2019005).

ACKNOWLEDGMENTS

The authors are thankful to other colleagues in their laboratory for their understanding and help.

REFERENCES

1. Allen L, Beijersbergen MW, Spreeuw RJC, Woerdman JP. Orbital Angular Momentum of Light and the Transformation of Laguerre-Gaussian Laser Modes. *Phys Rev A* (1992) 45:8185–9. doi:10.1103/physreva.45.8185
2. Fürhapter S, Jesacher A, Bernet S, Ritsch-Marte M. Spiral Interferometry. *Opt Lett* (2005) 30:1953–5. doi:10.1364/ol.30.001953
3. Tamburini F, Anzolin G, Umbriaco G, Bianchini A, Barbieri C. Overcoming the Rayleigh Criterion Limit with Optical Vortices. *Phys Rev Lett* (2006) 97: 163903. doi:10.1103/physrevlett.97.163903
4. Friese MEJ, Nieminen TA, Heckenberg NR, Rubinsztein-Dunlop H. Optical Alignment and Spinning of Laser-Trapped Microscopic Particles. *Nature* (1998) 394:348–50. doi:10.1038/28566
5. Toyoda K, Miyamoto K, Aoki N, Morita R, Omatsu T. Using Optical Vortex to Control the Chirality of Twisted Metal Nanostructures. *Nano Lett* (2012) 12:3645–9. doi:10.1021/nl301347j
6. Dholakia K, Čižmár T. Shaping the Future of Manipulation. *Nat Photon* (2011) 5:335–42. doi:10.1038/nphoton.2011.80
7. Padgett M, Bowman R. Tweezers with a Twist. *Nat Photon* (2011) 5:343–8. doi:10.1038/nphoton.2011.81
8. Zhang X, Shen B, Shi Y, Wang X, Zhang L, Wang W, et al. Generation of Intense High-Order Vortex Harmonics. *Phys Rev Lett* (2015) 114:173901. doi:10.1103/PhysRevLett.114.173901
9. Ni R. *Nonlinear Generation and Steering of Light in Second-Order Nonlinear Optical Materials*. [dissertation/master's thesis]. Nanjing(Jiangsu)]: Nanjing: Nanjing University (2017).
10. Liu J, Nape I, Wang Q, Vallés A, Wang J, Forbes A. Multidimensional Entanglement Transport through Single-Mode Fiber. *Sci Adv* (2020) 6: eaay0837. doi:10.1126/sciadv.aay0837
11. Wang X-L, Cai X-D, Su Z-E, Chen M-C, Wu D, Li L, et al. Quantum Teleportation of Multiple Degrees of freedom of a Single Photon. *Nature* (2015) 518:516–9. doi:10.1038/nature14246
12. Zhao Y. *Applied Basic Research on Multi-Scenario Short-Reach Optical Interconnects Based on Orbital Angular Momentum Modes*. [dissertation/ doctoral thesis]. [Wuhan(Hubei)]: Huazhong University of Science and Technology (2019).
13. Wang J, Yang J-Y, Fazal IM, Ahmed N, Yan Y, Huang H, et al. Terabit Free-Space Data Transmission Employing Orbital Angular Momentum Multiplexing. *Nat Photon* (2012) 6:488–96. doi:10.1038/nphoton.2012.138
14. Yan Y, Xie G, Lavery MPJ, Huang H, Ahmed N, Bao C, et al. High-capacity Millimetre-Wave Communications with Orbital Angular Momentum Multiplexing. *Nat Commun* (2014) 5:4876. doi:10.1038/ncomms5876
15. Ke X, Guo X. Realization of Optical Phase Information Encode by Using Orbital Angular Momentum of Light Beam. *Chin J Quant Elect* (2015) 32: 69–76. doi:10.3969/j.issn.1007-5461.2015.01.010
16. Randel S, Ryf R, Sierra A, Winzer PJ, Gnauck AH, Bolle CA, et al. 6×56-Gb/s Mode-Division Multiplexed Transmission over 33-km Few-Mode Fiber Enabled by 6×6 MIMO Equalization. *Opt Express* (2011) 19:16697–707. doi:10.1364/OE.19.016697
17. Milione G, Huang H, Lavery M, Willner A, Padgett MJ. *Orbital-Angular-Momentum Mode (De)Multiplexer: A Single Optical Element for MIMO-Based and Non-MIMO-based Multimode Fiber Systems[Conference Presentation]*. San Francisco, California, United States: OFC 2014 (2014).
18. Zhang Z, Xiao Y, Ma Z, Xiao M, Ding Z, Lei X, et al. 6G Wireless Networks: Vision, Requirements, Architecture, and Key Technologies. *IEEE Veh Technol Mag* (2019) 14:28–41. doi:10.1109/mvt.2019.2921208
19. Yao AM, Padgett MJ. Orbital Angular Momentum: Origins, Behavior and Applications. *Adv Opt Photon* (2011) 3:161–204. doi:10.1364/aop.3.000161
20. Curtis JE, Grier DG. Modulated Optical Vortices. *Opt Lett* (2003) 28:872–87. doi:10.1364/ol.28.000872
21. Yan L, Gregg P, Karimi E, Rubano A, Marrucci L, Boyd R, et al. Q-plate Enabled Spectrally Diverse Orbital-Angular-Momentum Conversion for Stimulated Emission Depletion Microscopy. *Optica* (2015) 2:900. doi:10.1364/optica.2.000900
22. Liu J, Xing D, Zeng X, Lu J. Orbital Angular Momentum Multiplexing Technology Based on Optical Fiber. *Laser Optoelectronics Prog* (2018) 55: 42–54. doi:10.3788/lop55.050005
23. Wang Y, Bao C, Geng W, Lu Y, Fang Y, Mao B, et al. Air-Core Ring Fiber with >1000 Radially Fundamental OAM Modes across O, E, S, C, and L Bands. *IEEE Access* (2020) 8:68280–7. doi:10.1109/access.2020.2985776
24. Zhang X, Wang A, Chen R, Zhou Y, Ming H, Zhan Q. Generation and Conversion of Higher Order Optical Vortices in Optical Fiber with Helical Fiber Bragg Gratings. *J Lightwave Technol* (2016) 34:2413–8. doi:10.1109/ jlt.2016.2536037
25. Wen J, He X, Xing J, Yang J, Pang F, Zeng X, et al. All-Fiber OAM Amplifier with High Purity and Broadband Spectrum Gain Based on Fused Taper Vortex-Beam Coupler. *IEEE Photon J.* (2018) 10:1–8. doi:10.1109/ jphot.2018.2872040
26. Tao R. *Simulation and Realization of Vector Beam in Optical Fiber Waveguide*. [dissertation/doctoral thesis]. [Hefei(Anhui)]: University of Science and Technology of China (2020).
27. Zhou H. *Research on Measurement Techniques of Optical Orbital Angular Momentum*. [dissertation/doctoral thesis]. [Wuhan(Hubei)]: Huazhong University of Science and Technology (2017).
28. Sun P. *Generation of Vector Vortex Beams in an Optical Fiber*. [dissertation/ master's thesis]. [Harbin(Heilongjiang)]: Harbin University of Science and Technology (2016).
29. Holleczek A, Aiello A, Gabriel C, Marquardt C, Leuchs G. Classical and Quantum Properties of Cylindrically Polarized States of Light. *Opt Express* (2011) 19:9714–36. doi:10.1364/OE.19.009714

30. Jiang Y, Ren G, Jin W, Xu Y, Jian W, Jian S. Polarization Properties of Fiber-Based Orbital Angular Momentum Modes. *Opt Fiber Technol* (2017) 38: 113–8. doi:10.1016/j.yofte.2017.09.002
31. Zhang H, Liu Y, Wang Z, Mao B, Han Y, Yang K. Generation of Arbitrary Polarized OAM Mode Based on a Fiber Mode Selective Coupler. *J Opt* (2019) 21:085705. doi:10.1088/2040-8986/ab2c4a
32. Alexeyev AN, Fadeyeva TA, Fadeyeva TA, Volyar AV, Soskin MS. Optical Vortices and the Flow of Their Angular Momentum in a Multimode Fiber. *Semiconductor Phys Quan Electron Optoelectronics* (1998) 1:82–9. doi:10.15407/spqeo1.01.082
33. Tian W, Zhang H, Zhang X, Xi L, Zhang W, Tang X. A Circular Photonic crystal Fiber Supporting 26 OAM Modes. *Opt Fiber Technol* (2016) 30:184–9. doi:10.1016/j.yofte.2016.07.009
34. Nejad RM, Allahverdyan K, Vaity P, Amiralizadeh S, Brunet C, Messaddeq Y, et al. Mode Division Multiplexing Using Orbital Angular Momentum Modes over 1.4-km Ring Core Fiber. *J Lightwave Technol* (2016) 34:4252–8. doi:10.1109/jlt.2016.2594698
35. Huang W, Liu Y-g., Wang Z, Zhang W, Luo M, Liu X, et al. Generation and Excitation of Different Orbital Angular Momentum States in a Tunable Microstructure Optical Fiber. *Opt Express* (2015) 23:33741–52. doi:10.1364/OE.23.033741
36. Zhu G, Wang X, Chen Y, Hui C, Li S. *Microstructured Optical Fibers for Transmitting Orbital Angular Momentum (OAM) Mode[Conference Presentation]*. Hong Kong, China: ACP 2015 (2015).
37. Wang W, Hou L. Present Situation and Future Development in Photonic Crystal Fibers. *Las Optoelect Prog* (2008) 45:43–58. doi:10.3788/lop20084502.0043
38. Knight JC, Birks TA, Russell PSJ, Atkin DM. All-silica Single-Mode Optical Fiber with Photonic crystal Cladding. *Opt Lett* (1996) 21:1547–9. doi:10.1364/ol.21.001547
39. Yue Y, Zhang L, Yan Y, Ahmed N, Yang J-Y, Huang H, et al. Octave-spanning Supercontinuum Generation of Vortices in an As_2S_3 Ring Photonic crystal Fiber. *Opt Lett* (2012) 37:1889–91. doi:10.1364/OL.37.001889
40. Zhang H, Zhang W, Xi L, Tang X, Tian W, Zhang X. *Design of a Circular Photonic Crystal Fiber Supporting OAM Modes[Conference Presentation]*. Hong Kong, China: ACP 2015 (2015).
41. Jia C, Jia H, Wang N, Chai J, Xu X, Lei Y, et al. Theoretical Analysis of a 750-nm Bandwidth Hollow-Core Ring Photonic Crystal Fiber with a Graded Structure for Transporting 38 Orbital Angular Momentum Modes. *IEEE Access* (2018) 6:20291–7. doi:10.1109/access.2018.2817577
42. Hassan MM, Kabir MA, Hossain MN, Nguyen TK, Paul BK, Ahmed K, et al. Numerical Analysis of Circular Core Shaped Photonic crystal Fiber for Orbital Angular Momentum with Efficient Transmission. *Appl Phys B* (2020) 126:145. doi:10.1007/s00340-020-07497-2
43. Huang W, You Y, Song B-b., Chen S-y. A Photonic crystal Fiber for Supporting 30 Orbital Angular Momentum Modes with Low Dispersion. *Optoelectron Lett* (2020) 16:34–9. doi:10.1007/s11801-020-9072-7
44. Israk MF, Razzak MA, Ahmed K, Hassan MM, Kabir MA, Hossain MN, et al. Ring-based Coil Structure Photonic crystal Fiber for Transmission of Orbital Angular Momentum with Large Bandwidth: Outline, Investigation and Analysis. *Opt Commun* (2020) 473:126003. doi:10.1016/j.optcom.2020.126003
45. Zhang L, Meng Y. Design and Analysis of a Photonic crystal Fiber Supporting Stable Transmission of 30 OAM Modes. *Opt Fiber Technol* (2021) 61:102423. doi:10.1016/j.yofte.2020.102423
46. Nandam A, Shin W. Spiral Photonic crystal Fiber Structure for Supporting Orbital Angular Momentum Modes. *Optik* (2018) 169:361–7. doi:10.1016/j.ijleo.2018.05.055
47. Hu Z-A, Huang Y-Q, Luo A-P, Cui H, Luo Z-C, Xu W-C. Photonic crystal Fiber for Supporting 26 Orbital Angular Momentum Modes. *Opt Express* (2016) 24:17285–91. doi:10.1364/OE.24.017285
48. Jiao X, Zhang H, Zhang X, Li H, Wei J, Wang Z, et al. Performance of Circular Photonic crystal Fiber Transmitting Orbital Angular Momentum Modes under Macro-Bending. *J Opt* (2019) 21:065703. doi:10.1088/2040-8986/ab1c44
49. Bai X, Chen H, Yang H. Design of a Circular Photonic crystal Fiber with Square Air-Holes for Orbital Angular Momentum Modes Transmission. *Optik* (2018) 158:1266–74. doi:10.1016/j.ijleo.2018.01.015
50. Yang H. *Design and Performance Analysis of a Novel Photonic crystal Fiber for OAM Mode Transmission*. [dissertation/master's thesis]. [Nanjing(Jiangsu)]: Nanjing University of Posts and Telecommunications (2018).
51. Ke X, Wang S. Design of Photonic Crystal Fiber Capable of Carrying Multiple Orbital Angular Momentum Modes Transmission. *Opt Photon J* (2020) 10: 49–63. doi:10.4236/opj.2020.104005
52. Hassan MM, Kabir MA, Hossain MN, Biswas B, Paul BK, Ahmed K. Photonic crystal Fiber for Robust Orbital Angular Momentum Transmission: Design and Investigation. *Opt Quant Electron* (2019) 52:8. doi:10.1007/s11082-019-2125-0
53. Kabir MA, Hassan MM, Hossain MN, Paul BK, Ahmed K. Design and Performance Evaluation of Photonic crystal Fibers of Supporting Orbital Angular Momentum States in Optical Transmission. *Opt Commun* (2020) 467:125731. doi:10.1016/j.optcom.2020.125731
54. Wang W, Sun C, Wang N, Jia H. A Design of Nested Photonic crystal Fiber with Low Nonlinear and Flat Dispersion Supporting 30+50 OAM Modes. *Opt Commun* (2020) 471:125823. doi:10.1016/j.optcom.2020.125823
55. Wang W, Wang N, Li K, Geng Z, Jia H. A Novel Dual Guided Modes Regions Photonic crystal Fiber with Low Crosstalk Supporting 56 OAM Modes and 4 LP Modes. *Opt Fiber Technol* (2020) 57:102213. doi:10.1016/j.yofte.2020.102213
56. Al-Zahrani FA, Ahmed K. Novel Design of Dual Guided Photonic crystal Fiber for Large Capacity Transmission in High-Speed Optics Communications with Supporting Good Quality OAM and LP Modes. *Alexandria Eng J* (2020) 59:4889–99. doi:10.1016/j.aej.2020.09.004
57. He T. *Design of Photonic Crystal Fiber for Orbital Angular Momentum Mode and Study on its Magnetic Tunability*. [dissertation/master's thesis]. [Chengdu(Sichuan)]: University of Electronic Science and Technology of China (2020).
58. Ramachandran S, Kristensen P, Yan MF. Generation and Propagation of Radially Polarized Beams in Optical Fibers. *Opt Lett* (2009) 34:2525–7. doi:10.1364/ol.34.002525
59. Jung Y, Kang Q, Zhou H, Rui Z, Richardson DJ. *Low-loss 25.3km Few-Mode Ring-Core Fibre for Mode-Division Multiplexed transmission[Conference Presentation]*. Dusseldorf, Germany: ECOC 2016 (2016).
60. Jin X, Gomez A, Shi K, Thomsen BC, Feng F, Gordon GSD, et al. Mode Coupling Effects in Ring-Core Fibers for Space-Division Multiplexing Systems. *J Lightwave Technol* (2016) 34:3365–72. doi:10.1109/jlt.2016.2564991
61. Shen L, Zhang J, Liu J, Zhu G, Yu S. *MIMO-free WDM-MDM Transmission over 100-KM Single-Span Ring-Core fibre[Conference Presentation]*. Dublin, Ireland: ECOC 2019 (2019).
62. Gregg P, Kristensen P, Rubano A, Golowich S, Marrucci L, Ramachandran S. Enhanced Spin Orbit Interaction of Light in Highly Confining Optical Fibers for Mode Division Multiplexing. *Nat Commun* (2019) 10:4707. doi:10.1038/s41467-019-12401-4
63. Brunet C, Ung B, Belanger P-A, Messaddeq Y, LaRochelle S, Rusch LA. Vector Mode Analysis of Ring-Core Fibers: Design Tools for Spatial Division Multiplexing. *J Lightwave Technol* (2014) 32:4648–59. doi:10.1109/jlt.2014.2361432
64. Brunet C, Vaity P, Ung B, Messaddeq Y, Larochelle S, Rusch LA. *Design of a Family of Ring-Core Fiber for OAM[Conference Presentation]*. Los Angeles, California, United States: OFC 2015 (2015).
65. Wang H, Liang Y, Zhang X, Chen S, Shen L, Zhang L, et al. Low-loss Orbital Angular Momentum Ring-Core Fiber: Design, Fabrication and Characterization. *J Lightwave Technol* (2020) 38:1. doi:10.1109/jlt.2020.3012285
66. Huang G, Zhou S, Qin Y, Xue L, Yan M. Modal Characteristics Analysis of Orbital Angular Momentum in a Modified Ring Fiber. *Las Optoelect Prog* (2015) 52:080604. doi:10.3788/lop52.080604
67. Li S, Wang J. A Compact Trench-Assisted Multi-Orbital-Angular-Momentum Multi-Ring Fiber for Ultrahigh-Density Space-Division Multiplexing (19 Rings × 22 Modes). *Sci Rep* (2014) 4:3853. doi:10.1038/srep03853
68. Zhu G, Hu Z, Wu X, Du C, Luo W, Chen Y, et al. Scalable Mode Division Multiplexed Transmission over a 10-km Ring-Core Fiber Using High-Order Orbital Angular Momentum Modes. *Opt Express* (2018) 26:594–604. doi:10.1364/OE.26.000594
69. Zhu L, Zhu G, Wang A, Wang L, Ai J, Chen S, et al. 18 Km Low-Crosstalk OAM + WDM Transmission with 224 Individual Channels Enabled by a Ring-Core Fiber with Large High-Order Mode Group Separation. *Opt Lett* (2018) 43:1890–3. doi:10.1364/OL.43.001890
70. Tan H, Zhang J, Liu J, Shen L, Yu S. *Low-Loss Ring-Core Fiber Supporting 4 Mode Groups[Conference Presentation]*. San Jose, California, United States: CLEO: Science and Innovations 2019 (2019).

71. Zhang J, Liu J, Shen L, Zhang L, Luo J, Liu J, et al. Mode-division Multiplexed Transmission of Wavelength-Division Multiplexing Signals over a 100-km Single-Span Orbital Angular Momentum Fiber. *Photon Res* (2020) 8:1236. doi:10.1364/prj.394864
72. Gregg P, Kristensen P, Golowich SE, Olsen JØ, Steinvurzel P, Ramachandran S. *Stable Transmission of 12 OAM States in Air-Core Fiber[Conference Presentation]*. San Jose, California, United States: CLEO: Science and Innovations 2013 (2013).
73. Brunet C, Ung B, Messaddeq Y, Larochelle S, Rusch LA. *Design of an Optical Fiber Supporting 16 OAM Modes [Conference Presentation]*. San Francisco, California, United States: OFC 2014 (2014).
74. Brunet C, Vaity P, Messaddeq Y, LaRochelle S, Rusch LA. Design, Fabrication and Validation of an OAM Fiber Supporting 36 States. *Opt Express* (2014) 22: 26117–27. doi:10.1364/OE.22.026117
75. Gregg P, Kristensen P, Ramachandran S. Conservation of Orbital Angular Momentum in Air-Core Optical Fibers. *Optica* (2015) 2:267. doi:10.1364/optica.2.000267
76. Wang Y, Bao C, Jiang J, Fang Y, Geng W, Wang Z, et al. Two-Octave Supercontinuum Generation of High-Order OAM Modes in Air-Core As_2S_3 Ring Fiber. *IEEE Access* (2020) 8:114135–42. doi:10.1109/access.2020.3002767
77. Ung B, Vaity P, Wang L, Messaddeq Y, Rusch LA, LaRochelle S. Few-mode Fiber with Inverse-Parabolic Graded-index Profile for Transmission of OAM-Carrying Modes. *Opt Express* (2014) 22:18044–55. doi:10.1364/OE.22.018044
78. Chen Y. *Design and Research of Transmission Fiber with High Order Orbital Angular Momentum Mode*. [dissertation/master's thesis]. [Xi'an(Shanxi)]: Xi'an University of Technology (2019).
79. Zhang Z, Liu X, Wei W, Ding L, Tang L, Li Y. The Simulation of Vortex Modes in Twisted Few-Mode Fiber with Inverse-Parabolic Index Profile. *IEEE Photon J.* (2020) 12:1–8. doi:10.1109/jphot.2020.2994819
80. Ma Y, Chen H, Bai X. A New Type Graded-index Ring Fiber Supporting Multi-OAM Modes. *Study Opt Commun* (2017) 02:47–50. doi:10.13756/j.gtxyj.2017.02.013
81. Tu J, Gao S, Wang Z, Liu Z, Li W, Du C, et al. Bend-insensitive Grapefruit-type Holey Ring-Core Fiber for Weakly-Coupled OAM Mode Division Multiplexing Transmission. *J Lightwave Technol* (2020) 38:4497–503. doi:10.1109/jlt.2020.2987328
82. Ma J, Xia F, Chen S, Li S, Wang J. Amplification of 18 OAM Modes in a Ring-Core Erbium-Doped Fiber with Low Differential Modal Gain. *Opt Express* (2019) 27:38087–97. doi:10.1364/OE.27.038087
83. Liu J, Chen S, Wang H, Zheng S, Zhu L, Wang A, et al. Amplifying Orbital Angular Momentum Modes in Ring-Core Erbium-Doped Fiber. *Research* (2020) 2020:1–12. doi:10.34133/2020/7623751
84. Jung Y, Kang Q, Sidharthan R, Ho D, Yoo S, Gregg P, et al. Optical Orbital Angular Momentum Amplifier Based on an Air-Hole Erbium-Doped Fiber. *J Lightwave Technol* (2017) 35:430–6. doi:10.1109/jlt.2017.2651145
85. Beijersbergen MW, Coerwinkel RPC, Kristensen M, Woerdman JP. Helical-wavefront Laser Beams Produced with a Spiral Phaseplate. *Opt Commun* (1994) 112:321–7. doi:10.1016/0030-4018(94)90638-6
86. Gibson G, Courtial J, Padgett MJ, Vasnetsov M, Pas'ko V, Barnett SM, et al. Free-space Information Transfer Using Light Beams Carrying Orbital Angular Momentum. *Opt Express* (2004) 12:5448–56. doi:10.1364/opex.12.005448
87. Marrucci L, Karimi E, Slussarenko S, Piccirillo B, Santamato E, Nagali E, et al. Spin-to-orbital Conversion of the Angular Momentum of Light and its Classical and Quantum Applications. *J Opt* (2011) 13:064001. doi:10.1088/2040-8978/13/6/064001
88. Zhang X. *Generation and Conversion of Optical Vortices in Optical Fiber*. [dissertation/doctoral thesis]. [Hefei(Anhui)]: University of Science and Technology of China (2016).
89. Wu H. *High-order Optical Vortex Generation and Modulation Based on Long-Period Grating in a Few-Mode Fiber*. [dissertation/master's thesis]. Guangzhou(Guangdong): Jinan University (2018).
90. Zhang Y. *The Generation and Regulation of Orbital Angular Momentum Mode Based on Few-Mode Fiber Grating*. [dissertation/master's thesis]. [Shenzhen(Guangdong)]: Shenzhen University (2019).
91. Jiang Y, Ren G, Shen Y, Xu Y, Jin W, Wu Y, et al. Two-dimensional Tunable Orbital Angular Momentum Generation Using a Vortex Fiber. *Opt Lett* (2017) 42:5014–7. doi:10.1364/OL.42.005014
92. Fujisawa T, Saitoh K. Geometric-phase-induced Arbitrary Polarization and Orbital Angular Momentum Generation in Helically Twisted Birefringent Photonic crystal Fiber. *Photon Res* (2020) 8:1278. doi:10.1364/prj.393255
93. Fu C, Liu S, Wang Y, Bai Z, He J, Liao C, et al. High-order Orbital Angular Momentum Mode Generator Based on Twisted Photonic crystal Fiber. *Opt Lett* (2018) 43:1786–9. doi:10.1364/OL.43.001786
94. Ye J, Li Y, Han Y, Deng D, Guo Z, Gao J, et al. Excitation and Separation of Vortex Modes in Twisted Air-Core Fiber. *Opt Express* (2016) 24:8310–6. doi:10.1364/OE.24.008310
95. Fang L. *Theoretical Study of Mode-Selective Couplers Based on Optical Fiber Gratings*. [dissertation/master's thesis]. [Shanghai]: University of Shanghai for Science and Technology (2014).
96. Ge T. *Theoretical and Experimental Reserch on the Use of Optical Fiber to Generate Vortex Beam*. [dissertation/master's thesis]. [Xi'an(Shanxi)]: Xi'an University of Technology (2018).
97. Bozinovic N, Golowich S, Kristensen P, Ramachandran S. Control of Orbital Angular Momentum of Light with Optical Fibers. *Opt Lett* (2012) 37:2451–3. doi:10.1364/OL.37.002451
98. Mao B, Liu Y, Zhang H, Yang K, Han Y, Wang Z, et al. Complex Analysis between CV Modes and OAM Modes in Fiber Systems. *Nanophotonics* (2018) 8:271–85. doi:10.1515/nanoph-2018-0179
99. Zhang H, Mao B, Han Y, Wang Z, Yue Y, Liu Y. Generation of Orbital Angular Momentum Modes Using Fiber Systems. *Appl Sci* (2019) 9:1033. doi:10.3390/app9051033
100. Zhao Y, Liu Y, Zhang L, Zhang C, Wen J, Wang T. Mode Converter Based on the Long-Period Fiber Gratings Written in the Two-Mode Fiber. *Opt Express* (2016) 24:6186–95. doi:10.1364/OE.24.006186
101. Zhao Y, Liu Y, Zhang C, Zhang L, Zheng G, Mou C, et al. All-fiber Mode Converter Based on Long-Period Fiber Gratings Written in Few-Mode Fiber. *Opt Lett* (2017) 42:4708–11. doi:10.1364/OL.42.004708
102. Han Y, Liu Y-G, Wang Z, Huang W, Chen L, Zhang H-W, et al. Controllable All-Fiber Generation/conversion of Circularly Polarized Orbital Angular Momentum Beams Using Long Period Fiber Gratings. *Nanophotonics* (2018) 7:287–93. doi:10.1515/nanoph-2017-0047
103. Li S, Mo Q, Hu X, Du C, Wang J. Controllable All-Fiber Orbital Angular Momentum Mode Converter. *Opt Lett* (2015) 40:4376–9. doi:10.1364/OL.40.004376
104. Wu H, Gao S, Huang B, Feng Y, Huang X, Liu W, et al. All-fiber Second-Order Optical Vortex Generation Based on strong Modulated Long-Period Grating in a Four-Mode Fiber. *Opt Lett* (2017) 42:5210–3. doi:10.1364/OL.42.005210
105. Li Y, Jin L, Wu H, Gao S, Feng Y-H, Li Z. Superposing Multiple LP Modes with Microphase Difference Distributed along Fiber to Generate OAM Mode. *IEEE Photon J.* (2017) 9:1–9. doi:10.1109/jphot.2017.2674022
106. Han Y, Chen L, Liu Y-G, Wang Z, Zhang H, Yang K, et al. Orbital Angular Momentum Transition of Light Using a Cylindrical Vector Beam. *Opt Lett* (2018) 43:2146–9. doi:10.1364/OL.43.002146
107. Xu H, Yang L. Conversion of Orbital Angular Momentum of Light in Chiral Fiber Gratings. *Opt Lett* (2013) 38:1978–80. doi:10.1364/OL.38.001978
108. Fu C, Yu B, Wang Y, Liu S, Bai Z, He J, et al. Orbital Angular Momentum Mode Converter Based on Helical Long Period Fiber Grating Inscribed by Hydrogen-Oxygen Flame. *J Lightwave Technol* (2018) 36:1683–8. doi:10.1109/jlt.2017.2787120
109. Bai Z, Wang Y, Zhang Y, Fu C, Liu S, Li M, et al. Helical Long-Period Fiber Gratings as Wavelength-Tunable Orbital Angular Momentum Mode Generators. *IEEE Photon Technol Lett* (2020) 32:418–21. doi:10.1109/lpt.2019.2958385
110. Wang L, Vaity P, Ung B, Messaddeq Y, Rusch LA, LaRochelle S. Characterization of OAM Fibers Using Fiber Bragg Gratings. *Opt Express* (2014) 22:15653–61. doi:10.1364/OE.22.015653
111. Zhao Y, Wang C, Liu Z, Zhou K, Mou C, Liu Y. *Generation of Multiple-Order OAM Modes Using a Tilted Few-Mode Fiber Bragg Grating[Conference Presentation]*. Guangzhou, Guangdong, China: ACP 2017 (2017).
112. Yang K, Liu Y-g., Wang Z, Li Y, Han Y, Zhang H-w., et al. Triple-order Orbital-Angular-Momentum Modes Generation Based on Single Tilted Fiber Bragg Grating in a Few-Mode Ring-Core Fiber. *Opt Fiber Technol* (2020) 55: 102155. doi:10.1016/j.yofte.2020.102155
113. Lin Z, Wang A, Xu L, Zhang X, Sun B, Gu C, et al. Generation of Optical Vortices Using a Helical Fiber Bragg Grating. *J Lightwave Technol* (2014) 32: 2152–6. doi:10.1109/jlt.2014.2320539

114. Huang G. *Modal Characteristics of OAM in a Modified Ring Fiber*. [dissertation/master's thesis]. [Hangzhou(Zhejiang)]: Zhejiang University of Technology (2015).
115. Wang T, Wang F, Shi F, Pang F, Huang S, Wang T, et al. Generation of Femtosecond Optical Vortex Beams in All-Fiber Mode-Locked Fiber Laser Using Mode Selective Coupler. *J Lightwave Technol* (2017) 35:2161–6. doi:10.1109/jlt.2017.2676241
116. Zhang H, Mao B, Han Y, Yang K, Wang Z, Liu Y. Generation of Orbital Angular Momentum Mode Using a Single Cylindrical Vector Mode Based on Mode Selective Coupler. *Opt Fiber Technol* (2019) 52:101934. doi:10.1016/j.yofte.2019.101934
117. Pidishety S, Khudus M, Gregg P, Ramachandran S, Brambilla G. *OAM Beam Generation Using All-Fiber Fused Couplers[Conference Presentation]*. San Jose, California, United States: CLEO: Science and Innovations 2016 (2016).
118. Pidishety S, Pachava S, Gregg P, Ramachandran S, Brambilla G, Srinivasan B. Orbital Angular Momentum Beam Excitation Using an All-Fiber Weakly Fused Mode Selective Coupler. *Opt Lett* (2017) 42:4347–50. doi:10.1364/OL.42.004347
119. Heng X, Gan J, Zhang Z, Li J, Li M, Zhao H, et al. All-fiber Stable Orbital Angular Momentum Beam Generation and Propagation. *Opt Express* (2018) 26:17429–36. doi:10.1364/OE.26.017429
120. Jin X, Pang F, Zhang Y, Huang S, Li Y, Wen J, et al. Generation of the First-Order OAM Modes in Single-Ring Fibers by Offset Splicing Technology. *IEEE Photon Technol Lett* (2016) 28:1581–4. doi:10.1109/lpt.2016.2552223
121. Li S, Xu Z, Zhao R, Shen L, Du C, Wang J. Generation of Orbital Angular Momentum Beam Using Fiber-To-Fiber Butt Coupling. *IEEE Photon J.* (2018) 10:1–7. doi:10.1109/jphot.2018.2856263
122. Wong GKL, Kang MS, Lee HW, Biancalana F, Conti C, Weiss T, et al. Excitation of Orbital Angular Momentum Resonances in Helically Twisted Photonic crystal Fiber. *Science* (2012) 337:446–9. doi:10.1126/science.1223824
123. Cui Y, Ye J, Li Y, Dai P, Qu S. Vortex Chirality-dependent Filtering in Helically Twisted Single-Ring Photonic crystal Fibers. *Opt Express* (2019) 27:20816–23. doi:10.1364/OE.27.020816
124. Dashti PZ, Alhassen F, Lee HP. Observation of Orbital Angular Momentum Transfer between Acoustic and Optical Vortices in Optical Fiber. *Phys Rev Lett* (2006) 96:043604. doi:10.1103/PhysRevLett.96.043604
125. Zhang W, Huang L, Wei K, Li P, Jiang B, Mao D, et al. High-order Optical Vortex Generation in a Few-Mode Fiber via Cascaded Acoustically Driven Vector Mode Conversion. *Opt Lett* (2016) 41:5082–5. doi:10.1364/OL.41.005082
126. Zhang W, Wei K, Huang L, Mao D, Jiang B, Gao F, et al. Optical Vortex Generation with Wavelength Tunability Based on an Acoustically-Induced Fiber Grating. *Opt Express* (2016) 24:19278–85. doi:10.1364/OE.24.019278
127. Yan Y, Wang J, Zhang L, Yang J-Y, Fazal IM, Ahmed N, et al. Fiber Coupler for Generating Orbital Angular Momentum Modes. *Opt Lett* (2011) 36:4269–71. doi:10.1364/OL.36.004269
128. Yan Y, Yue Y, Huang H, Yang J-Y, Chitgarha MR, Ahmed N, et al. Efficient Generation and Multiplexing of Optical Orbital Angular Momentum Modes in a Ring Fiber by Using Multiple Coherent Inputs. *Opt Lett* (2012) 37:3645–7. doi:10.1364/OL.37.003645
129. Yan Y, Zhang L, Wang J, Yang J-Y, Fazal IM, Ahmed N, et al. Fiber Structure to Convert a Gaussian Beam to Higher-Order Optical Orbital Angular Momentum Modes. *Opt Lett* (2012) 37:3294–6. doi:10.1364/OL.37.003294
130. Li L, Zhu S, Li J, Shao X, Galvanauskas A, Ma X. All-in-fiber Method of Generating Orbital Angular Momentum with Helically Symmetric Fibers. *Appl Opt* (2018) 57:8182–6. doi:10.1364/AO.57.008182
131. Lin Z. *Nonlinear Frequency Conversion of Beams Carrying Orbital Angular Momentum*. [dissertation/master's thesis]. Nanjing(Jiangsu): Nanjing University (2019).
132. Wang A, Zhu L, Chen S, Du C, Mo Q, Wang J. Characterization of LDPC-Coded Orbital Angular Momentum Modes Transmission and Multiplexing over a 50-km Fiber. *Opt Express* (2016) 24:11716–26. doi:10.1364/OE.24.011716
133. Zhu B, Taunay TF, Fishteyn M, Liu X, Chandrasekhar S, Yan MF, et al. 112-Tb/s Space-Division Multiplexed DWDM Transmission with 14-b/s/Hz Aggregate Spectral Efficiency over a 768-km Seven-Core Fiber. *Opt Express* (2011) 19:16665–71. doi:10.1364/OE.19.016665
134. Lv W. *Theoretical Research of Orbital Angular Momentum of Beam and Experimental Research of Optical Tweezers Sort Cell*. [dissertation/master's thesis]. [Qinhuangdao(Hebei)]: Yanshan University (2010).
135. Fürhapter S, Jesacher A, Bernet S, Ritsch-Marte M. Spiral Phase Contrast Imaging in Microscopy. *Opt Express* (2005) 13:689–94. doi:10.1364/opex.13.000689
136. Padgett M, Courtial J, Allen L. Light's Orbital Angular Momentum. *Phys Today* (2004) 57:35–40. doi:10.1063/1.1768672
137. Wu Y. *Phase-Matching Controlled Nonlinear Frequency Conversion of Orbital Angular Momentum*. [dissertation/master's thesis]. [Nanjing(Jiangsu)]: Nanjing University (2019).
138. Fang W-T, Tao R-X, Zhang Y-m., Zhou Z-Y, Yao P-j., Shi B-S, et al. Tailoring Nonlinear Processes of Orbital Angular Momentum with Dispersion Engineering in Vortex Fibers. *Phys Rev Appl* (2019) 12:034007. doi:10.1103/PhysRevApplied.12.034007
139. Yang H. *Nonlinear Multiplexing Holography Based on Orbital Angular Momentum of Light*. [dissertation/master's thesis]. [Nanjing(Jiangsu)]: Nanjing University (2020).
140. Shuhui Li S, Jian Wang J. Multi-Orbital-Angular-Momentum Multi-Ring Fiber for High-Density Space-Division Multiplexing. *IEEE Photon J.* (2013) 5:7101007. doi:10.1109/jphot.2013.2272778
141. Huang H, Milione G, Lavery MPJ, Xie G, Ren Y, Cao Y, et al. Mode Division Multiplexing Using an Orbital Angular Momentum Mode Sorter and MIMO-DSP over a Graded-index Few-Mode Optical Fibre. *Sci Rep* (2015) 5:14931. doi:10.1038/srep14931
142. Zhang J, Zhu G, Liu J, Wu X, Zhu J, Du C, et al. Orbital-angular-momentum Mode-Group Multiplexed Transmission over a Graded-index Ring-Core Fiber Based on Receive Diversity and Maximal Ratio Combining. *Opt Express* (2018) 26:4243. doi:10.1364/oe.26.004243
143. Feng F, Guo X, Gordon G, Jin X, Wilkinson TD. *All-optical Mode-Group Division Multiplexing over a Graded-Index Ring-Core Fiber with Single Radial Mode [Conference Presentation]*. Los Angeles, California, United States: OFC 2016 (2016).
144. Gahagan KT, Swartzlander GA. Trapping of Low-index Microparticles in an Optical Vortex. *J Opt Soc Am B* (1998) 15:524. doi:10.1364/josab.15.000524
145. O'Neil AT, MacVicar I, Allen L, Padgett MJ. Intrinsic and Extrinsic Nature of the Orbital Angular Momentum of a Light Beam. *Phys Rev Lett* (2002) 88:053601. doi:10.1103/PhysRevLett.88.053601
146. Gao Ming-Wei M, Gao Chun-Qing C, He Xiao-Yan X, Li Jia-Ze J, Wei Guang-Hui G. Rotation of Particles by Using the Beam with Orbital Angular Momentum. *Acta Physica Sinica* (2004) 53:413–7. doi:10.7498/aps.53.413
147. Lehmuskero A, Li Y, Johansson P, Käll M. Plasmonic Particles Set into Fast Orbital Motion by an Optical Vortex Beam. *Opt Express* (2014) 22:4349–56. doi:10.1364/OE.22.004349
148. Li L. *The Analysis of High-Capacity Quantum Secure Direct Communication Using Polarization and Orbital Angular Momentum of Photons*. [dissertation/master's thesis]. [Beijing: Beijing University of Posts and Telecommunications (2020).
149. Malik M, Erhard M, Huber M, Krenn M, Fickler R, Zeilinger A. Multi-photon Entanglement in High Dimensions. *Nat Photon* (2016) 10:248–52. doi:10.1038/nphoton.2016.12
150. Lavery MPJ, Robertson DJ, Berkhout GCG, Love GD, Padgett MJ, Courtial J. Refractive Elements for the Measurement of the Orbital Angular Momentum of a Single Photon. *Opt Express* (2012) 20:2110–5. doi:10.1364/OE.20.002110
151. Swartzlander GA. Peering into Darkness with a Vortex Spatial Filter. *Opt Lett* (2001) 26:497–9. doi:10.1364/ol.26.000497

Conflict of Interest: The authors declare that the research was conducted in the absence of any commercial or financial relationships that could be construed as a potential conflict of interest.

frontiers in Physics

ORIGINAL RESEARCH
published: 03 January 2022
doi: 10.3389/fphy.2021.771260

Observation of the Rotational Doppler Effect With Structured Beams in Atomic Vapor

Shuwei Qiu[1], Jinwen Wang[1], Xin Yang[1], Mingtao Cao[2], Shougang Zhang[2], Hong Gao[1]* and Fuli Li[1]*

[1]Ministry of Education Key Laboratory for Nonequilibrium Synthesis and Modulation of Condensed Matter, Shaanxi Province Key Laboratory of Quantum Information and Quantum Optoelectronic Devices, School of Physics, Xi'an Jiaotong University, Xi'an, China, [2]Key Laboratory of Time and Frequency Primary Standards, National Time Service Center, Chinese Academy of Science, Xi'an, China

A vector beam with the spatial variation polarization has attracted keen interest and is progressively applied in quantum information, quantum communication, precision measurement, and so on. In this letter, the spectrum observation of the rotational Doppler effect based on the coherent interaction between atoms and structured light in an atomic vapor is realized. The geometric phase and polarization of the structured beam are generated and manipulated by using a flexible and efficacious combination optical elements, converting an initial linearly polarized Gaussian beam into a phase vortex beam or an asymmetric or symmetric vector beam. These three representative types of structured beam independently interact with atoms under a longitudinal magnetic field to explore the rotational Doppler shift associated with the topological charge. We find that the rotational Doppler broadening increases obviously with the topological charge of the asymmetric and symmetric vector beam. There is no rotational Doppler broadening observed from the spectrum of the phase vortex beam, although the topological charge, and spatial profile of the beam change. This study can be applied to estimate the rotational velocity of the atom-level or molecule-level objects, measure the intensity of magnetic fields and study the quantum coherence in atomic ensembles.

Keywords: structured beam, vector beam, orbital angular momentum, rotational Doppler effect, electromagnetically induced transparency, spiral phase plate, retardation wave plate

OPEN ACCESS

Edited by:
Junjie Yu,
Shanghai Institute of Optics and Fine Mechanics (CAS), China

Reviewed by:
Qing Ai,
Beijing Normal University, China
GuoPing Guo,
University of Science and Technology of China, China

****Correspondence:***
Mingtao Cao
mingtaocao@ntsc.ac.cn
Hong Gao
honggao@xjtu.edu.cn

Specialty section:
This article was submitted to Optics and Photonics, a section of the journal Frontiers in Physics

Received: *06 September 2021*
Accepted: *18 November 2021*
Published: *03 January 2022*

Citation:
Qiu S, Wang J, Yang X, Cao M, Zhang S, Gao H and Li F (2022) Observation of the Rotational Doppler Effect With Structured Beams in Atomic Vapor. Front. Phys. 9:771260. doi: 10.3389/fphy.2021.771260

1 INTRODUCTION

The quantum coherent interaction of light with an atomic system results in various fascinating phenomena. For instance, Hanle effect [1], coherent population trapping (CPT) [2], electromagnetically induced transparency (EIT) [3]and electromagnetically induced absorption (EIA) [4]. In particular, coherent effects arise strong interest based on Hanle-effect configuration for only needing a single light field such as Hanle-CPT, Hanle-EIT, and Hanle-EIA [5–7], which have been utilized in sensitive atomic magnetometer and light storage [8–10].

In recent years, an optical field known as vector beam (VB) has materially enriched the study of structured light interacting with atoms [11]. A VB with the spatial variation of polarization state can be decomposed into two orthogonal circularly polarized components with different orbital angular momentum (OAM) [12]. And then, it has been applied in a variety of realms over the last decades, such as high-resolution imaging [13–15], optical communication [16, 17], optical manipulation [18]

and quantum application [19–21]. Generally, there are two methods for generating the VB. The first one is the intra-cavity generation technique, which provides an efficient way to generate the VB directly from the laser source [22]. The second method is the extra-cavity technique, including using phase-dependent optical elements [23] or an interferometer associated with the spatial light modulator [24, 25]. Thus, benefiting from the mature technology for generating the VB allows us to explore vectorial light-matter interaction thoroughly. Recently, some researches show that employing the VB in atomic medium can realize manipulating spatial anisotropy [26–28], spatially dependent EIT [29, 30], quantum memory [31, 32], and non-linear optical propagation [33]. One of the most exciting works is using symmetric beams to observe the rotational Doppler effect (RDE) of atoms [34]. In their study, an interferometer combined with the spiral phase plates (SPP) is applied to generate experimental beams containing two phase vortex beams (OAM beams) with equal but opposite of topological charge ($\ell_1 = -\ell_2$). Nevertheless, the disadvantage of this superposition approach to generating the VB is that the alignment of two arms is an extremely difficult challenge, especially utilizing OAM beams with different $|\ell|$, since a tiny misalignment can lead to undesired Doppler broadening in atomic medium. For instance, a small angle β between the two beams results in broadening the order of $\beta\Delta_{\mathrm{Dopp}}$ ($\Delta_{\mathrm{Dopp}} \simeq$ 500 MHz) and also decrease the EIT peak transmission. Hence, in order to accurately study the RDE with atoms, an approach to generating VBs in a more stable and convenient way is imperative.

In this letter, instead of the interferometer configuration, a more convenient procedure to generate the symmetric and asymmetric VB is presented. The symmetric VB is that the OAM topological charges of two orthogonal circularly polarized components of VB are equivalent ($|\ell_1| = |\ell_2|$), and the asymmetric VB is unequal ($|\ell_1| \neq |\ell_2|$). By using a combination of spiral phase plate and vortex retarder plate (VRP), the geometric phase of initial linearly polarized beams are manipulated and converted into VB in the experiment. The advantage of our method is that generated VBs with varied OAM topological charges ($|\ell_1| = |\ell_2|$ or $|\ell_1| \neq |\ell_2|$) are directly produced without considering the misalignment or mismatching when interacting with atoms. Furthermore, asymmetric VBs, symmetric VBs and phase vortex beams (OAM beams) are utilized to detect the RDE in atoms, respectively. The experimental results show that RDE does not have an impact on the resonance linewidths of single linearly polarized OAM beams. However, the spectrum with rotational Doppler broadening is increasingly apparent as the difference ($|\ell_1 - \ell_2|$) of both asymmetric and symmetric VBs increases. One thing should be noted is that any decoherent effects (or noise effects) will dramatically decrease the peak transmission and large width of the EIT signal [35, 36], same as other coherent processions [37–39]. Thus, the broadened signal associated with the RDE will be drowned in the background noise and become too weak to be observed. However, we only change the topological charge combination of vector beams and set other parameters appropriately in the experiment, which make linewidth narrow enough to study the influence of RED.

2 EXPERIMENTAL SETUP

The experimental setup is shown in **Figure 1**. The output of a 795 nm external cavity diode laser is split into two parts. One part is sent to a saturated absorption spectroscopy setup to lock laser frequency. The other part passes through a single-mode fiber (SMF) to improve the mode quality of the laser beam. After the fiber, the beam is adjusted by a half-wave plate and a polarizing beam splitter (PBS) to control the intensity and also fix it with horizontal polarization state. A telescope is applied to expand the beam size and the achieved high-quality Gaussian beam's waist is 4 mm. The VB is generated by sending the linearly polarized beam through a setup composed of an SPP and a VRP. SPP is an optical element with a helical surface where the optical thickness of the component increases with azimuthal position according to $\ell\lambda\theta/2\pi(\mathrm{n}-1)$, where n is the refractive index of the medium [40]. Moreover, VRP is a liquid-crystal-based retardation wave plate with an inhomogeneous optical axis that displays an azimuthal topological charge [23]. The laser frequency is locked to the $5S_{1/2}, F = 2 \rightarrow 5P_{1/2}, F' = 1$ transition of the ^{87}Rb D_1-line. The Rb cell has a length of 50 mm. A three-layer μ-metal magnetic shield is used to isolate the atoms from the environmental magnetic fields. A solenoid coil inside the inner layer offers a uniform longitudinal magnetic field whose direction is parallel to the light propagation direction, **k**. The temperature of the cell is set at 40°C with a temperature controller. A neutral density filter is used to control the power of the incident laser beam. In the experiment, the beam intensity at the cell is approximately 17.98 μW/cm^2. After the beam transmits through the cell, the total intensity as a function of the applied longitudinal magnetic field is recorded by a photodiode.

Next, we briefly present the process of generating the light field we needed. It is known that a linear polarization Gaussian beam can be represented by a superposition of right- ($|\mathrm{R}\rangle$) and left-circular ($|\mathrm{L}\rangle$) polarized beams as

$$|\Phi\rangle_0 = \frac{1}{\sqrt{2}}\left(|\mathrm{L}\rangle + |\mathrm{R}\rangle\right) \tag{1}$$

A SPP can transform the linear polarization Gaussian beam $|\Phi\rangle_0$ into an OAM mode with linear polarization state and an azimuthal phase component $e^{i\ell\theta}$, where ℓ is the OAM topological charge and θ is the azimuthal angle, resulting in the beam carrying the orbital angular momentum ($\ell\hbar$). Then the beam can be expressed as:

$$|\Phi\rangle_1 = \frac{1}{\sqrt{2}}\left(|\ell, \mathrm{L}\rangle + |\ell, \mathrm{R}\rangle\right) \tag{2}$$

To convert a linear polarization OAM beam $|\Phi\rangle_1$ into an asymmetric VB, a VRP is used, which couples OAM with spin angular momentum. After passing through the VRP, the beam $|\Phi\rangle_1$ is transformed into an asymmetric vector beam $|\Phi\rangle_2$ that

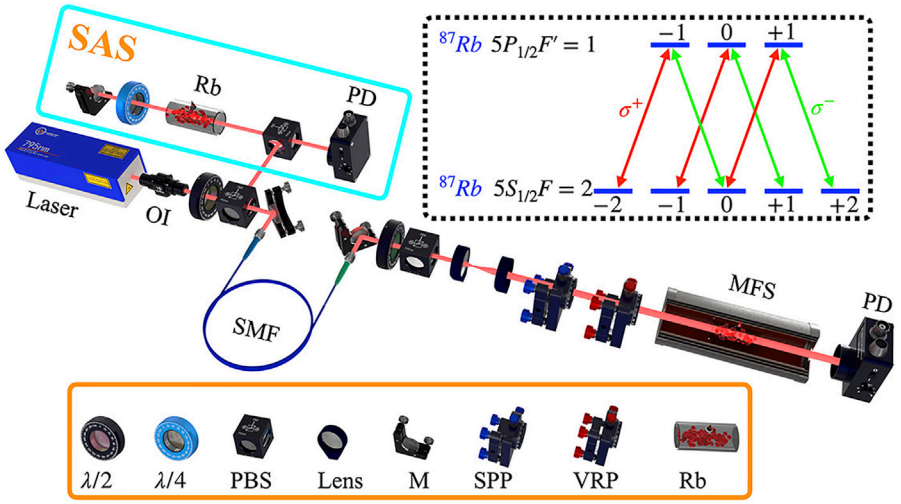

FIGURE 1 | Schematic of the experimental setup and atomic energy levels. HWP: half-wave plate; QWP: quarter-wave plate; PBS: polarization beam splitter; M: mirror; SPP: spiral phase plate; VRP: vortex retarder plate; OI: optics isolator; SMF: single-mode fiber; MFS: magnetic field shielding; PD: photo-detector; Rb: rubidium vapor; SAS: saturated absorption spectroscopy.

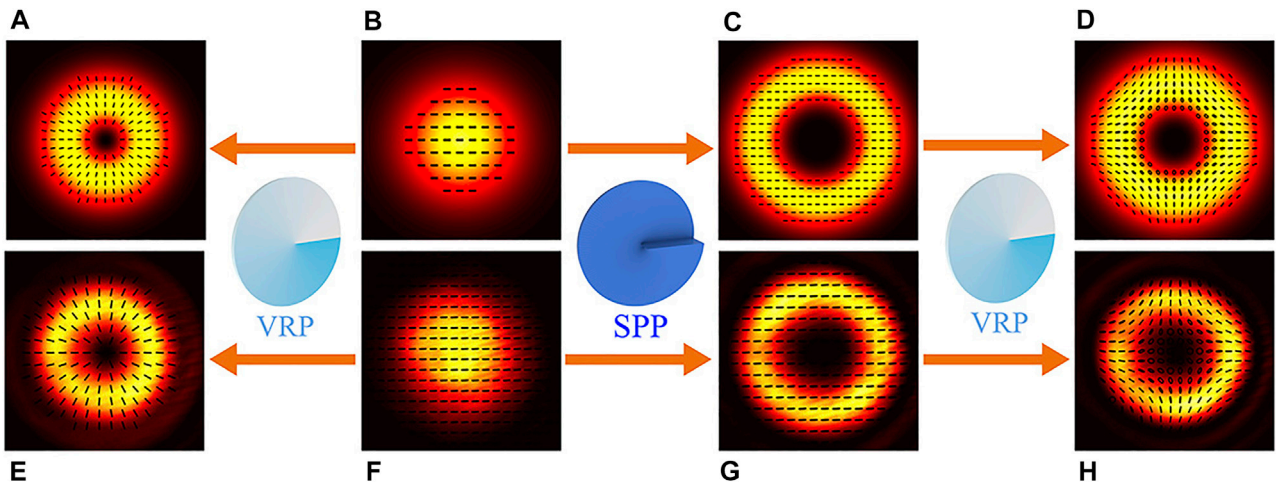

FIGURE 2 | Schematic of generating the experimental light beams. SPP: spiral phase plate; VRP: retardation wave plate. **(B, F)** the theoretical and experimental Gaussian beam, respectively. **(A, C, D)** the generation of OAM beams, symmetric and asymmetric VBs in theory. **(E, G, H)** the generation of OAM beams, symmetric and asymmetric vector beams in experiment. Linearly polarized Gaussian beam **(F)** directly passes through a VRP (or SPP) to generate a symmetric vector beam **(E)** [or a linearly polarized OAM beam **(G)**]. For the generation of an asymmetric vector beam **(H)**, the linearly polarized OAM beam **(G)** continues to run through a VRP.

has polarization variations along the azimuthal direction. Then the asymmetric VB can be written as

$$|\Phi\rangle_2 = \frac{1}{\sqrt{2}}\left(|\ell + \mathrm{m}, \mathrm{L}\rangle + |\ell - \mathrm{m}, \mathrm{R}\rangle\right) \tag{3}$$

where m is the azimuthal charge induced by the VRP. As shown in **Eq. 3**, the $|\Phi\rangle_2$ beam is turned into a superposition state with different OAM ($|\ell + \mathrm{m}, \mathrm{L}\rangle$, $|\ell - \mathrm{m}, \mathrm{R}\rangle$).

For the generation of a symmetric VB, an initial linearly polarized Gaussian beam directly runs through a VRP. Thereby, the symmetric VB $|\Phi\rangle_3$ also has polarization variations as the azimuth varies and can be expressed:

$$|\Phi\rangle_3 = \frac{1}{\sqrt{2}}\left(|\mathrm{m}, \mathrm{L}\rangle + |-\mathrm{m}, \mathrm{R}\rangle\right) \tag{4}$$

It's seen that the symmetric VB $|\Phi\rangle_3$ possesses two OAMs with equal absolute value but different sign ± m.

3 EXPERIMENTAL RESULTS AND DISCUSSION

As is known, in addition to the usual axial Doppler and radial shifts, moving atoms interacting with light beams carrying OAM also experience an azimuthal frequency shift under the resonant

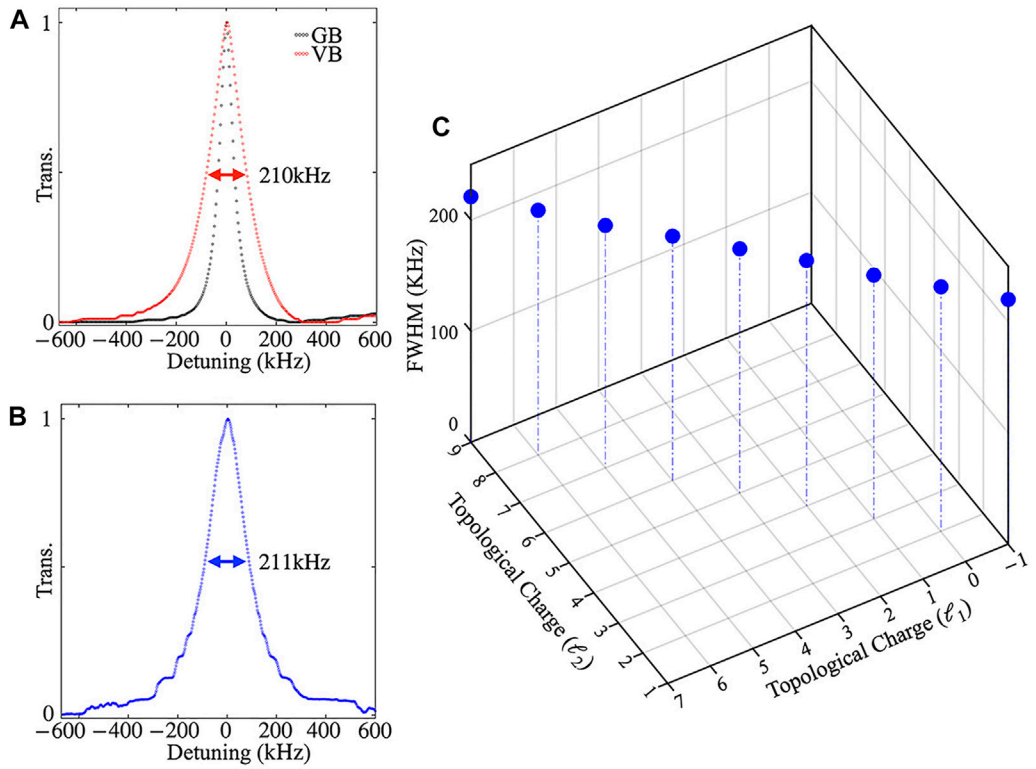

FIGURE 3 | FWHM depending on topological charge as a function of the total Zeeman shift $\delta = 2g\mu_B|\mathbf{B}|$. **(A)** The transmission spectrum of Gaussian beam (GB) and vector beam (VB) with $\ell_1 = -1$ and $\ell_2 = 1$; **(B)** The transmission spectrum of vector beam with $\ell_1 = 7$ and $\ell_2 = 9$; **(C)** FWHM of different asymmetric VB. One asymmetric VB brings two OAMs with unequal quantum number absolute value $|\ell_1| \neq |\ell_2|$. And the difference $(|\ell_2 - \ell_1|)$ of these asymmetric VBs are equal, namely $|\ell_2 - \ell_1| = 2$.

frequency. Thus, the total frequecy shift of an OAM beam is given by [41, 42].

$$\delta^{\ell}_{\mathrm{OAM}} = \kappa_z \mathrm{V}_z + \kappa_r \mathrm{V}_r + \kappa\phi \mathrm{V}_\phi \tag{5}$$

where $\kappa_z = -\mathrm{k} + \mathrm{kr}^2/2\,(z^2 + z_R^2)[2z^2/(z^2 + z_R^2) - 1] - (|\ell| + 1)\mathrm{z}_R/(z^2 + z_R^2)$, $\kappa_r = -\mathrm{kr}/\bar{z}$, $\kappa_\phi = -\ell/\mathrm{r}$, and (r, z, ϕ) represents the position in cylindrical coordinates. V_z, V_r, and V_ϕ are the axial, radial and azimuthal velocity components of the atom. $\mathrm{z}_\mathrm{R} = \pi\omega_0^2/\lambda$ is the Rayleigh range and ω_0 is the beam waist and $\bar{z} = (z_R^2 + z^2)/z$.

The axial Doppler shift, corresponding to the usual Doppler shift, is the first term of **Eq. 5**, associated with motion (V_z) along the beam vector **k** directed along z. The second term of **Eq. 5** is the radial Doppler shift induced by the wave front curvature and proportional to the radial velocity V_r. The only OAM related influence is the last term in **Eq. 5** corresponding to the azimutal Doppler shift, also known as rotational Doppler effect (RDE). The RDE is directly proportional to the OAM quantum number ℓ as $(-\frac{\ell}{\mathrm{r}})\mathrm{V}_\phi$. The only problem is that this term is too small to be directly detected. However, based on Hanle-EIT, the RDE can be easily observed through the spectroscopy of atoms associated with two light beams carrying OAM without being influenced by other unnecessary Doppler shifts [34].

The Hanle-EIT, a well-known phenomenon, is that light beams stimulate the atomic transitions between Zeeman sublevels of two hyper-fine states (ground state and exited state) to reach the condition of two-photon resonance. Thus, the coherence between atomic energy levels (**Figure 1**) allows the absorption of the light significantly reduced, leading to a transparent peak when scanning the longitudinal magnetic field **B** around zero and along the beam propagation direction **k** [1]. However, when two orthogonally circular polarized beams (σ^+ and σ^-) with different OAM (ℓ_1 and ℓ_2) simultaneously couple transitions satisfying the selection rule $\Delta\mathrm{m}_\mathrm{F} = \pm 1$, the frequency shift will occur due to the Doppler effect, leading to broadening of the transparent peak. In the condition of the moving atom, the two-photon resonance condition is:

$$\bar{\delta}_{\mathrm{OAM}} - \delta = 0 \tag{6}$$

where $\delta = \Delta m_F g_F \mu_B B$ (g_F is the gyromagnetic factor of the ground state, μ_B is the Bohr magneton) is the Zeeman shift caused by the magnetic field **B** and

$$\bar{\delta}_{\mathrm{OAM}} = \delta^{\ell_1}_{\mathrm{OAM}} - \delta^{\ell_2}_{\mathrm{OAM}} \tag{7}$$

Combined with **Eqs 5**, **7**, the axial and radial Doppler shift are eliminated, and the remaining shift only relates to the RDE as:

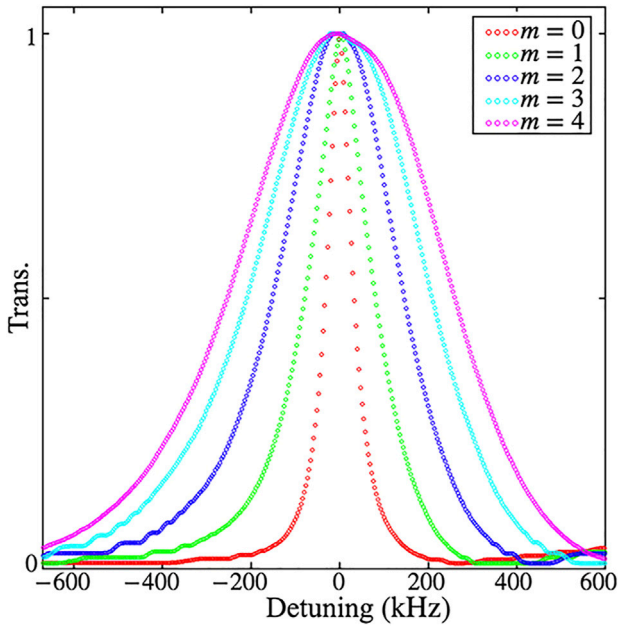

FIGURE 4 | The Hanle resonance signals of symmetric VBs as a function of the total Zeeman shift $\delta = 2g\mu_B|\mathbf{B}|$. **m** = 0 is the linearly polarized Gaussian beam.

$$\bar{\delta}_{\mathrm{OAM}} = \left(\frac{\ell_1 - \ell_2}{\mathrm{r}}\right)\mathrm{V}_\phi \tag{8}$$

When the magnetic field is modulated around zero value, the azimutal Doppler broadening will not happen in the Hanle-EIT spectroscopic with the situation of $\ell_1 = \ell_2$. Under the condition of $\ell_1 \neq \ell_2$, there is a fascinating phenomenon that the Hanle resonance spectroscopic presents the Doppler broadening induced by the RDE.

Now we turn our attention to the experimental phenomena of different light beams interacting with atoms. A horizontally polarized Gaussian beam passes through a SPP or a VRP or both two to produce a series of structured beams, as shown in **Figure 2**. The beam transmission is recorded by a photodiode as a function of applied longitude magnetic field modulated parallel to the direction of the beam.

Firstly, asymmetric VBs generated by the combination of SPPs and VRPs go through the vapor to interact with atoms. As shown in **Figures 2F–H**, a horizontally polarized beam (**Figure 2F**) first passes through the SPP to generate an OAM beam (**Figure 2G**). After that, the beam runs through a VRP and transforms into an asymmetric VB (**Figure 2H**). An asymmetric VB can be considered as a superposition of two orthogonal circularly polarized beams with different OAM absolute values $|\ell|$, i.e., $|\ell_1, R\rangle + |\ell_2, R\rangle$. After passing through the vapor, the transmission spectroscopy of the beam presents a Hanle resonance curve with the magnetic field scanning. As shown in **Figure 3A**, the resonance linewidth of the vector beam ($\mathrm{VB}_{-1\cap1}$) with m = 1 is wider than that of the Gaussian beam, since the linearly polarized Gaussian beam can be considered as two circular polarization beams without OAM. However, the basis of $\mathrm{VB}_{-1\cap1}$ carries different topological charge $\ell_1 = -1$ and $\ell_2 = 1$, respectively. Thereby, the resonance linewidth of the $\mathrm{VB}_{-1\cap1}$ is broaden by the RDE. **Figure 3B** shows the Hanle resonance curve contains the RDE of asymmetric VB ($\mathrm{ASVB}_{7\cap9}$) with two circularly polarized orthogonal basis possessing different topological charge $\ell_1 = 7$ and $\ell_2 = 9$, respectively. Compared **Figure 3B** with **Figure 3A**, the resonance linewidth of $\mathrm{ASVB}_{7\cap9}$ is about equal to the $\mathrm{VB}_{-1\cap1}$ due to the equivalent value of $|\ell_1 - \ell_2| = 2$. In the case, two circularly polarized orthogonal basis of different asymmetric VBs $|\ell_1, \mathrm{R}\rangle$ and $|\ell_2, \mathrm{L}\rangle$ has the

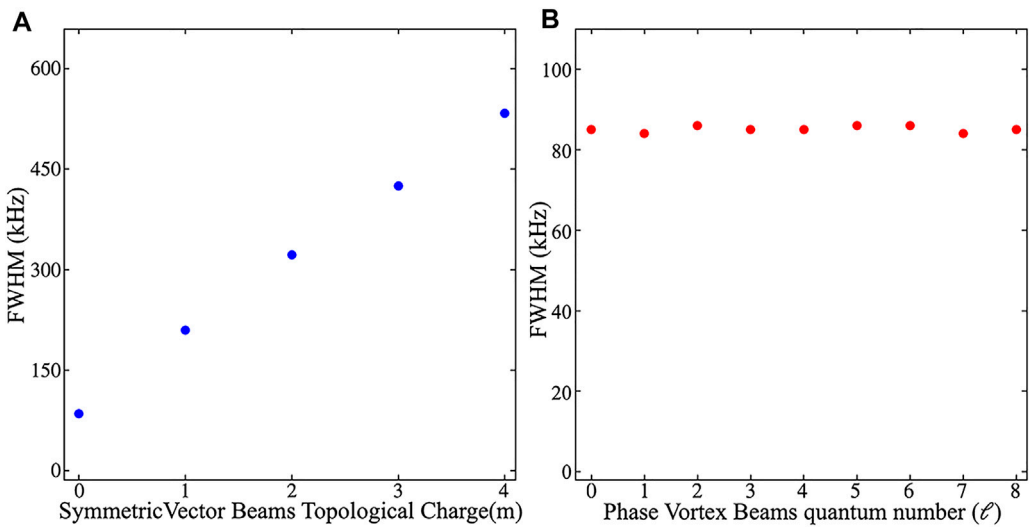

FIGURE 5 | Linewidths depend on the topological charge of the symmetric vector beam and the phase vortex beam. **(A)** FWHMs depend on the symmetric vector beam topological charge m; **(B)** FWHMs depend on the phase vortex beam topological charge ℓ.

same nonzero-difference $|\ell_1 - \ell_2|$, so the Hanle resonance linewidths have the similar broadening with each other induced by the RDE. The equivalent of linewidth FWHM (full width at half maximum) of the different asymmetric VBs with the equal difference $|\ell_1 - \ell_2| = 2$ is seen in **Figure 3C**.

Secondly, in order to observe the increase of Doppler broadening due to the RDE along with the topological charge m, symmetric VBs with different m generated by the VRP are used to interact with atoms (**Figure 2E**). As shown in **Figure 4**, an interesting phenomenon is that the Hanle resonance linewidths are gradually broadened with m increasing. It should be noted that in the case of m = 0, there is no RDE due to the beam without carrying the OAM. As a result, the resonance linewidth of m = 0 beam exhibits the normal Hanle resonance linewidth without the RDE related broadening. For normal Hanle resonance, the linewidth is determined by few factors, such as the beam intensity, the decay rate between ground states, the laser linewidth itself and other decoherence effects. In the case of m $\neq 0$, $\bar{\delta}_{\mathrm{OAM}} = [(\ell_1 - \ell_2)/\mathrm{r}]\mathrm{V}_\phi = (2\mathrm{m}/\mathrm{r})\mathrm{V}_\phi$, the transmission signal broadens with m increasing and is broader than that of the case of m = 0 induced by the RDE. Moreover, **Figure 5A** shows that the spectral FWHM increases with the VB topological charge m.

Furthermore, a series of OAM beams (**Figure 2G**) are produced by the SPP with different topological charges ℓ to measure the Hanle resonance signal. A linearly polarized OAM beam can be decomposed into a couple of orthogonal circularly polarized beams with the same ℓ as $|\ell, \mathrm{R}\rangle + |\ell, \mathrm{L}\rangle$. In this case, the resonance linewidth of any OAM beams coincides with each other and is the same as that of the Gaussian beam with no RDE as $\bar{\delta}_{\mathrm{OAM}} = [(\ell_1 - \ell_2)/\mathrm{r}]\mathrm{V}_\phi = [(\ell - \ell)/\mathrm{r}]\mathrm{V}_\phi = 0$. As shown in **Figure 5B**, the FWHM of ℓ from 0 to 8 are about equal.

4 CONCLUSION

In conclusion, we invest a simple and efficient procedure for the generation of the asymmetric and symmetric VB. A flexible and efficacious combination of SPP and VRP is used to manipulate the geometric phase of initial linearly polarized beams and convert initial beams into VBs. Furthermore, asymmetric VBs, symmetric VBs, and phase vortex beams interact with atoms under the longitudinal magnetic field to observe the rotational Doppler effect, respectively. We find that the rotational Doppler broadening is increasingly obvious as the difference ($|\ell_1 - \ell_2|$) of VB increase. The Hanle resonance of phase vortex beams are no rotational Doppler broadening. These results may have applications in estimating the rotational velocity of the atom-level or molecule-level objects, measuring the intensity of magnetic fields and studying the quantum coherence in atomic ensembles. Furthermore, recent research also showed that the Doppler effect induced nonreciprocity in coherent media [43, 44], which opens up new possibilities for our system.

DATA AVAILABILITY STATEMENT

The original contributions presented in the study are included in the article/Supplementary Material, further inquiries can be directed to the corresponding authors.

AUTHOR CONTRIBUTIONS

SQ, MC and HG contributed to conception and design of the study. JW organized the database. XY performed the statistical analysis. SQ wrote the first draft of the manuscript. JW, XY, SZ and FL wrote sections of the manuscript. All authors contributed to manuscript revision, read, and approved the submitted version.

FUNDING

This work was supported by the National Natural Science Foundation of China (92050103, 11774286, 11534008, 11604257, and 11574247) and the Fundamental Research Funds for the Central Universities of China.

REFERENCES

1. Renzoni F, Maichen W, Windholz L, Arimondo E. Coherent Population Trapping with Losses Observed on the Hanle Effect of theD1sodium Line. *Phys Rev A* (1997) 55:3710–8. doi:10.1103/PhysRevA.55.3710
2. Stähler M, Wynands R, Knappe S, Kitching J, Hollberg L, Taichenachev A, et al. Coherent Population Trapping Resonances in thermal 85Rb Vapor: D_1 versus D_2 Line Excitation. *Opt Lett* (2002) 27:1472–4. doi:10.1364/OL.27.001472
3. Fleischhauer M, Imamoglu A, Marangos JP. Electromagnetically Induced Transparency: Optics in Coherent media. *Rev Mod Phys* (2005) 77:633–73. doi:10.1103/RevModPhys.77.633
4. Lezama A, Barreiro S, Akulshin AM. Electromagnetically Induced Absorption. *Phys Rev A* (1999) 59:4732–5. doi:10.1103/PhysRevA.59.4732
5. Valente P, Failache H, Lezama A. Comparative Study of the Transient Evolution of Hanle Electromagnetically Induced Transparency and Absorption Resonances. *Phys Rev A* (2002) 65(8):023814. doi:10.1103/PhysRevA.65.023814
6. Alzetta G, Gozzini S, Lucchesini A, Cartaleva S, Karaulanov T, Marinelli C, et al. Complete Electromagnetically Induced Transparency in Sodium Atoms Excited by a Multimode Dye Laser. *Phys Rev A* (2004) 69(9):063815. doi:10.1103/PhysRevA.69.063815
7. Anupriya J, Ram N, Pattabiraman M. Hanle Electromagnetically Induced Transparency and Absorption Resonances with a Laguerre Gaussian Beam. *Phys Rev A* (2010) 81(6):043804. doi:10.1103/PhysRevA.81.043804
8. Kastler A. The Hanle Effect and its Use for the Measurements of Very Small Magnetic fields. *Nucl Instr Methods* (1973) 110:259–65. doi:10.1016/0029-554X(73)90698-8
9. Phillips DF, Fleischhauer A, Mair A, Walsworth RL, Lukin MD. Storage of Light in Atomic Vapor. *Phys Rev Lett* (2001) 86:783–6. doi:10.1103/PhysRevLett.86.783
10. Gao H, Rosenberry M, Batelaan H. Light Storage with Light of Arbitrary Polarization. *Phys Rev A* (2003) 67(4):053807. doi:10.1103/PhysRevA.67.053807
11. Wang J, Castellucci F, Franke-Arnold S. Vectorial Light-Matter Interaction: Exploring Spatially Structured Complex Light fields. *AVS Quan Sci.* (2020) 2(12):031702. doi:10.1116/5.0016007

12. Milione G, Sztul HI, Nolan DA, Alfano RR. Higher-Order Poincaré Sphere, Stokes Parameters, and the Angular Momentum of Light. *Phys Rev Lett* (1999) 107(4):053601. doi:10.1103/PhysRevLett.107.053601
13. Dorn R, Quabis S, Leuchs G. Sharper Focus for a Radially Polarized Light Beam. *Phys Rev Lett* (1999) 91(4):233901. doi:10.1103/PhysRevLett.91.233901
14. Moh KJ, Yuan X-C, Bu J, Zhu SW, Gao BZ. Surface Plasmon Resonance Imaging of Cell-Substrate Contacts with Radially Polarized Beams. *Opt Express* (2008) 16:20734–41. doi:10.1364/OE.16.020734
15. Xie X, Chen Y, Yang K, Zhou J. Harnessing the point-spread Function for High-Resolution Far-Field Optical Microscopy. *Phys Rev Lett* (2014) 113(5): 263901. doi:10.1103/PhysRevLett.113.263901
16. Milione G, Nguyen TA, Leach J, Nolan DA, Alfano RR. Using the Nonseparability of Vector Beams to Encode Information for Optical Communication. *Opt Lett* (2015) 40:4887–90. doi:10.1364/OL.40.004887
17. Zhao Y, Wang J. High-base Vector Beam Encoding/decoding for Visible-Light Communications. *Opt Lett* (2015) 40:4843–6. doi:10.1364/OL.40.004843
18. Otte E, Denz C. Optical Trapping Gets Structure: Structured Light for Advanced Optical Manipulation. *Appl Phys Rev* (2020) 7(22):041308. doi:10.1063/5.0013276
19. Erhard M, Fickler R, Krenn M, Zeilinger A. Twisted Photons: New Quantum Perspectives in High Dimensions. *Light Sci Appl* (2018) 7(11):17146. doi:10.1038/lsa.2017.146
20. Cozzolino D, Da Lio B, Bacco D, Oxenløwe LK. High-Dimensional Quantum Communication: Benefits, Progress, and Future Challenges. *Adv Quan Tech* (2019) 2:1900038. doi:10.1002/qute.201900038
21. Ndagano B, Nape I, Cox MA, Rosales-Guzman C, Forbes A. Creation and Detection of Vector Vortex Modes for Classical and Quantum Communication. *J Lightwave Technol* (2018) 36:292–301. doi:10.1109/JLT.2017.2766760
22. Forbes A. Structured Light from Lasers. *Laser Photon Rev* (2019) 13:1900140. doi:10.1002/lpor.201900140
23. Marrucci L, Manzo C, Paparo D. Optical Spin-To-Orbital Angular Momentum Conversion in Inhomogeneous Anisotropic media. *Phys Rev Lett* (2006) 96:163905. doi:10.1103/PhysRevLett.96.163905
24. Forbes A, Dudley A, McLaren M. Creation and Detection of Optical Modes with Spatial Light Modulators. *Adv Opt Photon* (2016) 8:200–27. doi:10.1364/AOP.8.000200
25. Scholes S, Kara R, Pinnell J, Rodríguez-Fajardo V, Forbes A. Structured Light with Digital Micromirror Devices: a Guide to Best Practice. *Opt Eng* (2019) 59: 1. doi:10.1117/1.OE.59.4.041202
26. Fatemi FK. Cylindrical Vector Beams for Rapid Polarization-dependent Measurements in Atomic Systems. *Opt Express* (2011) 19:25143–50. doi:10.1364/OE.19.025143
27. Wang J, Yang X, Li Y, Chen Y, Cao M, Wei D, et al. Optically Spatial Information Selection with Hybridly Polarized Beam in Atomic Vapor. *Photon Res* (2018) 6:451–6. doi:10.1364/PRJ.6.000451
28. Wang J, Yang X, Dou Z, Qiu S, Liu J, Chen Y, et al. Directly Extracting the Authentic Basis of Cylindrical Vector Beams by a Pump-Probe Technique in an Atomic Vapor. *Appl Phys Lett* (2019) 115:221101. doi:10.1063/1.5125988
29. Radwell N, Clark TW, Piccirillo B, Barnett SM, Franke-Arnold S. Spatially Dependent Electromagnetically Induced Transparency. *Phys Rev Lett* (2015) 114:123603. doi:10.1103/PhysRevLett.114.123603
30. Yang X, Chen Y, Wang J, Dou Z, Cao M, Wei D, et al. Observing Quantum Coherence Induced Transparency of Hybrid Vector Beams in Atomic Vapor. *Opt Lett* (2019) 44:2911–4. doi:10.1364/OL.44.002911
31. Parigi V, D'Ambrosio V, Arnold C, Marrucci L, Sciarrino F, Laurat J. Storage and Retrieval of Vector Beams of Light in a Multiple-Degree-Of-freedom Quantum Memory. *Nat Commun* (2015) 6:7706. doi:10.1038/ncomms8706
32. Ye Y-H, Dong M-X, Yu Y-C, Ding D-S, Shi B-S. Experimental Realization of Optical Storage of Vector Beams of Light in Warm Atomic Vapor. *Opt Lett* (2019) 44:1528–31. doi:10.1364/OL.44.001528
33. Bouchard F, Larocque H, Yao AM, Travis C, De Leon I, Rubano A, et al. Polarization Shaping for Control of Nonlinear Propagation. *Phys Rev Lett* (2016) 117:233903. doi:10.1103/PhysRevLett.117.233903
34. Barreiro S, Tabosa JWR, Failache H, Lezama A. Spectroscopic Observation of the Rotational Doppler Effect. *Phys Rev Lett* (2006) 97:113601. doi:10.1103/PhysRevLett.97.113601
35. Figueroa E, Vewinger F, Appel J, Lvovsky AI. Decoherence of Electromagnetically Induced Transparency in Atomic Vapor. *Opt Lett* (2006) 31:2625–7. doi:10.1364/OL.31.002625
36. Shuker M, Firstenberg O, Pugatch R, Ben-Kish A, Ron A, Davidson N. Angular Dependence of Dicke-Narrowed Electromagnetically Induced Transparency Resonances. *Phys Rev A* (2007) 76:023813. doi:10.1103/PhysRevA.76.023813
37. Ishizaki A, Fleming GR. On the Adequacy of the redfield Equation and Related Approaches to the Study of Quantum Dynamics in Electronic Energy Transfer. *J Chem Phys* (2009) 130:234110. doi:10.1063/1.3155214
38. Ishizaki A, Fleming GR. Unified Treatment of Quantum Coherent and Incoherent Hopping Dynamics in Electronic Energy Transfer: Reduced Hierarchy Equation Approach. *J Chem Phys* (2009) 130:234111. doi:10.1063/1.3155372
39. Wang B-X, Tao M-J, Ai Q, Xin T, Lambert N, Ruan D, et al. Efficient Quantum Simulation of Photosynthetic Light Harvesting. *Npj Quan Inf* (2018) 4:52. doi:10.1038/s41534-018-0102-2
40. Yao AM, Padgett MJ. Orbital Angular Momentum: Origins, Behavior and Applications. *Adv Opt Photon* (2011) 3:161–204. doi:10.1364/AOP.3.000161
41. Allen L, Babiker M, Power WL. Azimuthal Doppler Shift in Light Beams with Orbital Angular Momentum. *Opt Commun* (1994) 112:141–4. doi:10.1016/0030-4018(94)00484-6
42. Power WL, Allen L, Babiker M, Lembessis VE. Atomic Motion in Light Beams Possessing Orbital Angular Momentum. *Phys Rev A* (1995) 52:479–88. doi:10.1103/PhysRevA.52.479
43. Zhang S, Hu Y, Lin G, Niu Y, Xia K, Gong J, et al. Thermal-motion-induced Non-reciprocal Quantum Optical System. *Nat Photon* (2018) 12:744–8. doi:10.1038/s41566-018-0269-2
44. Huang HB, Lin JJ, Yao YX, Xia KY, Yin ZQ, Ai Q. Optical Nonreciprocity in Rotating diamond with Nitrogen-Vacancy center. arXiv preprint arXiv:2109.03588 (2021). Available at: https://arxiv.org/abs/2109.03588#:~:text=Optical%20nonreciprocity%20in%20rotating%20diamond%20with%20nitrogen%2Dvacancy%20center,-Hong%2DBo%20Huang&text=When%20the%20control%20and%20probe,two%20fields%20are%20the%20same.

Conflict of Interest: The authors declare that the research was conducted in the absence of any commercial or financial relationships that could be construed as a potential conflict of interest.

Publisher's Note: All claims expressed in this article are solely those of the authors and do not necessarily represent those of their affiliated organizations, or those of the publisher, the editors and the reviewers. Any product that may be evaluated in this article, or claim that may be made by its manufacturer, is not guaranteed or endorsed by the publisher.

frontiers in Physics

ORIGINAL RESEARCH
published: 25 February 2022
doi: 10.3389/fphy.2022.846718

Broadband Achromatic and Polarization Insensitive Focused Optical Vortex Generator Based on Metasurface Consisting of Anisotropic Nanostructures

Naitao Song[1,2], Nianxi Xu[1], Jinsong Gao[2,3], Xiaonan Jiang[1], Dongzhi Shan[1,2], Yang Tang[1], Qiao Sun[1], Hai Liu[1] and Xin Chen[1]*

[1]Key laboratory of Optical System Advanced Manufacturing Technology, Changchun Institute of Optics, Fine Mechanics and Physics, Chinese Academy of Sciences, Changchun, China, [2]College of Da Heng, University of the Chinese Academy of Sciences, Beijing, China, [3]Jilin Provincial Key Laboratory of Advanced Optoelectronic Equipment, Instrument Manufacturing Technology, Changchun, China

OPEN ACCESS

Edited by:
Pei Zhang,
Xi'an Jiaotong University, China

Reviewed by:
Arka Majumdar,
University of Washington, United States
Kai Guo,
Hefei University of Technology, China
Zi-Lan Deng,
Jinan University, China
Hua Cheng,
Nankai University, China
Li Deng,
Beijing University of Posts and Telecommunications (BUPT), China

***Correspondence:**
Jinsong Gao
gaojs999@163.com

Specialty section:
This article was submitted to Optics and Photonics, a section of the journal Frontiers in Physics

Received: *31 December 2021*
Accepted: *31 January 2022*
Published: *25 February 2022*

Citation:
Song N, Xu N, Gao J, Jiang X, Shan D, Tang Y, Sun Q, Liu H and Chen X (2022) Broadband Achromatic and Polarization Insensitive Focused Optical Vortex Generator Based on Metasurface Consisting of Anisotropic Nanostructures. Front. Phys. 10:846718. doi: 10.3389/fphy.2022.846718

Optical vortex (OV) beams are ideal carriers for high-capacity optical communication, and long-wave infrared (LWIR) is the ideal wavelength band for long-range optical communication. Here, we propose a method for the achromatic generation of focused optical vortex (FOV) beams with arbitrary homogenous polarization states in the LWIR using a single all-germanium metasurface. The chromatic aberration and polarization sensitivity are eliminated by superimposing a polarization-insensitive geometric phase and a dispersion-engineered dynamic phase. The method is validated using two broadband FOV generators with the same diameter and focal length but different topological charges. The results indicate that the FOV generators are broadband achromatic and polarization insensitive. The proposed method may pave the way for chip-scale optical communication devices.

Keywords: broadband achromatism, optical vortex, germanium metasurface, polarization insensitive, orbital angular momentum, modal purity, anisotropic nanostructure, longwave infrared

INTRODUCTION

Optical vortex (OV) beams characterized by the Hilbert factor $\exp(i\ell\theta)$ (ℓ is the topological charge) can carry the orbital angular momentum (OAM) $\ell\hbar$ per photon in addition to the spin angular momentum (SAM) associated with photon spin. Unlike SAM, which is limited to $\pm 1\hbar$ per photon, the OAM per photon is theoretically unbounded. Such properties make OV beams an ideal carrier for high-capacity wireless communications [1, 2]. In addition to optical communication, OV beams have important applications in manipulating nanoparticles [3], high-security encryption [4], assembly of DNA biomolecules [5], quantum optics [6], and diffraction limit imaging [7]. In conventional optical systems, spiral phase plates [8, 9], q-waveplates [10], pitch-fork holograms [11] and spatial light modulators [12] are used to generate helical wavefronts of OV beams. For most applications, the generated vortex beam also needs to be focused by a lens to increase the light intensity. However, the bulky and high cost of such optical systems severely hinders the development of integrated focused optical vortex (FOV) generators.

Metasurfaces are two-dimensional metamaterials that possess powerful light modulation capabilities and can manipulate the phase, amplitude, and polarization of light locally, making them highly promising as a powerful platform for integrated optics. To date, a wide range of metasurfaces with sophisticated features have been demonstrated, such as beam deflector [13], metalens [14–20], cloak [21–23], polarizer [24], information encryption [25–29], analog computation [30–32], metasurface interferometry [33], and meta-holograms [34], covering a wide spectrum from visible to terahertz frequencies. Yu [35] et al. were the first to demonstrate the generation of OV beams via a metasurface consisting of a V-shaped plasmonic antenna. Owing to the intrinsic absorption loss of metals in the visible region, the efficiency of such metasurfaces is highly limited. To overcome this, all-dielectric metasurfaces composed of high-refractive-index materials have been proposed to achieve high efficiency in generating OV beams [36, 37]. Zhan [38] et al. proposed an OV generator based on a silicon nitride metasurface with an efficiency much higher than its plasmonic counterparts. By superimposing hyperbolic and helical phase profiles, Tang [39] further reduced the bulk of the optical system by generating FOV beams using only a single metasurface. Sroor et al. [40] integrated the metasurface into the laser cavity, which increased the mode purity of the generated OV beam to 92%. Although a wide variety of FOV generator metasurfaces have been developed, most of them are monochromatic. Considering the needs of practical applications, it is clear that broadband achromatic FOV generators are more desirable owing to their powerful functionalities. Recently, Ou et al. [41, 42] proposed a broadband achromatic FOV generator based on silicon metasurface in the mid-infrared region. However, such silicon metasurfaces are highly sensitive to the state of polarization (SOP) of incident light. The longwave infrared (LWIR) corresponds to an atmospheric transparent window, which makes it an ideal spectrum for optical wireless communications. However, to the best of our knowledge, no achromatic flat FOV generator for LWIR has been reported thus far.

In this study, we demonstrate a general method to achromatically generate FOV beams via a single germanium metasurface with high efficiency and high mode purity in the LWIR band. It should be noted that our metasurface is polarization-insensitive and can transform plane waves with arbitrary SOP to FOV with an arbitrary OAM state. The proposed metasurface is composed of anisotropic nanostructures, and each nanostructure behaves as a quasi-ideal half-wave plate that flips the chirality of the incident circularly polarized (CP) light. A polarization-insensitive geometric phase is imparted on the metasurface by limiting the rotation angle of each nanostructure to 0° or 90° [43]. The anisotropic geometry also allows us to finely regulate the dispersion of the dynamic phase [44, 45]. By combining the polarization-insensitive geometric phase and dispersion-engineered dynamic phase, the desired group delay and phase profile are simultaneously imparted on the metasurface, resulting in good polarization insensitivity and achromatic performance.

To validate our method, we designed and simulated two broadband achromatic flat-FOV generators. The two FOV generators have the same diameter of 200 μm, the same focal length of 300 μm, and different topological charge numbers ($\ell = 0$ for metasurface I and $\ell = -2$ for metasurface II). The metasurface with $\ell = 0$ behaves as a metalens. The metalens has a stable focus from 9.6 to 11.6 μm, and the relative focal shift is less than 4%, which indicates good achromatic performance. The average focusing efficiency under right-handed circularly polarized (RCP) incidence, left-hand circularly polarized (LCP) incidence, and linear polarized incidence along the *x*-axis (XLP) were 44%, 43%, and 45%, respectively, which confirms polarization-insensitive performance. Further analysis of the Strehl ratio indicates that the metalens show broadband diffraction-limited focusing ability. The metasurface with $\ell = -2$ shows a donut-shaped intensity profile and spiral-shaped phase profile from 9.6 to 11.6 μm, indicating the existence of OV at the origin in the broadband. The average efficiency of the FOV generator was 34% under RCP, LCP, and XLP incidence, which confirms polarization-insensitive functionality. The average modal purity of the desired OAM eigenstate mode under RCP, LCP, and XLP incidence were 95.5%, 95.3%, and 92.9%, respectively. The high modal purity shows that the FOV beams are of good quality, which indicates that the FOV generator is both achromatic and polarization insensitive. We believe that our results represent a substantial advance and would pave the way for applications such as chip-scale optical communication.

MATERIALS AND METHODS

For most applications, intrinsic divergence of the OV beam is not preferred, and lenses are used to control the beam radius and increase the light intensity. The functionality of generating and focusing OV beams can be integrated on a single metasurface by superimposing radially hyperbolic and azimuthally linear phase profiles as follows:

$$\varphi = -\frac{\omega}{c}\left(\sqrt{r^2 + f^2} - f\right) + \ell\theta \tag{1}$$

Where ω is the angular frequency, c is the speed of light in vacuum, r is the radial coordinate, θ is the azimuthal coordinate, f is the constant focal length, and ℓ is the topological charge. Formula [1] can be Taylor expanded around the design frequency as follows:

$$\varphi(r,\theta,\omega) = \varphi(r,\theta,\omega_d) + \left.\frac{\partial\varphi}{\partial\omega}\right|_{\omega=\omega_d}(\omega-\omega_d) + \left.\frac{\partial^2\varphi}{\partial\omega^2}\right|_{\omega=\omega_d}(\omega-\omega_d)^2 + \ldots \tag{2}$$

where $\varphi(r,\theta,\omega_d)$, $\frac{\partial\varphi}{\partial\omega}|_{\omega=\omega_d}$, and $\frac{\partial^2\varphi}{\partial\omega^2}|_{\omega=\omega_d}$ are the phase, group delay, and group delay dispersion that should be satisfied at the corresponding polar coordinates (r,θ) at the design frequency ω_d, respectively. It is very difficult to satisfy all derivatives in Formula [2] for the selected nanostructures at every coordinate on the metasurface. To achieve achromatic dispersion, a simple

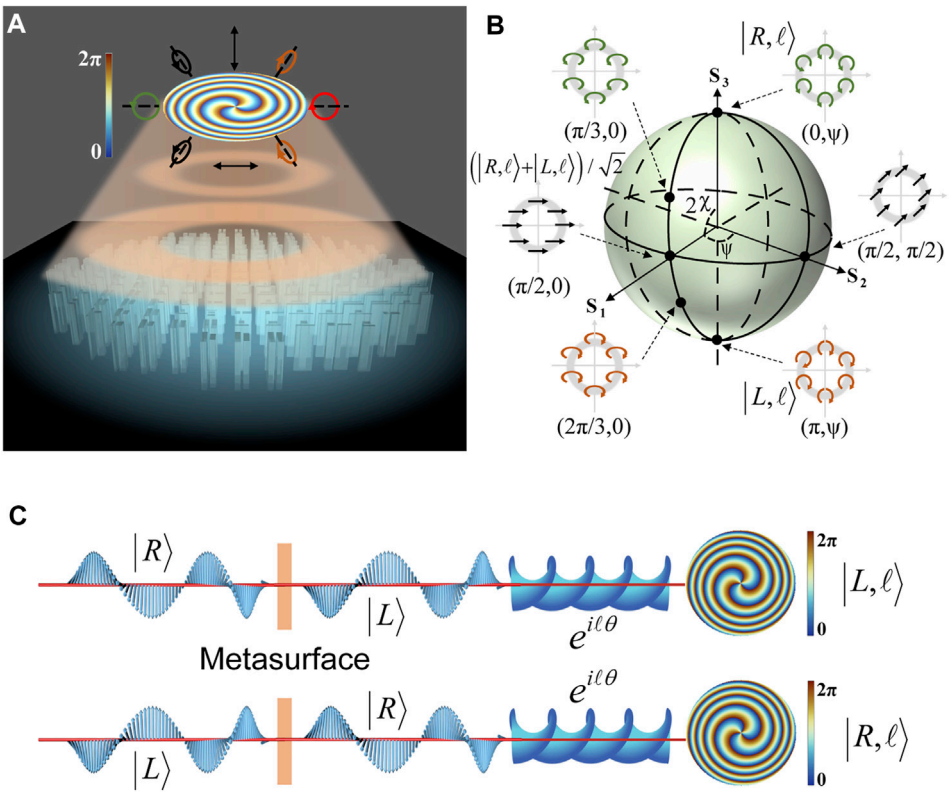

FIGURE 1 | Schematic of the flat FOV generator. **(A)** Schematic of the metasurface consisting of anisotropic nanostructures for generating FOV beams with arbitrary SOP. **(B)** Schematic illustration of $HOP_{\ell,\ell}$. OV beams with any scalar SOP can be obtained by superimposing the SOP corresponding to the north and south poles on the HOP sphere. **(C)** Spin-orbit angular momentum conversion when light passes through the proposed metasurface.

and intuitive approach is to let group delay dispersion and other higher-order derivative terms be zero; thus, the phase is linearly related to the frequency at each coordinate. In this case, the condition for achieving achromatism is simplified as follows:

$$\left.\frac{\partial\varphi}{\partial\omega}\right|_{\omega=\omega_d} = -\frac{1}{c}\left(\sqrt{r^2+f^2}-f\right) \tag{3}$$

$$\varphi(r,\theta,\omega_d) = -\frac{\omega_d}{c}\left(\sqrt{r^2+f^2}-f\right)+\ell\theta \tag{4}$$

Formula [3] and Formula [4] show the group delay condition and phase condition, respectively, that need to be fulfilled by the achromatic FOV generator.

To precisely modulate the dispersion of meta-atoms, anisotropic nanopillar combinations were chosen as the archetypes of the meta-atom, as shown in the inset of **Figure 2A**. Moreover, each nanostructure on the metasurface is designed to be a miniature half-wave plate, which can flip the chirality of the incident CP wave. When RCP light is incident from the substrate, the metasurface converts it into an LCP converged vortex beam with a topological charge of ℓ and vice versa, as shown in **Figure 1C**. This process is called spin-orbit angular conversion [46] and can be represented by Jones calculus as follows:

$$\exp(i\varphi_{lens})|L,\ell\rangle = [J_{meta}]|R\rangle \tag{5}$$

$$\exp(i\varphi_{lens})|R,\ell\rangle = [J_{meta}]|L\rangle \tag{6}$$

where $[J_{meta}]$ is the Jones matrix of the metasurface, $\varphi_{lens} = -\frac{\omega}{c}(\sqrt{r^2+f^2}-f)$ is the phase profile of a planar lens, $|R\rangle$ and $|L\rangle$ are the RCP and LCP bases, respectively. $|L,\ell\rangle$ and $|R,\ell\rangle$ are the orthonormal high-order circular polarization basis [47], which can be expressed as

$$|L,\ell\rangle = \exp(i\ell\theta)(\hat{x}-i\hat{y})/\sqrt{2} \tag{7}$$

$$|R,\ell\rangle = \exp(i\ell\theta)(\hat{x}+i\hat{y})/\sqrt{2} \tag{8}$$

For incident light with a more general SOP $E^{in} = \psi_L|L\rangle + \psi_R|R\rangle$, the corresponding outgoing light after passing through the metasurface can be expressed as

$$E^{out} = \exp(i\varphi_{lens})[\psi_R|L,\ell\rangle + \psi_L|R,\ell\rangle] \tag{9}$$

The SOP corresponding to any point on the high-order Poincaré sphere (HOP) can be decomposed into a linear combination of the SOP corresponding to the north and south poles, as shown in **Figure 1B**. For all possible scalar SOPs of the vortex beam, we can find the corresponding points on the corresponding $HOP_{\ell,\ell}$; thus, Formula [9] shows that our method can generate an FOV with an arbitrary homogeneous SOP.

In addition, the Jones matrix of the metasurface can be expressed as

$$[J_{meta}] = \exp(i\varphi_{lens}) \exp(i\ell\theta) \begin{bmatrix} 1 & 0 \\ 0 & -1 \end{bmatrix} \tag{10}$$

Formula [10] implies that a metasurface with only one wavelength thickness integrates the functions of a half-wave plate, spiral phase plate, and lens. Considering that the metasurface also has the ability to eliminate chromatic aberration, we can see that the entire optical system is highly integrated.

Although it is counterintuitive to utilize anisotropic nanostructures to form polarization-insensitive metasurfaces, this can be understood in terms of the geometric phase. For the anisotropic meta-atom shown in **Figure 2A**, its transmittance properties after a rotation angle α can be described by the Jones matrix as follows:

$$E^{out} = R(\alpha)^T \cdot \begin{bmatrix} t_l & 0 \\ 0 & t_s \end{bmatrix} \cdot R(\alpha) \cdot E^{in}$$

$$= \frac{1}{2}(t_l + t_s) \cdot E^{in} + \frac{1}{2}(t_l - t_s) \cdot \left(\exp(i2\alpha) \cdot \hat{\sigma}_R + \exp(-i2\alpha) \cdot \hat{\sigma}_L\right) \cdot E^{in} \tag{11}$$

where $R(\alpha) = \begin{bmatrix} \cos\alpha & \sin\alpha \\ -\sin\alpha & \cos\alpha \end{bmatrix}$ is the rotation matrix, and t_l and t_s are the complex transmission coefficients for light polarized along the long and short axes of the meta-atom, respectively. $\hat{\sigma}_R = \frac{1}{2}\begin{bmatrix} 1 & -i \\ -i & -1 \end{bmatrix}$ and $\hat{\sigma}_L = \frac{1}{2}\begin{bmatrix} 1 & i \\ i & -1 \end{bmatrix}$ are chirality flip operators, and when the incident light is RCP or LCP, there exists $\hat{\sigma}_R \cdot |R\rangle = 0$ (or $\hat{\sigma}_L \cdot |L\rangle = 0$) and $\hat{\sigma}_R \cdot |L\rangle = |R\rangle$ (or $\hat{\sigma}_L \cdot |R\rangle = |L\rangle$). It can be observed from Formula [11] that under CP illumination, the first part represents the co-polarized component which causes unwanted scattering and can be minimized when the meta-atom is designed to be a half-wave plate, and the second part represents the cross-polarized component whose phase can be decomposed into two parts: the dynamic phase $\varphi_d = \arg(t_l - t_s)$ and the geometric phase 2α (for LCP incident light) and -2α (for RCP incident light). Generally, the geometric phase is dispersionless and polarization-sensitive, since it is only dependent on the rotation angle, and it is different for RCP and LCP light incidence. However, if the rotation angle is limited to 0° or 90°, the geometric phases of the RCP and LCP incident light will be identical, as illustrated in **Figure 2C**. Therefore, both the RCP and LCP incident light will experience the same phase profile imparted by the metasurface. Because any incident light can be decomposed into a combination of RCP and LCP, this property implies that the metasurface is polarization-insensitive.

The properties of meta-atoms are also fundamentally determined by the constituent materials. Due to mature fabrication methods, silicon is widely used as the base material for metasurfaces. However, in the LWIR band, germanium has smaller absorption and higher refractive index than silicon, so the nanostructures composed of germanium materials can modulate light more efficiently. Therefore, germanium was selected as the constituent material for the meta-atom. Currently, it is still very challenging to deposit tens of microns of germanium on other materials due to material stress, so we also chose germanium as a substrate material so that in the future, we can inexpensively process metasurfaces on a single germanium wafer. We built up a meta-atoms library, and there were multiple mutually parallel nanopillars in a single meta-atom. **Figure 2A** shows the case of two nanopillars in one meta-atom, and a detailed discussion on the meta-atoms library is included in Supplementary Material. The nanopillars in every unit cell have the same height H = 10 μm and the same gap g = 0.5 μm, and the finest structure size is forced to be larger than 1 μm. The lattice constant P of the unit cell was chosen to be 6.2 μm to satisfy both the Nyquist law and the requirement to suppress higher-order diffraction [48].

To obtain the phase spectrum of each nanostructure, we conducted simulations using a finite-difference time-domain (FDTD) solver from Lumerical [49]. Periodic conditions were applied in the transverse direction, and the perfect matched layer (PML) condition was applied in the longitudinal direction with respect to the propagation of light, and CP illumination was applied from the substrate. After obtaining the phase spectra of all meta-atoms, we screened the meta-atoms suitable for constituting the achromatic FOV metasurface according to Formula [2]. We used a homemade linear regression program to screen the meta-atoms in the library, with an R-squared number greater than 0.98 and an avaverage conversion efficiency greater than 80%. The phase spectra and conversion efficiency spectra of the five meta-atoms meeting the above screening conditions are shown in **Figure 2B,C**. As shown in **Figure 2E**, nanostructure rotation does not affect the dispersion (group delay) of meta-atoms, but nanostructures with 0° and 90° rotation angles have a phase difference of π, which enriches the number of combinations of phase and group delays that can be implemented in our library, allowing us to meet the requirements of more achromatic FOV metasurface designs.

RESULTS

Polarization-Insensitive and Achromatic Metalens

When the topological charge ℓ of the FOV beam is 0, which is considered as a special case, there is no helical component in the phase profile, as indicated in Formula [1], and the flat FOV generator behaves as a metalens.

To validate our method, we designed and simulated an achromatic metalens with a diameter of 200 μm and a numerical aperture (NA) of 0.32. We calculated the phase distribution and group delay distribution required for the achromatic metalens according to Formula [3] and Formula [4], respectively. We then discretized the required phase profile and group delay profile and selected the meta-atom in the library that best matched the required phase and group delay pairs, as shown in **Figures 3B,C**. **Figure 3A** shows the layout of a quarter of the designed metalens. **Figure 4A** shows the simulated intensity profile in the *x-z* plane under RCP, LCP, and XLP illumination. The metalens can focus light over a wide range of

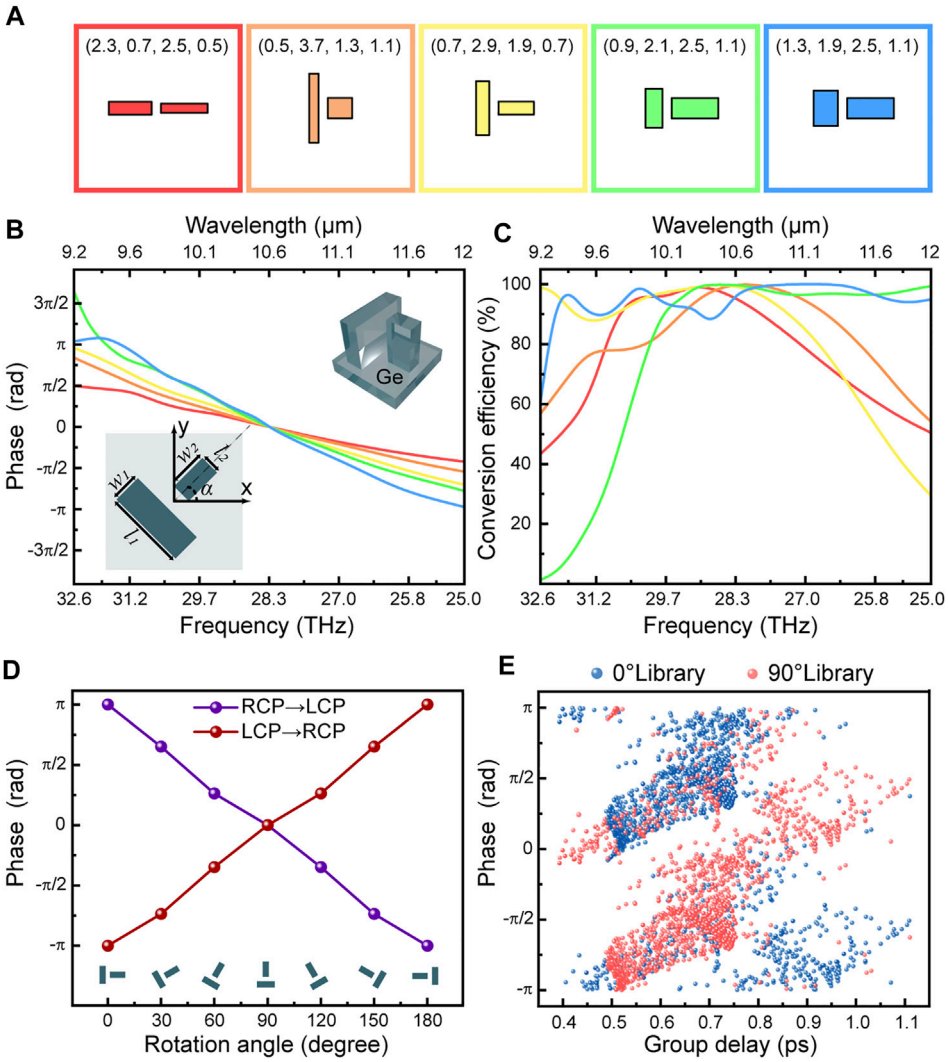

FIGURE 2 | Numerical results of the meta-atoms. **(A)** Schematic of the five selected meta-atoms. **(B,C)** Phase and polarization conversion efficiency of the five selected meta-atoms. The five meta-atoms with different geometrical dimensions satisfy the screening conditions mentioned in the text, i.e. linear phase versus frequency and high polarization conversion efficiency within the designed bandwidth, but different group delays (the slope of phase with respect to the frequency). Each color curve corresponds to a meta-atom in the same colored box in **(A)**. The parameters in the colored boxes correspond to the geometric parameters (l1, w1, l2, w2) of the nanopillars shown in the inset of **(B)** in microns, and the gap between nanopillars is g = 0.5 μm. **(D)** Geometric phase with respect to rotation angle for the same meta-atom under LCP and RCP incidence. The meta-atom has the same geometrical parameters as that in the yellow box in **(A)**. **(E)** The phase and group delay for all meta-atoms in the library. Each meta-atom is represented by a blue and red point in the plot because a 90° rotation can impart a phase change of πwithout changing the group delay.

wavelengths, and the focal point does not shift with wavelength, indicating good achromatic performance. The metalens has the same intensity profile under three polarized incidences, which indicates good polarization insensitivity performance. We extracted the focal length of the metalens at the selected wavelengths by analyzing the intensity distribution in the x–z plane, where the focal point is defined as the position corresponding to the maximum intensity on the z-axis. **Figure 5A** shows the relative focal shift of the metalens, and the relative focal shift is defined as $\Delta f = \frac{f-f_0}{f_0} \times 100\%$, where f_0 is the focal length at the designed wavelength ($\lambda = 10.6\mu m$), and f is the focal length at the sampled wavelength. The relative shift of the focal length was less than 4% over the entire broadband range, confirming the excellent achromatic properties of our metalens.

Figure 4B shows the point spread function (PSF) of the metalens in the focal plane under RCP, LCP, and XLP illumination. The symmetric focal spot was clear, and no focal spot diffusion caused by defocusing and spherical aberration was evident at any wavelength [50]. Based on the intensity distribution in the focal plane, we extracted some metrics to quantify the performance of the metalens, such as full width half maximum (FWHM), Strehl ratio, and efficiency. **Figure 5C** shows the FWHM of the metalens, where the black dashed line indicates the FWHM corresponding to the ideal Airy disk. **Figure 5D** shows the Strehl ratio of the metalens. The

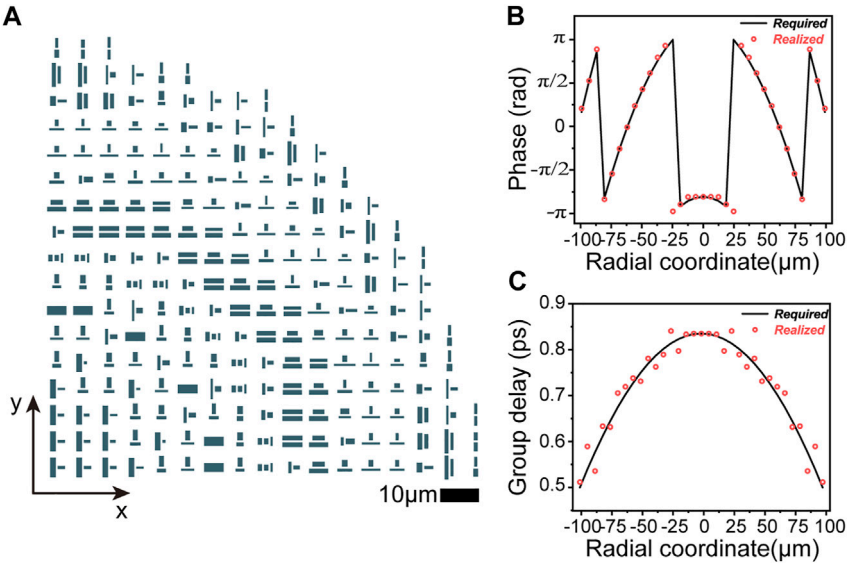

FIGURE 3 | Design result of the broadband achromatic metalens. **(A)** Layout of the quarter of the metalens. **(B,C)** Realized (red circles) and required (black curves) phase and group delay at each radial coordinate on the metalens.

Strehl ratio is defined as in Ref. [51], and the black dashed line in **Figure 5D** indicates the diffraction limit criterion referred to by Marehal. From the FWHM and Strehl ratio, we can conclude that our metalens is capable of diffraction-limited focusing in the continuous wavelength band. **Figure 5B** illustrates the efficiency of the metalens, which is defined as the power in the focal spot (circles of radius three times the FWHM spanning the center of the focal spot) compared to the power of the incident light. The efficiency of the metalens is highest around the design wavelength $\lambda = 10.6\mu m$, and the decrease in efficiency at other wavelengths is mainly due to the decrease in polarization conversion efficiency of the selected meta-atoms. The average efficiency of the metalens under RCP, LCP, and XLP incidence were 44%, 43%, and 45%, respectively. It should be emphasized that these efficiency values already exceed that of the previously reported monochromatic metalens in LWIR [52]. It should be noted that the average efficiency of the metalens is much lower than the polarization conversion efficiency shown in **Figure 2C**. This is mainly because the polarization conversion efficiency reflects the proportion of transmitted light that is focused to the focal point without considering the reflected light. We believe that achromatic metalens will pave the way for broad applications in LWIR, such as thermal imaging and wireless communications.

Polarization-Insensitive and Achromatic FOV Generator

We designed and simulated an FOV generator based on the method proposed above. The FOV generator has a diameter of 200 μm, focal length of 300 μm, design wavelength of 10.6 μm, topological number of −2, and design operating bandwidth of 2 μm. **Figure 6A** shows the layout of the metasurface, which consists of mutually parallel or perpendicular nanopillars arranged in a square lattice. The design process of the FOV generator was the same as that of the metalens. First, we calculated the desired phase and group delay profiles using Formula [2] and Formula [3]. Then, we discretized the group delay and phase profiles according to the lattice constant and selected a meta-atom at each coordinate that provided the best match to the desired group delay and phase pair in the library. **Figures 6B,C** illustrate the group delay and phase required for the ideal achromatic FOV generator, as well as the group delay and phase that can be realized by the metasurface. The required group delay and phase exhibit small inconsistencies with the realized ones.

Figure 7A shows the intensity distribution in the *x-z* plane for the FOV generator under LCP, RCP, and XLP illumination. The focal length of the FOV generator is constant at all selected wavelengths, which indicates that the FOV generator has good achromatic performance, and a similar intensity distribution under LCP, RCP, and XLP incidence confirms that the FOV generator is polarization-insensitive. **Figure 7B** shows the intensity and phase distributions of the FOV generator in the focal plane. The donut-shaped intensity distribution and the spiral-shaped phase distribution are clear in the focal plane, both of which confirm the existence of OV at the origin. The phase distribution confirms that the transmitted beams carry an OAM of $-2\hbar$ according to the branches stemming from the origin.

Figure 8D shows the efficiency of the FOV generator. Efficiency is defined as the power inside the donut ring divided by the power of the incident light, which can be expressed as follows:

$$\eta = \frac{\frac{1}{2}\int_0^{2\pi}\int_{r_0-\Delta r}^{r_0+\Delta r}\left(E_x \cdot H_y - E_y \cdot H_x\right)d\mathrm{r}d\theta}{P_{in}} \tag{12}$$

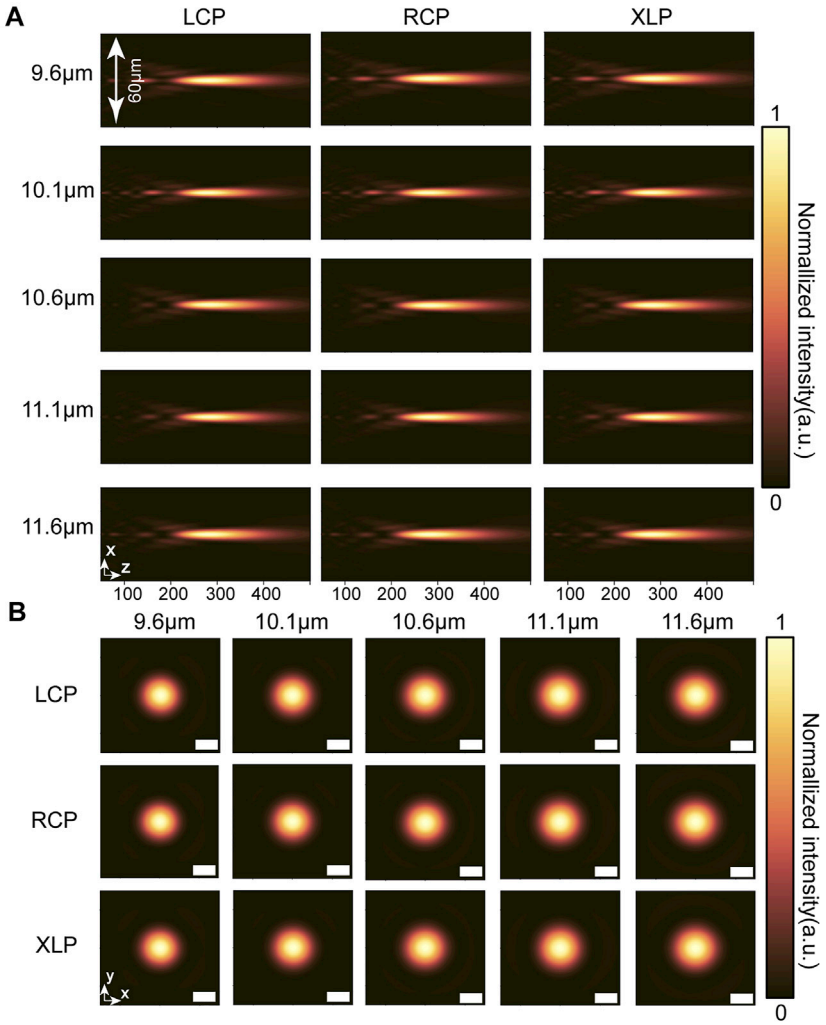

FIGURE 4 | Intensity distribution of the broadband achromatic metalens. **(A)** Intensity profiles in the x-z plane at selected wavelengths. From left to right, each column corresponds to LCP incidence, RCP incidence, and XLP incidence. **(B)** Intensity distribution at the focal plane at selected wavelengths. From top to bottom, each column corresponds to LCP incidence, RCP incidence, and XLP incidence. Scale bar is 10 μm.

where r_0 is the radial coordinate corresponding to the peak intensity, and Δr is the FWHM of the intensity profile. The average efficiency of the FOV was 34% for RCP, LCP, and XLP incidence, as shown in **Figure 8D**.

To quantitatively describe the modal purity of the OV beams, we performed a modal decomposition analysis of the phase in the focal plane [53]. The Fourier relationship between the OAM mode and the phase distribution can be expressed as

$$A_\ell = \frac{1}{2\pi}\int_0^{2\pi} \varphi(\theta)\cdot e^{-i\ell\theta}d\theta \tag{13}$$

$$\varphi(\theta) = \sum_{-\infty}^{+\infty} A_\ell \cdot e^{i\ell\theta} \tag{14}$$

where $\varphi(\theta)$ is the phase distribution of the circle corresponding to the intensity maximum in the focal plane, and $e^{i\ell\theta}$ is the harmonic related to the OAM eigenstate. **Figures 8A–C** show the OAM spectra of the FOV under LCP, RCP, and XLP incidence, respectively. The average purity of the modes corresponding to OAM = $-2\hbar$ is 95.5%, 95.3%, and 92.9% for LCP, RCP, and XLP incidence, respectively. The high percentage of the desired mode indicates that our FOV generator can substantially preserve the mode crosstalk at a relatively low level.

DISCUSSION

We proposed a general method to implement a metasurface for generating FOV beams with arbitrary scalar SOPs in a broad continuous wavelength range. Although the proposed FOV generator works in the LWIR band, this design principle can be applied to arbitrary regions of the electromagnetic spectrum.

The average efficiency of the metasurfaces demonstrated in the main text is approximately 44% (metasurface Ⅰ with $\ell = 0$) and 34%

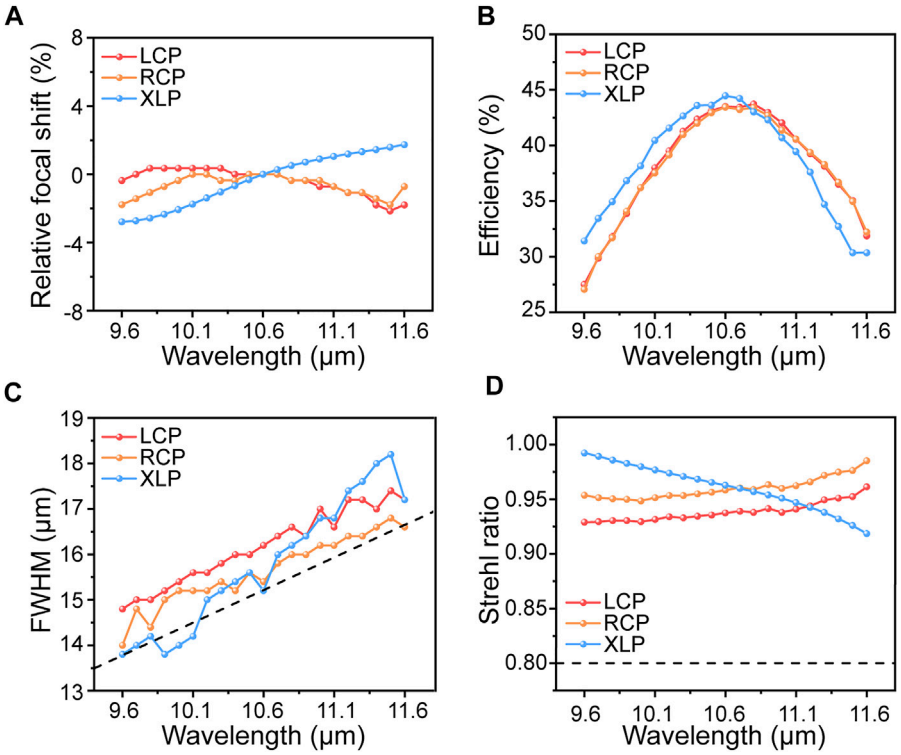

FIGURE 5 | Performance characterization of the metalens. **(A)** Relative focal shift of the metalens. **(B)** Efficiency of the metalens. **(C)**Full-width-half-maximum of the intensity at the focal plane. **(D)** Strehl ratio of the metalens. The black dashed lines in **(C)** and **(D)** represent the diffraction limit.

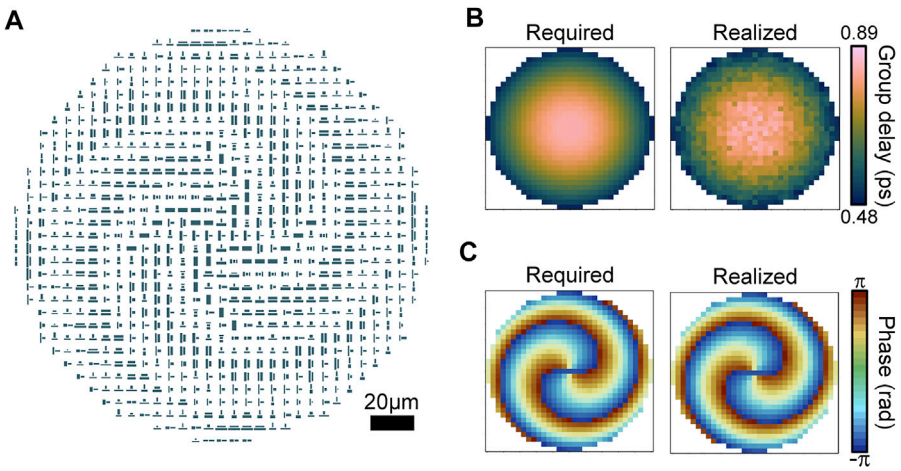

FIGURE 6 | Design of the broadband achromatic and polarization insensitive flat FOV generator. **(A)** Layout of the flat FOV generator. **(B)** Required group delay (left) and realized group delay (right) of the flat FOV generator at each coordinate. **(C)** Required phase (left) and realized phase (right) of the flat FOV generator at each coordinate.

(metasurface II with $\ell = -2$), respectively. The efficiency of metasurface II is lower than that of metasurface I because the phase distribution of metasurface II is not rotationally symmetric, while the phase distribution of metasurface I is rotationally symmetric. Therefore, it is more difficult to satisfy both the phase and group delay conditions for metasurface II, which eventually leads to the selection of meta-atoms with low conversion efficiency. Considering that the germanium–air interface causes a reflection loss of 36%, the efficiency of the metasurface can be further enhanced by replacing the substrate with a low-refractive-index material. For

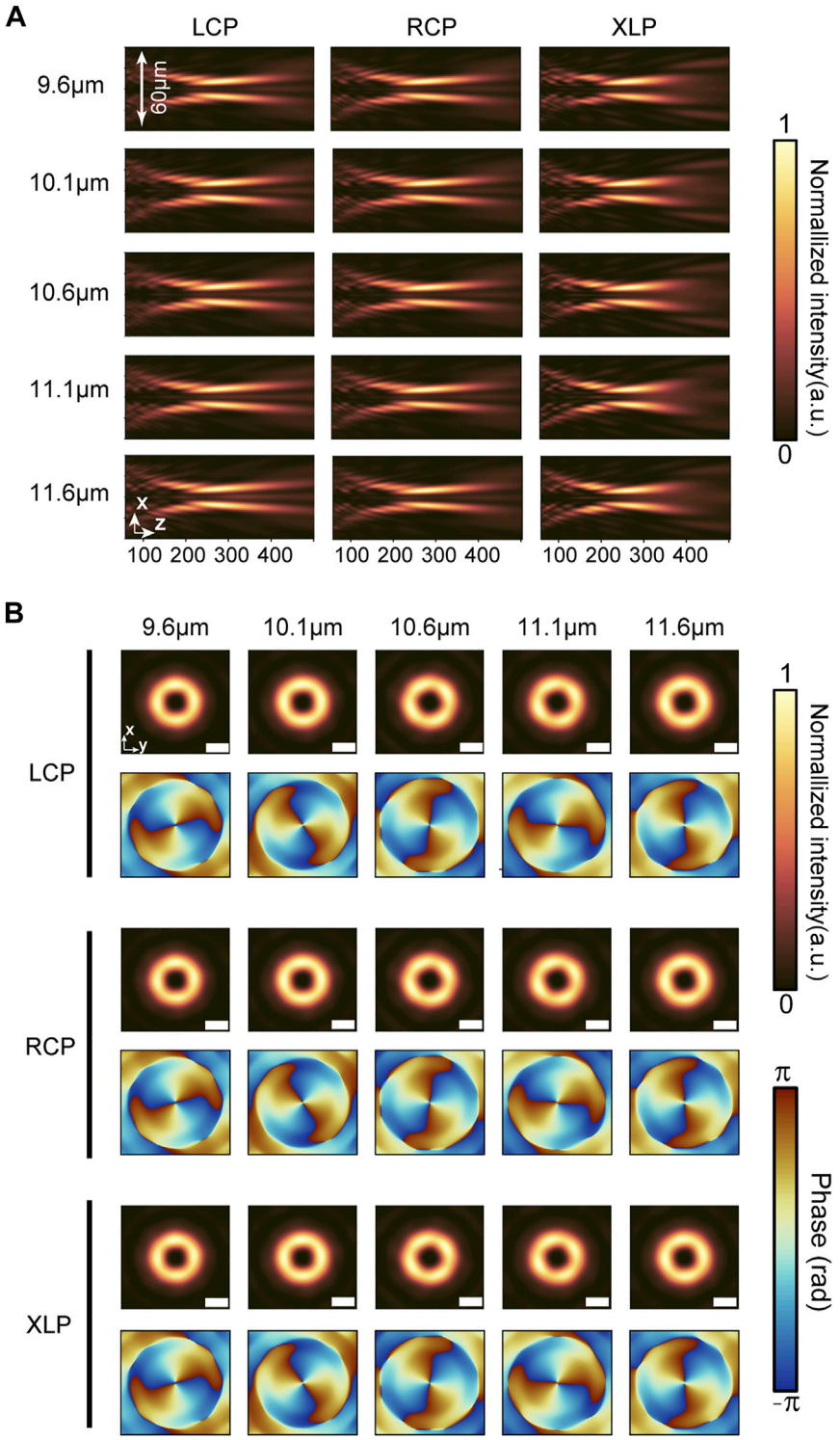

FIGURE 7 | Intensity and phase distributions for the FOV generator. **(A)** Intensity profiles in the *x-z* plane at selected wavelengths. From left to right, each column corresponds to LCP incidence, RCP incidence, and XLP incidence. **(B)** Intensity profiles and phase profiles at the focal plane at selected wavelengths. From top to bottom, each column corresponds to LCP incidence, RCP incidence, and XLP incidence. Scale bar is 10 μm.

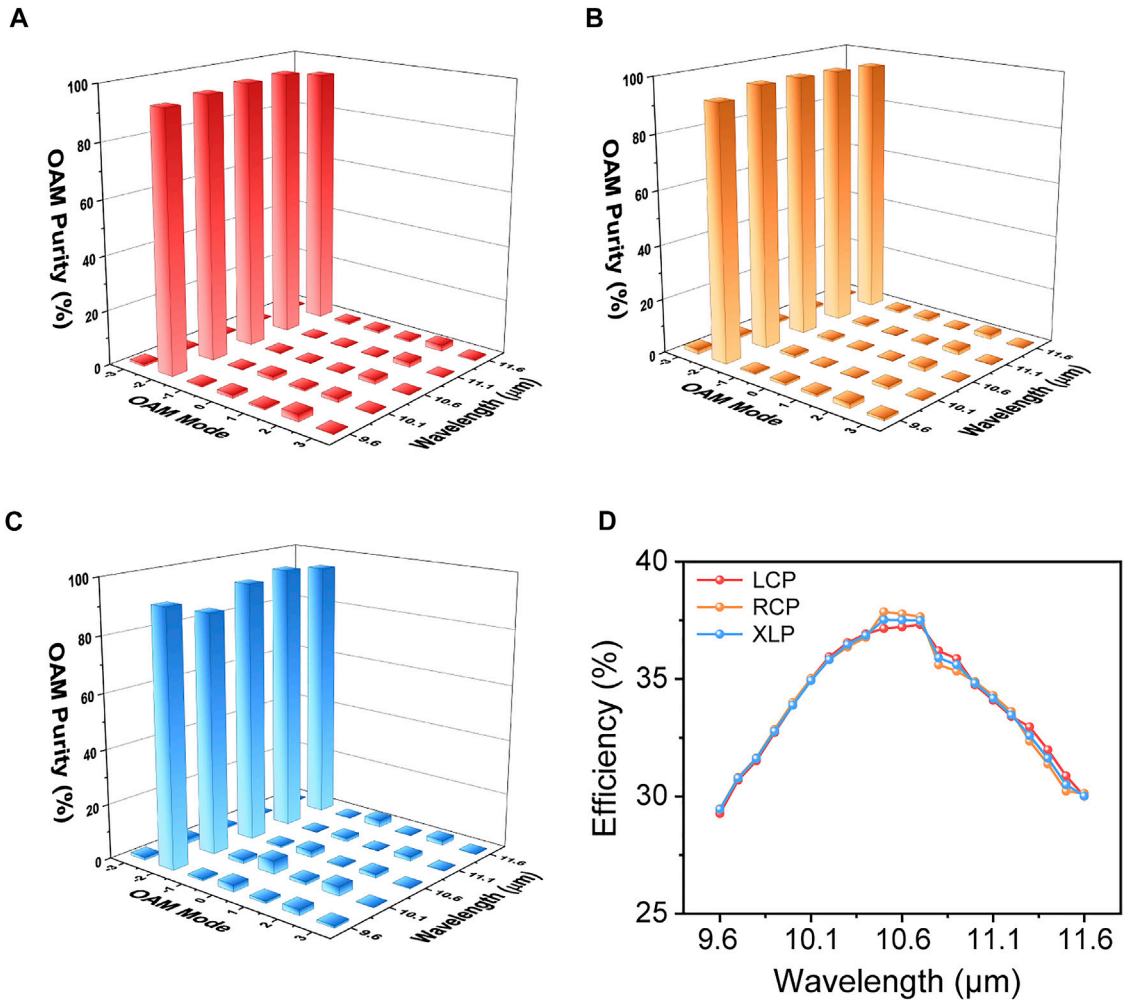

FIGURE 8 | Efficiency and mode purity of the FOV generator. **(A,B,C)** Mode purity of the generated OV under LCP incidence, RCP incidence, and XLP incidence, respectively. **(D)** Efficiency of the flat FOV generator under LCP, RCP, and XLP incidence.

TABLE 1 | Comparison between this work and previously reported flat FOV generators.

Ref	Bandwidth	Relative bandwidth	Materials	Polarization	Efficiency	Mode purity
[55]	780 nm	N/A	Gold	Circular	~1%	N/A
[56]	455 nm; 540 nm	N/A	Titanium Dioxide	Insensitive	~34%	N/A
[38]	633 nm	N/A	Silicon Nitride	Insensitive	~10%	N/A
[57]	0.695 THz	N/A	Silicon	Circular	~28%	N/A
[58]	9–11 GHz	20%	Copper	Circular	~80%	~90%
[42]	3.5–5 μm	35.3%	Silicon	Linear	N/A	N/A
This work	9.6–11.6 μm	18.9%	Germanium	Insensitive	~34%	~92.9%

example, by replacing the substrate with zinc sulfide (n = 2.2), the reflection loss at the interface will be reduced to 14%, which means that in this case, the efficiencies of metasurfaces I and II can reach 59% and 46%, respectively. Another factor limiting the efficiency of our metasurface is that the polarization conversion efficiency cannot maintain high values over a wide bandwidth, as shown in **Figure 2C**. This can be solved by using a three-dimensional structure such as a stacked cross to form a broadband achromatic half-wave plate [54]. It should be noted that our results are based on simulations, and the dimensional errors in the samples during fabricating can lead to lower measured efficiency and mode purity than simulated results.

A comparison between this study and previously reported flat FOV generators is presented in **Table 1**. Compared to previously reported works, our metasurfaces have the advantage of broadband achromatic, high mode purity and polarization insensitivity.

CONCLUSION

In summary, we theoretically proposed two broadband achromatic polarization-insensitive FOV generators in the LWIR range based on an all-germanium metasurface. Metasurface I with ℓ = 0 shows broadband achromatic diffraction-limited focusing ability with an average efficiency of 44%. Metasurface II with ℓ = -2 can achromatically transform a planewave with an arbitrary SOP to a high-purity FOV beam with an average efficiency of 34%. We believe that the metasurfaces demonstrated here will pave the way for a broad range of applications, such as chip-scale optical communication and quantum optics.

DATA AVAILABILITY STATEMENT

The original contributions presented in the study are included in the article/**Supplementary Material**, further inquiries can be directed to the corresponding author.

AUTHOR CONTRIBUTIONS

JG and XJ proposed the idea and supervised the entire work. NS and NX performed the simulation and wrote the original manuscript. HL and XC deduced the theory method. QS conducted the design work and reviewed the manuscript. YT and DS discussed the results and analyzed the data.

FUNDING

This research was funded by the National Natural Science Foundation of China (NSFC), grant number 61901437.

SUPPLEMENTARY MATERIAL

The Supplementary Material for this article can be found online at: https://www.frontiersin.org/articles/10.3389/fphy.2022.846718/full#supplementary-material

REFERENCES

1. Willner AE, Huang H, Yan Y, Ren Y, Ahmed N, Xie G, et al. Optical Communications Using Orbital Angular Momentum Beams. *Adv Opt Photon* (2015) 7(1):66–106. doi:10.1364/AOP.7.000066
2. Shen Y, Wang X, Xie Z, Min C, Fu X, Liu Q, et al. Optical Vortices 30 Years on: OAM Manipulation from Topological Charge to Multiple Singularities. *Light Sci Appl* (2019) 8:90. doi:10.1038/s41377-019-0194-2
3. He H, Friese MEJ, Heckenberg NR, Rubinsztein-Dunlop H. Direct Observation of Transfer of Angular Momentum to Absorptive Particles from a Laser Beam with a Phase Singularity. *Phys Rev Lett* (1995) 75(5): 826–9. doi:10.1103/PhysRevLett.75.826
4. Fang X, Ren H, Gu M. Orbital Angular Momentum Holography for High-Security Encryption. *Nat Photon* (2020) 14(2):102–8. doi:10.1038/s41566-019-0560-x
5. Zhuang X. Unraveling DNA Condensation with Optical Tweezers. *Science* (2004) 305(5681):188–90. doi:10.1126/science.1100603
6. Stav T, Faerman A, Maguid E, Oren D, Kleiner V, Hasman E, et al. Quantum Entanglement of the Spin and Orbital Angular Momentum of Photons Using Metamaterials. *Science* (2018) 361(6407):1101–4. doi:10.1126/science.aat9042
7. Tamburini F, Anzolin G, Umbriaco G, Bianchini A, Barbieri C. Overcoming the Rayleigh Criterion Limit with Optical Vortices. *Phys Rev Lett* (2006) 97(16):163903. doi:10.1103/PhysRevLett.97.163903
8. Sueda K, Miyaji G, Miyanaga N, Nakatsuka M. Laguerre-Gaussian Beam Generated with a Multilevel Spiral Phase Plate for High Intensity Laser Pulses. *Opt Express* (2004) 12(15):3548–53. doi:10.1364/OPEX.12.003548
9. Turnbull GA, Robertson DA, Smith GM, Allen L, Padgett MJ. The Generation of Free-Space Laguerre-Gaussian Modes at Millimetre-Wave Frequencies by Use of a Spiral Phaseplate. *Opt Commun* (1996) 127(4):183–8. doi:10.1016/0030-4018(96)00070-3
10. Karimi E, Piccirillo B, Nagali E, Marrucci L, Santamato E. Efficient Generation and Sorting of Orbital Angular Momentum Eigenmodes of Light by Thermally Tuned Q-Plates. *Appl Phys Lett* (2009) 94(23):231124. doi:10.1063/1.3154549
11. Wang X, Nie Z, Liang Y, Wang J, Li T, Jia B. Recent Advances on Optical Vortex Generation. *Nanophotonics* (2018) 7(9):1533–56. doi:10.1515/nanoph-2018-0072
12. Liu J, Wang J. Demonstration of Polarization-Insensitive Spatial Light Modulation Using a Single Polarization-Sensitive Spatial Light Modulator. *Sci Rep* (2015) 5(1):9959. doi:10.1038/srep09959
13. Wang D, Hwang Y, Dai Y, Si G, Wei S, Choi DY, et al. Broadband High-Efficiency Chiral Splitters and Holograms from Dielectric Nanoarc Metasurfaces. *Small* (2019) 15(20):1900483. doi:10.1002/smll.201900483
14. McClung A, Mansouree M, Arbabi A. At-will Chromatic Dispersion by Prescribing Light Trajectories with Cascaded Metasurfaces. *Light Sci Appl* (2020) 9:93. doi:10.1038/s41377-020-0335-7
15. Zhao M, Chen MK, Zhuang Z-P, Zhang Y, Chen A, Chen Q, et al. Phase Characterisation of Metalenses. *Light Sci Appl* (2021) 10(1):52. doi:10.1038/s41377-021-00492-y
16. Chung H, Miller OD. High-NA Achromatic Metalenses by Inverse Design. *Opt Express* (2020) 28(5):6945–65. doi:10.1364/OE.385440
17. She A, Zhang S, Shian S, Clarke DR, Capasso F. Large Area Metalenses: Design, Characterization, and Mass Manufacturing. *Opt Express* (2018) 26(2):1573–85. doi:10.1364/OE.26.001573
18. Huang L, Coppens Z, Hallman K, Han Z, Böhringer KF, Akozbek N, et al. Long Wavelength Infrared Imaging under Ambient thermal Radiation via an All-Silicon Metalens. *Opt Mater Express* (2021) 11(9):2907–14. doi:10.1364/OME.434362
19. Zhou H, Chen L, Shen F, Guo K, Guo Z. Broadband Achromatic Metalens in the Midinfrared Range. *Phys Rev Appl* (2019) 11(2):024066. doi:10.1103/PhysRevApplied.11.024066
20. Ding X, Kang Q, Guo K, Guo Z. Tunable GST Metasurfaces for Chromatic Aberration Compensation in the Mid-infrared. *Opt Mater* (2020) 109:110284. doi:10.1016/j.optmat.2020.110284
21. Chu H, Li Q, Liu B, Luo J, Sun S, Hang ZH, et al. A Hybrid Invisibility Cloak Based on Integration of Transparent Metasurfaces and Zero-index Materials. *Light Sci Appl* (2018) 7(1):50. doi:10.1038/s41377-018-0052-7
22. Xu H-X, Hu G, Wang Y, Wang C, Wang M, Wang S, et al. Polarization-insensitive 3D Conformal-Skin Metasurface Cloak. *Light Sci Appl* (2021) 10(1): 75. doi:10.1038/s41377-021-00507-8
23. Wang C, Yang Y, Liu Q, Liang D, Zheng B, Chen H, et al. Multi-frequency Metasurface Carpet Cloaks. *Opt Express* (2018) 26(11):14123–31. doi:10.1364/OE.26.014123
24. Wang S, Deng Z-L, Wang Y, Zhou Q, Wang X, Cao Y, et al. Arbitrary Polarization Conversion Dichroism Metasurfaces for All-In-One Full Poincaré Sphere Polarizers. *Light Sci Appl* (2021) 10(1):24. doi:10.1038/s41377-021-00468-y
25. Cui T-J, Liu S, Li L-L. Information Entropy of Coding Metasurface. *Light Sci Appl* (2016) 5(11):e16172. doi:10.1038/lsa.2016.172
26. Deng Y, Wang M, Zhuang Y, Liu S, Huang W, Zhao Q. Circularly Polarized Luminescence from Organic Micro-/nano-structures. *Light Sci Appl* (2021) 10(1):76. doi:10.1038/s41377-021-00516-7

27. Jang J, Badloe T, Rho J. Unlocking the Future of Optical Security with Metasurfaces. *Light Sci Appl* (2021) 10(1):144. doi:10.1038/s41377-021-00589-4
28. Zhao R, Sain B, Wei Q, Tang C, Li X, Weiss T, et al. Multichannel Vectorial Holographic Display and Encryption. *Light Sci Appl* (2018) 7(1):95. doi:10.1038/s41377-018-0091-0
29. Deng ZL, Tu QA, Wang Y, Wang ZQ, Shi T, Feng Z, et al. Vectorial Compound Metapixels for Arbitrary Nonorthogonal Polarization Steganography. *Adv Mater* (2021) 33(43):2103472. doi:10.1002/adma.202103472
30. Mohammadi Estakhri N, Edwards B, Engheta N. Inverse-designed Metastructures that Solve Equations. *Science* (2019) 363(6433):1333–8. doi:10.1126/science.aaw2498
31. Silva A, Monticone F, Castaldi G, Galdi V, Alù A, Engheta N. Performing Mathematical Operations with Metamaterials. *Science* (2014) 343(6167):160–3. doi:10.1126/science.1242818
32. Qian C, Lin X, Lin X, Xu J, Sun Y, Li E, et al. Performing Optical Logic Operations by a Diffractive Neural Network. *Light Sci Appl* (2020) 9(1):59. doi:10.1038/s41377-020-0303-2
33. Georgi P, Massaro M, Luo K-H, Sain B, Montaut N, Herrmann H, et al. Metasurface Interferometry toward Quantum Sensors. *Light Sci Appl* (2019) 8(1):70. doi:10.1038/s41377-019-0182-6
34. Overvig AC, Shrestha S, Malek SC, Lu M, Stein A, Zheng C, et al. Dielectric Metasurfaces for Complete and Independent Control of the Optical Amplitude and Phase. *Light Sci Appl* (2019) 8(1):92. doi:10.1038/s41377-019-0201-7
35. Yu N, Genevet P, Kats MA, Aieta F, Tetienne J-P, Capasso F, et al. Light Propagation with Phase Discontinuities: Generalized Laws of Reflection and Refraction. *Science* (2011) 334(6054):333–7. doi:10.1126/science.1210713
36. Yan C, Li X, Pu M, Ma X, Zhang F, Gao P, et al. Generation of Polarization-Sensitive Modulated Optical Vortices with All-Dielectric Metasurfaces. *ACS Photon* (2019) 6(3):628–33. doi:10.1021/acsphotonics.8b01119
37. Zhang F, Zeng Q, Pu M, Wang Y, Guo Y, Li X, et al. Broadband and High-Efficiency Accelerating Beam Generation by Dielectric Catenary Metasurfaces. *Nanophotonics* (2020) 9(9):2829–37. doi:10.1515/nanoph-2020-0057
38. Zhan A, Colburn S, Trivedi R, Fryett TK, Dodson CM, Majumdar A. Low-Contrast Dielectric Metasurface Optics. *ACS Photon* (2016) 3(2):209–14. doi:10.1021/acsphotonics.5b00660
39. Tang S, Ding F. High-efficiency Focused Optical Vortex Generation with Geometric gap-surface Plasmon Metalenses. *Appl Phys Lett* (2020) 117(1):011103. doi:10.1063/5.0014822
40. Sroor H, Huang Y-W, Sephton B, Naidoo D, Vallés A, Ginis V, et al. High-purity Orbital Angular Momentum States from a Visible Metasurface Laser. *Nat Photon* (2020) 14(8):498–503. doi:10.1038/s41566-020-0623-z
41. Ou K, Yu F, Li G, Wang W, Miroshnichenko AE, Huang L, et al. Mid-infrared Polarization-Controlled Broadband Achromatic Metadevice. *Sci Adv* (2020) 6(37):eabc0711. doi:10.1126/sciadv.abc0711
42. Ou K, Yu F, Li G, Wang W, Chen J, Miroshnichenko AE, et al. Broadband Achromatic Metalens in Mid-Wavelength Infrared. *Laser Photon Rev* (2021) 15:2100020. doi:10.1002/lpor.202100020
43. Chen WT, Zhu AY, Sisler J, Bharwani Z, Capasso F. A Broadband Achromatic Polarization-Insensitive Metalens Consisting of Anisotropic Nanostructures. *Nat Commun* (2019) 10(1):355. doi:10.1038/s41467-019-08305-y
44. Wang S, Wu PC, Su V-C, Lai Y-C, Hung Chu C, Chen J-W, et al. Broadband Achromatic Optical Metasurface Devices. *Nat Commun* (2017) 8(1):187. doi:10.1038/s41467-017-00166-7
45. Chen WT, Zhu AY, Sanjeev V, Khorasaninejad M, Shi Z, Lee E, et al. A Broadband Achromatic Metalens for Focusing and Imaging in the Visible. *Nat Nanotech* (2018) 13(3):220–6. doi:10.1038/s41565-017-0034-6
46. Devlin RC, Ambrosio A, Rubin NA, Mueller JPB, Capasso F. Arbitrary Spin-To-Orbital Angular Momentum Conversion of Light. *Science* (2017) 358(6365):896–901. doi:10.1126/science.aao5392
47. Milione G, Sztul HI, Nolan DA, Alfano RR. Higher-Order Poincaré Sphere, Stokes Parameters, and the Angular Momentum of Light. *Phys Rev Lett* (2011) 107(5):053601. doi:10.1103/PhysRevLett.107.053601
48. Khorasaninejad M, Shi Z, Zhu AY, Chen WT, Sanjeev V, Zaidi A, et al. Achromatic Metalens over 60 Nm Bandwidth in the Visible and Metalens with Reverse Chromatic Dispersion. *Nano Lett* (2017) 17(3):1819–24. doi:10.1021/acs.nanolett.6b05137
49. Lumerical. Lumerical Is Now Part of the Ansys Family (2022). Available from: https://www.lumerical.com/ (Accessed January 31, 2022).
50. Song N, Xu N, Shan D, Zhao Y, Gao J, Tang Y, et al. Broadband Achromatic Metasurfaces for Longwave Infrared Applications. *Nanomaterials* (2021) 11(10):2760. doi:10.3390/nano11102760
51. Aieta F, Kats MA, Genevet P, Capasso F. Multiwavelength Achromatic Metasurfaces by Dispersive Phase Compensation. *Science* (2015) 347(6228):1342–5. doi:10.1126/science.aaa2494
52. Fan Q, Liu M, Yang C, Yu L, Yan F, Xu T. A High Numerical Aperture, Polarization-Insensitive Metalens for Long-Wavelength Infrared Imaging. *Appl Phys Lett* (2018) 113(20):201104. doi:10.1063/1.5050562
53. Jack B, Padgett MJ, Franke-Arnold S. Angular Diffraction. *New J Phys* (2008) 10(10):103013. doi:10.1088/1367-2630/10/10/103013
54. Zhao Y, Belkin MA, Alù A. Twisted Optical Metamaterials for Planarized Ultrathin Broadband Circular Polarizers. *Nat Commun* (2012) 3:870. doi:10.1038/ncomms1877
55. Karimi E, Schulz SA, De Leon I, Qassim H, Upham J, Boyd RW. Generating Optical Orbital Angular Momentum at Visible Wavelengths Using a Plasmonic Metasurface. *Light Sci Appl* (2014) 3(5):e167. doi:10.1038/lsa.2014.48
56. Shi Z, Khorasaninejad M, Huang Y-W, Roques-Carmes C, Zhu AY, Chen WT, et al. Single-Layer Metasurface with Controllable Multiwavelength Functions. *Nano Lett* (2018) 18(4):2420–7. doi:10.1021/acs.nanolett.7b05458
57. Zhou T, Liu Q, Liu Y, Zang X. Spin-independent Metalens for Helicity-Multiplexing of Converged Vortices and Cylindrical Vector Beams. *Opt Lett* (2020) 45(21):5941–4. doi:10.1364/OL.404436
58. Zhang F, Song Q, Yang G-M, Jin Y-Q. Generation of Wideband Vortex Beam with Different OAM Modes Using Third-Order Meta-Frequency Selective Surface. *Opt Express* (2019) 27(24):34864–75. doi:10.1364/OE.27.034864

Conflict of Interest: The authors declare that the research was conducted in the absence of any commercial or financial relationships that could be construed as a potential conflict of interest.

frontiers in Physics

ORIGINAL RESEARCH
published: 04 March 2022
doi: 10.3389/fphy.2022.835159

Exploring for New Insights in the Performance of a 3D Orbital Angular Momentum Mode-Sorter

Shlomi Lightman[1]*, *Jonathan M. Wengrowitcz*[2], *Ayelet Teitelboim*[1], *Raz Gvishi*[1] and *Gilad Hurvitz*[1]

[1]Applied Physics Division, Soreq NRC, Yavne, Israel, [2]Physics Department, Weizmann Institute, Rehovot, Israel

Optical vortex beams are light beams that can carry orbital angular momentum (OAM). Hence, such beams may serve as potential candidates for carriers of information in optical communication and quantum optics applications. This is owing to their spatial orthogonality, as these beams can be combined (multiplex) or separated (demultiplexed). We recently demonstrated a new method to detect OAM states by using a 3D-direct laser printing fabrication process. Measuring the mode-sorter performance was challenging, mainly due to mechanical and optical sensitivities originated from misalignments. In this work, this sensitivity was thoroughly examined. Pure OAM states having lateral and angular misalignments relative to the mode-sorter were introduced, and cross-talk between resolved states was theoretically simulated. The system is relatively vulnerable to small misalignments, which challenge its implementations in free-space communication systems. However, this might be an advantage for counseled communication, in which eavesdropping becomes more challenging, due to the angle-dependent increased modal cross-talk.

Keywords: vortex beam, 3D printing, orbital angular moment, mode sorter, phase modulated

OPEN ACCESS

Edited by:
Pei Zhang,
Xi'an Jiaotong University, China

Reviewed by:
Dong Mao,
Northwestern Polytechnical University, China
Cuicui Lu,
Beijing Institute of Technology, China

***Correspondence:**
Shlomi Lightman
shlomili@soreq.gov.il

Specialty section:
This article was submitted to Optics and Photonics, a section of the journal Frontiers in Physics

Received: *14 December 2021*
Accepted: *17 January 2022*
Published: *04 March 2022*

Citation:
Lightman S, Wengrowitcz JM, Teitelboim A, Gvishi R and Hurvitz G (2022) Exploring for New Insights in the Performance of a 3D Orbital Angular Momentum Mode-Sorter. Front. Phys. 10:835159. doi: 10.3389/fphy.2022.835159

INTRODUCTION

Optical vortex beams are characterized by a winding azimuthal phase, exp (ilϕ), where l is the topological charge and ϕ the azimuthal angle [2]. These beams can carry orbital angular momentum (OAM). This unique property enables implementations of such beams in various applications, including particle manipulation [3], microfabrication [4], astronomy [5], quantum optics [6], high-resolution microscopy [7], and space-division multiplexed communication systems [8]. There are several types of beams that can carry OAM. A commonly used type is the Laguerre-Gaussian (LG) family of beams which is an example of a set of vortex beams that are also solutions of the paraxial Helmholtz equation. In this case, beams with different OAM values are orthogonal; hence, they can be spatially multiplexed and demultiplexed on the same physical channel. These beams can then be used as carriers of information, thereby increasing the information capacity of an optical communication channel [9]. An efficient way to separate OAM states is by applying a Cartesian to log-polar transformation, based on two refractive optical elements [10]. This transformation maps the azimuthal phase profile of an OAM mode into a tilted planar wavefront. As a result, linear combination of OAM states can be simultaneously transformed into a set of planar waves with tilted wavefronts, where the tilt angle depends on the topological charge. These tilted waves can therefore be easily separated in the far field by a lens, enabling OAM analysis, as each mode is located at a different location on a detector. The desired two refractive optical elements are characterized by a

non-trivial 3D shapes. Hence, reaching small scale, 3D, and high optical quality is a challenging task. Conventional implementations of such transformation are based on spatial light modulators (SLMs) [11], or large-scale (cm) diamond-turned surfaces [10]. In general, fabrication or manufacturing of small-scale (below hundreds of micrometers) high-quality optical surfaces, characterized by tens of nanometer surface roughness (RMS) is a challenging task. An innovative new approach was able to minimize the two elements into only one, along with 2D high-resolution diffractive surfaces using electron beam lithography [12, 13]. Furthermore, the generation of vortex beams ($l \leq 1$) and mode analysis was demonstrated in an all-fiber device [14]. However, all mentioned approaches do not provide direct integration to other optical elements (such as optical fiber), enable cost-effective processes, or provide simple and straightforward lithography procedures for various states. Our recent work showed a new fabrication method that provides high-quality and integrated mode-sorter, based on the two optical elements [1]. This method used a 3D-Direct laser writing (3D-DLW) [15] system, which is based on a nonlinear two-photon absorption process [16]. This concept allows reaching accurate 3D elements of complicated surfaces using the polymerization of a light-sensitive material volume (Voxel). Although implementations of 3D-DLW technology for micro-optics devices are widely reported [15–20], we were able to harness, for the first time, this platform for analyzing OAM modes using the transformation optics theory [21, 22]. This approach may induce new and exciting opportunities for vortex beam detection and analysis in integrated devices, in communication systems, or for quantum optical applications. In our previous work [1], we demonstrated that the two-element 3D-printed free-space mode sorter is capable of handling both pure and mixed vortex beams with topological charges $l \leq |3|$. These results were rather preliminary, as further analysis was needed to explore its functionality and performance. Some of the remaining open questions regard the system capabilities upon lateral misalignment and optical directionality (i.e. incoming tilted waves). Hence, in this work, these issues are examined, as various calculations were performed to study the sensitivity of this system.

PRINCIPLE OF THE OAM MODE-SORTER

The Cartesian to log-polar transformation is constructed by two refractive optical elements [11]. These two elements map the coordinates of the incoming beam (in the x-y plane) to an output plane (u-v) using the following relations:

$$u = -a \cdot \ln\left(\frac{\sqrt{x^2+y^2}}{b}\right) \tag{1}$$

$$v = a \cdot tan^{-1}\left(\frac{y}{x}\right) \tag{2}$$

The coordinates u and v describe the Cartesian coordinates at the first element's Fourier plane. The parameter a is a scaling factor, equals to $d/2\pi$, as d is the width of the second element, and

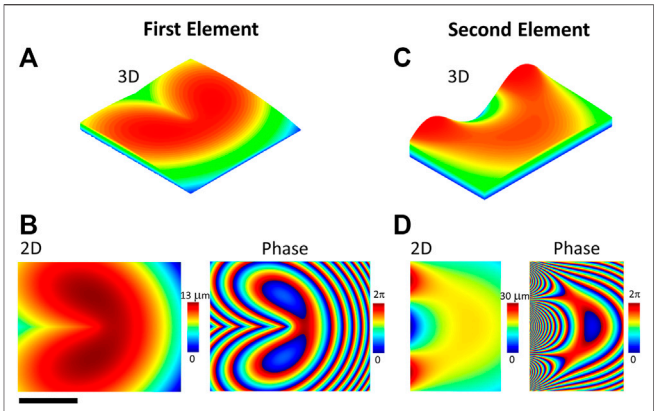

FIGURE 1 | The mode-sorter comprising two elements. 3D **(A,C)** and 2D **(B,D)** representations of the first **(A,B)** and second **(C,D)** elements are presented. In 2D, both height and phase accumulation are described. Scale bar, 50 µm.

b determines the beam location along the v axis. The elements' surfaces are hereby described:

$$Z_1(x,y) = -\left(\frac{a}{f(n_m - n_{air})}\right)\left[y \cdot \tan^{-1}\left(y/x\right) - x \cdot \ln\left(\frac{\sqrt{x^2+y^2}}{b}\right) + x - \frac{1}{2a}\left(x^2+y^2\right)\right] \tag{3}$$

$$Z_2(u,v) = -\left(\frac{a \cdot b}{f(n_m - n_{air})}\right)\left[\cos\left(v/a\right) \cdot exp\left(u/a\right) - -\frac{1}{2a \cdot b}\left(u^2+v^2\right)\right] \tag{4}$$

Z_1 and Z_2 describe the height profiles of the first and second element, accordingly. The distance between the elements is determined by f, and the material and air refractive indices are denoted as n_m and n_{air} accordingly. Modes carrying OAM values that pass through the second element are characterized by rectangular shapes and tilted wave-fronts, dictated by $2\pi l$. Introducing a lens to the tilted waves will result in a focus movement perpendicular to the elongated diffraction limited spot size, by the following connection:

$$\Delta = l \cdot \left(\frac{\lambda f}{d}\right) \tag{5}$$

THEORETICAL DESIGN AND CALCULATIONS

In order to reach optimal phase elements, based on the two surfaces provided in **Eqs 3**, **4**, a simulation code based on a split-step Fourier method [23] was used to study the OAM beam propagation through those surfaces. In this way, the elements' functionality was explored and tailored to the experimental system, as the free parameters were determined. The

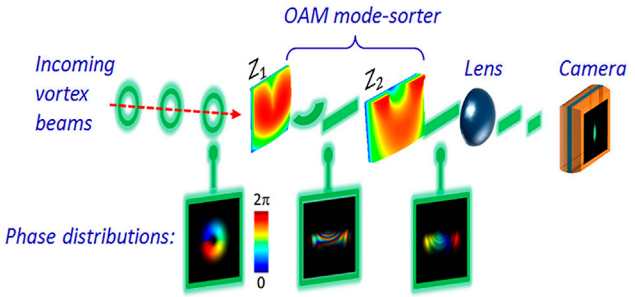

FIGURE 2 | Schematic illustration of the mode-sorter as incoming $l = 1$ OAM mode propagates through the elements. Additional phase and intensity profiles are presented at certain locations with respect to the two elements.

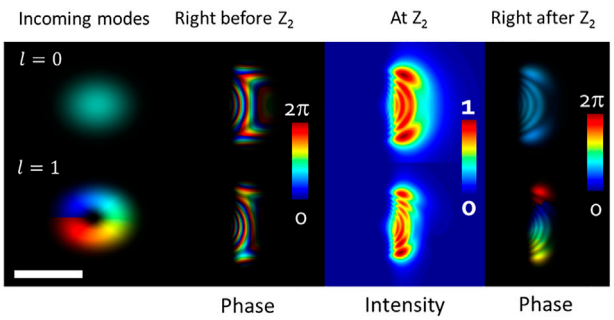

FIGURE 3 | Combined representations of the intensities and phases of modes $l = 0$, 1 are provided before and as after the elements, as brightness and colors refer, respectively, to intensity and phase of each beam. Scale bar, 50 μm.

parameters a, b, and f were chosen to be 19, 25, and 800 μm, accordingly. The final obtained elements are brought in **Figure 1**, as 3D structural representation (top) and 2D surfaces and phase modulations (bottom) can be seen. The lateral dimensions of the first element were chosen to be 100 × 100 μm^2 reaching 12.5 μm at maximum height. The second element lateral size was 160 × 100 μm^2 with maximal height of 30 μm. **Figure 2** provides a schematic illustration of the operating principle. Here, an OAM mode of $l = 1$, characterized by a ring-shaped intensity profile passes through the first element, as the ring gradually becomes open until reaching a rectangular shape at the second element plane. The second element return the mode's initial phase. Then, a lens focuses the mode into an elongated shape at the detector. Combined representations of the mode's intensity and phase are also provided before and after the elements, as brightness and colors refer, respectively, to intensity and phase of each beam. **Figure 3** provides further understanding of the OAM mode sorter operation, as front view intensity and phase calculations of $l = 0$ and $l = 1$ modes can be seen in the vicinity of Element 2 (surface Z_2). Here, the two modes possess unresolved phase distribution prior entering the element. However, passing through the second element reorganizes the phases according to the OAM values. It is worth emphasizing that the intensity profile of all modes remains the same before and after each element, as only the phase is transformed, which enables a gradient phase change that is manifested in the focused spot position variations on the detector.

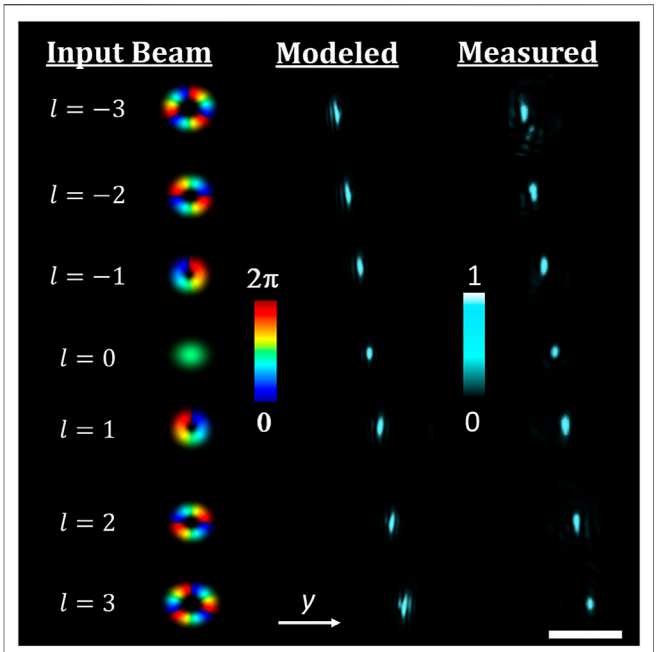

FIGURE 4 | Simulation results of a free-space OAM mode-sorter followed by experimental results. Each OAM state propagates onto a different location on the detector, with correlation to the state's topological charge. Scale bar, 100 μm.

NOMINAL PERFORMANCE OF THE MODE-SORTER

The nominal performance of the OAM mode-sorter is hereby described. This means that OAM states were injected to the mode-sorter perpendicular to the elements, with no tilt or spherical aberration. The detector that registered the incoming mode-dependent spots was also located at the center of the beam's axis (for $l = 0$). This provides a reference point for further understanding the sensitivity and misalignment issues. By using a measurement system, consisting of a CW laser source (690 nm), phase-only spatial light modulator (SLM), and additional optics, the mode-sorter performance was examined, according to a previous work [1]. The SLM provided various OAM modes, $-3 \leq l \leq 3$, that propagated toward the mode sorter two-element system, which were than detected using a CCD. The element fabrication process, detailed measurement system, and additional results and information are further elaborated in a previous work [1]. **Figure 4** provides the experimental results along with predicted simulations of the mode-sorter functionality for the mentioned OAM values at the detector plane. The incoming modes are also provided for convenience. It can be seen that the modes are clearly resolved, as various states are introduced to the system. High l values may cause fringes that lower the ability to determine the OAM state. In general, small beams have short Reighley length. When working with longer distances, the beam

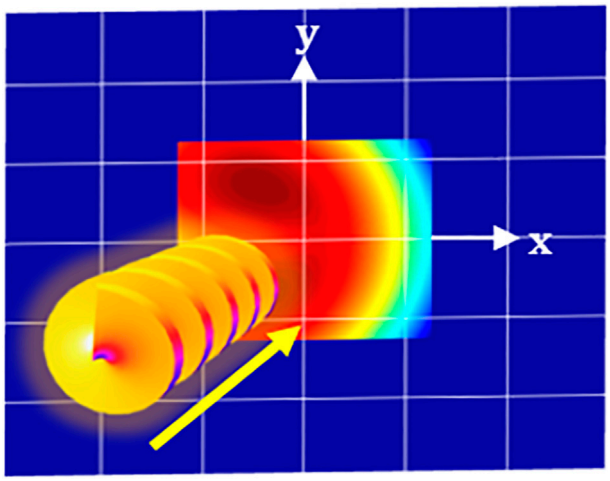

FIGURE 5 | Schematic representation of the lateral displacement calculative method. The entire two-element system moves together in each direction (only the first element is shown).

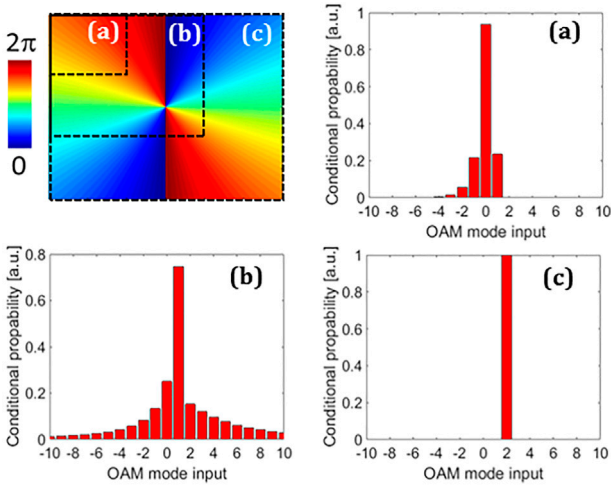

FIGURE 6 | OAM attained spectrum, in the case of $l = 2$, when phase analysis is carried out for different areas and locations in the phase distribution. The pure state is screened, as modal spanning is formed.

carries a spherical phase front rather a plane one. This induces fringes and reduces the device performance to detect accurately OAM states. Furthermore, the influence of production inaccuracies tends to minimize as dimensions increase. The mode sorter consists of two refractive phase elements. The coupling loss for an incoming LG_{10} mode in this system is 30%. The main cause for such losses is due to Fresnel reflections. Additional losses such as absorption and diffraction caused by the device itself are negligible. This is because it is a phase-only device that is made of a transparent polymer.

SORTING SENSITIVITY

In this chapter, the system performance is investigated under lateral misalignment of the incoming beam. Such misalignment often happens in free optic applications. This was carried out by moving the mode-sorter laterally to the beam propagation axis. Since the two-phase structures consisting the mode-sorter device have a complex 3D surface, the performance and OAM spectral purity are expected to be affected. It is convenient to describe the OAM of an LG light beam by its optical axis. Hence, by choosing different axis, these light beams could be represented by a span of various LG modes, which also serve as orthogonal states of the paraxial wave equation, providing discrete OAM spectrum. A lateral displacement of a symmetric beam will not alter its OAM value [24]. However, such a displacement may alter a single photon OAM state, with respect to the reference axis. Meaning, the pure OAM state of an individual photon will be represented by a superposition of many OAM states in the new displaced coordinate system [25]. In other words, by changing the observation axis, the mode purity is disturbed and redistributed as a span of discrete states. Hence, the ability to analyze the OAM state of a certain mode becomes more challenging due to this spectrum broadening. As shown here and in [1], the mode-sorter is capable of detecting various OAM states. However, exploring the system's performance upon displacements or due to beam wondering effects should be further investigated. In this

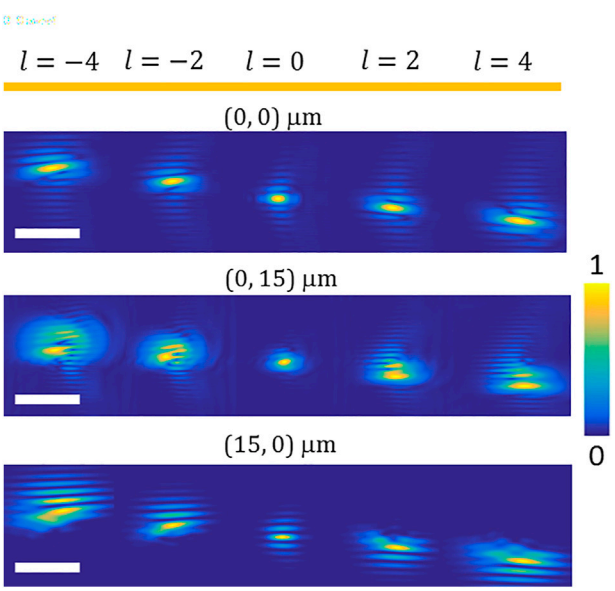

FIGURE 7 | OAM modes of $l = 0, \pm 2, \pm 4$ reaching the detector upon various lateral displacements. Scale bars, 60 μm.

work, we characterize theoretically the system ability to detect incoming OAM states, when the whole mode-sorter system is displaced from its center $(x = 0, y = 0)$, and also when the mode-sorter is not displaced but is introduced to tilted modes at different angles. **Figure 5** provides a schematic illustration of the calculation principle. The mode-sorter, as one system, is displaced to various (x, y) locations, with respect to the axis origin, and then introduced to incoming LG modes carrying different OAM values. As a first step, we show an example that exhibits the challenging task to detect the OAM spectrum solely from the incoming spiraling phase front. This is given in **Figure 6**, where the phase of OAM state $l = 2$ (**Figure 6**, top left) is

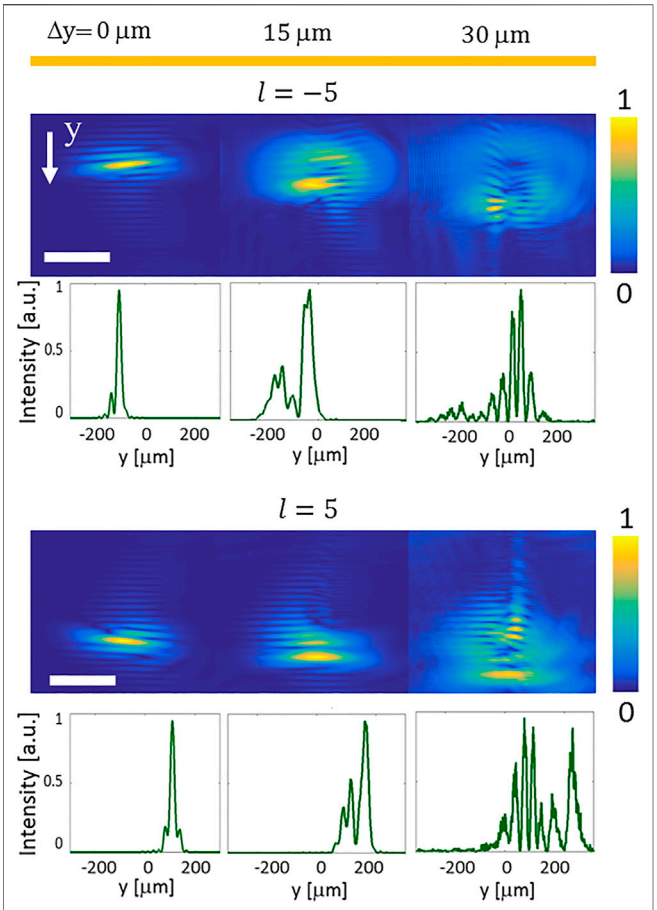

FIGURE 8 | Intensity profiles of the $l = \pm 5$ modes on the detector when displacements on *y*-axis are added. The OAM spectrum is analyzed for each case. The OAM spectrum is obtained by line scanning the obtained modes in the *y*-axis of the intensity distribution picture. Scale bars, 60 μm.

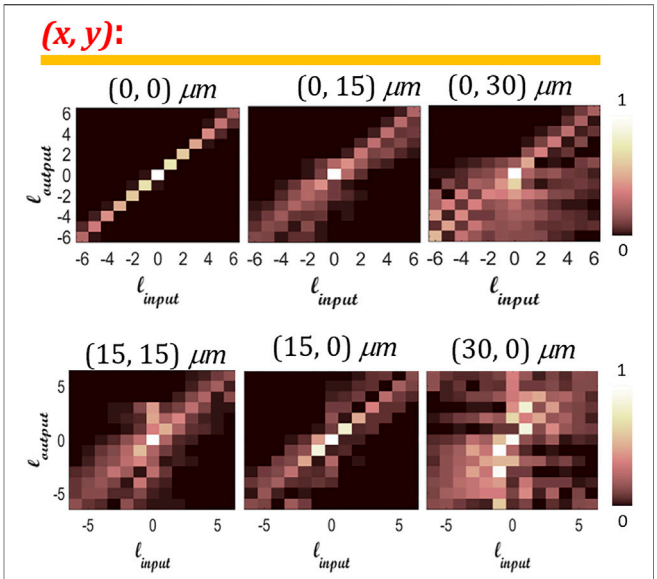

FIGURE 9 | Calculated cross-talk matrix for 13 modes, for various cases of system displacements (15, 30 μm).

redistributed to regions (a, b, c). Analysis of only partial areas of the phase distribution will lead to mixed states rather than a pure OAM determination. It can be seen that for different, smaller, and displaced regions, the OAM spectrum is increased (a, b), compared to a pure state (c). **Figure 7** describes how the simulated beams appear on the detector. Here, the system was introduced to $l = 0, \pm 2, \pm 4$ OAM states when also subjected to lateral displacements $(x = 0,\ 15\mu m;\ y = 0,\ 15\mu m)$. The top row of **Figure 7** describes a process without displacement, as center and bottom rows provide shifts of 15 μm in *y*- and *x*-axis, accordingly. Movement in the *y*-axis blurs the center spot, by broadening the lobes. Displacement in the orthogonal dimension narrows the lobes, as more fringes appear. **Figure 8** provides spectrum analysis of $l = \pm 5$ states, for $\Delta y = 0,\ 15,\ 30\ \mu m$ displacements. The focused spots are accompanied with line scans (*y*-axis) that provide the spectral broadening. It seems that there are no symmetrical effects for $l = \pm 5$. As expected, increasing the displacement up to $30\ \mu m$ decreases the modal purity, as the intensity of the peaks is rather similar. Meaning, it would be difficult to differentiate algorithmically the desired mode from the spectrum. To summarize these results, a light beam that has a partial vortex phase, or only partially detected, would induce wider OAM spectrum that interfere with the desired state sent. This is without even using any sorting devices. Since the mentioned mode-sorter is highly sensitive to misalignments, separating higher modes becomes challenging. This is manifested in wider OAM spectrum and additional fringes that screen the required specific state. It seems that small displacements, even as 10% from the sorter dimensions, induce sufficient disturbance to analyze the OAM states.

THE SYSTEM'S MODAL CROSS-TALK

Here, the cross-talk between various OAM states due to lateral and angular misalignment is investigated. This provides a two dimensional map of all modes there were sent and detected.

Another representation of the modal purity could be described as the modal cross-talk. In this approach, the system misalignment $(x, y \leq 30\mu m)$ is analyzed, where the lateral size of each mode is plotted with respect to the modes that were sent versus those that were detected. By sending an OAM mode through the system and calculating the intensities in each subsection, it is possible to construct a 7×7 discrete cross-talk matrix for detecting all OAM modes, with respect to the existence of additional signal. **Figure 9** presents the cross-talk matrices for six cases of misalignments, for $l \leq |6|$. It seems that displacement in *y* provides distinguishable spectrum for 15 μm, as only positive states could be detected when reaching 30 μm. There is a spectrum broadening for displacement in *x*, as could be seen in the case of $(30\ \mu m,\ 0)$ compared to $(0,\ 30\ \mu m)$. So far, the cross talk was investigated upon lateral misalignment. Now the mode-sorter performance is examined with correlation to the angle of the incoming modes reaching the system's center $(0,\ 0)$. In **Figure 10**, the cross-talk matrix is constructed by various incoming beams, with directionalities that equal to phase tilts of 3–12 *mrad*, at each axis. For a small tilt of 3 *mrad*, there is no clear symmetry in both

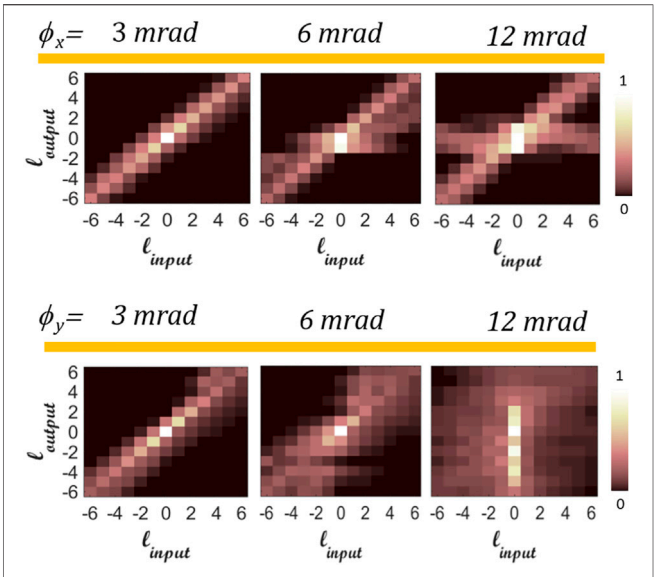

FIGURE 10 | Calculated cross-talk matrix for 13 modes, as the incoming modes propagate off-axis to the mode-sorter center. Each case describes modes that propagate with an additional linear phase gradient terms.

directions, and there is a spectral blur that exists in the *y*-axis. This effect further increases for stronger tilts in the *y* direction. For the orthogonal (*x*) direction, there is a rather unchanged spectrum width, as the tilt in *x* increased. Furthermore, a strong blur effect disables the ability to analyze low-order modes. By analyzing the cross talk maps, it is clear to comprehend the necessary sensitivity requirements for such system. Small shifts and phase gradients damage the ability to analyze currently the OAM states. However, this sensitivity could be an advantage for secure communication systems as any interference could be noticed in the receiver plane. In any case, to eliminate their effects, the system may need to be designed differently, for example, printing the two elements as one for better accurate alignment, or by adding a light-collecting term that collects the shifted light to the elements, to reduce tilting issues.

CONCLUSION

The system is highly sensitive to misalignments, which is a disadvantage in most cases. However, this might be an advantage for private/secret communication, in which "listening" is almost impossible. The operation of the 3D-miniature mode-sorter system was examined. Two concerns were theoretically investigated, shedding more light on the system functionality to serve as a key element for future OAM-based communication systems: first, the system performance when misalignments (respect to the optical axis) are introduced; second, the ability of the mode-sorter to distinguish the OAM states as the beams arrive from various directions, as each beam has a different tilt, but still reach the center of the system. All calculations were based on a mode-sorter that was experimentally capable to separate pure and mixed OAM states, up to $l \leq |3|$; however, higher modes were also being investigated here. The cause for achieving limited experimental sorting capability ($l \leq |3|$) is investigated as the vast calculation enabling shedding more light on this limitation. The calculative approach displaced the mode sorter laterally, in respect to the incoming beams as the performance was examined. Displacements of 15 and 30 μm were chosen for $l \leq |5|$. From the results, the sorting process is sensitive to displacements of 15 μm and above, as the ability to analyze the modes become challenging. Hence, a robust system should be printed directly on the optical axis of the entire system, which would limit misalignments to the printer precision lateral ability. The printed 3D is equipped with a 3D-sensitive (nm) piezo stage. Hence, a 3D-DLW process could be suitable for robust systems. The mode-sorter performance is sensitive to incoming beams, characterized with tilted phase fronts, except for values down to 3 *mrad* which do not affect the system performance substantially. However, increasing the linear phase gradient to 12 *mrad* would damage the ability to separate incoming OAM states. This effect is more dominant for one angle ($\varnothing_y$), rather the perpendicular one ($\varnothing_x$). For conclusion, the system can be operated for small OAM values, as the measurement system is well aligned. The power of the 3D-DLW method allows allocating the printed elements with high precision according to the optical axis. This ability would improve the system demultiplexing performance.

The conclusion of the carried out analysis of the mode-sorter exhibits high sensitivity to optical and mechanical misalignments. This is commonly conceived as a disadvantage in most cases. However, this might be an advantage for secure communication, where the eavesdropper encounters signal broadening and impure states. Thus, our future goal is to construct a free-space integrated communication system, based on the reported insights. Furthermore, the mode-sorter could also be integrated on top of a suitable optical vortex fibers [26–28], combined with a collimating lens. This would enable precise alignment between the fiber core and the mode-sorter center, with low-probability for tilted modes, along with fiber-based communication system foothold.

DATA AVAILABILITY STATEMENT

The original contributions presented in the study are included in the article/Supplementary Material, further inquiries can be directed to the corresponding authors.

AUTHOR CONTRIBUTIONS

All authors listed have made a substantial, direct, and intellectual contribution to the work and approved it for publication.

FUNDING

This work was supported by the Pazy foundation.

REFERENCES

1. Lightman S, Hurvitz G, Gvishi R, Arie A. Miniature Wide-Spectrum Mode Sorter for Vortex Beams Produced by 3D Laser Printing. *Optica* (2017) 4: 605–10. doi:10.1364/optica.4.000605
2. Allen L, Beijersbergen MW, Spreeuw RJC, Woerdman JP. Orbital Angular Momentum of Light and the Transformation of Laguerre-Gaussian Laser Modes. *Phys Rev A* (1992) 45:8185–9. doi:10.1103/physreva.45.8185
3. Garcés-Chávez V, McGloin D, Padgett MJ, Dultz W, Schmitzer H, Dholakia K. Observation of the Transfer of the Local Angular Momentum Density of a Multiringed Light Beam to an Optically Trapped Particle. *Phys Rev Lett* (2003) 91:93602. United States.
4. Hamazaki J, Morita R, Chujo K, Kobayashi Y, Tanda S, Omatsu T. Optical-vortex Laser Ablation. *Opt Express* (2010) 18:2144–51. doi:10.1364/oe.18.002144
5. Swartzlander, Jr. GA, Ford EL, Abdul-Malik RS, Close LM, Peters MA, Palacios DM, et al. Astronomical Demonstration of an Optical Vortex Coronagraph. *Opt Express* (2008) 16:10200–7. OSA. doi:10.1364/oe.16.010200
6. García-Escartín JC, Chamorro-Posada P. Quantum Multiplexing with the Orbital Angular Momentum of Light. *Phys Rev A - Mol Opt Phys* (2008) 78:1–10.
7. Hell SW, Wichmann J. Breaking the Diffraction Resolution Limit by Stimulated Emission: Stimulated-Emission-Depletion Fluorescence Microscopy. *Opt Lett* (1994) 19:780–2. doi:10.1364/ol.19.000780
8. Bozinovic N, Yue Y, Ren Y, Tur M, Kristensen P, Huang H, et al. Terabit-Scale Orbital Angular Momentum Mode Division Multiplexing in Fibers. *Science* (2013) 340:1545–8.
9. Baghdady J, Miller K, Morgan K, Byrd M, Osler S, Ragusa R, et al. Multi-gigabit/s Underwater Optical Communication Link Using Orbital Angular Momentum Multiplexing. *Opt Express* (2016) 24:9794. doi:10.1364/oe.24.009794
10. Lavery MPJ, Robertson DJ, Berkhout GCG, Love GD, Padgett MJ, Courtial J. Refractive Elements for the Measurement of the Orbital Angular Momentum of a Single Photon. *Opt Express* (2012) 20:2110–5. doi:10.1364/oe.20.002110
11. Berkhout GC, Lavery MP, Courtial J, Beijersbergen MW, Padgett MJ. Efficient Sorting of Orbital Angular Momentum States of Light. *Phys Rev Lett* (2010) 105:153601–11. doi:10.1103/PhysRevLett.105.153601
12. Ruffato G, Massari M, Parisi G, Romanato F. Test of Mode-Division Multiplexing and Demultiplexing in Free-Space with Diffractive Transformation Optics. *Opt Express* (2017) 25:7859. doi:10.1364/oe.25.007859
13. Ruffato G, Massari M, Romanato F. Compact Sorting of Optical Vortices by Means of Diffractive Transformation Optics. *Opt Lett* (2017) 42:551. doi:10.1364/ol.42.000551
14. Mao D, Zheng Y, Zeng C, Lu H, Wang C, Zhang H, et al. Generation of Polarization and Phase Singular Beams in Fibers and Fiber Lasers. *Adv Photon* (2021) 3:1–18. doi:10.1117/1.ap.3.1.014002
15. Zhou X, Hou Y, Lin J. A Review on the Processing Accuracy of Two-Photon Polymerization. *AIP Adv* (2015) 5. doi:10.1063/1.4916886
16. Chichkov BN, Ostendorf A. Two-Photon Polymerization: A New Approach to Micromachining. *Photon Spectra* (2006) 40:72–9.
17. Schiappelli F, Kumar R, Prasciolu M, Cojoc D, Cabrini S, De Vittorio M, et al. Efficient Fiber-To-Waveguide Coupling by a Lens on the End of the Optical Fiber Fabricated by Focused Ion Beam Milling. *Microelectronic Eng* (2004) 73-74:397–404. doi:10.1016/s0167-9317(04)00143-1
18. Kabouraki E, Giakoumaki AN, Danilevicius P, Gray D, Vamvakaki M, Farsari M. Redox Multiphoton Polymerization for 3D Nanofabrication. *Nano Lett* (2013) 13:3831–5. doi:10.1021/nl401853k
19. Thiel M, Fischer J, Von Freymann G, Wegener M. Direct Laser Writing of Three-Dimensional Submicron Structures Using a Continuous-Wave Laser at 532 Nm. *Appl Phys Lett* (2010) 97:10–3. doi:10.1063/1.3521464
20. Lightman S, Gvishi R, Hurvitz G, Arie A. Shaping of Light Beams by 3D Direct Laser Writing on Facets of Nonlinear Crystals. *Opt Lett* (2015) 40:4460. doi:10.1364/ol.40.004460
21. Hossack WJ, Darling AM, Dahdouh A. Coordinate Transformations with Multiple Computer-Generated Optical Elements. *J Mod Opt* (1987) 34: 1235–50. doi:10.1080/09500348714551121
22. Bryngdahl O. Geometrical Transformations in Optics*. *J Opt Soc Am* (1974) 64:1092. doi:10.1364/josa.64.001092
23. Sinkin OV, Holzlohner R, Zweck J, Menyuk CR. Optimization of the Split-step Fourier Method in Modeling Optical-Fiber Communications Systems. *J Lightwave Technol* (2003) 21:61–8. OSA. doi:10.1109/jlt.2003.808628
24. Berry MV. Paraxial Beams of Spinning Light," in. *Proc SPIE* (1998) 3487.
25. Molina-Terriza G, Torres JP, Torner L. Management of the Angular Momentum of Light: Preparation of Photons in Multidimensional Vector States of Angular Momentum. *Phys Rev Lett* (2002) 88:4.
26. Jiang Y, Ren G, Shen Y, Xu Y, Jin W, Wu Y, et al. Two-dimensional Tunable Orbital Angular Momentum Generation Using a Vortex Fiber. *Opt Lett* (2017) 42:5014–7. doi:10.1364/ol.42.005014
27. Ramachandran S, Kristensen P. Optical Vortices in Fiber. *Nanophotonics* (2013) 2:455–74. doi:10.1515/nanoph-2013-0047
28. Brunet C, Vaity P, Messaddeq Y, LaRochelle S, Rusch LA. Design, Fabrication and Validation of an OAM Fiber Supporting 36 States. *Opt Express* (2014) 22: 26117. doi:10.1364/oe.22.026117

Conflict of Interest: The authors declare that the research was conducted in the absence of any commercial or financial relationships that could be construed as a potential conflict of interest.

frontiers | Frontiers in Physics

ORIGINAL RESEARCH
published: 09 May 2022
doi: 10.3389/fphy.2022.879689

Perfect Optical Vortex to Produce Controllable Spot Array

Xiaotong Jiang[1], Yuyuan Tian[1], Meiyu Sun[1], Zhigang Li[1], Dengying Zhang[1], Kunjian Cao[1], Qiang Shi[1,2]* and Linwei Zhu[1]*

[1]School of Physics and Optoelectronic Engineering, Ludong University, Yantai, China, [2]Yantai Magie-Nano Technology Co. Ltd., Yantai, China

The perfect optical vortex has successfully aroused substantial interest from researchers for its central dark hollow caused by spatial phase singularity in recent years. However, the traditional methods of combining the axicon and helical phase to generate the perfect optical vortex lead to an additional focus deviation in the tightly focused systems. Here, we report a multi-foci integration (MFI) method to produce the perfect optical vortex by accumulating a finite number of foci in the focal plane to overcome the additional focus deviation. Furthermore, based on MFI, we superposed two perfect optical vortices to obtain the spot array with controllable phase distribution and the number of spots. This work deepens our knowledge about superposed vortices and facilitates new potential applications. The micromanipulated experimental results agree well with our theoretical simulation. The spot array field provides new opportunities in direct laser writing, optical tweezers, optical communications, and optical storage.

Keywords: perfect optical vortex, orbital angular momentum, interference superposition, spatial light modulator, optical manipulation

OPEN ACCESS

Edited by:
Gianluca Ruffato, University of Padua, Italy

Reviewed by:
Svetlana Khonina, Image Processing Systems Institute, Russia
Mingzhou Chen, University of St Andrews, United Kingdom

****Correspondence:***
Meiyu Sun
s.m.y.2008@163.com
Qiang Shi
shi.qiang@magie-nano.com

Specialty section:
This article was submitted to Optics and Photonics, a section of the journal Frontiers in Physics

Received: *20 February 2022*
Accepted: *29 March 2022*
Published: *09 May 2022*

Citation:
Jiang X, Tian Y, Sun M, Li Z, Zhang D, Cao K, Shi Q and Zhu L (2022) Perfect Optical Vortex to Produce Controllable Spot Array. Front. Phys. 10:879689. doi: 10.3389/fphy.2022.879689

INTRODUCTION

Research on vortex beams has attracted increasing attention since L. Allen et al. proved that optical vortex carried orbital angular momentum [1]. Owing to its special optical character and dynamic property by phase gradient [2], vortex beams expanded their applications in various areas, including optical communication [3, 4], micromanipulation [5–8], direct laser writing [9–13], multiple spot arrays [14–19], and complicated optical vortex fields [20–22]. The concept of the perfect optical vortex (POV) has been proposed among vortex beams, whose dark hollow radius does not depend on the topological charge [2, 23, 24]. In 2015, Vaity et al. demonstrated that a POV is the Fourier transform of a Bessel beam [25]. Since then, research has been performed on POV generation [26], modulation [19, 27, 28], and measurements [29, 30]. Particularly, many complicated vortex beam geometries can be obtained through the superposition of Bessel beams and were applied in diverse research fields such as propagation property measurement [31, 32] and the femtosecond two-photon polymerization [33]. In practice, an ideal Bessel beam cannot be created due to the infinite lateral extent of the energy, while the bounded visions of the Bessel beam can be generated by various methods, such as axicon lens [34–38], computer-generated hologram [39–42], focusing of ring-shaped narrow aperture [43–45], and curved fork grating [46, 47]. In addition, the ring-toric lens can also form the annular beam in the focal plane [48–50]. Among the aforementioned methods, the versatile axicon phase hologram can provide more flexibility for generating the Bessel beam. However, the focus deviation caused by the axicon phase was aggravated in the focused field of the high-NA objectives. The dispersive three-dimensional (3D) intensity distribution around the focal region may

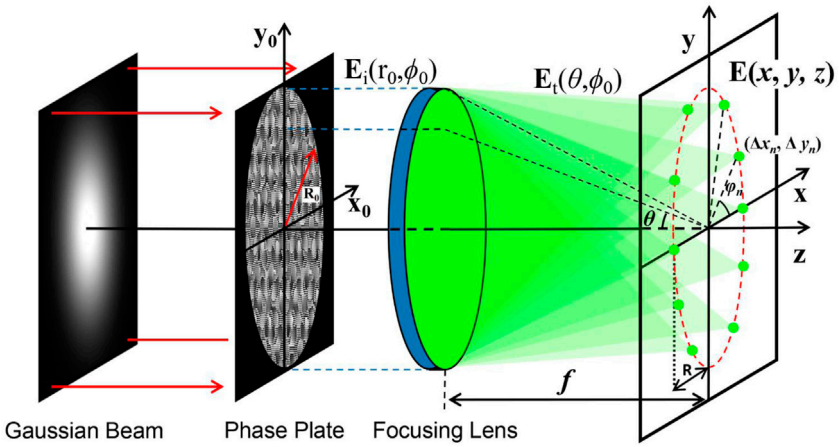

FIGURE 1 | Schematic diagram of the MFI method in a tightly focused system.

cause the loss of stability and accuracy in micromanipulation and fabrication. Hence, this focus deviation issue remains in the further superposition of POVs to generate more complicated optical fields.

In this article, we reported a multi-foci integration (MFI) method to overcome the focus deviation. A POV with tunable radius and topological charge can be generated directly by creating a large number of foci with a diffraction limit size at the focal plane. In practice, a similar method to create the ring-shaped field and the accumulation of multiple concentric rings has been reported in [51]. These methods provide a new solution for (de)multiplexing beams [52, 53]. Based on MFI, we also superposed the complex field of two complete POVs to produce the spot array. The multiple spots are equally spaced arrangements in an annular region of the original POV, and the different spot numbers and phase gradient distribution cannot change the profile of the array. Here, we further investigate the degrees of freedom of the array, including the radius, number of spots, and the periods of phase gradient. The dynamic and static trapping results yield good agreement with theoretical analysis, and it significantly developed the orbital angular momentum and intensity distribution structure controllability of the beam in the tightly focused field.

METHODS

As previously reported in [25], the POV in the focusing field of an objective lens can be described as a Dirac delta function $\delta(r)$ with a helical phase, that is,

$$E(r,\varphi) = \frac{j^{l-1}}{k_r}\delta(r-R)\exp(jl\varphi). \tag{1}$$

Herein, (r, φ) are the polar coordinates of the focal plane, k_r is the radial wave vector, and l is the topological charge. The delta function defines the annular amplitude range of POV, and R is the radius of POV. It is clear from **Eq. 1** that an ideal annular amplitude (i.e., the delta function) is impossible to achieve in the experiment. Generally, the axicon lens phase exp ($jk\alpha r$) is frequently utilized to generate the annular amplitude, where α is the angle parameter of the axicon lens. Subsequently, the POV can be produced *via* an axicon and helical phase, that is, exp ($jk\alpha r + jl\varphi$). In some applications, such as micromanipulation and microfabrication, the axicon and Fourier lens (or objective) must be combined to realize the microscopic imaging, and then we can obtain the annular intensity in the focal plane. Unfortunately, the additional axicon phase of exp ($jk\alpha r$) produces focus deviation into the focal region of the focusing lens, which leads to the maximum intensity deviating from the focal plane. The deviation becomes more serious in a tightly focused system with a high-NA objective.

To overcome the focus deviation caused by the axicon phase, we proposed the MFI method, which is accumulated by abundant foci to form the annular amplitude. In theory, the premise of this method is that the annular intensity region is decomposed to obtain an abundant number of diffraction limit foci, and we reverse this process to reconstruct the annular beam. As shown in **Figure 1**, 10 foci were generated in a circular trajectory. Theoretically, the electric field distribution in the focal region of an aberration-free high-NA objective can be calculated by the Richards–Wolf vectorial diffraction theory [52].

$$\mathbf{E}(x,y,z) = A\int_0^{\beta}\int_0^{2\pi} P(\theta)\mathbf{E}_t(\theta,\phi_0) \times \exp\{-jk\sqrt{x^2+y^2}\sin\theta\cos[\tan^{-1}(y/x) - \phi_0]\}\exp(jkz\cos\theta)\sin\theta d\phi_0 d\theta, \tag{2}$$

where A is a constant related to the focal length f and the wavelength λ, $k = 2\pi/\lambda$ is the wavenumber, (r_0, ϕ_0) are the polar coordinates of the incident plane, and x, y, and z are the Cartesian coordinates in the focal region. $P(\theta)$ is the apodization function of the incident pupil, which can be expressed as

$$P(\theta) = \begin{cases} 1, & \theta \le \beta \\ 0, & \text{otherwise} \end{cases}, \tag{3}$$

where $\beta = \sin^{-1}(NA/n_t)$ is the maximum aperture angle of the objective. θ is the deflection angle, which has the relationship $\sin\theta = r_0 NA/(R_0 n_t)$, where R_0 is the aperture stop radius, n_t is the refractive index behind the objective, and NA is the numerical aperture of the objective lens. $\mathbf{E}_t$ (θ, ϕ_0) is the transmitted field, which has a relationship of the input field, that is

$$\begin{bmatrix} E_{tx} \\ E_{ty} \\ E_{tz} \end{bmatrix} = \sqrt{\cos\theta} \begin{bmatrix} 1 + (\cos\theta - 1)\cos^2\phi_0 & (\cos\theta - 1)\cos\phi_0 \sin\phi_0 & -\sin\theta\cos\phi_0 \\ (\cos\theta - 1)\cos\phi_0 \sin\phi_0 & 1 + (\cos\theta - 1)\sin^2\phi_0 & -\sin\theta\sin\phi_0 \\ \sin\theta\cos\phi_0 & \sin\theta\sin\phi_0 & \cos\theta \end{bmatrix} \times \begin{bmatrix} E_{ix} \\ E_{iy} \\ E_{iz} \end{bmatrix}. \tag{4}$$

Here, E_{tx}, E_{ty}, and E_{tz} are the components of the Cartesian coordinate system, that is, $\mathbf{E}_t = E_{tx}\mathbf{e}_x + E_{ty}\mathbf{e}_y + E_{tz}\mathbf{e}_z$, where $\mathbf{e}_x$, $\mathbf{e}_y$, and $\mathbf{e}_z$ are the unit vectors. E_{ix}, E_{iy}, and E_{iz} are the polarized components of the incident field $\mathbf{E}_i$, $\mathbf{E}_i = E_{ix}\mathbf{e}_x + E_{iy}\mathbf{e}_y + E_{iz}\mathbf{e}_z$. In the Debye approximation, the electric field of **Eq. 2** can be further expressed as the Fourier transform of the weighted field $\mathbf{E}_t$:

$$\mathbf{E}(x, y, z) = F\{P(\theta)\mathbf{E}_t(\theta, \phi_0)/\cos\theta \times \exp(jk_z z)\}, \tag{5}$$

where F{·} denotes the Fourier transform (FT). Then, based on the shift theorem of the FT, a phase-only analytical expression for controlling the 2D lateral displacement of the highly focused spot can be given as (17, 53)

$$\psi(x_0, y_0, \Delta x_n, \Delta y_n) = \frac{2\pi}{\lambda f}(x_0 \Delta x_n + y_0 \Delta y_n), \tag{6}$$

where (x_0, y_0) are the Cartesian coordinates of the incident plane, $f = R_0 n_t/NA$ is the focal length of the objective, and Δx_n and Δy_n are the shifted displacements of the nth deviated focus versus the original focal center in the focal plane. Based on the phase-only distribution calculated using **Eq. 6**, the position of the highly focused spots can be controlled in the focal region of a high-NA objective. As shown in **Figure 1**, the positions of the shifting spots are set along a circular trajectory, the nth focus coordinates $\Delta x_n = R\cos\varphi_n$, $\Delta y_n = R\sin\varphi_n$, $\varphi_n = 2\pi n/N$, and R is the radius of the circle in the focal plane. Then, we can obtain a superposition field by summing up the finite foci, that is,

$$U_i(x_0, y_0) = \sum_{n=1}^{N} \exp\left[j\frac{2\pi}{\lambda f}(x_0 R\cos\varphi_n + y_0 R\sin\varphi_n) \right]. \tag{7}$$

Using **Eq. 7**, multifocal spots along the circular trajectory can be generated. Furthermore, in theory, annular amplitude will be achieved when the number of foci is infinite. After combining a helical phase, a POV with an arbitrary topological charge can be generated. Thus, **Eq. 7** can be rewritten as an integral form, that is,

$$U_i(x_0, y_0) = \int_0^{2\pi} \exp\left[j\frac{2\pi}{\lambda f}(x_0 R\cos\varphi + y_0 R\sin\varphi) \right] \times \exp(jl\varphi)d\varphi, \tag{8}$$

where $\exp(jl\varphi)$ is the helical phase with a topological charge l. **Eq. 8** is the key formula of the multi-foci integration (MFI) method to produce the field of the POV. Consequently, when the incident field of the objective lens is modulated by the optical distribution of **Eq. 8**, the electric field of **Eq. 5** in the focal plane can be expressed as

$$\mathrm{F}\{U_i(x_0, y_0) \times G(\theta, \phi_0)\} = \mathrm{F}\{U_i(x_0, y_0)\} * \mathrm{F}\{G(\theta, \phi_0)\}, \tag{9}$$

where $G(\theta, \phi_0) = P(\theta)\,\mathbf{E_0}(\theta, \phi_0)\exp(jkz\cos\theta)/\cos\theta$, and $\mathbf{E_0}(\theta, \phi_0)$ indicates the transmitted field when the incident optical field is a plane wave without any phase modulation. Therefore, in this case, the focal field can be expressed as $\mathrm{F}\{G(\theta, \phi_0)\} = E_{\mathrm{Airy}}$, which indicates an Airy spot with a diffraction limit size without modulation. The symbol * denotes the convolution operation. Based on the convolution theorem of the Fourier transform, **Eq. 9** means that the focal field can be expressed as a convolution of the Airy spot and the Fourier transform of the superposition field calculated by **Eq. 8**. Then, based on the shift theorem of the Fourier transform, the additional phase shift introduces a linear displacement in the spatial domain, that is, the Fourier transform of the superposition field is

$$\begin{aligned} &\mathrm{F}\{U_i(x_0, y_0)\} = \\ &\int_0^{2\pi} \mathrm{F}\left\{ \exp\left[j\frac{2\pi}{\lambda f}(x_0 R\cos\varphi + y_0 R\sin\varphi) \right] \right\} \\ &\times \exp(jl\varphi)d\varphi = \int_0^{2\pi} \delta(x - R\cos\varphi, y \\ &\qquad - R\sin\varphi) \times \exp(jl\varphi)d\varphi \\ &\qquad = \delta(r - R) \times \exp(jl\varphi). \end{aligned} \tag{10}$$

From **Eq. 10**, we can observe that an ideal annular amplitude with helical phase can be produced when the incident field is modulated by the superposition field. Finally, the electric field of **Eq. 9** in the focal plane can be given as

$$\mathrm{F}\{U_i(x_0, y_0) \times G(\theta, \phi_0)\} = \delta(r - R)\exp(jl\varphi) * E_{\mathrm{Airy}}. \tag{11}$$

Thus, from **Eq. 11**, we can observe that an annular amplitude with diffraction limit width and helical phase has been generated by the MFI method. In the experiment, due to the diffraction limit of the focal spot, an annular intensity distribution with a smooth profile can be formed by finite value N (for example, $N = 100$–200 corresponding to the radius $R = 5$–10 μm). According to **Eq. 2** and **Eq. 11**, we can observe that a POV with a controllable radius R and topological charge l can be generated in the tightly focused plane through the MFI method.

To verify that the MFI method does not cause the focus deviation, we theoretically simulated the POV intensity distribution in the longitudinal and transverse plane using the axicon phase method and MFI method generated phase pattern, respectively. In this case, we supposed the incident beam is a plane wave, and the simulation parameters are $\lambda = 532$ nm, $NA = 1.4$, $n_t = 1.518$, $R = 3.5$ μm, and $l = 5$. When the incident beam is modulated by the axicon phase, the optical field can be expressed as $U_i = \exp(jk\alpha r + jl\varphi)$. **Figure 2A** shows the simulated results of the axicon phase method with $\alpha = 0.065$. Thus, the incident field is

only modulated by the axicon phase, so the amplitude distribution is a constant, as shown in the top-left of **Figure 2A**. From **Figure 2A**, we can observe that the maximum intensity deviates from the focal plane, although the radius of the POV is the same as designed.

Figure 2B shows the simulated results of the MFI method. It should be noted that the MFI method generates a complex field; thus, the incident field can be modulated by amplitude and phase. As shown in the top-left of **Figure 2B**, a Bessel amplitude can be generated by the MFI method. In the experiment, we used the complex field encoding method to obtain the phase-only patterns [54]. From **Figure 2B**, we can observe that the modulated field produced by the MFI method can lead to symmetrical intensity distribution in the focal region. In addition, the desired radius and the maximum intensity distribution of the POV are precisely located at the focal plane. Thus, the MFI method provides an alternative scheme to produce the POV in the tightly focused plane.

Based on the aforementioned calculation, we obtain the POV with the tunable parameter of radius and topological charges in the tightly focused system. Then, we take the superposition of two POVs calculated by the MFI method to obtain the spot array field and possess a controllable phase gradient. The number of spots and phase gradient periods depends on the topological charges of two POVs. To describe the character of the phase gradient of the spot array, we begin with the definition of topological charge. It is defined as a closed path integral of the gradient of the wavefield phase in the transverse plane [21]:

$$l = \frac{1}{2\pi}\oint_C \nabla\zeta(s)ds, \tag{12}$$

where $\zeta(\cdot)$, C, and ∇ are the wavefield phase, closed path around the phase singularity, and vector differential operator, respectively.

The superposition of two POVs can be considered as coaxial interference. Then, the phase of the array at any position on the annular region can be expressed as

$$\mathrm{Ph}_{Array}(\varphi) = mod\left[\mathrm{Ph}_{l_1}(\varphi)+\mathrm{Ph}_{l_2}(\varphi), 2\pi\right]. \tag{13}$$

Here, the $\mathrm{Ph}(\varphi)$ is the phase distribution in polar coordinate (R, φ) of the focal plane, and mod $[\mathrm{Ph}(\varphi),2\pi]$ denotes the remainder of the division of $\mathrm{Ph}(\varphi)$ by 2π. Then, the η can be calculated by

$$\eta = \frac{1}{2\pi}\oint_C \nabla\zeta_{Array}(s)ds. \tag{14}$$

In practice, the η can be calculated directly by

$$\eta = \begin{cases} \dfrac{l_1 + l_2}{2}, \mathrm{sgn}(l_1) = \mathrm{sgn}(l_2) \\ l_1 + l_2, \mathrm{sgn}(l_1) \neq \mathrm{sgn}(l_2) \end{cases}, \tag{15}$$

where sgn $(\cdot)$ is the signum function, and zero is considered a positive. In addition, the number of spots is γ, and it is calculated by

$$\gamma = abs(l_1 - l_2). \tag{16}$$

To generate the spot array field, we take the superposition method using two complex amplitudes of POVs; the transmission function for superposed POVs is

$$T_\gamma(x_0, y_0) = U_{l_1}(x_0, y_0) + U_{l_2}(x_0, y_0). \tag{17}$$

According to **Eq. 17**, the spot array field can be generated in the tightly focused plane using the MFI method. In **Figure 3A**, the

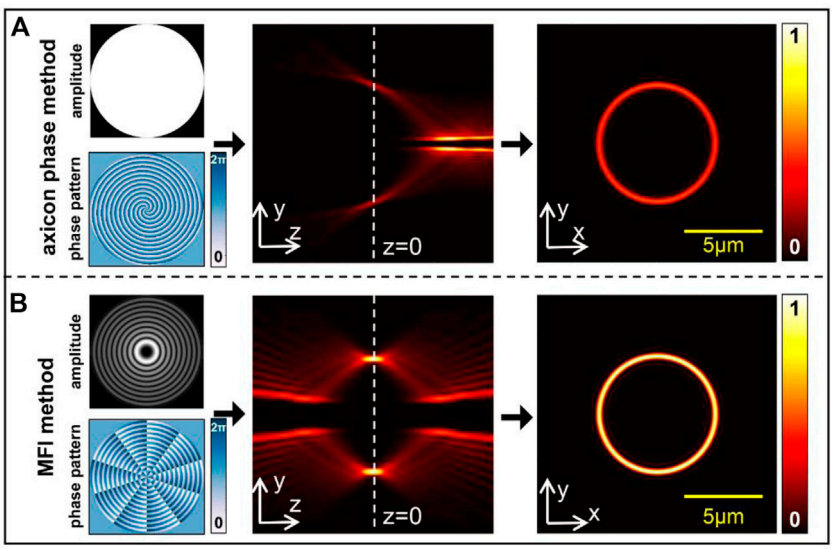

FIGURE 2 | Phase pattern, amplitude, and intensity distribution of generated POV by different methods. **(A)** Axicon phase method. **(B)** MFI method. Scale bar: 5 μm.

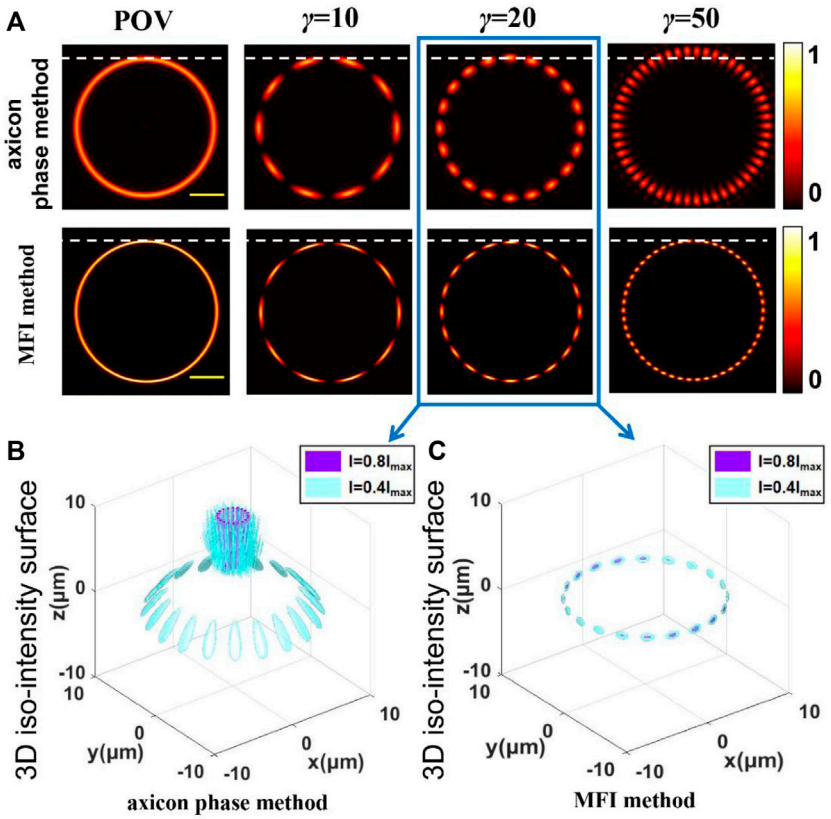

FIGURE 3 | (A) Simulated intensity distribution of POV and spot array field in the focal plane produced by the axicon phase method and MFI method. **(B,C)** Simulation result of the normalized 3D intensity distribution of 20 spots produced by different methods. Scale bar: 4 μm.

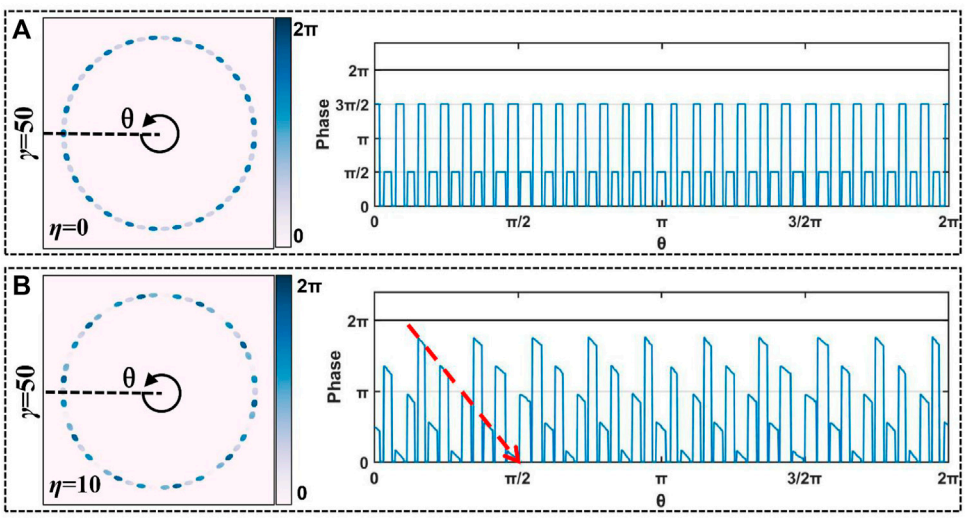

FIGURE 4 | Simulation results of decomposed phase distribution in 50 spots with different total phase gradient periods. **(A)** η = 0, **(B)** η = 10.

two methods show similar intensity distribution in the focal plane when there are fewer spots, but in the case of the beam having dozens of spots, the generated array *via* the axicon phase method is shown to be defocusing with inconstant radius. In contrast, the MFI method maintains the superior focusing property in all situations. In **Figures 3B,C**, the

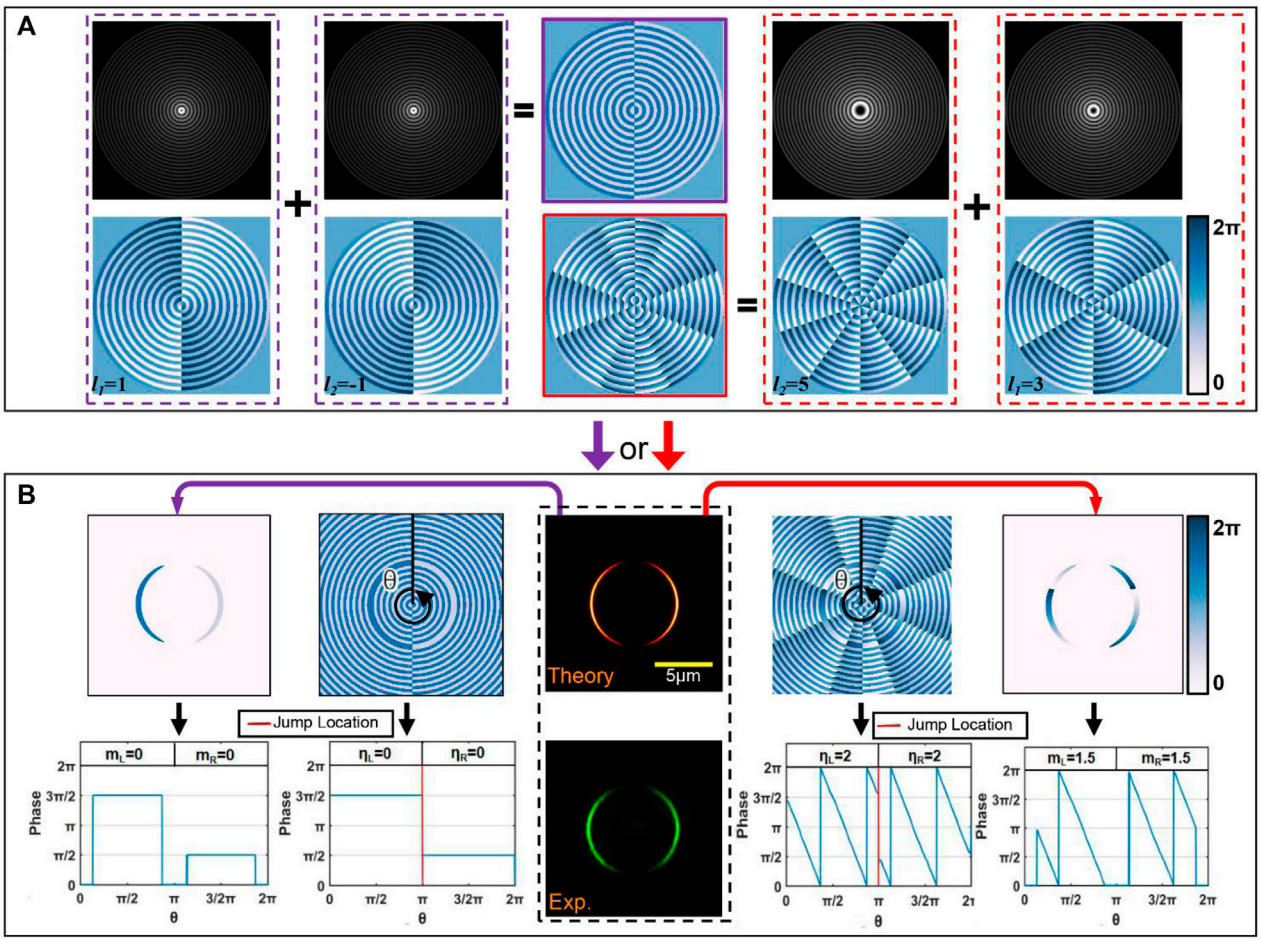

FIGURE 5 | (A) Superposition process diagram. **(B)** Corresponding intensity and phase distribution in the focal plane. Scale bar: 5 μm.

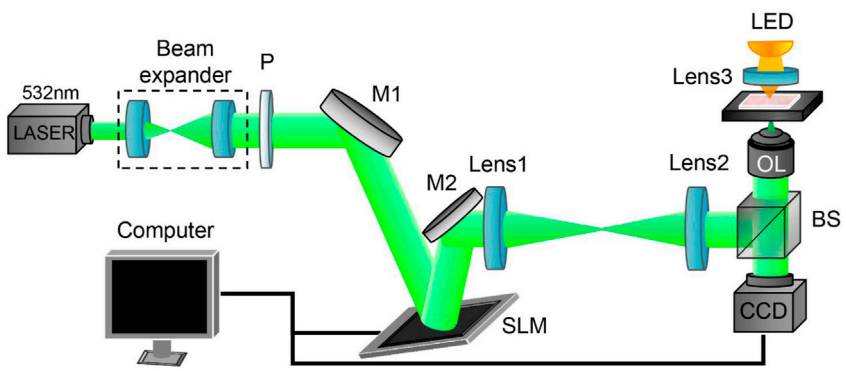

FIGURE 6 | Schematic of the experimental configuration. P: polarizer; BS: beam splitter; M: mirror; SLM: spatial light modulator; OL: objective lens.

normalized 3D intensity distribution of 20 spots produced by different methods demonstrates this problem more intuitively. As discussed previously, the issue of deviation caused by the axicon phase still exists, demonstrating that the axicon phase method is not suitable for generating high-order POVs, while the MFI method shows a splendid capability to maintain the focusing property in the tightly focused plane of the superimposed POVs.

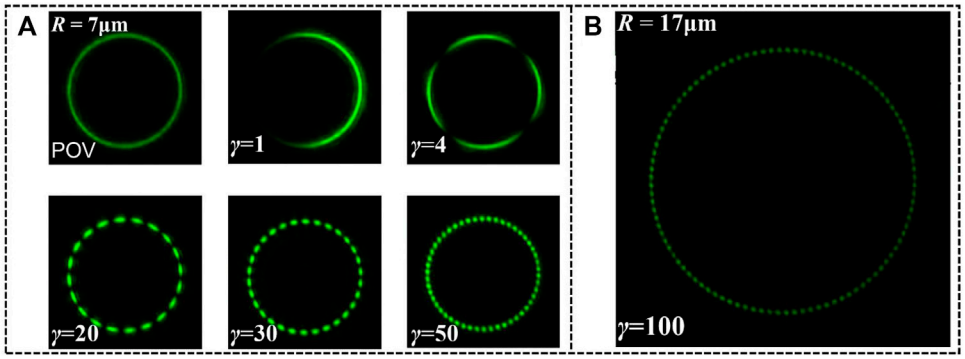

FIGURE 7 | (A) Experimental contrast of intensity distribution of POV and spot array. **(B)** Intensity distribution of high-order spot array with 100 spots.

Except that perfect focusing property in the tightly focused plane, the spot array field has a tunable phase gradient. We envision that the intensity gradient and phase gradient forces are competitive [55], that is, more spots lead to affect the orbital transport (driven by the phase gradient). In the case that $\eta < \gamma$ (meaning that the number of spots is greater than the total phase gradient periods), it will show the decomposition of phase gradient in the spot array field. As shown in **Figure 4A**, when $\eta = 0$ and $\gamma = 50$, the phase is decomposed to $3\pi/2$ and $\pi/2$, respectively. When the total periods of phase gradient $\eta = 10$ in **Figure 4B** ($l_1 = 30$ and $l_2 = -20$), each of the same phases of spots is repeated 10 times, and the 10 periods of $0\sim2\pi$ will be evenly decomposed into 50 spots. Each period occupies five spots, and they were mutually crosswise; the phase distribution cannot be continuous. However, the red dotted line in **Figure 4B** shows the phase continuity of five spots, even though one period of the phase gradient is decomposed. Such multiple spots with phase step profiles is more beneficial to capture particles.

In addition, when there are few spots in the array, they will have stripe-shaped profiles. Here, we demonstrate the diagram of the superposition method and take $\gamma = 2$ as an example. In **Figure 5A**, the figures with purple edges indicate that the topological charges of superposed POVs are $l_1 = 1$ and $l_2 = -1$, and the red edge figures mean $l_1 = 3$ and $l_2 = 5$. It shows that when $\eta > \gamma$, each stripe-shaped focus carries more than one phase gradient period. Moreover, the different phase gradients do not affect the intensity of the spot array. We define m to represent the phase gradient periods carried by the

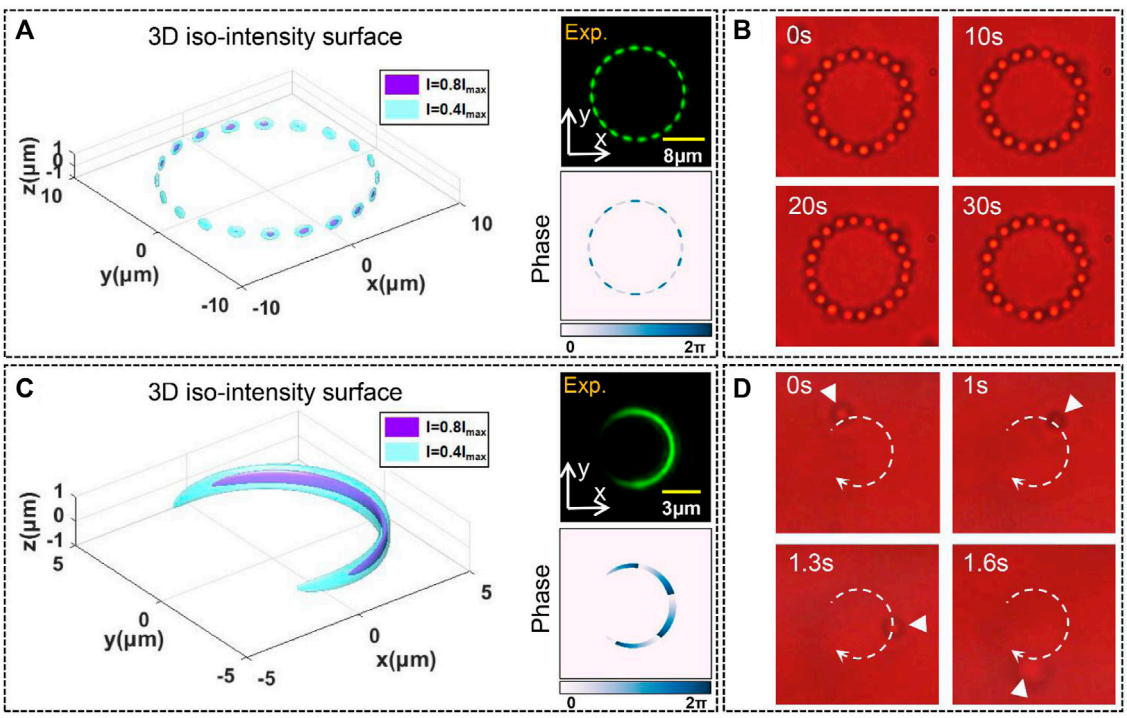

FIGURE 8 | (A,C) Intensity and phase distribution of spot array in the focal region. **(B,D)** Corresponding trapping snapshots.

spot array since the noncontinuous intensity distribution in the original annular region cannot carry the total topological charge. In **Figure 5B**, the intensity and phase distribution of the spot array are given; the first and second columns show the phase distribution corresponding to the procedure marked in purple, and the fourth and fifth columns correspond to the red-marked procedure. η_L, η_R, m_L, and m_R are the left and right half-section of η and m. The phase in some positions is not jumped from 0 to 2π but from 3π/2 to π/2; the phase jump location is marked by the red line in the line chart of **Figure 5B**. Due to the phase start location of two superposed POVs being in different azimuthal positions, the position difference is π (it also can explain the line chart in **Figure 4A**). To obtain the designed phase gradient of the spot array, appropriate topological charges should be chosen. From the competition of intensity- and phase-gradient forces, this has great significance for the arbitrary selection of phase-gradient forces to manipulate micro-objects on stripe-shaped spot fields.

EXPERIMENTAL RESULTS

We perform the optical imaging experiment with our homemade setup shown schematically in **Figure 6**. The beam with a wavelength of 532 nm (LWGL532, Beijing Laserwave Optoelectronics Technology Co., Ltd., China) is expanded and collimated onto a spatial light modulator (Pluto2-NIR-011, HOLOEYE Photonics AG, Germany) and then relayed to the back-aperture plane of a ×100 magnification, NA = 1.4 oil immersion objective (UPlanSApo ×100, Olympus, Japan), using a 4f filter system. The LED lighting source is used to illuminate the microparticle-trapping plane. A CCD (EO-5012, Edmund Optics, US) camera is utilized to record the images of the focal spots and the trapping particles.

The spot array field produced by the superposition of two POVs maintains the focusing property in the tightly focused plane as the spot number increases, as shown in **Figure 7A**. It has an application value to improve the efficiency of optical imaging, micromanipulation, direct laser writing, etc. In **Figure 7B**, we produced 100 spots, and l_1 and l_2 were chosen to be ±50 (the maximum spot number $\gamma_{\max}$ is limited by the radius of the array, see **Supplementary Material**). The experimental results substantiate that the high order spot array can be achieved and observed (here, the order of spot array is equal to the spot number). It is one particular advantage of the spot array based on the MFI method.

A spot array field carrying arbitrary orbital angular momentum should have the capability to manipulate the microparticle. In the following optical trapping experiment, silica beads with a diameter of 1 μm, dispersed in deionized water within a glass chamber (100 μm thickness), are applied as the sample for trapping. As shown in **Figure 8A**, we can observe the intensity and phase distribution of the spot array with 20 spots (R = 8μm, η = 0, topological charges of superposed POVs l_1 = 10 and l_2 = −10) in the focal plane. This spot array field with multi-spot intensity distribution could capture the particles steadily; the corresponding experiment snapshots are shown in **Figure 8B**.

As the spot number decreases, the phase gradient force could contribute more to the time-averaged optical force acting on a particle. The field with one spot (R = 3μm, η = 5.5, m = 4, l_1 = 6 and l_2 = 4) is chosen to achieve the orbital transportation; the intensity and phase distribution in the focal region are shown in **Figure 8C**. The snapshots of the experiment in **Figure 8D** show that one silica particle was moving along the orbital-shaped spot, which was then released rapidly (see Video 2). This unique orbital-shaped spot may have a significant contribution to the application of particle sorting [56, 57]and optical storage [58, 59]. Moreover, more types of spot array beams with different parameters were used to investigate the effects of different experimental parameters on trapping (for more experimental details, see **Supplementary Material**). The stabilization and dynamic manipulation in the tightly focused plane indicate that the spot array field has independent controllable multiple parameters with radius, number of spots, and phase gradient, greatly expanding the degree of freedom of focusing vortex beams.

DISCUSSION

In this study, we have presented and demonstrated the MFI method for generating POV in the focal plane of tightly focused systems. By creating a finite number of diffraction limit foci at the focal plane, we formed the annular ring with arbitrary radius and combined the helical phase to construct a POV. Subsequently, we took the superposition procedure of two POVs and created a spot array in the focal plane. The independent multiple parameters of spot arrays include radius, number of spots, and distribution of phase gradient. In particular, in the superposition of high-order beams, we also produced a 100-order array, which has no deviation and maintains a clear profile in the focal region. In the further trapping experiment, the behavior of trapped particles showed that the spot array has more “perfect” focusing properties than the traditional superposed Bessel beams. Such a complicated vortex beam with a dynamically controlled structure and phase gradient providing a novel optical field deepened the research into the orbital angular momentum communication, fast femtosecond two-photon polymerization, micromanipulation, and optical momentum measurement.

DATA AVAILABILITY STATEMENT

The original contributions presented in the study are included in the article/**Supplementary Material**, further inquiries can be directed to the corresponding authors.

AUTHOR CONTRIBUTIONS

MS, QS, and XJ contributed to conception and design of the study. XJ and LZ organized the database. XJ and YT performed

the experiment. XJ wrote the first draft of the manuscript. ZL, DZ, and KC gave suggestions in numerical simulations. All authors contributed to the revision of the manuscript and approved the final version.

FUNDING

This work was supported by the National Natural Science Foundation of China (62174073 and 61675093), the Key Research and Development Project of Shandong Province (2019JZZY020219), and the Program of Science and Technology Development of Yantai (2020XDRH095).

SUPPLEMENTARY MATERIAL

The Supplementary Material for this article can be found online at: https://www.frontiersin.org/articles/10.3389/fphy.2022.879689/full#supplementary-material

REFERENCES

1. Allen L., Beijersbergen M. W., Spreeuw R. J. C., Woerdman J. P. Orbital Angular Momentum of Light and the Transformation of Laguerre-Gaussian Laser Modes. *Phys Rev A* (1992) 45(11):8185–8189. doi:10.1103/physreva.45.8185
2. Roichman Y., Sun B., Roichman Y., Amato-Grill J., Grier D. G. Optical Forces Arising from Phase Gradients. *Phys Rev Lett* (2008) 100(1):013602. doi:10.1103/PhysRevLett.100.013602
3. Dennis M. R., O'Holleran K., Padgett M. J. Chapter 5 Singular Optics: Optical Vortices and Polarization Singularities. *Progress Opt* (2009) 53, 293–363. doi:10.1016/s0079-6638(08)00205-9
4. Gibson G., Courtial J., Padgett M. J., Vasnetsov M., Pas'ko V., Barnett S. M, et al. Free-Space Information Transfer Using Light Beams Carrying Orbital Angular Momentum. *Opt Express* (2004) 12(22):5448–56. doi:10.1364/OPEX.12.005448
5. Kotlyar V. V., Kovalev A. A., Porfirev A. P. An Optical Tweezer in Asymmetrical Vortex Bessel-Gaussian Beams. *J Appl Phys* (2016) 120(2):023101. doi:10.1063/1.4958309
6. Chen M, Mazilu M, Arita Y, Wright EM, Dholakia K. Optical Trapping with a Perfect Vortex Beam. In: Proceedings of SPIE - The International Society for Optical Engineering (2014). doi:10.1117/12.2064080
7. Chen M., Mazilu M., Arita Y., Wright E. M., Dholakia K. Creating and Probing of a Perfect Vortex *In Situ* with an Optically Trapped Particle. *Opt Rev* (2015) 22(1):162–165. doi:10.1007/s10043-015-0031-7
8. Chen M., Mazilu M., Arita Y., Wright E. M., Dholakia K. Dynamics of Microparticles Trapped in a Perfect Vortex Beam *Opt Lett* (2013) 38(22):4919–22. doi:10.1364/OL.38.004919
9. Ni J., Wang C., Zhang C., Hu Y., Yang L., Lao Z, et al. Three-Dimensional Chiral Microstructures Fabricated by Structured Optical Vortices in Isotropic Material. *Light Sci Appl* (2017) 6(7):e17011. doi:10.1038/lsa.2017.11
10. Yang L., Chen X., Wang L., Hu Z., Xin C., Hippler M, et al. Targeted Single-Cell Therapeutics with Magnetic Tubular Micromotor by One-Step Exposure of Structured Femtosecond Optical Vortices. *Adv Funct Mater* (2019) 29(45):1905745. doi:10.1002/adfm.201905745
11. Yang L., Qian D., Xin C., Hu Z., Ji S., Wu D, et al. Direct Laser Writing of Complex Microtubes Using Femtosecond Vortex Beams. *Appl Phys Lett* (2017) 110(22):221103. doi:10.1063/1.4984744
12. Hu Z-Y., Tian Z-N., Hua J-G., Chen Q-D., Sun H-B. Axially Controllable Multiple Orbital Angular Momentum Beam Generator. *Appl Phys Lett* (2020) 117(2):021101. doi:10.1063/5.0011445
13. Qin F., Liu B., Zhu L., Lei J., Fang W., Hu D, et al. π-Phase Modulated Monolayer Supercritical Lens. *Nat Commun* (2021) 12(1):32. doi:10.1038/s41467-020-20278-x
14. Jiang M., Song S., Li Y., Zeng X., Zhu L., Zhang M, et al. 3d High Precision Laser Printing of a Flat Nanofocalizer for Subwavelength Light Spot Array. *Opt Lett* (2021) 46(2):356–9. doi:10.1364/OL.413302
15. Zhu L., Yu J., Zhang D., Sun M., Chen J. Multifocal Spot Array Generated by Fractional Talbot Effect Phase-Only Modulation. *Opt Express* (2014) 22(8):9798–808. doi:10.1364/OE.22.009798
16. Zhu L., Sun M., Zhu M., Chen J., Gao X., Ma W, et al. Three-Dimensional Shape-Controllable Focal Spot Array Created by Focusing Vortex Beams Modulated by Multi-Value Pure-phase Grating. *Opt Express* (2014) 22(18):21354–67. doi:10.1364/oe.22.021354
17. Zhu L., Sun M., Zhang D., Yu J., Wen J., Chen J. Multifocal Array with Controllable Polarization in Each Focal Spot. *Opt Express* (2015) 23(19):24688–98. doi:10.1364/oe.23.024688
18. Yu J., Zhou C., Jia W., Hu A., Cao W., Wu J, et al. Three-Dimensional Dammann Vortex Array with Tunable Topological Charge. *Appl Opt* (2012) 51(13):2485. doi:10.1364/AO.51.002485
19. Yu J., Zhou C., Lu Y., Wu J., Zhu L., Jia W. Square Lattices of Quasi-Perfect Optical Vortices Generated by Two-Dimensional Encoding Continuous-phase Gratings. *Opt Lett* (2015) 40(11):2513–6. doi:10.1364/OL.40.002513
20. Li X., Ma H., Yin C., Tang J., Li H., Tang M, et al. Controllable Mode Transformation in Perfect Optical Vortices. *Opt Express* (2018) 26(2):651–62. doi:10.1364/OE.26.000651
21. Ma H., Li X., Zhang H., Tang J., Li H., Tang M, et al. Optical Vortex Shaping via a Phase Jump Factor. *Opt Lett* (2019) 44(6):1379–82. doi:10.1364/OL.44.001379
22. Zhang H., Li X., Ma H., Tang M., Li H., Tang J, et al. Grafted Optical Vortex with Controllable Orbital Angular Momentum Distribution. *Opt Express* (2019) 27(16):22930–8. doi:10.1364/OE.27.022930
23. Ostrovsky A. S., Rickenstorff-Parrao C., Arrizón V. Generation of the "Perfect" Optical Vortex Using a Liquid-Crystal Spatial Light Modulator. *Opt Lett* (2013) 38(4):534–6. doi:10.1364/OL.38.000534
24. Andrews DL, Roichman Y, Galvez EJ, Grier DG, Nienhuis G. Three-Dimensional Holographic Ring Traps. Complex Light and Optical Forces. In: Proceedings of SPIE - The International Society for Optical Engineering (2007). doi:10.1117/12.701034
25. Vaity P., Rusch L. Perfect Vortex Beam: Fourier Transformation of a Bessel Beam. *Opt Lett* (2015) 40(4):597–600. doi:10.1364/OL.40.000597
26. Chen Y., Fang Z-X., Ren Y-X., Gong L., Lu R-D. Generation and Characterization of a Perfect Vortex Beam with a Large Topological Charge through a Digital Micromirror Device. *Appl Opt* (2015) 54(27):8030–5. doi:10.1364/AO.54.008030
27. Liu X., Li Y., Han Y., Deng D., Zhu D. High Order Perfect Optical Vortex Shaping. *Opt Commun* (2019) 435:93–96. doi:10.1016/j.optcom.2018.11.029
28. Chen Y., Wang J., Wang C., Zhang S., Cao M., Franke-Arnold S, et al. Phase Gradient Protection of Stored Spatially Multimode Perfect Optical Vortex Beams in a Diffused Rubidium Vapor. *Opt Express* (2021) 29(20):31582–93. doi:10.1364/OE.439716
29. Zheng S., Wang J. Measuring Orbital Angular Momentum (Oam) States of Vortex Beams with Annular Gratings. *Sci Rep* (2017) 7:40781. doi:10.1038/srep40781
30. Xie G., Song H., Zhao Z., Milione G., Ren Y., Liu C, et al. Using a Complex Optical Orbital-Angular-Momentum Spectrum to Measure Object Parameters. *Opt Lett* (2017) 42(21):4482–5. doi:10.1364/OL.42.004482
31. Litvin I. A., Dudley A., Forbes A. Poynting Vector and Orbital Angular Momentum Density of Superpositions of Bessel Beams. *Opt Express* (2011) 19(18):16760–71. doi:10.1364/OE.19.016760
32. Vasilyeu R., Dudley A., Khilo N., Forbes A. Generating Superpositions of Higher-Order Bessel Beams. *Opt Express* (2009) 17(26):23389–95. doi:10.1364/OE.17.023389
33. Yang L., Qian D., Xin C., Hu Z., Ji S., Wu D, et al. Two-Photon Polymerization of Microstructures by a Non-diffraction Multifoci Pattern Generated from a

Superposed Bessel Beam. *Opt Lett* (2017) 42(4):743–6. doi:10.1364/OL.42.000743
34. Khonina S. N., Kazanskiy N. L., Khorin P. A., Butt M. A. Modern Types of Axicons: New Functions and Applications. *Sensors* (2021) 21(19):6690. doi:10.3390/s21196690
35. Jaroszewicz Z, Burvall A, Friberg AT. Axicon - the Most Important Optical Element. *Opt Photon News* (2005) 16(4). doi:10.1364/opn.16.4.000034
36. Mcleod JH. The Axicon : A New Type of Optical Element. *J Opt Soc Am* (1954) 44. doi:10.1364/josa.44.000592
37. Khonina S. N., Porfirev A. P. 3d Transformations of Light Fields in the Focal Region Implemented by Diffractive Axicons. *Appl Phys B* (2018) 124(9). doi:10.1007/s00340-018-7060-4
38. Khonina S. N., Kazanskiĭ N. L., Ustinov A. V., Volotovskiĭ S. G. The Lensacon: Nonparaxial Effects. *J Opt Technol* (2011) 78(11):724–9. doi:10.1364/JOT.78.000724
39. Khonina S. N., Kotlyar V. V., Skidanov R. V., Soifer V. A., Jefimovs K., Simonen J, et al. Rotation of Microparticles with Bessel Beams Generated by Diffractive Elements. *J Mod Opt* (2004) 51(14):2167–2184. doi:10.1080/09500340408232521
40. Vasara A., Turunen J., Friberg A. T. Realization of General Nondiffracting Beams with Computer-Generated Holograms. *J Opt Soc Am A* (1989) 6(11):1748–54. doi:10.1364/josaa.6.001748
41. Jiménez-Gambín S., Jiménez N., Benlloch J. M., Camarena F. Generating Bessel Beams with Broad Depth-Of-Field by Using Phase-Only Acoustic Holograms. *Sci Rep* (2019) 9(1):20104. doi:10.1038/s41598-019-56369-z
42. Khonina S, Kotlyar V. *Bessel-Mode Formers*. SPIE (1995).
43. McGloin D., Dholakia K. Bessel Beams: Diffraction in a New Light. *Contemp Phys* (2005) 46(1):15–28. doi:10.1080/0010751042000275259
44. López-Aguayo S., Kartashov Y. V., Vysloukh V. A., Torner L. Method to Generate Complex Quasinondiffracting Optical Lattices. *Phys Rev Lett* (2010) 105(1):013902. doi:10.1103/PhysRevLett.105.013902
45. Durnin J. Exact Solutions for Nondiffracting Beams I the Scalar Theory. *J Opt Soc Am A* (1987) 4(4):651–4. doi:10.1364/josaa.4.000651
46. Topuzoski S. Generation of Optical Vortices with Curved Fork-Shaped Holograms. *Opt Quant Electron* (2016) 48(2). doi:10.1007/s11082-016-0405-5
47. Khonina S. N., Ustinov A. V., Kirilenko M. S., Kuchmizhak A. A., Porfirev A. P. Application of a Binary Curved Fork Grating for the Generation and Detection of Optical Vortices outside the Focal Plane. *J Opt Soc Am B* (2020) 37(6):1714–21. doi:10.1364/josab.388431
48. Zhang C., Hu Y., Li J., Li G., Chu J., Huang W. A Rapid Two-Photon Fabrication of Tube Array Using an Annular Fresnel Lens. *Opt Express* (2014) 22(4):3983–90. doi:10.1364/OE.22.003983
49. Descour M. R., Simon D. I., Yeh W-H. Ring-Toric Lens for Focus-Error Sensing in Optical Data Storage. *Appl Opt* (1999) 38(8):1388–92. doi:10.1364/ao.38.001388
50. Khonina S. N., Kharitonov S. I., Volotovskiy S. G., Soifer V. A. Caustics of Non-paraxial Perfect Optical Vortices Generated by Toroidal Vortex Lenses. *Photonics* (2021) 8(7):259. doi:10.3390/photonics8070259
51. Kotlyar V. V., Kovalev A. A., Porfirev A. P. Optimal Phase Element for Generating a Perfect Optical Vortex. *J Opt Soc Am A* (2016) 33(12):2376–84. doi:10.1364/JOSAA.33.002376
52. Richards B, Wolf E. Electromagnetic Diffraction in Optical Systems. Ii. Structure of the Image Field in an Aplanatic System. *Proc R Soc, Ser A* (1959) 253:358–79.
53. Zhu L., Yang R., Zhang D., Yu J., Chen J. Dynamic Three-Dimensional Multifocal Spots in High Numerical-Aperture Objectives. *Opt Express* (2017) 25(20):24756–66. doi:10.1364/OE.25.024756
54. Mendoza-Yero O., Mínguez-Vega G., Lancis J. Encoding Complex Fields by Using a Phase-Only Optical Element. *Opt Lett* (2014) 39(7):1740–3. doi:10.1364/ol.39.001740
55. Nan F., Yan Z. Synergy of Intensity, Phase, and Polarization Enables Versatile Optical Nanomanipulation. *Nano Lett* (2020) 20(4):2778–2783. doi:10.1021/acs.nanolett.0c00443
56. Wu W., Zhu X., Zuo Y., Liang L., Zhang S., Zhang X, et al. Precise Sorting of Gold Nanoparticles in a Flowing System. *ACS Photon* (2016) 3(12):2497–2504. doi:10.1021/acsphotonics.6b00737
57. Nan F., Yan Z. Optical Sorting at the Single-Particle Level with Single-Nanometer Precision Using Coordinated Intensity and Phase Gradient Forces. *ACS Nano* (2020) 14(6):7602–7609. doi:10.1021/acsnano.0c03478
58. Zhu L., Cao Y, Cao Y., Chen Q., Ouyang X., Xu Y, et al. Near-Perfect Fidelity Polarization-Encoded Multilayer Optical Data Storage Based on Aligned Gold Nanorods. *Oea* (2021) 4(11):210002. doi:10.29026/oea.2021.210002
59. Ouyang X., Xu Y., Xian M., Feng Z., Zhu L., Cao Y, et al. Synthetic Helical Dichroism for Six-Dimensional Optical Orbital Angular Momentum Multiplexing. *Nat Photon* (2021) 15(12):901–907. doi:10.1038/s41566-021-00880-1

Conflict of Interest: QS was employed by Yantai Magie Nano-Technology Co. Ltd.

The remaining authors declare that the research was conducted in the absence of any commercial or financial relationships that could be construed as a potential conflict of interest.

frontiers | Frontiers in Physics

BRIEF RESEARCH REPORT
published: 27 June 2022
doi: 10.3389/fphy.2022.951516

Generation of the Anomalous Vortex Beam by Spiral Axicon Implemented on Spatial Light Modulator

Xiaoting Huang, Zehong Chang, Yuanyuan Zhao, Yunlong Wang, Xindong Zhu and Pei Zhang**

Ministry of Education Key Laboratory for Nonequilibrium Synthesis and Modulation of Condensed Matter, Shaanxi Province Key Laboratory of Quantum Information and Quantum Optoelectronic Devices, School of Physics, Xi'an Jiaotong University, Xi'an, China

The anomalous vortex beam (AVB), whose paraxial local topological charge varies with propagation, has potential applications in quantum information, laser beam shaping, and other fields. However, there are currently no efficient optical devices to generate AVBs. In this paper, we propose an efficient pure-phase device called spiral axicons. We theoretically analyze the spiral axicon, and then experimentally verify its performance by implementing a spiral axicon on spatial light modulator. Our work provides an alternative method for generating AVB, which will facilitate its application in different fields.

Keywords: vortex beam, orbital angular momentum, axicon, structured beam, beam shaping

OPEN ACCESS

Edited by:
Yangjian Cai,
Soochow University, China

Reviewed by:
Yuanjie Yang,
University of Electronic Science and Technology of China, China
Chenghou Tu,
Nankai University, China
Chengliang Zhao,
Soochow University, China

****Correspondence:***
Xindong Zhu
xdzhu0@xjtu.edu.cn
Pei Zhang
zhangpei@mail.ustc.edu.cn

Specialty section:
This article was submitted to Optics and Photonics, a section of the journal Frontiers in Physics

Received: *24 May 2022*
Accepted: *31 May 2022*
Published: *27 June 2022*

Citation:
Huang X, Chang Z, Zhao Y, Wang Y, Zhu X and Zhang P (2022) Generation of the Anomalous Vortex Beam by Spiral Axicon Implemented on Spatial Light Modulator. Front. Phys. 10:951516. doi: 10.3389/fphy.2022.951516

1 INTRODUCTION

An axicon refers to a cone-shaped optical element with central rotational symmetry. It was first proposed to generate a Bessel beam with quasi-non-diffraction properties [1–4]. Due to its excellent properties, it is widely used in optical shaping [5], laser capture [6] and other fields [7, 8].

The vortex beam refers to the beam with the phase factor $e^{il\phi}$, and carries $l\hbar$ orbital angular momentum per photon [9]. Here ϕ is the azimuthal angle and l is the topological charge. The vortex beam has been extensively studied over the past 30 years [10–17], and has significant applications in optical communications [18–20], optical micro-manipulation [21, 22], optical trapping [23, 24], and so on. The most common vortex beams, such as Laguerre Gaussian beams [25–27], Bessel Gaussian beams [28–30] and perfect optical vortex beams [31–33], have fixed paraxial local topological charge (PLTC) during propagation.

Different from the above vortex beams, the PLTC of the AVB can vary with propagation. Therefore, this beam has unique advantages in many fields including optical shaping, optical communications, and optical micro-manipulation [5, 20, 22]. Research on AVBs started late thus the method generated AVBs efficiently is still lacking. Recently, many efforts have been made on the AVB [34–39]. Dorrah et al. [34] used nondiffracting frozen waves to control the sign and value of the PLTC of the beam along the propagation direction. But the method can only non-continuously change the PLTC of the beam in integer orders. Moreover, using a spiral slit to generate a vortex beam whose PLTC continuously decreases with propagation has also been proposed [36]. Since only the beam that passes through the spiral slit can be utilized, the generation efficiency is low. The lack of efficient methods to generate the AVB limits its applications.

In this paper, we propose an efficient pure-phase device called spiral axicons to generate AVBs. First, we introduce the structure and principle. Then we verify that spiral axicon can efficiently

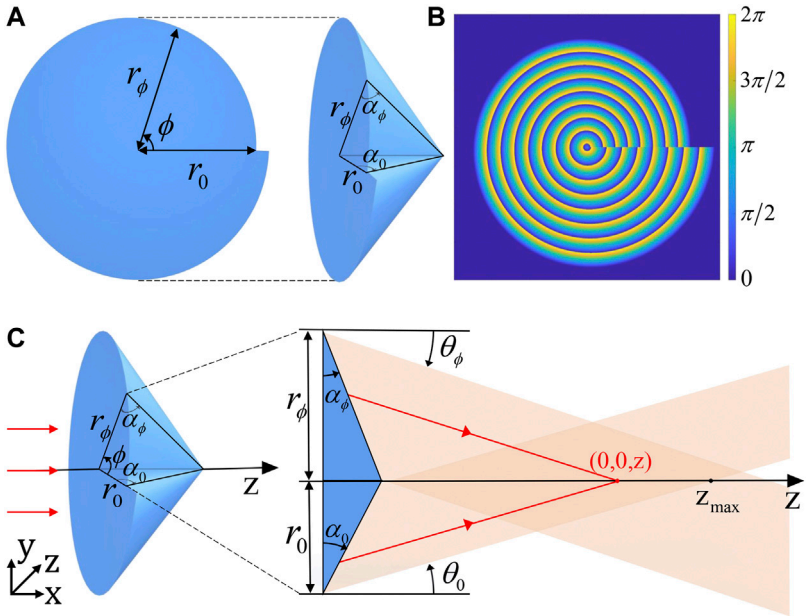

FIGURE 1 | (A) Schematic diagram of the spiral axicon: it has a spiral bottom and a fixed central height, and a clearer structure is shown in the supplementary material; **(B)** phase diagram of the spiral axicon; **(C)** analysis diagram of beam propagation through spiral axicon.

generate AVBs whose PLTC varies linearly and continuously with propagation both in simulations and experiments. Furthermore, we analyze how the generated AVB changes when the parameters of the spiral axicon are changed.

2 SPIRAL AXICON

The mathematical form of the Bessel beam can be explained as the superposition of plane waves, and the wave vectors of these plane waves are distributed on a cone. Therefore, Graeme Scott et al. [2] realized the efficient generation of Bessel beams through an axicon for the first time. However, the Bessel beam generated by the axicon does not have the property that the PLTC varies with propagation. Inspired by Yang et al. [36], they turned a circular slit that generates a Bessel beam into a spiral slit to generate an anomalous Bessel beam, we propose the spiral axicon to effectively generate the AVB. The AVB in cylindrical coordinate can be expressed as:

$$E(r,\phi,z) = E_0 e^{il\phi}, \tag{1}$$

$$l = \mathrm{C}\frac{z}{\lambda}, \tag{2}$$

where r is used to refer to the radial coordinates and ϕ to the azimuthal coordinates. E_0 is the amplitude, and l is the PLTC, λ is the wavelength. **Eq. 2** indicates that for a certain wavelength, the l increases linearly with the increase of propagation distance z, and C is the device parameter that determines the l variation. In addition, spiral axicon responds differently to beams of different wavelengths. At the same propagation distance, the longer the wavelength, the smaller the PLTC of the generated AVB.

We theoretically analyze how spiral axicon generates the AVB. The structure of the spiral axicon is first described. As shown in **Figure 1A**, the spiral axicon has a spiral bottom and a fixed central height. On the spiral bottom surface, r_0 is the initial radius at azimuthal coordinate $\phi = 0^\circ$ and r_ϕ is the radius at any angle ϕ. In the spiral axicon, α_0 is the initial base angle at $\phi = 0^\circ$ and α_ϕ is the base angle at ϕ. To convey the structure more clearly, a video is also provided as supplementary material. And **Figure 1B** shows the phase diagram of the spiral axicon. The fixed center height is $r_0 \tan\alpha_0$, so that the spiral bottom surface radius can be expressed as

$$r_\phi = \frac{r_0 \tan\alpha_0}{\tan\alpha_\phi}. \tag{3}$$

As long as the base angle α_ϕ is calculated, the structure of the spiral axicon can be determined. The α_ϕ is obtained by calculating the propagation of the plane wave through the spiral axicon to generate the AVB.

As shown in **Figure 1C**, we analyze the propagation by geometrical optics. Based on the propagation law of the axicon, the angle of refraction after passing through the axicon is $\theta = (n-1)\alpha$ for a given base angle α, where n is the refractive index of the axicon. The maximum non-diffraction distance $z_{\max} = r/(n-1)\alpha$, where r is the radius of the axicon. Thus, in the spiral axicon, the angle of refraction can be described as

$$\theta_\phi = (n-1)\alpha_\phi, \tag{4}$$

where n is the refractive index of the spiral axicon. The maximum effective propagation distance can be obtained as

$$z_{\max} = \frac{\min(r_\phi)}{(n-1)\max(\alpha_\phi)}. \tag{5}$$

The spiral axicon lies in the plane $z = 0$, and a plane wave passes through the spiral axicon as incident light. At any observation plane z, the optical path in the small neighborhood (Δr, ϕ, z) of the center of the plane is $z/\cos\theta_\phi$, where Δr tends to zero. Therefore, the optical path difference between (Δr, ϕ, z) and (Δr, 0, z) can be calculated as

$$\int_0^\phi \frac{z}{\cos\theta_{\phi+\Delta\phi}} - \frac{z}{\cos\theta_\phi} d\phi = \frac{z}{\cos\theta_\phi} - \frac{z}{\cos\theta_0}. \tag{6}$$

The optical path difference can be written as $l\lambda$, where l is a constant for the determined propagation position z. The phase change of the vortex beam along with the azimuthal coordinates ϕ should be uniform, so we can obtain

$$\frac{z}{\cos\theta_\phi} - \frac{z}{\cos\theta_0} = \frac{\phi}{2\pi} l\lambda, \tag{7}$$

when $\phi = 2\pi$, the optical path difference of one circle change in azimuthal coordinates is $l\lambda$ with the phase change $2\pi l$. Thus an AVB, whose PLTC l related to the propagation distance z, is generated in the paraxial region.

Based on the above analysis, bring **Eq. 2** and **Eq. 4** into **Eq. 7** can obtain

$$\alpha_\phi = \frac{1}{n-1}\arccos\frac{2\pi\cos(n-1)\alpha_0}{2\pi + C\phi\cos(n-1)\alpha_0}, \tag{8}$$

the structure of the spiral axicon is determined. Its three-dimensional structure can be clearly expressed by the sag:

$$H(r,\phi) = \begin{cases} (r_\phi - r)\tan\alpha_\phi & (0 \le r \le r_\phi) \\ 0 & (r > r_\phi) \end{cases}, \tag{9}$$

where

$$r_\phi = \frac{r_0\tan\alpha_0}{\tan\alpha_\phi}, \alpha_\phi = \frac{1}{n-1}\arccos\frac{2\pi\cos(n-1)\alpha_0}{2\pi + C\phi\cos(n-1)\alpha_0}.$$

To give the simulation results, diffraction theory is used to calculate the propagation of a plane wave through a spiral axicon. Under paraxial approximation, the complex amplitude of the beam at z can be calculated through the Huygens-Fresnel diffraction integral:

$$E(r',\phi',z) = \frac{e^{ikz}}{i\lambda z} e^{i\frac{k}{2z}r'^2} \int_0^\infty \int_0^{2\pi} T(r,\phi) e^{i\frac{k}{2z}r^2} e^{i\frac{k}{z}r'r\cos(\phi-\phi')} r dr d\phi, \tag{10}$$

where r', ϕ' are expressed as the radial coordinates and azimuthal coordinates on the observation plane respectively. $k = 2\pi/\lambda$ is the wave vector. $T(r, \phi)$ is the transmission function of the spiral axicon, for the thin spiral axicon:

$$T(r,\phi) = \begin{cases} \exp(-ik(n-1)r\alpha_\phi) & (0 \le r \le r_\phi) \\ 0 & (r > r_\phi) \end{cases}. \tag{11}$$

3 EXPERIMENTS AND RESULTS

We conduct a proof-of-principle experimental demonstration following the above analysis. The experimental setup is shown in **Figure 2**. The laser source is a He-Ne laser running at 632.8 nm. The Gaussian beam from the laser passes through a half-wave plate (HWP) and a polarized beam splitter (PBS), which are used to adjust the intensity of the beam to avoid overexposure during measurement. The beam then passes through a 4f system composed of lens pair L1 (f_1 = 100 mm) and L2 (f_2 = 500 mm) for beam expansion. The expanded beam has a beam radius of 5 mm, which can cover the screen of a reflective liquid crystal pure phase spatial light modulator (SLM, UPOLabs, HDSLM80 R). The inset shows the phase holograms of the spiral axicon loaded on the SLM. Due to the reflectivity of the SLM, the PLTC of the experimentally generated AVB is opposite to that transmitted in the theoretical analysis. A CMOS camera (Basler ace acA4112-20 μm, 4,096 × 3,000 pixels, pixel size of 3.45 μm × 3.45 μm) is used to detect modulated beams at different distances, and the detecting distance is calculated from the position of the SLM. We measure the phase of the vortex beam by the interference method mentioned in Ref. [40], the signal light interferes with four reference plane waves $Ae^{is\pi/2}$ (where A is the amplitude, s = 1, 2, 3, 4). The reference beam is also loaded on the SLM, so the SLM is loaded with the phase hologram calculated by $T(r, \phi) + Ae^{is\pi/2}$. The phase-shifted interferogram is obtained by changing the phase of the interference beam. Therefore, the phase of the signal light is

$$\varphi(r',\phi') = \arg\left(\sum_{s=1}^{4} Ae^{is\pi/2} I_s\right), \tag{12}$$

where I_s the interferograms measured.

The experimental parameters of the spiral axicon are set to α_0 = 0.2°, r_0 = 6 mm, C/632.8 nm = 2 m^{-1}, n = 1.5, λ = 632.8 nm. In the experiments, only the region with a radius of 3 mm in the middle of the spiral axicon is used, so the maximum effective propagation distance of the beam is

$$z_{\max} = \frac{0.003}{(n-1)\max(\alpha_\phi)} = 1.71 \text{ m}. \tag{13}$$

Figure 3 shows the intensity and phase patterns at different propagation distances z. The PLTC increases linearly with propagation, and the intensity of the fractional-order beam does not exhibit rotational symmetry. According to **Eq. 2**, it can be calculated that $l/z = C/\lambda$ = 2 m^{-1}, so within the effective propagation distance, the absolute value of the topological charge is twice the propagation distance under the International System of Units. When the propagation distance increases from 0.5 m to 1.5 m, the absolute value of the topological load of the AVB also increases from 1 to 3. The plane wave passing through the clockwise spiral axicons should generate an AVB with a positive topological charge, and the negative topological charge is due to the SLM caused by

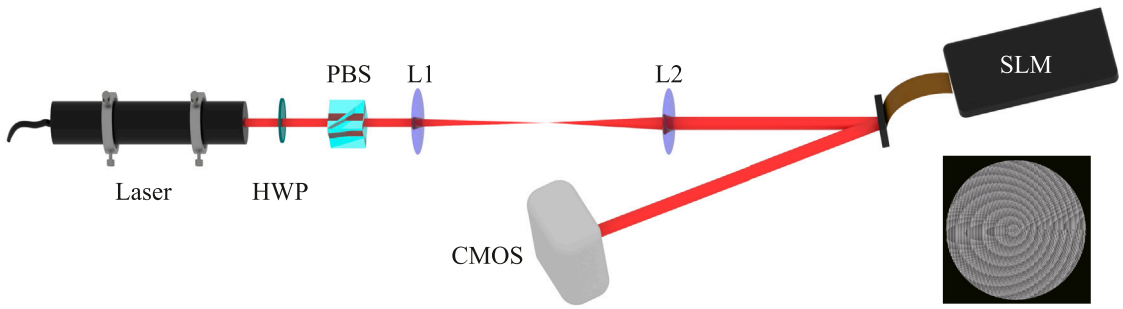

FIGURE 2 | Schematic of the experimental setup. The inset is the phase hologram of the spiral axicon loaded on the SLM. HWP, half-wave plate; PBS, polarized beam splitter; L, Lens; SLM, spatial light modulator. HWP, PBS, L1, and L2 are used to control the intensity and radius of the beam. The SLM implements a spiral axicon to produce the AVB. The CMOS detects the generated AVB.

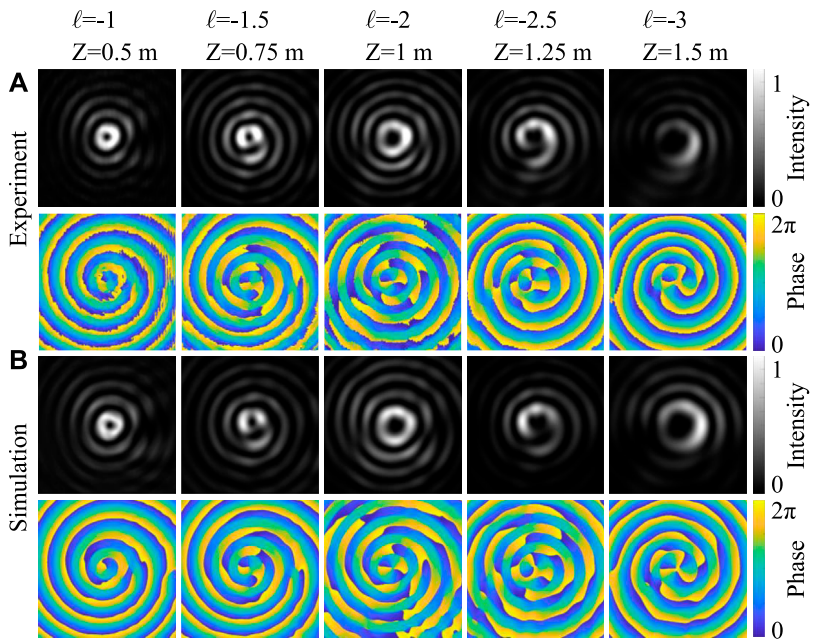

FIGURE 3 | Intensity and phase patterns of anomalous vortices generated by a beam of 632.8 nm through a clockwise spiral axicon at different distances *z*. **(A)** Experimental results; **(B)** simulation results. The top of the figure is marked with the PLTC *l* of the corresponding propagation distance *z* calculated by **Eq. 2**.

reflection. **Figure 3A** shows the result of the experimental measurement, and **Figure 3B** shows the result of the simulation by **Eqs. 10** and **11**. The experimental results and the simulation results are in good agreement.

Figure 4 shows the simulation and experimental results corresponding to different experimental parameters at z = 1 m. According to **Eq. 2**, when the device parameter C or the wavelength λ changes, the PLTC l changes. By comparing **Figure 4**(C1) and **Figure 4**(C2), it can be seen that when λ is fixed but C decreases, the l of the beam at the same position z decreases. By comparing **Figure 4**(C1) and **Figure 4**(C3), it can be known that when C is fixed but the wavelength increases, the PLTC of the beam at the same position z also decreases. It is consistent with the analysis result of **Eq. 2**. In addition, it is obvious that when the spiral direction of the bottom surface of the spiral axicon changes, the PLTC sign of the corresponding beam also changes. Using a plane wave as the incident light, when the bottom surface spiral direction of the spiral axicon load on the SLM is clockwise, the PLTC of the produced AVB decreases with propagation. When the bottom surface spiral direction of the spiral axicon is counterclockwise, the PLTC of the produced AVB increases with propagation. This can be demonstrated by comparing **Figure 4**(C4) with **Figure 4**(C1). **Figure 4**(C4) shows the counterclockwise spiral axicon situation. Compared with **Figure 4**(C1), the absolute value of the AVB PLTC still conforms to the theoretical analysis result, but its sign changes to plus.

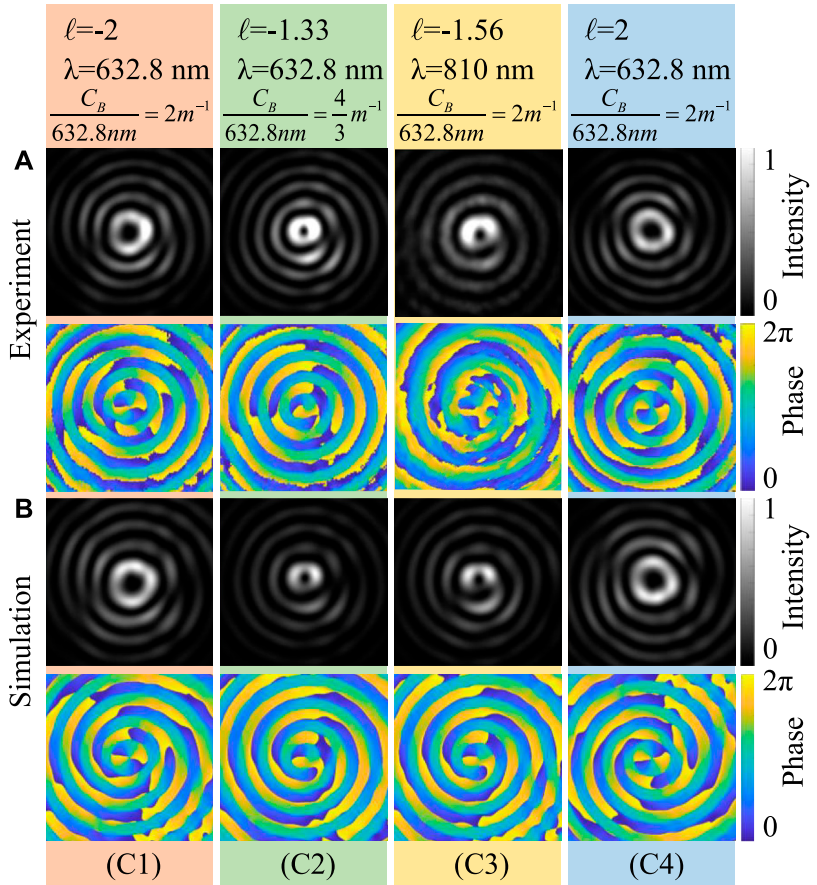

FIGURE 4 | Intensity and phase patterns of the AVB generated by different parameters of spiral axicon at z = 1 m. **(A)** Experimental results; **(B)** simulation results. The results of the clockwise spiral axicon whose parmeters are set to (C1) λ = 632.8 nm, C/632.8 nm =2 m^{-1}; (C2) λ = 632.8 nm, C/632.8 nm = 4/3 m^{-1}; (C3) λ = 810 nm, C/632.8 nm = 2 m^{-1}. (C4) The result of the counterclockwise spiral axicon whose parameters are set to λ = 632.8 nm, C/632.8 nm = 2 m^{-1}. The top of the figure is marked with the PLTC l of the corresponding propagation distance z calculated by **Eq. 2**.

4 CONCLUSION

In summary, we have proposed an efficient pure-phase device that can simply and efficiently generate AVB whose PLTC increases linearly with propagation. Using a SLM, we have experimentally demonstrated the performance of spiral axicon. By changing the parameters of the spiral axicon, we can control the PLTC variation of the AVB. Our work provides a new method to generate AVB, which is expected to promote its application in quantum information, laser beam shaping, and other fields.

DATA AVAILABILITY STATEMENT

The original contributions presented in the study are included in the article/**Supplementary Material**, further inquiries can be directed to the corresponding authors.

AUTHOR CONTRIBUTIONS

XH, XZ and PZ proposed the idea. XH, ZC and YZ performed the experiment. XH organized the database. XH, ZC and YW wrote the first draft of the manuscript. PZ and XZ supervised the project. All authors contributed to manuscript revision, read, and approved the submitted version.

FUNDING

This work was supported by the National Natural Science Foundation of China (NSFC) (Grant No. 51905412, 12174301, and 91736104).

SUPPLEMENTARY MATERIAL

The Supplementary Material for this article can be found online at: https://www.frontiersin.org/articles/10.3389/fphy.2022.951516/full#supplementary-material

REFERENCES

1. Durnin J, Miceli JJ, Eberly JH. Diffraction-free Beams. *Phys Rev Lett* (1987) 58: 1499–501. doi:10.1103/physrevlett.58.1499
2. Scott G, McArdle N. Efficient Generation of Nearly Diffraction-free Beams Using an Axicon. *Opt Eng* (1992) 31:2640–3. doi:10.1117/12.60017
3. Zhai Z, Zhao B. Diffraction Intensity Distribution of an Axicon Illuminated by Polychromatic Light. *J Opt A Pure Appl Opt* (2007) 9:862–7. doi:10.1088/1464-4258/9/10/015
4. Wei Z, Yuan Q, Ma X, Hu J, Zeng A, Huang H. Measurement of Base Angle of an Axicon Lens Based on Auto-Collimation Optical Path. *Opt Commun* (2019) 434:23–7. doi:10.1016/j.optcom.2018.10.034
5. Woerdemann M, Alpmann C, Esseling M, Denz C. Advanced Optical Trapping by Complex Beam Shaping. *Laser Photon Rev* (2013) 7:839–54. doi:10.1002/lpor.201200058
6. Shao B, Esener SC, Nascimento JM, Botvinick EL, Berns MW. Dynamically Adjustable Annular Laser Trapping Based on Axicons. *Appl Opt* (2006) 45: 6421–8. doi:10.1364/AO.45.006421
7. Jarutis V, Paškauskas R, Stabinis A. Focusing of Laguerre-Gaussian Beams by Axicon. *Opt Commun* (2000) 184:105–12. doi:10.1016/s0030-4018(00)00961-5
8. Dudutis J, Pipiras J, Schwarz S, Rung S, Hellmann R, Račiukaitis G, et al.Laser-fabricated Axicons Challenging the Conventional Optics in Glass Processing Applications. *Opt Express* (2020) 28:5715–30. doi:10.1364/oe.377108
9. Allen L, Beijersbergen MW, Spreeuw RJC, Woerdman JP. Orbital Angular Momentum of Light and the Transformation of Laguerre-Gaussian Laser Modes. *Phys Rev A* (1992) 45:8185–9. doi:10.1103/PhysRevA.45.8185
10. Shen Y, Wang X, Xie Z, Min C, Fu X, Liu Q, et al.Optical Vortices 30 Years on: Oam Manipulation from Topological Charge to Multiple Singularities. *Light Sci Appl* (2019) 8:697. doi:10.1038/s41377-019-0194-2
11. Yao AM, Padgett MJ. Orbital Angular Momentum: Origins, Behavior and Applications. *Adv Opt Photon* (2011) 3:161–204. doi:10.1364/AOP.3.000161
12. Padgett MJ, Miatto FM, Lavery MPJ, Zeilinger A, Boyd RW. Divergence of an Orbital-Angular-Momentum-Carrying Beam upon Propagation. *New J Phys* (2015) 17:023011. doi:10.1088/1367-2630/17/2/023011
13. Barnett SM, Allen L. Orbital Angular Momentum and Nonparaxial Light Beams. *Opt Commun* (1994) 110:670–8. doi:10.1016/0030-4018(94)90269-0
14. Beijersbergen MW, Allen L, Van der Veen HELO, Woerdman JP. Astigmatic Laser Mode Converters and Transfer of Orbital Angular Momentum. *Opt Commun* (1993) 96:123–32. doi:10.1016/0030-4018(93)90535-d
15. Yang Y, Dong Y, Zhao C, Cai Y. Generation and Propagation of an Anomalous Vortex Beam. *Opt Lett* (2013) 38:5418–21. doi:10.1364/ol.38.005418
16. Liu R, Long J, Wang F, Wang Y, Zhang P, Gao H, et al.Characterizing the Phase Profile of a Vortex Beam with Angular-Double-Slit Interference. *J Opt* (2013) 15:125712. doi:10.1088/2040-8978/15/12/125712
17. Zhu J, Zhang P, Li Q, Wang F, Wang C, Zhou Y, et al.Measuring the Topological Charge of Orbital Angular Momentum Beams by Utilizing Weak Measurement Principle. *Sci Rep* (2019) 9:7993–6. doi:10.1038/s41598-019-44465-z
18. Barreiro JT, Wei TC, Kwiat PG. Beating the Channel Capacity Limit for Linear Photonic Superdense Coding. *Nat Phys* (2008) 4:282–6. doi:10.1038/nphys919
19. Wang J, Yang J-Y, Fazal IM, Ahmed N, Yan Y, Huang H, et al.Terabit Free-Space Data Transmission Employing Orbital Angular Momentum Multiplexing. *Nat Photon* (2012) 6:488–96. doi:10.1038/nphoton.2012.138
20. Willner AE, Huang H, Yan Y, Ren Y, Ahmed N, Xie G, et al.Optical Communications Using Orbital Angular Momentum Beams. *Adv Opt Photon* (2015) 7:66–106. doi:10.1364/AOP.7.000066
21. Paterson L, MacDonald MP, Arlt J, Sibbett W, Bryant PE, Dholakia K. Controlled Rotation of Optically Trapped Microscopic Particles. *Science* (2001) 292:912–4. doi:10.1126/science.1058591
22. Padgett M, Bowman R. Tweezers with a Twist. *Nat Photon* (2011) 5:343–8. doi:10.1038/nphoton.2011.81
23. Yang Y, Ren Y, Chen M, Arita Y, Rosales-Guzmán C. Optical Trapping with Structured Light: A Review. *Adv Photon* (2021) 3:034001. doi:10.1117/1.ap.3.3.034001
24. Zhang D, Yang Y. Radiation Forces on Rayleigh Particles Using a Focused Anomalous Vortex Beam under Paraxial Approximation. *Opt Commun* (2015) 336:202–6. doi:10.1016/j.optcom.2014.10.034
25. Long J, Liu R, Wang F, Wang Y, Zhang P, Gao H, et al.Evaluating Laguerre-Gaussian Beams with an Invariant Parameter. *Opt Lett* (2013) 38:3047–9. doi:10.1364/ol.38.003047
26. Fu D, Chen D, Liu R, Wang Y, Gao H, Li F, et al.Probing the Topological Charge of a Vortex Beam with Dynamic Angular Double Slits. *Opt Lett* (2015) 40:788–91. doi:10.1364/ol.40.000788
27. Fontaine NK, Ryf R, Chen H, Neilson DT, Kim K, Carpenter J. Laguerre-gaussian Mode Sorter. *Nat Commun* (2019) 10:1865–7. doi:10.1038/s41467-019-09840-4
28. McGloin D, Dholakia K. Bessel Beams: Diffraction in a New Light. *Contemp Phys* (2005) 46:15–28. doi:10.1080/0010751042000275259
29. Mitri F. High-order Bessel Nonvortex Beam of Fractional Type *α*. *Phys Rev A (Coll Park)* (2012) 85:025801. doi:10.1103/physreva.85.025801
30. Chen WT, Khorasaninejad M, Zhu AY, Oh J, Devlin RC, Zaidi A, et al.Generation of Wavelength-independent Subwavelength Bessel Beams Using Metasurfaces. *Light Sci Appl* (2017) 6:e16259. doi:10.1038/lsa.2016.259
31. Ostrovsky AS, Rickenstorff-Parrao C, Arrizón V. Generation of the "perfect" Optical Vortex Using a Liquid-crystal Spatial Light Modulator. *Opt Lett* (2013) 38:534–6. doi:10.1364/ol.38.000534
32. Vaity P, Rusch L. Perfect Vortex Beam: Fourier Transformation of a Bessel Beam. *Opt Lett* (2015) 40:597–600. doi:10.1364/ol.40.000597
33. Zhao Y, Huang X, Chang Z, Wang X, Zhang P. Measure the Arbitrary Topological Charge of Perfect Optical Vortex Beams by Using the Dynamic Angular Double Slits. *Opt Express* (2021) 29:32966–72. doi:10.1364/oe.439031
34. Dorrah AH, Zamboni-Rached M, Mojahedi M. Controlling the Topological Charge of Twisted Light Beams with Propagation. *Phys Rev A* (2016) 93: 063864. doi:10.1103/PhysRevA.93.063864
35. Davis JA, Moreno I, Badham K, Sánchez-López MM, Cottrell DM. Nondiffracting Vector Beams where the Charge and the Polarization State Vary with Propagation Distance. *Opt Lett* (2016) 41:2270–3. doi:10.1364/ol.41.002270
36. Yang Y, Zhu X, Zeng J, Lu X, Zhao C, Cai Y. Anomalous Bessel Vortex Beam: Modulating Orbital Angular Momentum with Propagation. *Nanophotonics* (2018) 7:677–82. doi:10.1515/nanoph-2017-0078
37. Wang H, Liu L, Zhou C, Xu J, Zhang M, Teng S, et al.Vortex Beam Generation with Variable Topological Charge Based on a Spiral Slit. *Nanophotonics* (2019) 8:317–24. doi:10.1515/nanoph-2018-0214
38. Yang B, Su M, Lu L, Liu J, Chai G. Generation of Anomalous Vector Bessel Beams with Varying Polarization Order along the Propagation Direction. *Optik* (2021) 232:166578. doi:10.1016/j.ijleo.2021.166578
39. Fang J, Zhou C, Mou Z, Wang S, Yu J, Yang Y, et al.High Order Plasmonic Vortex Generation Based on Spiral Nanoslits. *New J Phys* (2021) 23:033013. doi:10.1088/1367-2630/abe72c
40. Lai S, King B, Neifeld MA. Wave Front Reconstruction by Means of Phase-Shifting Digital In-Line Holography. *Opt Commun* (2000) 173:155–60. doi:10.1016/S0030-4018(99)00625-2

Conflict of Interest: The authors declare that the research was conducted in the absence of any commercial or financial relationships that could be construed as a potential conflict of interest.

frontiers | Frontiers in Physics

ORIGINAL RESEARCH
published: 28 June 2022
doi: 10.3389/fphy.2022.870770

Design of Dual-Functional Metaoptics for the Spin-Controlled Generation of Orbital Angular Momentum Beams

Andrea Vogliardi[1,2], *Filippo Romanato*[1,2,3]* *and Gianluca Ruffato*[1,2]

[1]Department of Physics and Astronomy "G. Galilei", University of Padova, Padova, Italy, [2]Padua Quantum Technologies Research Center, University of Padova, Padova, Italy, [3]CNR-IOM Istituto Officina dei Materiali, Trieste, Italy

The capability of multiple orbital angular momentum (OAM) modes generation with high resolution and diversified functionalities in the visible and near-infrared regime is challenging for flat and integrated optical devices. Additionally, having a static tiny optical device capable of generating multiple structured spots in space reduces the complexity of optical paths that typically use dynamic optical components and/or many standard elements, leading to unprecedented miniaturization and compactness of optical systems. In this regard, we propose dual-functional transmission dielectric metalenses based on a set of Pancharatnam-Berry phase meta-atoms with different cross-sections, for the combined manipulation of the dynamic and geometric phases. In particular, we present and describe the numerical algorithms for the computation of dual-functional metaoptics and we apply those techniques to the design of optical elements which are able to generate and focus different OAM modes at distinct points in space. In the specific, the designed elements enable the independent or simultaneous manipulation of right-handed and left-handed circularly polarized waves, by acting on the helicity of the input beam to enable or disable a specific optical operation. The theoretical proof-of-concept results highlight the capability of the designed metalenses to generate multiple high-resolution focused OAM modes at different points in space by exploiting the polarization of the incident beam as a degree of freedom, thus providing new integrated optics for applications in the fields of high-resolution microscopy, optical manipulation, and optical communications, both in the classical and single-photon regimes.

Keywords: dual function, metasurface, orbital angular momentum, metalens, Metaoptics

OPEN ACCESS

Edited by:
Venu Gopal Achanta,
Tata Institute of Fundamental Research, India

Reviewed by:
Lei Zhang,
Xi'an Jiaotong University, China
Nirmal Kumar Viswanathan,
University of Hyderabad, India

***Correspondence:**
Filippo Romanato
filippo.romanato@unipd.it

Specialty section:
This article was submitted to Optics and Photonics, a section of the journal Frontiers in Physics

Received: *07 February 2022*
Accepted: *06 June 2022*
Published: *28 June 2022*

Citation:
Vogliardi A, Romanato F and Ruffato G (2022) Design of Dual-Functional Metaoptics for the Spin-Controlled Generation of Orbital Angular Momentum Beams. Front. Phys. 10:870770. doi: 10.3389/fphy.2022.870770

INTRODUCTION

Since the seminal paper of Allen and coworkers in 1992 [1], structured light ignited a flourishing research area, paving the way for scientific milestones and disruptive applications in an amazing variety of fields [2], including life science, soft and condensed matter, information and communication technology. In particular, orbital angular momentum (OAM) beams [3], also called optical vortices (OVs), offered a new degree of freedom to encode information in classical communications [4] or increase the Hilbert state space in quantum applications [5, 6], while their peculiar intensity and phase distributions enabled innovative and advanced techniques in microscopy [7], micro-manipulation [8], and light-matter interaction [9]. Concurrently, the necessity to tailor and control this spatial property of light inspired the design and engineering of new techniques with different levels of complexity and integration [10–14]. Among all, spiral

phase plates (SPPs) [15] represent one of the first optical elements purposely introduced to impart orbital angular momentum to common non-structured beams. Such optical elements are characterized by 3D spiral staircase profiles [16], reproducing the twisting wavefront to impart to the input beam. Their fabrication with high-resolution lithographic techniques [17] has proved the generation of OAM beams with high purity, while the introduction of radial discontinuities [18] in their design enabled the additional control on the radial number and the excitation of higher-order modes. While providing a stable, efficient, and compact method for OAM generation, a strong limitation of SPPs is given by their reduced functionality, which is basically limited to a specific OAM value. q-plates [19] provided a first evolution of standard SPPs, acting on the geometric phase to implement polarization-dependent OAM generators. Instead of spatially changing the local thickness of an isotropic material to tune the optical path, *i.e.*, the dynamic phase, q-plates rely on shaping the wavefront by acting on the polarization state with a 2D birefringent medium. The imparted phase, having a geometric nature, is equal to twice the local angle formed by the extraordinary axis, with a sign depending on the handedness of the circular polarization in input [20]. That is achieved by structuring the optical element at the subwavelength scale in the form of a spatially-variant half-wave plate, by exploiting the inherent anisotropy of liquid crystals [21, 22], or using properly-oriented digital gratings [23] or dielectric resonators [24], the so-called metaunits, to induce an effective form birefringence. Moreover, moving from 3D sculptured surfaces to 2D digital optics, metasurfaces open to the exploitation of semiconductor manufacturing [25], achieving the actual merging between optics and silicon photonics [26]. The metasurface paradigm opens to polarization as an additional degree of freedom, enabling the design of spin-dependent optical elements for the generation of beams with opposite values of OAM. However, it would be extremely advantageous to decouple spin from phase reshaping in order to effectively extend the optical functionality.

The solution is offered by the design of spin-decoupled dual-functional metasurfaces [27–30], which locally combine the dynamic phase from the refractive index profile with the geometric phase from the induced form birefringence. That is achieved by using anisotropic nanopillars with both different orientations and shapes. While the dynamic phases along the main axes of the nanopillars can be adjusted by tailoring their cross-section, an arbitrary geometric phase can be realized by controlling the local fast-axis orientation. The proper combination of the dynamic phase with the polarization-dependent geometric one enables the encoding of two totally different optical operations for the two circular polarization states.

In this work, we focus on the design of dual-functional metasurfaces for the generation of OAM beams. In particular, we provide a numerical recipe for the design of any dual-functional optical element, showing its application to the design of metaoptics enabling the spin-controlled generation of beams with different values of OAM. Moreover, by encoding different focal terms on the two contributions, we show the possibility to control the positions of the two beams independently. The design extends significantly the functionality of standard SPPs and q-plates, providing advanced optical elements for applications in microscopy, optical micromanipulation, and classical and quantum information, with unprecedented potential levels of compactness and integration into today's technology.

MATERIALS AND METHODS

In this work, we propose metaoptics which are able to generate and manipulate optical vortices (OVs) with different OAM values at distinct points in space. Mathematically, OVs are wavefront dislocations, with peculiar topological properties, due to phase singularities in the optical field. Light beams carrying OAM are characterized by a dark central region that arises from the destructive interference phenomena leading to the typical doughnut-shaped intensity distribution [31]. In order to generate an OV, the optical element is required to implement an azimuthal phase profile:

$$\Omega(r, \theta) = \ell\theta, \tag{1}$$

where ℓ, in units of the reduced Planck constant, is the amount of orbital angular momentum per photon transferred to the impinging beam, (r, θ) are polar coordinates on the plane of the optical element.

The metasurface proposed in this work is a dielectric dual-functional metalens (DFML), made of a 2D array of birefringent metaunits that exploit both the Pancharatnam-Berry (geometric) phase and the dynamic one. Our DFML is constituted of subwavelength metaunits (MUs), the so-called metaatoms (MAs), arranged over a square lattice, represented by amorphous silicon nanopillars on a silica substrate, surrounded by air. Each pillar belongs to a subset of nanostructures with different cross sections and orientations but the same height (**Figure 1A**), and acts as a half-wave plate in order to maximize the polarization conversion and, therefore, the optical efficiency [32–34] **.** While the pillar orientation allows controlling the geometric phase, by varying the cross section it is possible to act on the dynamic phase. Combining these two properties, the metalens is able to behave in two different ways depending on whether the input beam is right-handed (RCP) or left-handed circularly polarized (LCP) (**Figure 1B**).

In fact, while a variation on the dynamic phase has the same effects both on LCP or RCP input beams, on the other hand a change in the geometric phase implies symmetrical (opposite) response on a LCP beam compared to on a RCP one. In this way, controlling simultaneously both the shape of the pillars and their rotations, it is possible to generate totally different behaviors under LCP or RCP illumination in input [35, 36].

For the benefit of the reader, we provide in the following the theory underlying the working principle of anisotropic metaunits. As well known, in dual-functional MLs the incident beam is supposed to be either left-handed circularly polarized $|R\rangle = [\,1 \quad -i\,]^T$ or right-handed circularly polarized $|L\rangle = [\,1 \quad i\,]^T$, where the normalization factor $1/\sqrt{2}$ has been omitted. Then, the transmitted output waves are cross-polarized and carry the spatial phase shifts $\phi^-(x, y)$ or $\phi^+(x, y)$, respectively.

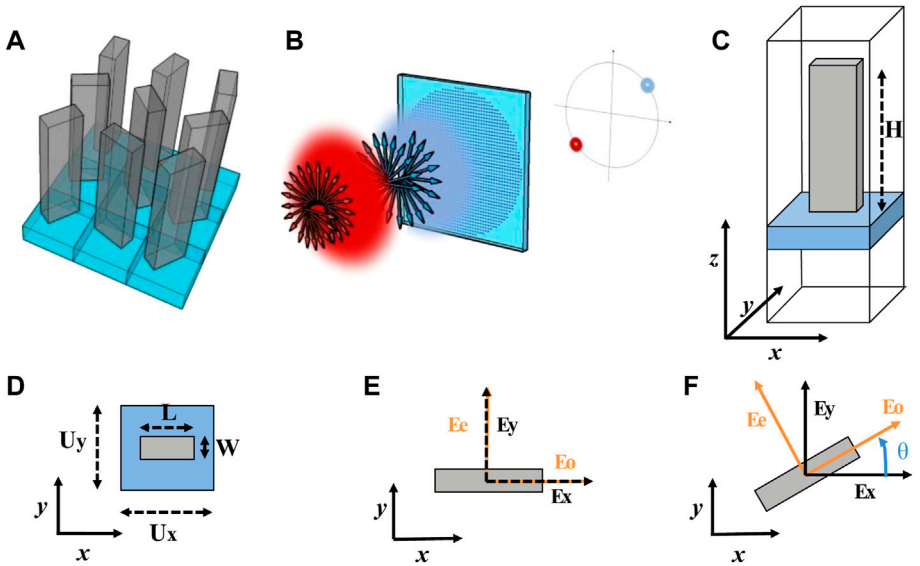

FIGURE 1 | (A) Schematic figure representing the 2D array of metaunits composing a metalens. **(B)** Working principle of a dual-functional metalens: two different structured beams are generated at distinct points in space, depending on the handedness of the circular polarization in input. **(C)** 3D view of a metaunit. **(D)** Top view of a metaunit illustrating its geometric features: length (*L*), width (*W*), and periods of the 2D array (in our case $U_x = U_y = 400$ *nm*). **(E)** Cross section of a pillar representing the extraordinary and ordinary axes for our simulations. Being E_e the electric field along the extraordinary axis, E_o the electric field along the ordinary axis, E_x the electric field along the *x*-axis, E_y the electric field along the *y*-axis, axis and E_{0i} the input electric field, we consider a TE input polarization when $E_o = Ex = E_{0i}$ and $E_e = E_y = 0$. Instead, we assume a TM input polarization when $E_o = E_x = 0$ and $E_e = E_y = E_{0i}$. **(F)** Cross section of a pillar showing a rotation θ in order to transfer a geometric phase term equal to 2θ.

In particular, the Jones matrix J for the metaatom at the coordinates (x, y) is:

$$J(x,y) = R(\theta(x,y))\begin{bmatrix} e^{i\delta_x(x,y)} & 0 \\ 0 & e^{i\delta_y(x,y)} \end{bmatrix} R(-\theta(x,y)), \quad (2)$$

where $R(\theta)$ is the unitary rotation matrix:

$$R(\theta) = \begin{bmatrix} \cos\theta & -\sin\theta \\ \sin\theta & \cos\theta \end{bmatrix}, \quad (3)$$

being θ the local orientation of the metaatom fast axis. After straightforward calculations, **Eq. 2** can be expressed in the form (the spatial dependence has been omitted to simplify the notation):

$$J = e^{i\frac{\delta_x+\delta_y}{2}} R(\theta) \begin{bmatrix} e^{-i\frac{\delta_y-\delta_x}{2}} & 0 \\ 0 & e^{+i\frac{\delta_y-\delta_x}{2}} \end{bmatrix} R(-\theta) =$$

$$= e^{i\frac{\delta_x+\delta_y}{2}} R(\theta) \begin{bmatrix} \cos\left(\frac{\Delta}{2}\right) - i\sin\left(\frac{\Delta}{2}\right) & 0 \\ 0 & \cos\left(\frac{\Delta}{2}\right) + i\sin\left(\frac{\Delta}{2}\right) \end{bmatrix} R(-\theta) =,$$

$$= e^{i\frac{\delta_x+\delta_y}{2}} \cos\left(\frac{\Delta}{2}\right)\begin{bmatrix} 1 & 0 \\ 0 & 1 \end{bmatrix} - ie^{i\frac{\delta_x+\delta_y}{2}} \sin\left(\frac{\Delta}{2}\right)\begin{bmatrix} \cos(2\theta) & \sin(2\theta) \\ \sin(2\theta) & -\cos(2\theta) \end{bmatrix} \quad (4)$$

where $\Delta = \delta_y - \delta_x$ is the phase retardation between the two axes of the metaunit. It is worth noting from **Eq. 4** that, under the choice $\Delta = \pi$, the optical behavior of the metaunit is that of a rotated half-wave plate. Therefore, for circularly-polarized light in input, each metaatom behaves as a polarization converter:

$$J|L\rangle = -ie^{i(\delta_x+\delta_y)/2} e^{+i2\theta}|R\rangle \quad (5)$$

$$J|R\rangle = -ie^{i(\delta_x+\delta_y)/2} e^{-i2\theta}|L\rangle \quad (6)$$

imparting a polarization-independent dynamic phase term equal to $(\delta_x + \delta_y)/2$, plus a polarization-sensitive geometric phase equal to twice the orientation angle θ, and with sign depending on the input handedness. Therefore, when the condition $\Delta = \pi$ is satisfied, the cosine term in **Eq. 4** representing the zero-order contribution is completely suppressed. Thus, in conclusion, the metaunit acts as a pure half-wave plate and, since the spurious zero-order component has been erased, the diffraction efficiency is optimized.

Then, it is possible to define a spin-decoupled optical response with the following definitions:

$$\delta_x = \frac{\phi^+(x,y) + \phi^-(x,y)}{2} \quad (7)$$

$$\delta_y = \frac{\phi^+(x,y) + \phi^-(x,y)}{2} + \pi \quad (8)$$

$$\theta = \frac{\phi^+(x,y) - \phi^-(x,y)}{4} \quad (9)$$

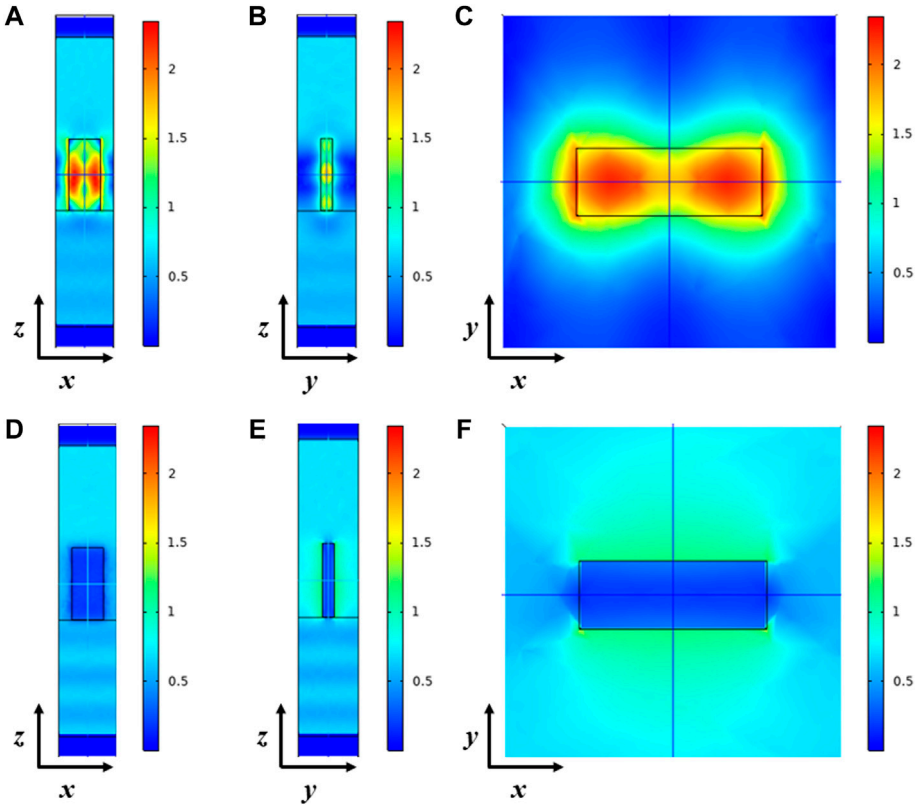

FIGURE 2 | Example of FEM simulations of a metaatom ($U_x = U_y$ = 400nm) composed by a silicon nanopillar (L = 220nm, W = 80nm and H = 500nm, *i.e.*, pillar #11 in **Figure 3**) on a glass substrate under TE **(A–C)** and TM **(D,E)** polarization in input from the air side. Lateral cross-sections at $y = 0$ **(A,D)** and $x = 0$ **(B,E)** and top-view cross-section at $z = H/2$ **(C,F)**. Input wavelength 775 nm. Colours refer to the intensity of the electric field (a.u.).

being ϕ^+ and ϕ^- the phase to impart to left-handed and right-handed circular polarization, respectively. As a matter of fact, it is straightforward to prove that:

$$J|L\rangle = e^{i\phi^+}|R\rangle \tag{10}$$

$$J|R\rangle = e^{i\phi^-}|L\rangle \tag{11}$$

Hence, by accurately selecting a set of nanopillars with different sizes, which satisfy the required phase delays, i.e., (δ_x, δ_y), and rotating each nanopillar of an angle θ with respect to the x-axis positive direction, it is possible to design a metalens that imparts a phase delay $\phi^+(x, y)$ to an LCP input light and a phase delay $\phi^-(x, y)$ to an RCP input light.

We exploit these properties to design and test DFMLs which are able to generate and focus different orbital angular momentum beams at distinct fixed points in space, depending on the input circularly-polarized state. To implement these functionalities, the spatial phase patterns $\phi^+(x, y)$ or $\phi^-(x, y)$ must be accurately engineered. To this purpose, we suggest a new converging lens profile ϕ, which is able to generate a focused beam carrying OAM at a desired position. In detail:

$$\phi(x, y) = \ell \arctan\left(\frac{y}{x}\right) - \frac{2\pi}{\lambda}\left(\sqrt{f^2 + (x - x_0)^2 + (y - y_0)^2} - f\right) \tag{12}$$

where ℓ is the amount of OAM per photon transferred to the impinging beam, in units of $\hbar$, λ is the working wavelength, f is the focal length, and (x_0, y_0), are the focus coordinates on the focal plane perpendicular to the propagation optical axis (z). The first part of the equation, *i.e.*, $\ell \arctan(y/x)$ is the azimuthal phase necessary to generate an optical vortex (**Eq. 1**), while the second part, *i.e.*, $-2\pi/\lambda(\sqrt{f^2 + (x - x_0)^2 + (y - y_0)^2} - |f|)$, is an hyperboloid focusing profile, without spherical aberration if illuminated by a plane-wave [37, 38], mandatory to focus the optical vortex onto a desired point in space.

After defining the theoretical framework for the wavefront engineering, we performed a custom Finite-Element Method (FEM) simulation in the wavelength domain using COMSOL Multiphysics® to extrapolate the set of metaunits which compose the metalens (**Figure 2**). The geometry of the metaatoms was modelled as an amorphous silicon pillar (n_{Si} = 3.425) deposited on a glass substrate (n_{Glass} = 1.450) and surrounded by air (n_{Air} = 1). Periodic port conditions were set at the base of the substrate (at a distance equal to λ) and at a distance greater than λ

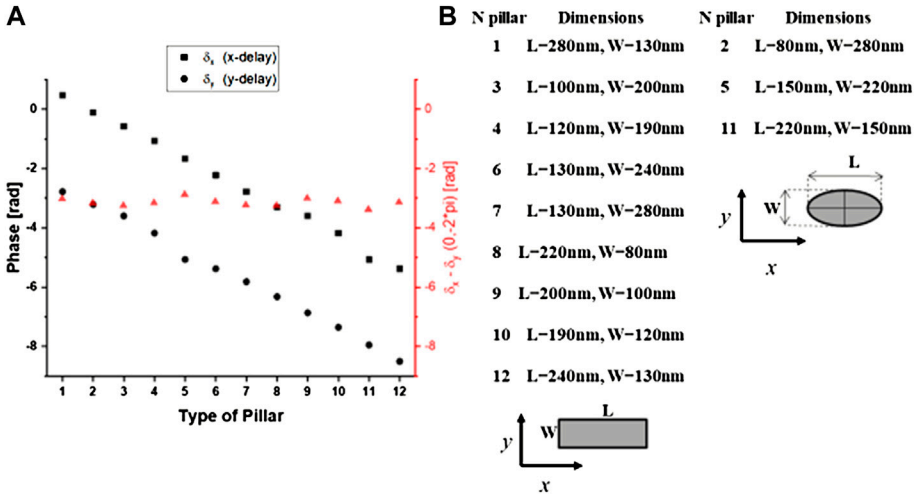

FIGURE 3 | (A) Graph showing the library of different pillars working at 775 nm and their phase delays under both TE polarization (*x*-delay) and TM polarization (*y*-delay), mandatory to built-up the metalens using the **Eqs 7–9**. **(B)** List of pillars composing the library with their corresponding geometric features.

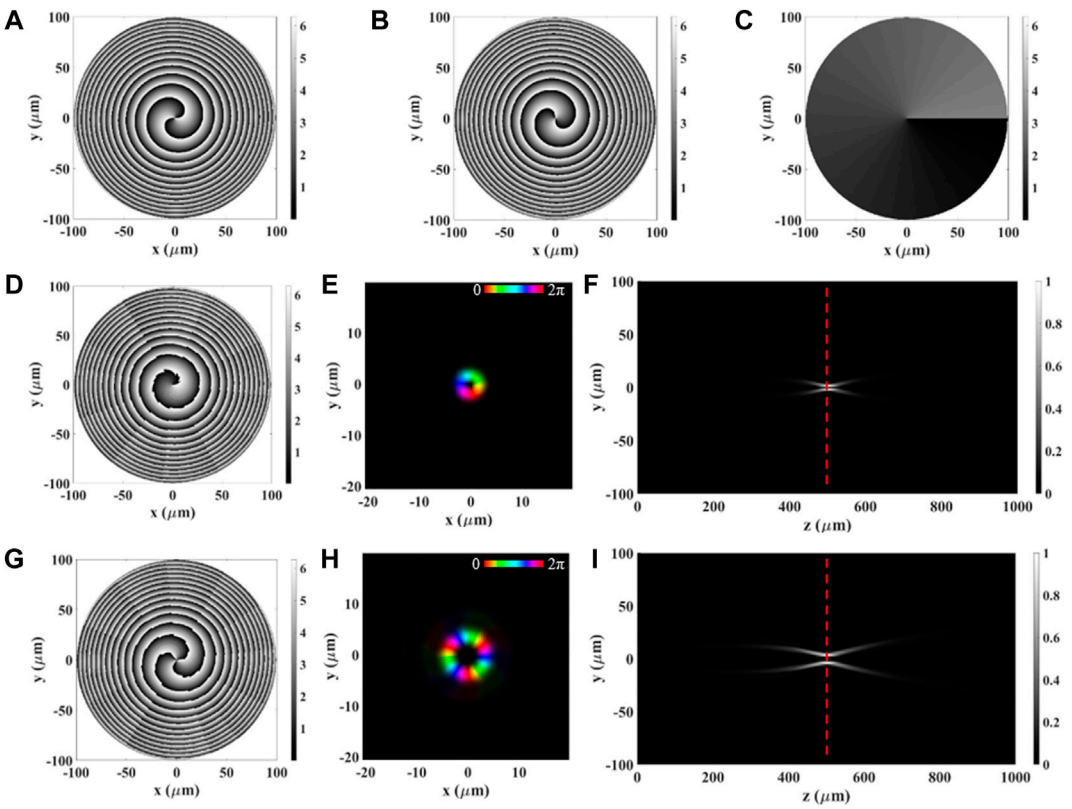

FIGURE 4 | Simulations of DFML implementing **Eqs 14**, **15**. **(A–C)** ML design phase maps of δ_x **(A)**, δ_y **(B)**, and θ **(C)** from **Eqs 7–9**. **(D,G)** show ϕ^+ and ϕ^- phase maps, respectively. **(E)** Intensity and phase of the propagated field under LCP polarization at $z = 500$ μm. **(F)** Intensity cross-section (*yz*-plane, from 0 to 1*mm*, $x = 0$)under LCP polarization. **(H)** Intensity and phase of the propagated field under RCP polarization at $z = 500$ μm. **(I)** Intensity cross-section (*yz*-plane from 0 to 1*mm*, $x = 0$) under RCP polarization. In **(E,H)**, brightness and colours refer to intensity and phase, respectively.

in the upper zone simulating air, to ensure the Fraunhofer regime [39]. Perfectly Matched Layers (PML) conditions were imposed in the areas outside the ports in order to absorb the field in the simulation volumes not of interest so to avoid multiple reflections. Finally, periodic boundary conditions were set (along the *xz* and *yz* planes) to correctly simulate the

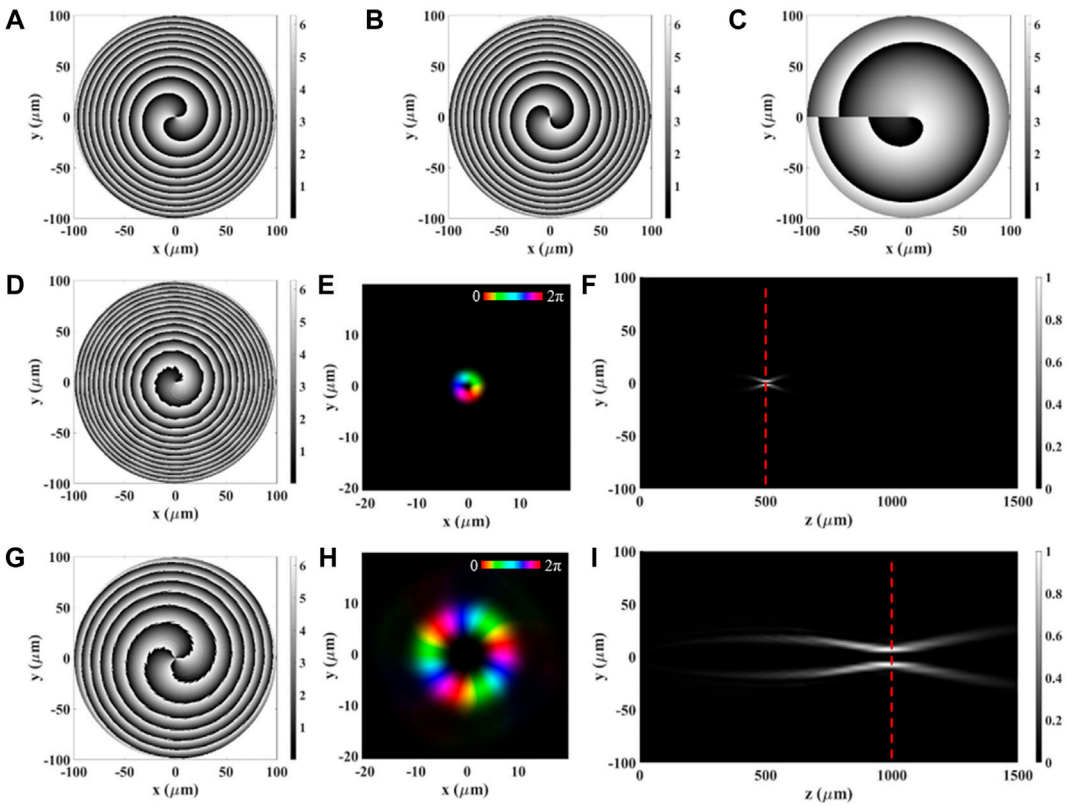

FIGURE 5 | Simulations of DFML implementing **Eqs 16**, **17**. **(A–C)** ML design phase maps of δ_x **(A)**, δ_y **(B)**, and θ **(C)** from **Eqs 7–9**. **(D,G)** show ϕ^+ and ϕ^- phase maps, respectively. **(E)** Intensity and phase of the propagated field under LCP polarization at z = 500 μm. **(F)** Intensity cross-section (yz-plane, from 0 to 1.5 mm, x = 0) under LCP polarization. **(H)** Intensity and phase of the propagated field under RCP polarization at z = 1000μm. **(I)** Intensity cross-section (yz-plane from 0 to 1.5 mm, x = 0) under RCP polarization. In **(E,F)**, brightness and colours refer to intensity and phase, respectively.

interaction between the various metaatoms of the metalens [40]. The period of the metaunits array was fixed at 400 nm in both directions, while the parameters of the pillar cross-section (L, W) were swept during the simulation considering the fabrication limits and the sub-wavelength working regime. In particular, the height (H) was fixed at 500 nm considering the fabrication limits (**Figures 1C–F**). For a given phase delay along the long axis of the pillar, the final cross-section was selected in order to satisfy the condition $\Delta = \pi$. Concurrently, provided the last condition is satisfied, the transmission values for TE and TM polarizations must be as close as possible, in order guarantee the expected polarization conversion under circularly-polarized light in input. Therefore, previous requirements significantly limit the choice of possible cross-sections for the given thickness and shape. Moreover, in order to increase the degrees of freedom to find the adequate nanostructures to cover the whole 2π range, both rectangular-based and elliptical-based silicon pillars were considered. Finally, a library of 12 different nanopillars has been extrapolated from the simulations, which permits to have a well-distributed 12-level discretization of the phase over the range 0-2π (**Figure 3**). Conversely, we assumed a continuous rotation of the metaatom, i.e., no discretization on the geometric phase was applied. Then, for given phase patterns ϕ^+ and ϕ^-, we were able to calculate the corresponding maps for the dynamic and geometric phases using **Eqs 7–9**. Those maps provide the recipe to compute the metaatoms pattern of the desired DFML. While the geometric phase map gives the local orientation of the metaatom, the required dynamic phase delay allows one to select the required cross-section referring to the lookup table in **Figure 3**.

RESULTS

Using a custom code implementing the Fresnel propagation integral [41] in MatLab® environment, we simulated the optical response of several dual functional metalenses designed according to **Eq. 12**. In particular, we selected different combinations of the parameters ℓ, f, x_0, and y_0, in such a way to exhibit all the potentialities emerging from the combination of the DFML paradigm **Eqs 7–11** with the converging spiral profile of **Eq. 12**. All the simulations were performed implementing metasurfaces of radius $100\mu m$, with 12 levels of phase discretization, working at $\lambda = 775nm$, and illuminated by a Gaussian beam, with a cross-section as given by $\exp(-r^2/w_0^2)$, being $r = \sqrt{x^2 + y^2}$, with $w_0 = 100\mu m$ chosen to properly illuminate the entire metasurface pattern. The intensities of the simulations have been normalized according to the formula:

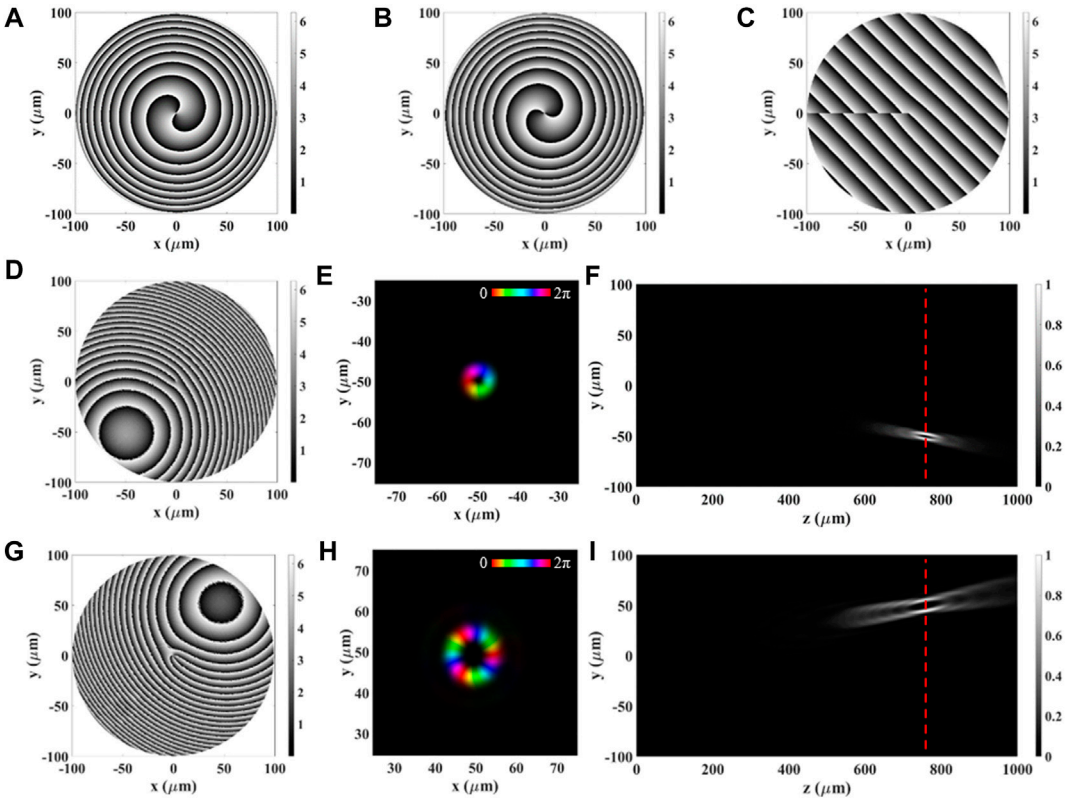

FIGURE 6 | Simulations of DFML implementing **Eqs 18**, **19**. **(A–C)** ML design phase maps of δ_x **(A)**, δ_y **(B)**, and θ **(C)** from **Eqs 7–9**. **(D,G)** show ϕ^+ and ϕ^- phase maps, respectively. **(E)** Intensity and phase of the propagated field under LCP polarization at z = 750μm. **(F)** Intensity cross-section (yz-plane, from 0 to 1 mm, x = −50 μm) under LCP polarization. **(H)** Intensity and phase of the propagated field under RCP polarization at z = 750μm. **(I)** Intensity cross-section (yz-plane from 0 to 1 mm, x = +50 μm) under RCP polarization. In **(E,H)**, brightness and colours refer to intensity and phase, respectively.

$$I_{normalized}(x,y) = \frac{|E(x,y)|^2}{\max(|E|^2)} \tag{13}$$

In the following, we report for each case of interest the phase patterns experienced by the two circular polarization states, and a simulation of their propagation after the optical element. In particular, we show a cross-section of the beam at the focal planes, in order to highlight the expected phase and intensity profiles.

We started implementing a dual-functional metalens able to focus two beams carrying different values of OAM at the same focus along the optical axis, with OAM depending on the input polarization.

Thus, we imposed the following focusing profiles:

$$\phi^+(x,y) = \ell_1 \arctan\left(\frac{y}{x}\right) - \frac{2\pi}{\lambda}\left(\sqrt{f^2+x^2+y^2} - f\right) \tag{14}$$

$$\phi^-(x,y) = \ell_2 \arctan\left(\frac{y}{x}\right) - \frac{2\pi}{\lambda}\left(\sqrt{f^2+x^2+y^2} - f\right) \tag{15}$$

being $\ell_1 = 1$, $\ell_2 = 3$, and $f = 500\mu m$. As shown in **Figure 4**, two structured beams are well generated under both LCP and RCP polarization. From the phase profile (**Figure 4**), it is clearly observable that the two beams carry different OAM. In particular, a first-order OAM beam is generated with a left-handed helicity, while under a right-handed helicity a third-order OAM beam is produced. In fact, there is only one phase variation from 0 to 2π in the first case, while in the second case 3 phase steps in the range 0-2π appear. That is further confirmed from the singularity size of the generated doughnut, which is larger in the OAM beam with $\ell = 3$ with respect to that with $\ell = 1$, as expected from the theory [31].

Subsequently, we implemented a DFML able to focus two beams carrying different OAM values at different focal lengths along the optical axis, depending on the input helicity. To obtain a metasurface as described above we encoded the following profiles:

$$\phi^+(x,y) = \ell_1 \arctan\left(\frac{y}{x}\right) - \frac{2\pi}{\lambda}\left(\sqrt{f_1^2+x^2+y^2} - f_1\right) \tag{16}$$

$$\phi^-(x,y) = \ell_2 \arctan\left(\frac{y}{x}\right) - \frac{2\pi}{\lambda}\left(\sqrt{f_2^2+x^2+y^2} - f_2\right) \tag{17}$$

being $\ell_1 = 1, \ell_2 = 3$, $f_1 = 500\mu m$, and $f_2 = 1000\mu m$. As expected, in this case two different doughnut spots are well generated at different focal lengths (**Figure 5**). Moreover, it can be noticed that the beam carrying OAM with $\ell = 3$ and focalized at 1000 μm (d-f)), is bigger than the same beam focalized at 500μm. This

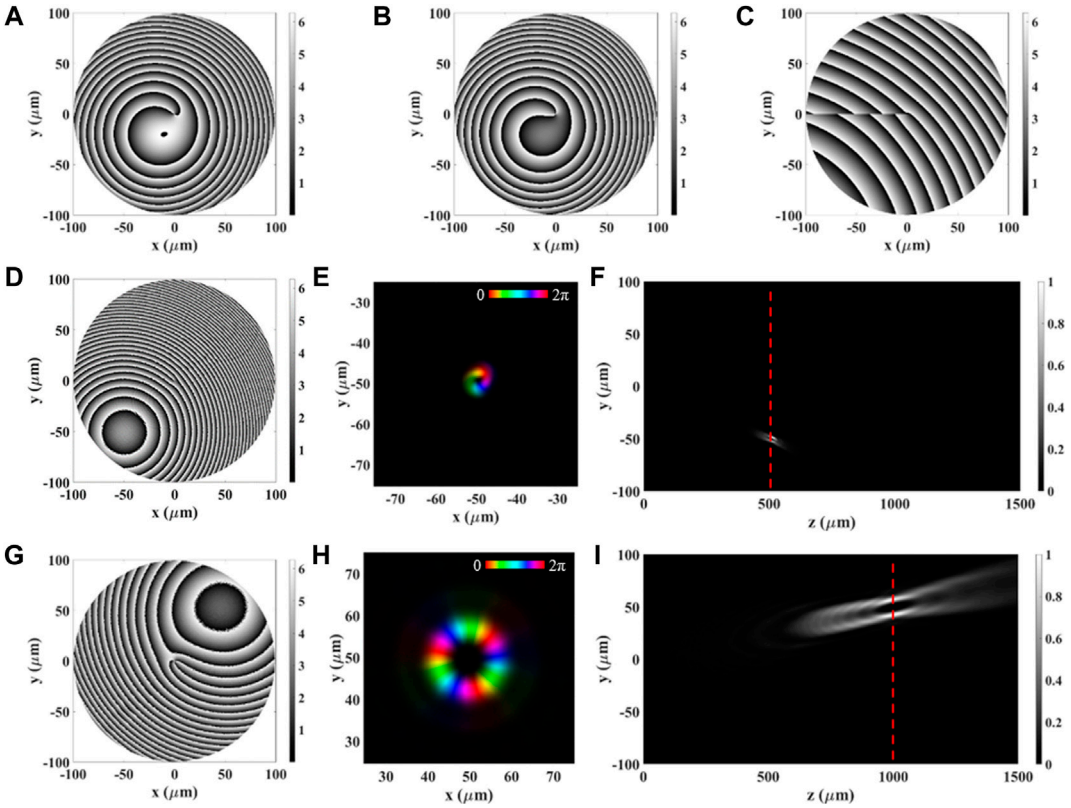

FIGURE 7 | Simulations of DFML implementing **Eqs 20**, **21**. **(A–C)** ML design phase maps of δ_x **(A)**, δ_y **(B)**, and θ **(C)** from **Eqs 7–9**. **(D,G)** show ϕ^+ and ϕ^- phase maps, respectively. **(E)** Intensity and phase of the propagated field under LCP polarization at z = 500μm. **(F)** Intensity cross-section (yz-plane, from 0 to 1.5 mm, x = −50 μm) under LCP polarization. **(H)** Intensity and phase of the propagated field under RCP polarization at z = 1000μm. **(I)** Intensity cross-section (yz-plane from 0 to 1.5 mm, x = +50 μm) under RCP polarization. In **(E,H)**, brightness and colours refer to intensity and phase, respectively.

behaviour is also due to the properties of the Fourier transform of a focusing lens [39] .

After that, we tried to further extend the focusing on different points in space not located along the propagation axis (z-axis). To this aim, we added two tilting parameters in the focusing formula according to **Eq. 12**. Initially we propose a DFML able to focus two beams carrying different OAM at the same focal length but onto two distinct points on the same focal plane. To exploit these functionalities the implemented formulas were:

$$\phi^+(x,y) = \ell_1 \arctan\left(\frac{y}{x}\right) - \frac{2\pi}{\lambda}\left(\sqrt{f_1^2 + (x-x_1)^2 + (y-y_1)^2} - f_1\right) \quad (18)$$

$$\phi^-(x,y) = \ell_2 \arctan\left(\frac{y}{x}\right) - \frac{2\pi}{\lambda}\left(\sqrt{f_1^2 + (x-x_2)^2 + (y-y_2)^2} - f_1\right) \quad (19)$$

being $\ell_1 = 1$, $\ell_2 = 3$, $f_1 = 750\mu m$, $x_1 = y_1 = -50\mu m$, and $x_2 = y_2 = +50\mu m$.

As shown in **Figure 6**, the focalized OAM beams are generated at the expected points in space for both the polarizations.

In order to demonstrate the ability to focalize two beams carrying different OAM onto two distinct points in space at different focal lengths, we tried to focalize a spot at the same coordinates xy but at a higher focal length. In this regard, we simulated a DFML implementing the phase profiles:

$$\phi^+(x,y) = \ell_1 \arctan\left(\frac{y}{x}\right) - \frac{2\pi}{\lambda}\left(\sqrt{f_1^2 + (x-x_1)^2 + (y-y_1)^2} - f_1\right) \quad (20)$$

$$\phi^-(x,y) = \ell_2 \arctan\left(\frac{y}{x}\right) - \frac{2\pi}{\lambda}\left(\sqrt{f_2^2 + (x-x_2)^2 + (y-y_2)^2} - f_2\right) \quad (21)$$

being $\ell_1 = 1$, $\ell_2 = 3$, $f_1 = 500\mu m$, $f_2 = 1000\mu m$, $x_1 = y_1 = -50\mu m$, and $x_2 = y_2 = +50\mu m$.

The resulting simulations (**Figure 7**) show how using the above formulas it is possible to focus different OAM beams in completely different points in space. Accurately choosing the design parameters of a DFML, it is possible to avoid symmetry problems due to both high deviation from the propagation axis and short focal lengths.

DISCUSSION AND CONCLUSIONS

We have here presented the numerical design and simulation of dual-functional metalenses for the spin-controlled generation of OAM beams. The designed optical elements have been engineered to focus different OAM beams at distinct points in space, depending on the handedness of the circularly polarized state in input. That is achieved by properly selecting the resonant metaunits in order to act both on the dynamic and geometric phase imparted to the input beam, so that the polarization-

dependent geometric term combines with the polarization-insensitive dynamic one in order to induce a spin-decoupled functionality. Numerical simulations based on FEM analysis have been performed to define an optimized set of silicon resonators, with fixed thickness and different cross-sections, acting as half-wave plates with different phase delays on two orthogonal optical axes. In such a way, while a rotation of the pillar enables the direct control on the geometric phase, the selection of the proper cross-section is dictated by the specific dynamic phase to be imparted. We provided a set of 12 different nanopillars optimized for the wavelength of 775 nm, which can be used as lookup table for the design of any dual-functional metasurface. In particular, we proved the dual-functional behavior for the specific case represented by the spin-controlled generation of OAM beams, showing the on-demand focusing of beams with different values of OAM at distinct points in space. Such optical elements represent the ultimate optical evolution of standard spiral phase plates and *q*-plates. While the former optical elements are refractive/diffractive optics restricted to the generation of a specific OAM value, the latter ones are their metaoptics evolution, introducing polarization as an additional degree of freedom to control the helicity of the output twisted wavefronts. Dual-functional metalenses allow to further extend the optical functionality to the generation of any pair of different OAM beams. Moreover, additional functionalities can be added, as the focus onto distinct points in space. Again, that is made possible by the dual-functional behavior, since a standard metalens would focus only one circular polarization in input, while defocusing the orthogonal one. Therefore, the dual-functional implementation could be of extreme interest in total angular momentum analysis, boosting the evolution from diffractive [42] to metasurface [43, 44] optical architectures. Moreover, the possibility to design polarization-switchable optical elements can be of high interest in imaging and microscopy, to enable the compact integration of a high-resolution analysis in the setup. Besides the undoubtful gain in functionality, the metasurface paradigm provides an unprecedented increase in compactness and integration, representing the real merging between lens design and silicon photonics. The designed pattern can be fabricated by transferring a lithographic mask to the silicon substrate by means of etching techniques [45], or chemical vapor deposition [46]. Furthermore, the possibility to select even more complicated metaunits, such as coupled resonant nanofins, opens to the possibility to tune the wavelength dispersion and achieve full achromaticity, as demonstrated for imaging metalenses [47, 48], further extending the working range of the designed metaoptics.

DATA AVAILABILITY STATEMENT

The original contributions presented in the study are included in the article/supplementary material, further inquiries can be directed to the corresponding author.

AUTHOR CONTRIBUTIONS

AV performed FEM numerical analyses, metasurfaces design and optical simulations. GR gave suggestions in numerical simulations and contributed to the algorithms for beam propagation and metasurface computation. FR addressed the aim of the project and defined the design target specs of the optics. All authors discussed the results and the optimization configurations, contributed to the writing of the manuscript, and approved the final version.

FUNDING

The work was supported by the project LifeLab (CORIS, Veneto Region), by the project VORTEX3 (CEPOLISPE, Italian Ministry of Defence), and by the project STRADA (Italian Government, Presidency of the Council of Ministers).

REFERENCES

1. Allen L., Beijersbergen M. W., Spreeuw R. J. C., Woerdman J. P. Orbital Angular Momentum of Light and the Transformation of Laguerre-Gaussian Laser Modes. *Phys Rev A* (1992) 45:8185–9. doi:10.1103/physreva.45.8185
2. Rubinsztein-Dunlop H., Forbes A., Berry M. V., Dennis M. R., Andrews D. L., Mansuripur M., et al.Roadmap on Structured Light. *J Opt* (2016) 19:013001. doi:10.1088/2040-8978/19/1/013001
3. Padgett M. J. Orbital Angular Momentum 25 Years on [Invited]. *Opt Express* (2017) 25(10):11265–74. doi:10.1364/oe.25.011265
4. Wang J. Twisted Optical Communications Using Orbital Angular Momentum. *Sci China Phys Mech Astron* (2019) 62(3):34201. doi:10.1007/s11433-018-9260-8
5. Sit A., Bouchard F., Fickler R., Gagnon-Bischoff J., Larocque H., Heshami K., et al.High-dimensional Intracity Quantum Cryptography with Structured Photons. *Optica* (2017) 4(9):1006–10. doi:10.1364/optica.4.001006
6. De Oliveira M., Nape I., Pinnell J., TabeBordbar N., Forbes A. Experimental High-Dimensional Quantum Secret Sharing with Spin-Orbit-Structured Photons. *Phys Rev A* (2020) 101(4):042303. doi:10.1103/physreva.101.042303
7. Willig K. I., Harke B., Medda R., Hell S. W. STED Microscopy with Continuous Wave Beams. *Nat Methods* (2007) 4(11):915–8. doi:10.1038/nmeth1108
8. MacDonald M. P., Paterson L., Volke-Sepulveda K., Arlt J., Sibbett W., Dholakia K. Creation and Manipulation of Three-Dimensional Optically Trapped Structures. *Science* (2002) 296:1101–3. doi:10.1126/science.1069571
9. Franke-Arnold S. Optical Angular Momentum and Atoms. *Phil Trans R Soc A* (20172087) 375:20150435. doi:10.1098/rsta.2015.0435
10. Fatkhiev D. M., Butt M. A., Grakhova E. P., Kutluyarov R. V., Stepanov I. V., Kazanskiy N. L., et al.Recent Advances in Generation and Detection of Orbital Angular Momentum Optical Beams-A Review. *Sensors* (2021) 21(15):4988. doi:10.3390/s21154988
11. Lian Y., Qi X., Wang Y., Bai Z., Wang Y., Lu Z. OAM Beam Generation in Space and its Applications: A Review. *Opt Lasers Eng* (2022) 151:106923. doi:10.1016/j.optlaseng.2021.106923
12. Balthasar Mueller J. P., Rubin N. A., Devlin R. C., Groever B., Capasso F. Metasurface Polarization Optics: Independent Phase Control of Arbitrary Orthogonal States of Polarization. *Phys Rev Lett* (2017) 118(11):113901. doi:10.1103/physrevlett.118.113901
13. Jin Z., Janoschka D., Deng J., Ge L., Dreher P., Frank B., et al.Phyllotaxis-inspired Nanosieves with Multiplexed Orbital Angular Momentum. *eLight* (2021) 1(1):1–11. doi:10.1186/s43593-021-00005-9

14. Wan C., Rui G., Chen J., Zhan Q. Detection of Photonic Orbital Angular Momentum with Micro- and Nano-Optical Structures. *Front Optoelectron* (2019) 12:88–96. doi:10.1007/s12200-017-0730-8
15. Khonina S. N., Kotlyar V. V., Shinkaryev M. V., Soifer V. A., Uspleniev G. V. The Phase Rotor Filter. *J Mod Opt* (1992) 39:1147–54. doi:10.1080/09500349214551151
16. Turnbull G. A., Robertson D. A., Smith G. M., Allen L., Padgett M. J. The Generation of Free-Space Laguerre-Gaussian Modes at Millimetre-Wave Frequencies by Use of a Spiral Phaseplate. *Opt Commun* (1996) 127:183–8. doi:10.1016/0030-4018(96)00070-3
17. Massari M., Ruffato G., Gintoli M., Ricci F., Romanato F. Fabrication and Characterization of High-Quality Spiral Phase Plates for Optical Applications. *Appl Opt* (2015) 54(13):4077–83. doi:10.1364/ao.54.004077
18. Ruffato G., Massari M., Carli M., Romanato F. Spiral Phase Plates with Radial Discontinuities for the Generation of Multiring Orbital Angular Momentum Beams: Fabrication, Characterization, and Application. *Opt Eng* (2015) 54(11):111307. doi:10.1117/1.oe.54.11.111307
19. Marrucci L., Manzo C., Paparo D. Optical Spin-To-Orbital Angular Momentum Conversion in Inhomogeneous Anisotropic media. *Phys Rev Lett* (2006) 96:163905. doi:10.1103/physrevlett.96.163905
20. Desiatov B., Mazurski N., Fainman Y., Levy U. Polarization Selective Beam Shaping Using Nanoscale Dielectric Metasurfaces. *Opt Express* (2015) 23(17):22611–8. doi:10.1364/oe.23.022611
21. Brasselet E. Tunable High-Resolution Macroscopic Self-Engineered Geometric Phase Optical Elements. *Phys Rev Lett* (2018) 121(3):033901. doi:10.1103/PhysRevLett.121.033901
22. Ruffato G., Brasselet E., Massari M., Romanato F. Electrically Activated Spin-Controlled Orbital Angular Momentum Multiplexer. *Appl Phys Lett* (2018) 113(1):011109. doi:10.1063/1.5030844
23. Ruffato G., Romanato F. Design of Continuously Variant Metasurfaces for Conformal Transformation Optics. *Opt Express* (2020) 28(23):34201–18. doi:10.1364/oe.400627
24. Devlin R. C., Ambrosio A., Wintz D., Oscurato S. L., Zhu A. Y., Khorasaninejad M., et al.Spin-to-orbital Angular Momentum Conversion in Dielectric Metasurfaces. *Opt Express* (2017) 25(1):377–93. doi:10.1364/oe.25.000377
25. Genevet P., Capasso F., Aieta F., Khorasaninejad M., Devlin R. Recent Advances in Planar Optics: from Plasmonic to Dielectric Metasurfaces. *Optica* (2017) 4:139–52. doi:10.1364/optica.4.000139
26. Capasso F. The Future and Promise of Flat Optics: a Personal Perspective. *Nanophotonics* (2018) 7(6):953–7. doi:10.1515/nanoph-2018-0004
27. Devlin R. C., Ambrosio A., Rubin N. A., Mueller J. P. B., Capasso F. Arbitrary Spin-To-Orbital Angular Momentum Conversion of Light. *Science* (2017) 358(6365):896–901. doi:10.1126/science.aao5392
28. Huo P., Zhang C., Zhu W., Liu M., Zhang S., Zhang S., et al.Photonic Spin-Multiplexing Metasurface for Switchable Spiral Phase Contrast Imaging. *Nano Lett* (2020) 20(4):2791–8. doi:10.1021/acs.nanolett.0c00471
29. Li S., Li X., Zhang L., Wang G., Zhang L., Liu M., et al.Efficient Optical Angular Momentum Manipulation for Compact Multiplexing and Demultiplexing Using a Dielectric Metasurface. *Adv Opt Mater.* (2020) 8(8):1901666. doi:10.1002/adom.201901666
30. Guo Y., Zhang S., Pu M., He Q., Jin J., Xu M., et al.Spin-decoupled Metasurface for Simultaneous Detection of Spin and Orbital Angular Momenta via Momentum Transformation. *Light: Sci Appl* (2021) 10(1):1–12. doi:10.1038/s41377-021-00497-7
31. D. L. Andrews M. Babiker, editors (2012).*The Angular Momentum of Light*. Cambridge University Press, Cambridge, United Kingdom.
32. Lin D., Fan P., Hasman E., Brongersma M. L. Dielectric Gradient Metasurface Optical Elements. *science* (2014) 345(6194):298–302. doi:10.1126/science.1253213
33. Khorasaninejad M., Crozier K. B. Polarization Splitting at Infrared Wavelengths Using Silicon Nanoridges. *Nat Commun* (2014) 5(1):1–6. doi:10.1364/cleo_si.2014.sf1o.1
34. Zheng G., Mühlenbernd H., Kenney M., Li G., Zentgraf T., Zhang S. Metasurface Holograms Reaching 80% Efficiency. *Nat Nanotechnol* (2015) 10(4):308–12. doi:10.1038/nnano.2015.2
35. Zhang K., Yuan Y., Ding X., Ratni B., Burokur S. N., Wu Q. High-efficiency Metalenses with Switchable Functionalities in Microwave Region. *ACS Appl Mater Inter* (2019) 11(31):28423–30. doi:10.1021/acsami.9b07102
36. Ruffato G. OAM-inspired New Optics: the Angular Metalens. *Light Sci Appl* (2021) 10:96. doi:10.1038/s41377-021-00541-6
37. Aieta F., Genevet P., Kats M., Capasso F. Aberrations of Flat Lenses and Aplanatic Metasurfaces. *Opt Express* (2013) 21(25):31530–9. doi:10.1364/oe.21.031530
38. Aieta F., Genevet P., Kats M. A., Yu N., Blanchard R., Gaburro Z., et al.Aberration-free Ultrathin Flat Lenses and Axicons at Telecom Wavelengths Based on Plasmonic Metasurfaces. *Nano Lett* (2012) 12(9):4932–6. doi:10.1021/nl302516v
39. Goodman J. W. (2005). *Introduction to Fourier Optics*, 3rd ed., by J. W. Goodman. Englewood, CO: Roberts & Co. Publishers p. 1.
40. Jin J. M. *The Finite Element Method in Electromagnetics*(2015). John Wiley & Sons. Hoboken, New Jersey, United States.
41. Li J., Peng Z., Fu Y. Diffraction Transfer Function and its Calculation of Classic Diffraction Formula. *Opt Commun* (2007) 280:243–8. doi:10.1016/j.optcom.2007.08.053
42. Ruffato G., Massari M., Girardi M., Parisi G., Zontini M., Romanato F. Non-paraxial Design and Fabrication of a Compact OAM Sorter in the Telecom Infrared. *Opt Express* (2019) 27(17):24123–34. doi:10.1364/oe.27.024123
43. Ruffato G., Capaldo P., Massari M., Mafakheri E., Romanato F. Total Angular Momentum Sorting in the Telecom Infrared with Silicon Pancharatnam-Berry Transformation Optics. *Opt Express* (2019) 27(11):15750–64. doi:10.1364/oe.27.015750
44. Wang B., Wen Y., Zhu J., Chen Y., Yu S. Sorting Full Angular Momentum States with Pancharatnam-Berry Metasurfaces Based on Spiral Transformation. *Opt Express* (2020) 28:16342–51. doi:10.1364/oe.393859
45. Capaldo P., Mezzadrelli A., Pozzato A., Ruffato G., Massari M., Romanato F. Nano-fabrication and Characterization of Silicon Meta-Surfaces provided with Pancharatnam-Berry Effect. *Opt Mater Express* (2019) 9(3):1015–32. doi:10.1364/ome.9.001015
46. Su V.-C., Chu C. H., Sun G., Tsai D. P. Greg Sun, and Din Ping TsaiAdvances in Optical Metasurfaces: Fabrication and Applications [Invited]. *Opt Express* (2018) 26(10):13148–82. doi:10.1364/oe.26.013148
47. Chen W. T., Zhu A. Y., Capasso F. Flat Optics with Dispersion-Engineered Metasurfaces. *Nat Rev Mater* (2020) 5:604–20. doi:10.1038/s41578-020-0203-3
48. Chen W. T., Zhu A. Y., Sanjeev V., Khorasaninejad M., Shi Z., Lee E.A Broadband Achromatic Metalens for Focusing and Imaging in the Visible. *Nat Nanotech* (2018) 13:220–6. doi:10.1038/s41565-017-0034-6

Conflict of Interest: The authors declare that the research was conducted in the absence of any commercial or financial relationships that could be construed as a potential conflict of interest.

frontiers | Frontiers in Physics

REVIEW
published: 28 June 2022
doi: 10.3389/fphy.2022.938593

Rotational Doppler Effect With Vortex Beams: Fundamental Mechanism and Technical Progress

Song Qiu[1,2], *Tong Liu*[1,2], *You Ding*[1,2], *Zhengliang Liu*[1,2], *Lixiang Chen*[3]* and *Yuan Ren*[2,4]*

[1]Department of Aerospace Engineering and Technology, Space Engineering University, Beijing, China, [2]Lab of Quantum Detection and Awareness, Space Engineering University, Beijing, China, [3]Department of Physics and Collaborative Innovation Center for Optoelectronic Semiconductors and Efficient Devices, Xiamen University, Xiamen, China, [4]Department of Basic Course, Space Engineering University, Beijing, China

Structured light beams such as optical vortices can carry the orbital angular momentum (OAM) with an unbounded quantum number. Recent years have witnessed a growing interest in the rotational Doppler effect with vortex light. Here we present an overview on the technical progress in measuring the rotational Doppler effect associated with OAM. This includes how a high-order OAM light beam is crucial for realizing high-sensitivity remote sensing of rotating objects. The basic physical mechanism of rotational Doppler effect is manifested from both perspectives of the wave property and the conservation law of energy. Besides, we summarize the extension of the rotational Doppler effect from linear optics to nonlinear optics, and to quantum realms. Also, we discuss the main challenges and opportunities of angular remote sensing in a realistic scenario for future applications.

Keywords: orbital angular momentum, rotational Doppler effect, structured light, sensing and detection, Doppler velocimetry

OPEN ACCESS

Edited by:
Junjie Yu,
Shanghai Institute of Optics and Fine Mechanics (CAS), China

Reviewed by:
Mingbo Pu,
Institute of Optics and Electronics (CAS), China
Peng Li,
Northwestern Polytechnical University, China

***Correspondence:**
Lixiang Chen
chenlx@xmu.edu.cn
Yuan Ren
renyuan_823@aliyun.com

Specialty section:
This article was submitted to Optics and Photonics, a section of the journal Frontiers in Physics

Received: *07 May 2022*
Accepted: *06 June 2022*
Published: *28 June 2022*

Citation:
Qiu S, Liu T, Ding Y, Liu Z, Chen L and Ren Y (2022) Rotational Doppler Effect With Vortex Beams: Fundamental Mechanism and Technical Progress. Front. Phys. 10:938593. doi: 10.3389/fphy.2022.938593

INTRODUCTION

What would happen when placing a watch at the center of a rotating turntable, and viewed from above? Obviously, the watch hands will speed up or slow down depending on the rotation direction of the turntable [1]. If one applies this effect to all rotating vectors, for example to the spatial pattern of the electric field of any light beam carrying angular momentum [2–4], the additional rotation of the beam will result in a frequency shift proportional to the rate of rotation of the beam [5, 6]. This is the direct understanding of the rotational Doppler effect (RDE).

At first, this effect was found related to the circular polarization (CP) of the photon and was called the angular Doppler effect [7]. When the CP photon interacts with the rotating matter, the interchanges of rotational kinetic energy will bring a rotational frequency shift of $\sigma\omega$ to the photon, where ω is the rotating frequency and $\sigma = \pm 1$ for the right and left CP state of the photon. This phenomenon can be observed with manifestations ranging from the quantum world to satellite-based global positioning systems [8], and also can be observed when the CP light wave propagates through a gas of synchronously spinning molecules [9]. In 1992, Allen et al. established that light beams with helical phase-fronts, described by a transverse phase structure of $\exp(i\ell\varphi)$, can carry the orbital angular momentum (OAM) many times greater than the spin angular momentum of the photon [10], where φ is the azimuthal angle and ℓ is the topological charge. The most typical beam carrying OAM is the Laguerre–Gaussian (LG) beam [11–13]. Subsequently, people realized that this kind of helical beam may also introduce an azimuthal Doppler shift which is many times larger than the angular Doppler effect induced by the CP of the photon [14]. This azimuthal Doppler

effect differs significantly from the conventional linear Doppler frequency shift when it is born [7, 15]. The azimuthal Doppler shift in frequency arises not from linear motion, but rotation [16]. This effect should also not be confused with the Doppler effect observed for rotating objects due to the object having a linear velocity with respect to the observer. Unlike the linear Doppler effect (LDE) which is maximal in the plane of the rotation, the RDE is maximal in the direction of the angular velocity vector where the linear Doppler shift is zero [17].

After a simple coaxial superposition between the LG beam and the Gaussian beam, the RDE frequency shift can be observed directly due to the beat frequency phenomenon [5]. The technique of the superposition beam is soon widely used in RDE observation and OAM recognition [6, 18–20]. Especially, people can generate any superposition mode and high-order OAM beam with the development of spatial light modulators [21]. If the two components of the superposition beam have the same OAM number but opposite signs, this superposition beam can be called the phase-conjugated beam which has the self-interference property and is immune to the influence of the linear motion [22, 23]. These concepts were soon extended from linear optics to nonlinear optics and even quantum physics and many new applications have been derived [24–27].

In the 40 years of development since the concept of angular Doppler effect was first proposed, the RDE associated with structured light has established itself as one of the most interesting topics in structured light sensing applications, with relevance from spin to orbital angular momentum, from linear optics to nonlinear optics, even in the quantum optics and elsewhere. The method of rotational speed measurement based on the rotational Doppler effect applies to both microscopic particles and macroscopic objects. In the ongoing research, it is believed that this effect will bring more surprise to people.

THE BASIC MECHANISM OF ROTATIONAL DOPPLER EFFECT

The Interpretation From the Wave Properties

In 1842, the Austrian physicist Christian Doppler proposed that the wavelength of the radiation of an object will change due to the relative motion of the wave source and the observer, that is, the Doppler effect. When the object moves in a certain direction at a constant speed v , the electromagnetic wave will have a path difference during the propagation process, so the frequency shift of the beam received by the observer on the surface of the object is,

$$\Delta f = \frac{f_0 v \cos\theta}{c} \tag{1}$$

where f_0 is the frequency of the wave source, θ is the angle between the velocity vector and the wave vector, c is the light speed.

For a beam with helical phase, its Poynting vector, and hence the optical momentum, has an azimuthal component at every position within the beam. The angle α between the Poynting vector and the beam axis can be deduced theoretically and measured experimentally [11, 28, 29], as shown in **Figure 1A** [30]. The magnitude of angle α can be written as $\alpha = \ell\lambda/2\pi r$, where r is the radius from the beam axis to the position of the photon in the light field and ℓ denotes the topological charge of the beam, λ represents the wavelength. Light scattered from a moving surface is Doppler-shifted in frequency that can be observed both in translation and rotation [31], as is shown in **Figures 1B,C**, respectively. When a vortex beam illuminates the rotating disk on its axis, the angle between the velocity vector of each scatter and the Poynting vector is α, whose relationship with θ is $\alpha + \theta = \pi/2$. Combined with **Eq. 1**, the rotational Doppler shift can be can be expressed by $\Delta f = \ell\Omega/2\pi$. This is the basic expression of the RDE frequency shift. A typical form of using vortex light to obtain the RDE frequency shift is by interfering the scattered light with a reference light, as shown in **Figure 1D**. The RDE frequency shift also can be directly observed by a superposition state light with two components of opposite values of ℓ, as illustrated in **Figure 1E**.

On one hand, the RDE can be seen to have the same origin as the traditional LDE [32]. On the other hand, there is a significant difference between the LDE and RDE, namely, RDE frequency shift is independent of the wave frequency of the detected beam, such that the RDE can be observed using a white-light source [33]. Actually, the same RDE frequency shift also can be observed in the OAM-based radar [34, 35].

Since the light frequency is too high to be detected, like the conventional laser Doppler velocimetry, the RDE frequency shift can be observed by the interference phenomenon. As shown in **Figure 1D**, through the interference between the scattered beam and the reference beam, this frequency shift can be observed by extracting the beat frequency. Besides, when the illuminating light comprises two helically phased beams with topological charge $\pm\ell$, their scattering into a common detection mode gives opposite frequency shifts, and thus yielding an intensity modulation of doubled frequency of the basic RDE frequency shift [31].

The above interpretation only considers the rotation of the object. When the scatter has a compound motion of linear motion and rotation, the particles in the vortex field would experience both linear and rotational Doppler frequency shift. This can be understood from the phase change of the vortex field. The incident radiation wave can be simply written as,

$$E(\vec{r},t) = E_0 \exp\left\{-i\left[2\pi f t - kz - \Phi(\vec{r}_\perp)\right]\right\} \tag{2}$$

where the longitude phase is determined by propagation distance z and the phase in the cross section is defined by $\Phi(\vec{r}_\perp)$. For the vortex beam, the transverse phase is given by $\Phi(\vec{r}_\perp) = \ell\varphi$, where φ is the angular coordinates. As shown in **Figure 2A**, when a particle with both linear motion and rotational in the vortex field, it generates a burst of optical echoes which can be expressed by [37],

$$i(t) = i_0 \exp\{i[2kz(t) + \ell\varphi(t)]\} \tag{3}$$

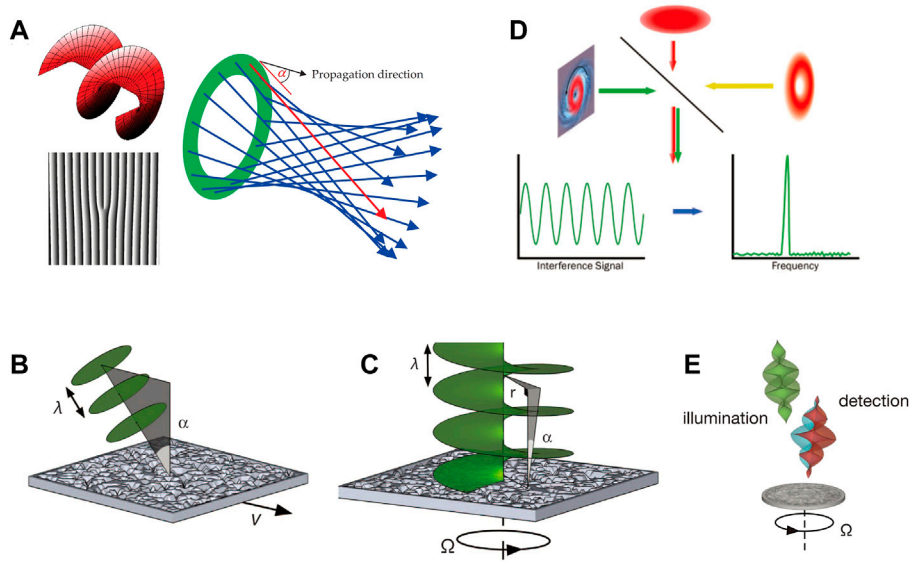

FIGURE 1 | The wave properties of optical vortex and the measurement of RDE frequency [30] **(A)** The Poynting vector of the vortex light **(B)** Translational Doppler frequency shift and **(C)** rotational Doppler frequency shift [31] **(D)** The detection scheme of the rotational Doppler shift with structured light [36] **(E)** A superposition of helically phased beams with opposite signs of ℓ incident on a surface rotating at a speed Ω, results in a Doppler shift of the coaxial light.

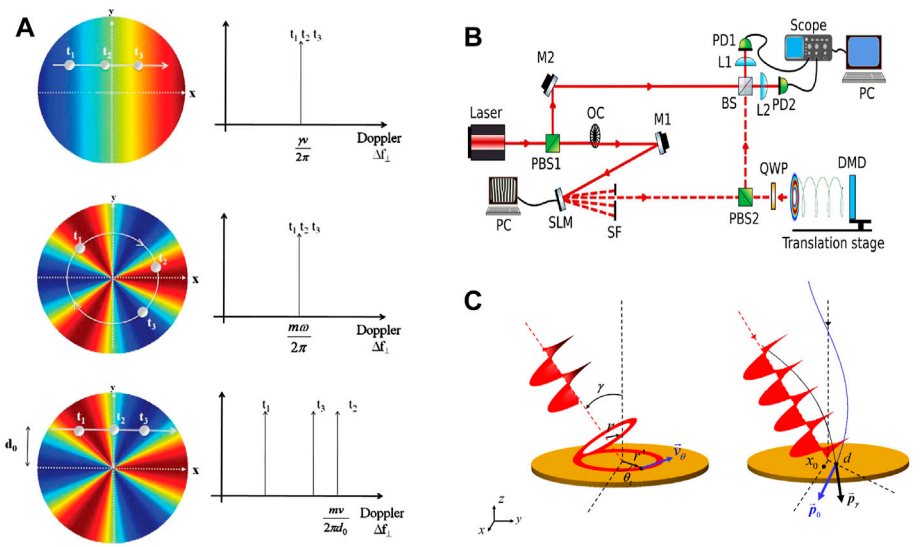

FIGURE 2 | (A) The production of Doppler effect with structured light [37]. **(B)** Compound motion detection scheme [38]. **(C)** Rotational Doppler effect at vortex light oblique incidence [23].

where $z(t) = v_z t$ and $\varphi(t) = \Omega t$. As a result, the total frequency shift can be expressed by $\Delta f = \frac{1}{2\pi}(2kv_z + \ell\Omega)$, appearing as a combination of the linear and the rotational frequency shift. Such a characteristics of the vortex light can then be used to detect the compound motion of the target as shown in **Figure 2B**.

Furthermore, the above deduction is effective only on the condition that the beam illuminates on the axis of the rotating object. When the vortex illuminates the rotating body non-coaxially as shown in **Figure 2C**, the RDE behaves differently. The radius of the vortex light and the radius of each small scatter on the rotating body under the light field are always the same when the vortex light illuminate the rotating object on its axis, while these two radii are unequal when the light illuminates non-coaxially. Based on the small scatterer model, Qiu et al. deduced the rotational Doppler shift when there is a small lateral misalignment or oblique angle between the vortex axis and rotating axis, respectively [23, 39]. The corresponding RDE frequency shift is given by,

$$\Delta f_d = \frac{\ell\Omega}{2\pi}\left(1 + \frac{d\cos\theta}{r_1}\right) \tag{4}$$

$$\Delta f_\theta = \frac{\ell\Omega\left(\sin^2\theta_z + \cos\gamma\cos^2\theta_z\right)}{2\pi\sqrt{1 - \left(\sin\gamma\sin\theta_z\right)^2}} \tag{5}$$

where d and γ denote the lateral misalignment distance and the oblique angle, respectively. When the illuminating light is not coaxial with the rotational axis, the RDE frequency spectrum would be broadened.

The Energy Transfer in RDE

It is also instructive to understand the RDE from the conservation laws of energy and angular momentum when photons interact with the medium. For a rotating particle, the rotational kinetic energy due to the rotational motion can be expressed as,

$$E = \frac{L^2}{2I} \tag{6}$$

where L is the angular momentum of the particle and its magnitude is given by $L = I\Omega$ ($\Omega = v/r$), I is the momentum of inertia whose value can be expressed by $I = mr^2$.

In the case of rotation, a system composed of rotating particles and the photons obeys the kinetic energy conversion, namely [7, 40],

$$\frac{L_1^2}{2I} + E_1 = \frac{L_2^2}{2I} + E_2 + h(\nu + \Delta\nu) \tag{7}$$

where L_1 and L_2 represent the angular momentum that the rotating particle has before and after interacting with the beam, respectively. E_1 and E_2 represent the intermediate electric energy of atoms or molecules that the particle receives and emits before and after the action of the detection light; ν represents the frequency of the scattered light at different times when the particle is stationary, and $\Delta\nu$ represents the angular Doppler frequency shift of the scattered photons due to the rotation of the particle.

During the emission or absorption of photons by atoms, the energy transfer can be expressed by $E_1 - E_2 = h\nu$. Combined with **Eq. 7** we have,

$$h\Delta\nu = \frac{L_1^2 - L_2^2}{2I} = \frac{(L_1 - L_2)(L_1 + L_2)}{2I} = \frac{\Delta L}{I}\left(\frac{L_1 + L_2}{2}\right) \tag{8}$$

For the systems interacted by beams and rotating particles, there is also a momentum conservation relationship,

$$L_a + \mathcal{L}_a^{'} = L_b + \mathcal{L}_b^{'} \tag{9}$$

where $\mathcal{L}_a^{'}$ and $\mathcal{L}_b^{'}$ represent the angular momentum carried by the photons before and after the beam interacts with the rotating particle, respectively. L_a and L_b denote the angular momentum carried by the rotating particle. For the linearly polarized vortex beam, the magnitude of the angular momentum is $\ell\hbar$. Therefore, the momentum transformation of the photons can be expressed as,

$$\mathcal{L}_b^{'} - \mathcal{L}_a^{'} = (\ell_b - \ell_a)\hbar \tag{10}$$

where ℓ_a and ℓ_b are the topological charge of the incident vortex light and the scatter light to be detected, respectively.

By combining **Eqs 8–10**, we can obtain the RDE frequency shift as,

$$\Delta\nu = (\ell_b - \ell_a)\Omega/2\pi \tag{11}$$

If the scattered light to be detected is in the fundamental Gaussian mode, i.e., $\ell_b = 0$, the above formula becomes exactly the same as that of the RDE frequency shift, namely, $\Delta\nu = \ell\Omega/2\pi$. Note that the LG modes form a complete and orthogonal basis for paraxial light beams. Therefore, the RDE frequency shift can also be observed by detecting the high-order OAM mode of the scattered light. When the scattered light is not in the fundamental mode, the RDE frequency shift can be calculated according to **Eq. 11**. The magnitude of the frequency shift is determined by the rotational speed and the OAM mode difference between the incident and the scattered light [41].

In the nonlinear regime, the perspective of energy and momentum conservation also can be used to interpret the origin of RDE. When the circularly polarized beam passes through a spinning nonlinear optical crystal with three-fold rotational symmetry, the beam would experience a Doppler shift of three times that of the optical crystal [24]. Furthermore, based on the mirror symmetry for electromagnetic interactions, the RDE frequency shift can be doubled through cascading two rotational Doppler processes [25]. This cascaded RDE can also be understood according to the law of conservation of momentum.

The magnitude of the frequency shift is proportional to both the topological charge and the rotational speed, as can be directly seen from the RDE formula. In order to ensure the frequency shift can be measured, this scheme is more available for measuring objects rotating at high speed rather than low speed [42]. On the other hand, the RDE frequency is also proportional to the topological charge of the illuminating beam; therefore, the detection sensitivity can be increased by using higher-order OAM beams. Up to now, a myriad of approaches have been developed for the generation of higher-order OAM beams, demonstrating up to $\ell = 100$ by using a metasurface OAM laser [43], up to $\ell = 600$ by using a spatial light modulator [44], and as high as $\ell \approx 10000$ with a spiral phase mirror [45].

APPLICATION OF ROTATIONAL DOPPLER EFFECT

RDE in the Rotational Motion Detection

Since Allen et al. proposed their inspiring scheme of the detection of a spinning object by using light's orbital angular momentum, there have been massive relevant research literatures in this area. In addition to the rotational speed, other rotation parameters such as rotating direction and acceleration rate have been measured as well. Since the beat frequency effect can only provide the magnitude of the frequency shift without the direction information [46], the acquisition of the rotation direction becomes a tricky problem. Rosales-Guzman et al.

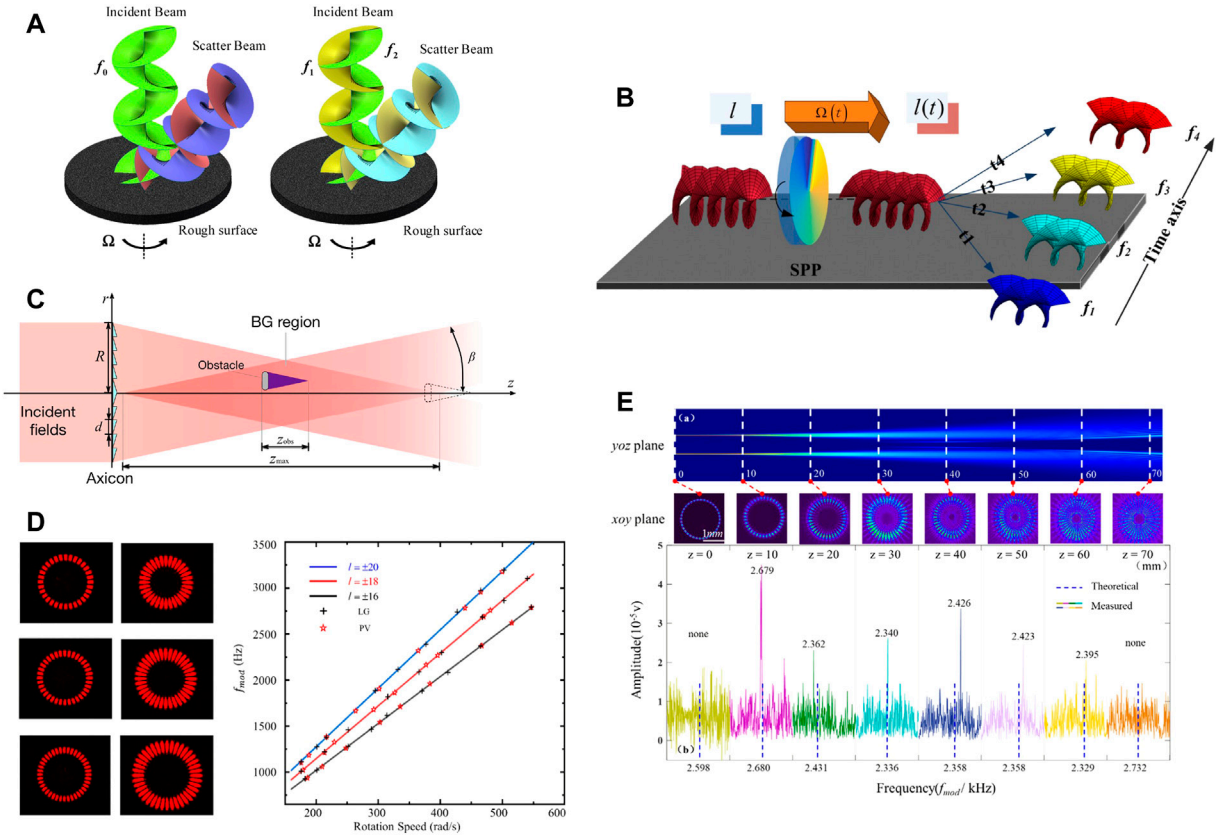

FIGURE 3 | RDE in rotational speed detection. **(A)** Direction-sensitive detection by dual-frequency optical vortex [48]. **(B)** Detection of angular acceleration based on optical RDE [51]. **(C)** Non-diffractive Bessel-Gaussian beams for the detection of rotational speed [57]. **(D)** RDE detection results by using perfect optical vortex [58]. **(E)** The measured results of RDE frequency shift along the propagation path of ring Airy Gaussian vortex [59].

devised a scheme to impart an additional rotation on the illuminating vortex beam, which can give a reference to identify the rotation direction [47]. By employing dual-frequency vortex light, as shown in **Figure 3A**, Li et al. transform the Doppler signals from the low-frequency domain to the medium-frequency domain, and thus distinguishing the rotational direction by comparing the modulated signal and the reference signal [48].

Recently, the vectorial counterpart of RDE was revealed, which uses vectorial polarization fields and shows the potential to retrieve the full vectorial motion information of the moving object [49, 50]. The above measurements are based on the constant rotation velocity. While for variable rotation, Zhai et al. succeeded in measuring the angular acceleration through a time-frequency analysis of the RDE frequency shift [51]. The transformation of OAM beams when passing through a non-uniform spinning SPP is shown in **Figure 3B**.

At present, the accuracy of RDE-based speed measurement is relatively high, generally reaching over 95% [31, 33, 47]. Even under the light noncoaxial incidence condition, the rotational speed still can be measured in a high accuracy through the extraction the frequency difference in the discrete frequency shift signals [52]. However, the accuracy of the speed measurement also fluctuates in response to changes in measurement conditions [53]. Moreover, since the frequency shift caused by the RDE is proportional to the object's angular velocity, in order to ensure the frequency shift can be measured, this scheme is more available for measuring objects rotating at high speed rather than low speed [54]. The rotational speed can be measured in most laboratory conditions is larger than 2π rad/s, and only a handful of measurement experiments those use the spatial light modulators to mimic real rotating objects can reach a lower speed [55, 56].

RDE Introduced by Different Types of Vortex Beams

Researchers have tried using different types of structured vortex beams to investigate RDE, including Laguerre–Gaussian (LG) beam [31], Bessel-Gaussian (BG) beam [57], Perfect Optical Vortex (POV) beam [58, 60, 61], and Ring Airy Gaussian Vortex (RAiGV) [59]. The LG beam is the most popular structured light used in the RDE detection which can stably propagates over a long distance. The transverse beam profile is a single intensity ring with zero radial index $p = 0$. For the LG beams with non-zero radial index, multiple rings would appear in

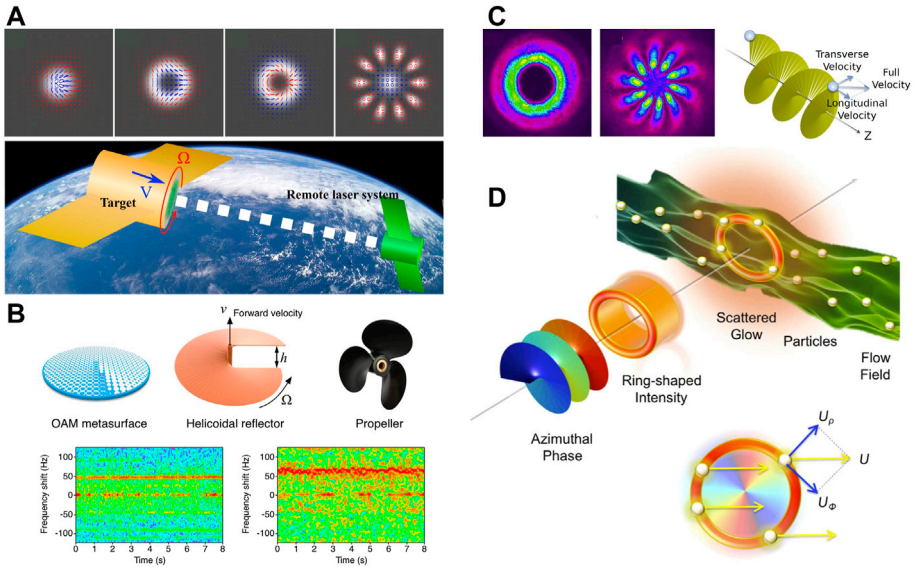

FIGURE 4 | Compound motion detection by RDE of structured light. **(A)** In-suit detection of a cooperative target's longitudinal and angular speed using structured light [66]. **(B)** Experimental observation of linear and rotational Doppler shift from several designer surface [67]. **(C)** Measuring the translational and rotational velocities of particles [38]. **(D)** Measurement of flow velocity with helical beams of light [69].

the radial direction. Experiments have shown that the LG beams of nonzero radial indices can enhance the light intensity and the amplitude of the RDE frequency signal, in comparison with those of zero radial index [62]. The BG beam has been proved to have non-diffractive and self-recovery characteristics which can be immune to the influence of the small obstacles in the optical path [57], as shown in **Figure 3C**.

Also, POV have recently attracted a lot of research attention, owing to its characteristic feature that they have the same intensity profile regardless of carrying different topological charges, as is shown in **Figure 3D** [58]. Therefore, the POV beam is more flexible when detecting the objects of different sizes. In particular, when the topological charges of the two components of a superposition beam are not the same magnitude, the POV performs better than the LG beam [58]. It was reported that, as is shown in **Figure 3E**, the RAiGV has the same well performance in spinning speed detection as other vortex beams [59]. Besides, the RAiGV beam has self-focusing property, which enables the best detection results on its focal length. These researches fully considered the RDE detection effect of the different types of vortex beams, which offers useful instructions in choosing suitable vortex beams for realistic applications.

RDE in Compound Motion Measurement

In the actual applications, we usually encounter the compound motion, e.g., translation, rotation, and other kinds of micro-motion. Accordingly, the scattered light would experience LDE, radial Doppler effect [63], RDE, and micro-Doppler effect [64, 65]. These frequency shifts are generally coupled to each other. Thus, a question arises naturally as to how we can measure them individually. It was reported that the translational and rotational velocities of the particles can both be determined by switching between two modes. They were able to isolate the longitudinal frequency shift by illuminating a Gaussian beam while measure the rotational frequency shift by using LG modes. In 2019, Carmelo et al. put forward a novel three-dimensional technique that enables the direct and simultaneous measurement of both the longitudinal and angular speed of cooperative targets [66], as was shown in **Figure 4A**.

The rotational Doppler shift could be separated from the micro-Doppler shift by using two microwave beams of opposite OAM [67]. **Figure 4B** shows the spectrogram of a normal 5.8 GHz incident wave reflected from a spinning helicoidal reflector, and the scattered waves produce both linear and rotational Doppler shifts. **Figure 4C** reveals the reason why a particle moving along a spiral trajectory will produce both linear and rotational frequency shifts. By employing the OAM interferometry of the multi-mode beam, decoupled measurement of linear velocity and rotational speed can be achieved [55, 68]. These methods can partially resolve the decoupled measurements of the compound motion with OAM beam. It is expected that the use of multidimensional information about light beams may provide new solutions to this engineering challenge in the future.

It was found that not only the rotational speed, but also the flow velocity could be accurately estimated by making use of the transversal Doppler effect of the returned signals that depend only on the azimuthal indices of the vortex beams [69], as was shown in **Figure 4D**. Also, the fluid flow vorticity could also be measured in a straightforward way by taking advantage of the RDE [70], which allowed for a localized real-time determination of vorticity in a fluid flow with three-dimensional resolution.

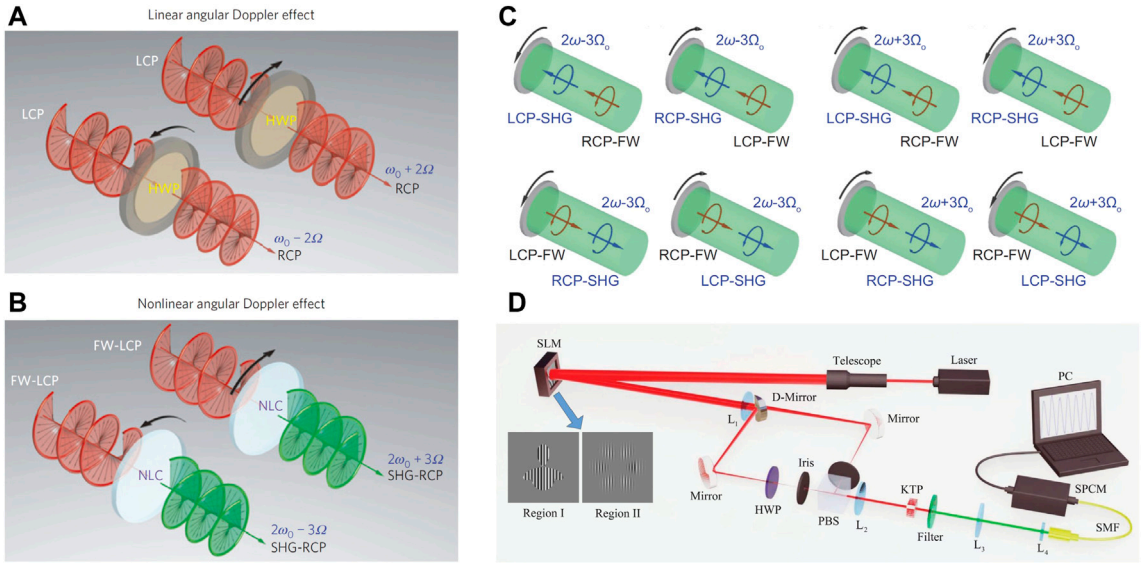

FIGURE 5 | RDE in nonlinear optics. RDE in **(A)** linear and **(B)** nonlinear optics. The second harmonic generation signal experiences a Doppler shift of three times [24]. **(C)** The evolution of RDE of second harmonic generation from a quartz coated with silver mirror [71]. **(D)** RDE detection by frequency up-conversion [72].

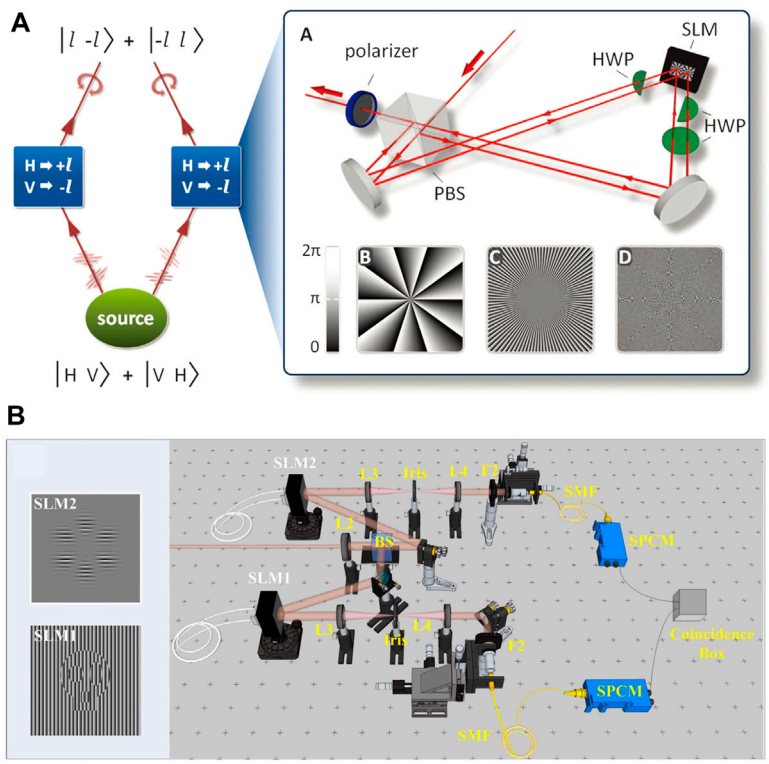

FIGURE 6 | RDE in quantum optics. **(A)** Quantum entanglement of high order angular momenta [26]. **(B)** Quantum remote sensing of the angular rotation of structured objects [74]. It suggests potential applications in developing a noncontact way for angular remote sensing of object.

RDE in Nonlinear and Quantum Optics Field

When the circularly polarized beam passes through a spinning nonlinear optical crystal with three-fold rotational symmetry, it was found that the second harmonic generation signals may experience a Doppler effect of three times the spinning speed [24]. **Figures 5A,B** illustrate the RDE in the linear and nonlinear optical regime. This demonstration of RDE provided us with an insight into the interaction of light with moving nonlinear media. By using the post-

selection and beating frequency techniques, researchers further simplified the conventional nonlinear RDE measurement setup and successfully observed the RDE of second harmonic generation waves [71]. As shown in **Figure 5C**, when the forward propagating fundamental wave with left- and right-circular polarization pass through the spinning nonlinear material with three-fold rotational symmetry, the RDE frequency shift is three times of the spinning speed [71]. Besides, the RDE also can be detected by using the near-infrared light to illuminate the rotating object, in which the rotational frequency shifts can be transferred to the visible regime after parametric up-conversion [72]. The corresponding up-conversion detection scheme is shown in **Figure 5D**.

In addition to those classical methods, quantum remote sensing with OAM-entangled photon pairs enabled an improved angular resolution that can be amplified by large OAM values [73]. By using photonic entanglement of high orbital angular momenta, Flicker *et al.* demonstrated a method of increasing the angular resolution in remote sensing [26]. As shown in **Figure 6A**, the polarization entanglement is created in a parametric down-conversion process and afterward transferred to modes with high quanta of OAM. Also, Zhang et al. showed that the object's angular rotational speed can be measured nonlocally, the corresponding experimental scheme is shown in **Figure 6B**. They revealed that the angular sensitivity of the object in the path of idler photons is proportional to the OAM values of signal photons, which can be considered as a quantum version of RDE [74].

RDE in Various Bands

Since the RDE has nothing to do with the wavelength of the detection beam [33]. In recent years, the RDE in the radio domain is investigated widely [65]. Zhao et al. used the phase accumulation method to experimentally verify the RDE in the microwave band [35]. Although the measurement accuracy of the rotational speed is high, phase accumulation takes relatively long time and has certain limitations in practical applications. Similar to the detection technique of the light wave, Brousseau et al. realized the RDE detection of the microwave at 2.47 GHz by the spectrum analyzer [75]. Both the rotational speed and the direction can be measured through this model. The RDE of uniformly accelerated targets has also been studied in the radio frequency band by means of time-frequency analysis [76].

For the microwave band, the signal extraction process when detecting the target is more convenient. However, vortex electromagnetic waves in the microwave band are difficult to propagate over long distances. Structured laser can be transmitted over long distances, but the probe beam is easy to be disturbed by the atmospheric turbulence [77]. Further, the extraction of weak light signals under long-distance detection is more troublesome.

CONCLUSION AND PERSPECTIVES

In summary, with the technological advancements in the structured light generation, propagation, manipulation, and detection, we have offered a systematic understanding on the physical origin and behaviors of the RDE, from both fundamental and applied points of view. We have analyzed the basic mechanism of the RDE from the perspective of the wave property of light and the conservation of energy. Moreover, we have summarized the recent developments in rotational speed measurement based on RDE, ranging from the molecular motion to the rotation of macro-objects, and from linear optics to nonlinear optics, and to quantum optical realms.

It is noted that, although a lot of studies have been conducted on the fundamental and applied aspects of RDE, there is still a long way to go in terms of developing a viable system and putting this technique into practical applications. There are various hurdles to solve in order to implement detection from the lab to the outside scale. Firstly, atmospheric turbulence has a significant impact on the mode purity of an OV beam as it propagates across free space [77–81]. This is a challenge that must be solved, both for OAM-based communication and detection applications. Secondarily, the relative pose between the detection OV beam and the rotating object has a significant influence on the detection signal [68, 82–84], therefore the distribution of the RDE signals under different conditions of motion and positions needs to be further investigated. Thirdly, the receiving and processing of signals is an important aspect for the detection system, especially for weak signals at the photon-counting level [54]. Also, as the RDE is independent of the wavelength of the beam [75, 76], we can anticipate that an extension of the RDE into the radar band might lead to some new discoveries. In future studies, we can imagine that the RDE with structured light will provide us with more and more surprises.

AUTHOR CONTRIBUTIONS

LC and YR conceived the idea. YR and LC supervised the project. SQ combed through the entire relevant literature. All authors discussed the results. SQ and TL drafted the papers with the input from all authors.

FUNDING

Key Research Projects of Foundation Strengthening Program of China (2019-JCJQ-ZD); National Natural Science Foundation of China (61805283 and 62173342).

REFERENCES

1. Padgett M. Electromagnetism: Like a Speeding Watch. *Nature* (2006) 443: 924–5. doi:10.1038/443924a
2. O'Neil AT, MacVicar I, Allen L, Padgett MJ. Intrinsic and Extrinsic Nature of the Orbital Angular Momentum of a Light Beam. *Phys Rev Lett* (2002) 88: 053601. doi:10.1103/PhysRevLett.88.053601
3. Mohammadi SM, Daldorff LKS, Forozesh K, Thidé B, Bergman JES, Isham B, et al. Orbital Angular Momentum in Radio: Measurement Methods. *Radio Sci* (2010) 45. doi:10.1029/2009rs004299
4. Bialynicki-Birula I, Bialynicka-Birula Z. Rotational Frequency Shift. *Phys Rev Lett* (1997) 78:2539–42. doi:10.1103/PhysRevLett.78.2539
5. Basistiy IV, Slyusar VV, Soskin MS, Vasnetsov MV, Bekshaev AY. Manifestation of the Rotational Doppler Effect by Use of an off-Axis Optical Vortex Beam. *Opt Lett* (2003) 28:1185–7. doi:10.1364/ol.28.001185

6. Vasnetsov MV, Torres JP, Petrov DV, Torner L. Observation of the Orbital Angular Momentum Spectrum of a Light Beam. *Opt Lett* (2003) 28:2285–7. doi:10.1364/ol.28.002285
7. Garetz BA. Angular Doppler Effect. *J Opt Soc Am* (1981) 71:609–11. doi:10.1364/josa.71.000609
8. Ashby N. Relativity in the Global Positioning System. *Living Rev Relativ* (2003) 6:1. doi:10.12942/lrr-2003-1
9. Korech O, Steinitz U, Gordon RJ, Averbukh IS, Prior Y. Observing Molecular Spinning via the Rotational Doppler Effect. *Nat Photon* (2013) 7:711–4. doi:10.1038/nphoton.2013.189
10. Allen L, Beijersbergen MW, Spreeuw RJC, Woerdman JP. Orbital Angular Momentum of Light and the Transformation of Laguerre-Gaussian Laser Modes. *Phys Rev A* (1992) 45:8185–9. doi:10.1103/PhysRevA.45.8185
11. Allen L, Padgett MJ. The Poynting Vector in Laguerre-Gaussian Beams and the Interpretation of Their Angular Momentum Density. *Opt Commun* (2000) 184:67–71. doi:10.1016/s0030-4018(00)00960-3
12. Molina-Terriza G, Torres JP, Torner L. Management of the Angular Momentum of Light: Preparation of Photons in Multidimensional Vector States of Angular Momentum. *Phys Rev Lett* (2002) 88:013601. doi:10.1103/PhysRevLett.88.013601
13. Padgett MJ, Allen L. Orbital Angular Momentum Exchange in Cylindrical-Lens Mode Converters. *J Opt B Quan Semiclass. Opt.* (2002) 4:S17–S19. doi:10.1088/1464-4266/4/2/362
14. Allen L, Babiker M, Power WL. Azimuthal Doppler Shift in Light Beams with Orbital Angular Momentum. *Opt Commun* (1994) 112:141–4. doi:10.1016/0030-4018(94)00484-6
15. Censor D. Theory of the Doppler Effect: Fact, Fiction and Approximation. *Radio Sci* (1984) 19:1027–40. doi:10.1029/RS019i004p01027
16. Marrucci L. Spinning the Doppler Effect. *Science* (2013) 341:464–5. doi:10.1126/science.1242097
17. Yao AM, Padgett MJ. Orbital Angular Momentum: Origins, Behavior and Applications. *Adv Opt Photon* (2011) 3:161–204. doi:10.1364/aop.3.000161
18. Zhou H-L, Fu D-Z, Dong J-J, Zhang P, Chen D-X, Cai X-L, et al. Orbital Angular Momentum Complex Spectrum Analyzer for Vortex Light Based on the Rotational Doppler Effect. *Light Sci Appl* (2016) 6:e16251. doi:10.1038/lsa.2016.251
19. Berkhout GCG, Lavery MPJ, Padgett MJ, Beijersbergen MW. Measuring Orbital Angular Momentum Superpositions of Light by Mode Transformation. *Opt Lett* (2011) 36:1863–5. doi:10.1364/OL.36.001863
20. Lavery MPJ, Berkhout GCG, Courtial J, Padgett MJ. Measurement of the Light Orbital Angular Momentum Spectrum Using an Optical Geometric Transformation. *J Opt* (2011) 13:064006. doi:10.1088/2040-8978/13/6/064006
21. Wang X, Nie Z, Liang Y, Wang J, Li T, Jia B. Recent Advances on Optical Vortex Generation. *Nanophotonics* (2018) 7:1533–56. doi:10.1515/nanoph-2018-0072
22. Okulov AY. Rotational Doppler Shift of a Phase-Conjugated Photon. *J Opt Soc Am B* (2012) 29:714–8. doi:10.1364/josab.29.000714
23. Qiu S, Liu T, Ren Y, Li Z, Wang C, Shao Q. Detection of Spinning Objects at Oblique Light Incidence Using the Optical Rotational Doppler Effect. *Opt Express* (2019) 27:24781–92. doi:10.1364/OE.27.024781
24. Li G, Zentgraf T, Zhang S. Rotational Doppler Effect in Nonlinear Optics. *Nat Phys* (2016) 12:736–40. doi:10.1038/nphys3699
25. Deng J, Li KF, Liu W, Li G. Cascaded Rotational Doppler Effect. *Opt Lett* (2019) 44:2346–9. doi:10.1364/OL.44.002346
26. Fickler R, Lapkiewicz R, Plick WN, Krenn M, Schaeff C, Ramelow S, et al. Quantum Entanglement of High Angular Momenta. *Science* (2012) 338:640–3. doi:10.1126/science.1227193
27. Guo Z, Meng J, An M, Cheng P, Jia J, Chang Z, et al. Remote Angular Velocity Measurement by the Cascaded Rotational Doppler Effect. *Appl Opt* (2021) 60:9892–5. doi:10.1364/AO.438997
28. Leach J, Keen S, Padgett MJ, Saunter C, Love GD. Direct Measurement of the Skew Angle of the Poynting Vector in a Helically Phased Beam. *Opt Express* (2006) 14:11919–24. doi:10.1364/oe.14.011919
29. Qiu S, Ren Y, Liu T, Liu Z, Wang C, Ding Y, et al. Directly Observing the Skew Angle of a Poynting Vector in an Oam Carrying Beam via Angular Diffraction. *Opt Lett* (2021) 46:3484–7. doi:10.1364/OL.432771
30. Padgett M. A New Twist on the Doppler Shift. *Phys Today* (2014) 67:58–9. doi:10.1063/pt.3.2286
31. Lavery MPJ, Speirits FC, Barnett SM, Padgett MJ. Detection of a Spinning Object Using Light's Orbital Angular Momentum. *Science* (2013) 341:537–40. doi:10.1126/science.1239936
32. Fang L, Padgett MJ, Wang J. Sharing a Common Origin between the Rotational and Linear Doppler Effects. *Laser Photon Rev* (2017) 11:1700183. doi:10.1002/lpor.201700183
33. Lavery MPJ, Barnett SM, Speirits FC, Padgett MJ. Observation of the Rotational Doppler Shift of a White-Light, Orbital-Angular-Momentum-Carrying Beam Backscattered from a Rotating Body. *Optica* (2014) 1:1–4. doi:10.1364/optica.1.000001
34. Kang L, Cheng Y, Xiang L, Wang H, Qin Y, Yue G. Spinning Target Detection Using Oam-Based Radar. In: International Workshop on Electromagnetics: Applications & Student Innovation Competition; 2017 May 30–Jun 1; London, United Kingdom. London, UK: IEEE (2017). p. 29–30.
35. Zhao M, Gao X, Xie M, Zhai W, Xu W, Huang S, et al. Measurement of the Rotational Doppler Frequency Shift of a Spinning Object Using a Radio Frequency Orbital Angular Momentum Beam. *Opt Lett* (2016) 41:2549–52. doi:10.1364/OL.41.002549
36. A Forbes, TE Lizotte, C Rosales-Guzmán, A Belmonte, JP Torres, editors. Optical Metrology with Structured Light. *Laser Beam Shaping XVII*. San Diego, CA: SPIE (2016). p. 995007.
37. Belmonte A, Torres JP. Optical Doppler Shift with Structured Light. *Opt Lett* (2011) 36:4437–9. doi:10.1364/OL.36.004437
38. Rosales-Guzmán C, Hermosa N, Belmonte A, Torres JP. Measuring the Translational and Rotational Velocities of Particles in Helical Motion Using Structured Light. *Opt Express* (2014) 22:16504–9. doi:10.1364/OE.22.016504
39. Qiu S, Liu T, Li Z, Wang C, Ren Y, Shao Q, et al. Influence of Lateral Misalignment on the Optical Rotational Doppler Effect. *Appl Opt* (2019) 58:2650–5. doi:10.1364/AO.58.002650
40. Garetz BA, Arnold S. Variable Frequency Shifting of Circularly Polarized Laser Radiation via a Rotating Half-Wave Retardation Plate. *Opt Commun* (1979) 31:1–3. doi:10.1016/0030-4018(79)90230-X
41. Zhou H, Fu D, Dong J, Zhang P, Zhang X. Theoretical Analysis and Experimental Verification on Optical Rotational Doppler Effect. *Opt Express* (2016) 24:10050–6. doi:10.1364/OE.24.010050
42. Deng D, Zhao H, Ni J, Li Y, Qiu C-W. A Phase-To-Intensity Strategy of Angular Velocity Measurement Based on Photonic Orbital Angular Momentum. *Nanophotonics* (2022) 11:865–72. doi:10.1515/nanoph-2021-0461
43. Sroor H, Huang Y-W, Sephton B, Naidoo D, Vallés A, Ginis V, et al. High-Purity Orbital Angular Momentum States from a Visible Metasurface Laser. *Nat Photon* (2020) 14:498–503. doi:10.1038/s41566-020-0623-z
44. Pinnell J, Rodríguez-Fajardo V, Forbes A. Probing the Limits of Orbital Angular Momentum Generation and Detection with Spatial Light Modulators. *J Opt* (2021) 23:015602. doi:10.1088/2040-8986/abcd02
45. Fickler R, Campbell G, Buchler B, Lam PK, Zeilinger A. Quantum Entanglement of Angular Momentum States with Quantum Numbers up to 10,010. *Proc Natl Acad Sci U.S.A* (2016) 113:13642–7. doi:10.1073/pnas.1616889113
46. Varghese B, Rajan V, van Leeuwen TG, Steenbergen W. Discrimination between Doppler-Shifted and Non-shifted Light in Coherence Domain Path Length Resolved Measurements of Multiply Scattered Light. *Opt Express* (2007) 15:13340–50. doi:10.1364/oe.15.013340
47. Rosales-Guzmán C, Hermosa N, Belmonte A, Torres JP. Direction-Sensitive Transverse Velocity Measurement by Phase-Modulated Structured Light Beams. *Opt Lett* (2014) 39:5415–8. doi:10.1364/OL.39.005415
48. Li Z, Liu T, Ren Y, Qiu S, Wang C, Wang H. Direction-Sensitive Detection of a Spinning Object Using Dual-Frequency Vortex Light. *Opt Express* (2021) 29:7453–63. doi:10.1364/OE.418192
49. Wan Z, Fang L, Wang J. Direction-discriminated Rotational Doppler Velocimetry with Circularly Polarized Vortex Beams. *Opt Lett* (2022) 47:1021–4. doi:10.1364/ol.443022
50. Fang L, Wan Z, Forbes A, Wang J. Vectorial Doppler Metrology. *Nat Commun* (2021) 12:4186. doi:10.1038/s41467-021-24406-z
51. Zhai Y, Fu S, Yin C, Zhou H, Gao C. Detection of Angular Acceleration Based on Optical Rotational Doppler Effect. *Opt Express* (2019) 27:15518–27. doi:10.1364/OE.27.015518

52. Qiu S, Ding Y, Liu T, Liu Z, Ren Y. Rotational Object Detection at Noncoaxial Light Incidence Based on the Rotational Doppler Effect. *Opt Express* (2022) 30: 20441–50. doi:10.1364/oe.461179
53. Ding Y, Liu T, Liu Z, Qiu S, Xu L, Ren Y. Detection of a Spinning Object with Circular Procession Using an Optical Vortex Beam. *Opt Lett* (2022) 47: 2398–401. doi:10.1364/ol.458270
54. Seghilani M, Myara M, Sagnes I, Chomet B, Bendoula R, Garnache A. Self-Mixing in Low-Noise Semiconductor Vortex Laser: Detection of a Rotational Doppler Shift in Backscattered Light. *Opt Lett* (2015) 40:5778–81. doi:10.1364/OL.40.005778
55. Ren Y, Qiu S, Liu T, Liu Z, Cai W. Non-Contact Ultralow Rotational Speed Measurement of Real Objects Based on Rotational Doppler Velocimetry. *IEEE Trans Instrum Meas* (2022) 71:1–8. doi:10.1109/tim.2022.3141155
56. Zhang W, Gao J, Zhang D, He Y, Xu T, Fickler R, et al. Free-Space Remote Sensing of Rotation at the Photon-Counting Level. *Phys Rev Appl* (2018) 10: 044014. doi:10.1103/PhysRevApplied.10.044014
57. Fu S, Wang T, Zhang Z, Zhai Y, Gao C. Non-Diffractive Bessel-Gauss Beams for the Detection of Rotating Object Free of Obstructions. *Opt Express* (2017) 25:20098–108. doi:10.1364/OE.25.020098
58. Qiu S, Ren Y, Liu T, Chen L, Wang C, Li Z, et al. Spinning Object Detection Based on Perfect Optical Vortex. *Opt Lasers Eng* (2020) 124:105842. doi:10.1016/j.optlaseng.2019.105842
59. Qiu S, Ren Y, Sha Q, Ding Y, Wang C, Li Z, et al. Observation of the Rotational Doppler Shift of the Ring Airy Gaussian Vortex Beam. *Opt Commun* (2021) 490:126900. doi:10.1016/j.optcom.2021.126900
60. Pinnell J, Rodríguez-Fajardo V, Forbes A. How Perfect Are Perfect Vortex Beams? *Opt Lett* (2019) 44:5614–7. doi:10.1364/OL.44.005614
61. García-García J, Rickenstorff-Parrao C, Ramos-García R, Arrizón V, Ostrovsky AS. Simple Technique for Generating the Perfect Optical Vortex. *Opt Lett* (2014) 39:5305–8. doi:10.1364/OL.39.005305
62. Qiu S, Ren Y, Liu T, Li Z, Liu Z, Wang C, et al. Rotational Doppler Effect Detection by Lg Beams with a Nonzero Radial Index. *Opt Express* (2021) 29: 10275–84. doi:10.1364/OE.421705
63. Zhai Y, Fu S, Zhang R, Yin C, Zhou H, Zhang J, et al. The Radial Doppler Effect of Optical Vortex Beams Induced by a Surface with Radially Moving Periodic Structure. *J Opt* (2019) 21:054002. doi:10.1088/2040-8986/ab146f
64. Chen VC, Fayin Li L, Shen-Shyang Ho H, Wechsler H. Micro-Doppler Effect in Radar: Phenomenon, Model, and Simulation Study. *IEEE Trans Aerosp Electron Syst* (2006) 42:2–21. doi:10.1109/taes.2006.1603402
65. Luo Y, Chen YJ, Zhu YZ, Li WY, Zhang Q. Doppler Effect and micro-Doppler Effect of Vortex-electromagnetic-wave-based Radar. *IET Radar Sonar Navigation* (2020) 14:2–9. doi:10.1049/iet-rsn.2019.0124
66. Hu X-B, Zhao B, Zhu Z-H, Gao W, Rosales-Guzmán C. *In Situ* Detection of a Cooperative Target's Longitudinal and Angular Speed Using Structured Light. *Opt Lett* (2019) 44:3070–3. doi:10.1364/OL.44.003070
67. Liu B, Chu H, Giddens H, Li R, Hao Y. Experimental Observation of Linear and Rotational Doppler Shifts from Several Designer Surfaces. *Sci Rep* (2019) 9: 8971. doi:10.1038/s41598-019-45516-1
68. Ren Y, Qiu S, Liu T, Liu Z. Compound Motion Detection Based on Oam Interferometry. *Nanophotonics* (2022) 11:1127–35. doi:10.1515/nanoph-2021-0622
69. Belmonte A, Rosales-Guzmán C, Torres JP. Measurement of Flow Vorticity with Helical Beams of Light. *Optica* (2015) 2:1002–5. doi:10.1364/optica.2.001002
70. Ryabtsev A, Pouya S, Safaripour A, Koochesfahani M, Dantus M. Fluid Flow Vorticity Measurement Using Laser Beams with Orbital Angular Momentum. *Opt Express* (2016) 24:11762–7. doi:10.1364/OE.24.011762
71. Li KF, Deng JH, Liu X, Li G. Observation of Rotational Doppler Effect in Second Harmonic Generation in Reflection Mode. *Laser Photon Rev* (2018) 12: 1700204. doi:10.1002/lpor.201700204
72. Guo H, Qiu X, Qiu S, Hong L, Lin F, Ren Y, et al. Frequency Upconversion Detection of Rotational Doppler Effect. *Photon Res* (2021) 10:183–8. doi:10.1364/prj.441785
73. Jha AK, Agarwal GS, Boyd RW. Supersensitive Measurement of Angular Displacements Using Entangled Photons. *Phys Rev A* (2011) 83:053829. doi:10.1103/PhysRevA.83.053829
74. Zhang W, Zhang D, Qiu X, Chen L. Quantum Remote Sensing of the Angular Rotation of Structured Objects. *Phys Rev A* (2019) 100:043832. doi:10.1103/PhysRevA.100.043832
75. Brousseau C, Mahdjoubi K, Emile O. Measurement of the Rotational Sense and Velocity of an Object Using OAM Wave in the Radio-frequency Band. *Electron Lett* (2019) 55:709–11. doi:10.1049/el.2019.0942
76. Zheng J, Zheng S, Shao Z, Zhang X. Analysis of Rotational Doppler Effect Based on Radio Waves Carrying Orbital Angular Momentum. *J Appl Phys* (2018) 124:164907. doi:10.1063/1.5050448
77. Rodenburg B, Lavery MPJ, Malik M, O'Sullivan MN, Mirhosseini M, Robertson DJ, et al. Influence of Atmospheric Turbulence on States of Light Carrying Orbital Angular Momentum. *Opt Lett* (2012) 37:3735–7. doi:10.1364/OL.37.003735
78. Ren Y, Xie G, Huang H, Bao C, Yan Y, Ahmed N, et al. Adaptive Optics Compensation of Multiple Orbital Angular Momentum Beams Propagating through Emulated Atmospheric Turbulence. *Opt Lett* (2014) 39:2845–8. doi:10.1364/OL.39.002845
79. Xie G, Ren Y, Huang H, Lavery MPJ, Ahmed N, Yan Y, et al. Phase Correction for a Distorted Orbital Angular Momentum Beam Using a Zernike Polynomials-Based Stochastic-Parallel-Gradient-Descent Algorithm. *Opt Lett* (2015) 40:1197–200. doi:10.1364/OL.40.001197
80. Fu S, Zhang S, Wang T, Gao C. Pre-turbulence Compensation of Orbital Angular Momentum Beams Based on a Probe and the Gerchberg-Saxton Algorithm. *Opt Lett* (2016) 41:3185–8. doi:10.1364/OL.41.003185
81. Krenn M, Handsteiner J, Fink M, Fickler R, Ursin R, Malik M, et al. Twisted Light Transmission over 143 Km. *Proc Natl Acad Sci U.S.A* (2016) 113: 13648–53. doi:10.1073/pnas.1612023113
82. Angelsky OV, Bekshaev AY, Popov AY. Noncollinear Rotational Doppler Effect. In: Sixth International Conference on Correlation Optics; 2004 Jun 4; Chernivsti, Ukraine. Chernivsti, Ukraine: Proc. SPIE (2004). p. 55–66.
83. Zhang Z, Cen L, Zhang J, Hu J, Wang F, Zhao Y. Rotation Velocity Detection with Orbital Angular Momentum Light Spot Completely Deviated Out of the Rotation Center. *Opt Express* (2020) 28:6859–67. doi:10.1364/OE.380324
84. Ding Y, Ren Y, Liu T, Qiu S, Wang C, Li Z, et al. Analysis of Misaligned Optical Rotational Doppler Effect by Modal Decomposition. *Opt Express* (2021) 29: 15288–99. doi:10.1364/oe.424943

Conflict of Interest: The authors declare that the research was conducted in the absence of any commercial or financial relationships that could be construed as a potential conflict of interest.

frontiers | Frontiers in Physics

ORIGINAL RESEARCH
published: 29 June 2022
doi: 10.3389/fphy.2022.931131

Propagation and Focusing Properties of Vortex Beams Based on Light Ray Tracing

Meng-Qiang Cai[1,2], *Qiang Wang*[1], *Yong-Nan Li*[1] *and Cheng-Hou Tu*[1]*

[1]*MOE Key Laboratory of Weak Light Nonlinear Photonics, School of Physics, Nankai University, Tianjin, China,* [2]*Institute of Space Science and Technology, Nanchang University, Nanchang, China*

By using the ray-tracing method based on geometric optics, we studied the propagating and focusing characteristics of vortex beams with a top-hat intensity distribution. An intuitive mathematical model is established for the propagation and focusing of vortex beams, revealing the mechanisms and physics underlying the spatial evolution, e.g., the dark spot formation in the center of a vortex beam, the relationship between the radius of the dark spot and the propagation distance, and the rotational angle varying with the propagation distance for an azimuthal asymmetric vortex beam. The experimental observations are consistent with theoretical predictions. The results and findings are helpful in intuitively understanding the propagation and evolution of specific vortex beams; therefore, they are of significance for explorations of the novel properties of twisted vortex beams and their applications.

Keywords: ray-tracing method, geometric optics, vortex beam, propagation, focusing

OPEN ACCESS

Edited by:
Pei Zhang,
Xi'an Jiaotong University, China

Reviewed by:
Xifeng Ren,
University of Science and Technology of China, China
Yangjian Cai,
Shandong Normal University, China

***Correspondence:**
Cheng-Hou Tu
tuchenghou@nankai.edu.cn

Specialty section:
This article was submitted to Optics and Photonics, a section of the journal Frontiers in Physics

Received: *28 April 2022*
Accepted: *16 May 2022*
Published: *29 June 2022*

Citation:
Cai M-Q, Wang Q, Li Y-N and Tu C-H (2022) Propagation and Focusing Properties of Vortex Beams Based on Light Ray Tracing. Front. Phys. 10:931131. doi: 10.3389/fphy.2022.931131

1 INTRODUCTION

Vortex beams, with a spiral phase term of $\exp(il\varphi)$ (where l is the topological charge) [1, 2], can carry an optical orbital angular momentum (OAM) of $l\hbar$ per photon, in addition to the intrinsic spin angular momentum. Vortex beams have excited a surge of academic interest because they bring a new degree of freedom for photons with unbounded quantum states, and great success has been achieved in the creation and manipulation of optical OAM. In optical tweezers, vortex beams can trap microparticles and make them move orbitally, and this intrinsic OAM takes the form of a tangential component to the beam's linear momentum density that can be transferred to illuminated objects [3–6]. In optical communications, OAM can be used as a new freedom degree of modulation/multiplexing to further increase the transmission capacity and density [7, 8]. In addition, vortex beams have been used to fabricate chiral structures in metals and spiral patterns in anisotropic polarization-dependent azobenzene polymers or 3D chiral microstructures in isotropic polymers [9–11]. In recent years, advanced control over OAM modes by changing the sign and value of the topological charge as the beam propagates has been explored, and these degrees of flexibility in beam manipulation are generic and can be utilized in many applications [12, 13].

The most common vortex beams are Laguerre–Gaussian beams or Bessel–Gaussian beams, which are eigensolutions of Helmholtz equations and have strict analytical forms, and their propagation and evolution behaviors in free space can be predicted precisely [14–16]. However, for specific vortex beams, such as the vortex beam with top-hat form intensity [16], a new kind of power-exponent-phase vortex beam [17], abruptly autofocusing vortex beams [18, 19], and even the beams with azimuthally nonuniform OAM [20, 21], although their propagating and focusing behavior can be derived by numerical methods, the exact analytical solution of the beam propagation is still not

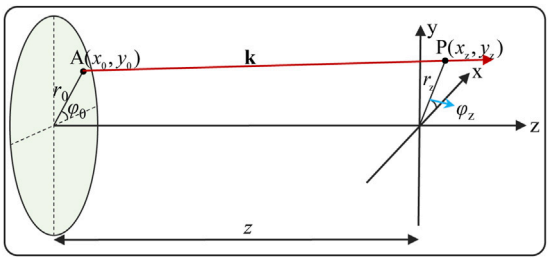

FIGURE 1 | Schematic diagram of a light ray's propagation for a vortex beam in the homogeneous medium.

available, which makes the research on beam propagation characteristics encounter some difficulties. The ray-tracing method based on geometric optics, in which the intensity of light is treated as bundles of light rays traced during scattering, absorption, and multiple reflections, is a convenient and intuitive tool in optical research.

In this study, we studied and derived analytically the relation between the propagation distance and radius (and rotation angle) of vortex beams with top-hat form intensity in the propagating (or focusing) process, and the results can help us understand intuitively the propagation behaviors and focusing characteristics for this specific vortex beam based on ray tracing in the geometrical optics. The proposed method can accurately reproduce the complete dynamic characteristics of the propagation and focusing process of the vortex beam, and the method is also suitable for studying other specific vortex beams.

2 VORTEX BEAM PROPAGATION THROUGH THE HOMOGENEOUS MEDIUM BASED ON LIGHT RAY TRACING

In geometrical optics, the straight propagation of light leads to two basic concepts: light ray and wavefront. As is known, the light ray is always perpendicular to the wavefront and travels in a straight line in the homogeneous and isotropic medium for the plane waves. However, the wavefront of a vortex beam is a helical surface, and it can be written as follows:

$$kz - l\varphi = C, \tag{1}$$

where C is a constant, $k = 2\pi n/\lambda$ (λ is the wavelength of the vortex beam, and n is the refractive index of the medium), z is the propagation distance, and φ is the azimuth coordinate in the transverse plane. Because the light ray travels in straight lines in a homogeneous medium and perpendicular to the wavefront (as shown in **Figure 1**), the normal direction AP of a helical surface at a certain point A(x_0, y_0, 0) can be written as follows:

$$\frac{x_z - x_0}{F_x(x_0, y_0, 0)} = \frac{y_z - y_0}{F_y(x_0, y_0, 0)} = \frac{z}{F_z(x_0, y_0, 0)}, \tag{2}$$

where $F(x, y, z) = kz - l\varphi - C$, $F_x = \partial F/\partial x$, $F_y = \partial F/\partial y$, and $F_z = \partial F/\partial z$, then F_x, F_y, and F_z can be represented as follows:

$$\begin{aligned} F_x(x_0, y_0, 0) &= l y_0/r_0^2, \\ F_y(x_0, y_0, 0) &= -l x_0/r_0^2, \\ F_z(x_0, y_0, 0) &= k, \end{aligned} \tag{3}$$

where $r_0 = \sqrt{x_0^2 + y_0^2}$, which is the initial radius of the light ray at the $z = 0$ plane. According to **Eqs 2**, **3**, the coordinate of point P for the light ray AP can be written as follows:

$$\begin{aligned} x_z &= l y_0 z/(k r_0^2) + x_0, \\ y_z &= -l x_0 z/(k r_0^2) + y_0. \end{aligned} \tag{4}$$

According to **Eq. 4**, the propagation properties of the light ray in space for the vortex beam can be derived. **Figure 2A** reflects the evolution of the light ray in a three-dimensional (3D) view for a vortex beam with $l = 10$ and $r_0 = 1$ mm. We can see that the direction of each light ray is different, and the unit vector direction of the light ray AP in the cylindrical coordinate system can be represented as follows:

$$\mathbf{e}_{\mathrm{AP}} = \frac{l}{\sqrt{l^2 + k^2 r_0^2}} \frac{lz}{\sqrt{l^2 z^2 + k^2 r_0^4}} \mathbf{e}_r - \frac{l}{\sqrt{l^2 + k^2 r_0^2}} \frac{k r_0^2}{\sqrt{l^2 z^2 + k^2 r_0^4}} \mathbf{e}_\varphi + \frac{k r_0}{\sqrt{l^2 + k^2 r_0^2}} \mathbf{e}_z. \tag{5}$$

According to **Eq. 5**, it can be seen that the radial component of the unit vector increases when r_0 decreases, but the longitudinal component is just the opposite. Because of the radial component, the rays at the center of the vortex beam diverge with the increase in the propagation distance during the propagation process, resulting in the zero intensity at the center of vortex beams. According to **Eq. 4**, the distance r_z between the point P and the origin of the xyz coordinate system (see **Figure 1**) can be written as follows:

$$r_z = \sqrt{l^2 z^2/(k^2 r_0^2) + r_0^2}, \tag{6}$$

where z is the propagation distance of the vortex beam as the light ray travels to the point P. **Figure 2B** shows the relationship between r_z with the topological charge l (or z) with the given value of z (or l). On the left of **Figure 2B** (or the right of **Figure 2B**), it can be seen that the increase rate of r_z with the propagation distance z (or topological charge l) increases when r_0 decreases for the given l (or z). As a result, a dark spot in the center of the vortex beam appears as it propagates.

In order to verify the correctness of our theoretical analysis and derivation, we have carried out the corresponding experiments, as shown in **Figure 3A**. In our experiment, a linearly polarized flat-top light beam (532 nm) is incident on the spatial light modulator (SLM), on which a forked holographic grating is loaded (where $z = 0$ m), and the +1 and −1 diffraction orders carry a spiral phase with the opposite topological charges. We then selected one of the diffraction orders and observed the intensity change during the propagation process with the help of a CCD. For easy comparison, we just generated different ring beams instead of whole beams (as shown in **Figures 3B1–B5**), which is realized by defining a ring-shape transmission function and inside which the forked holographic grating is loaded. As the rings have different radii, which are 0.86, 1.29, 1.72, 2.15, and 2.58 mm, respectively, the

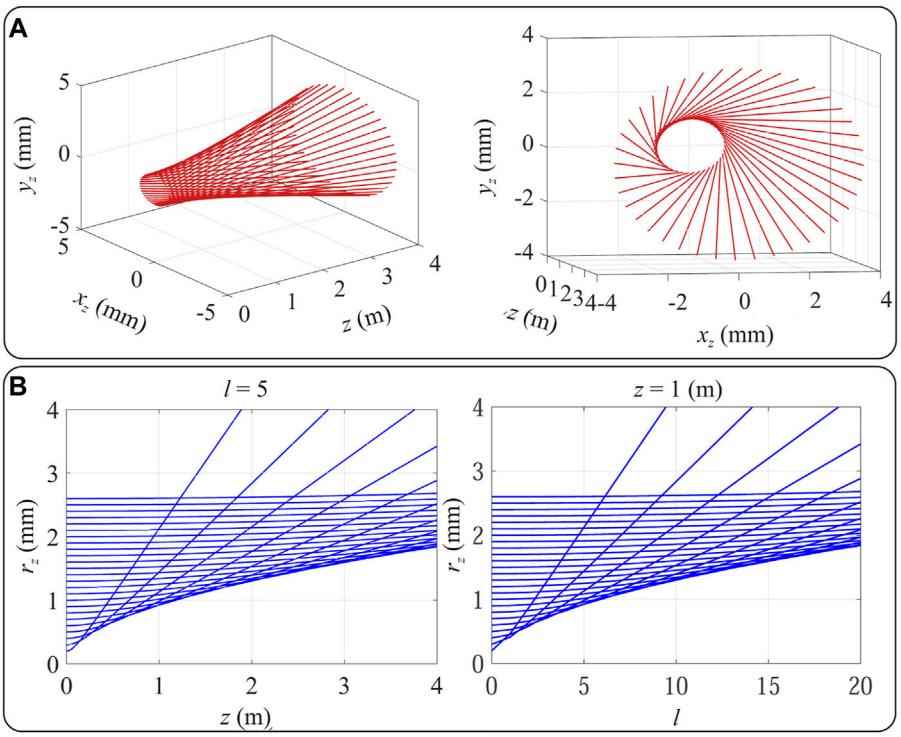

FIGURE 2 | Simulated propagation properties of light rays in free space for a vortex beam based on the ray-tracing method. **(A)** Distributions of light rays in three-dimensional space for different views. **(B)** Relationship between the parameter r_z and the propagation distance z in the case of $l = 5$ (left), and the relationship between the parameter r_z and the topological number l in the case of $z = 1$ m (right).

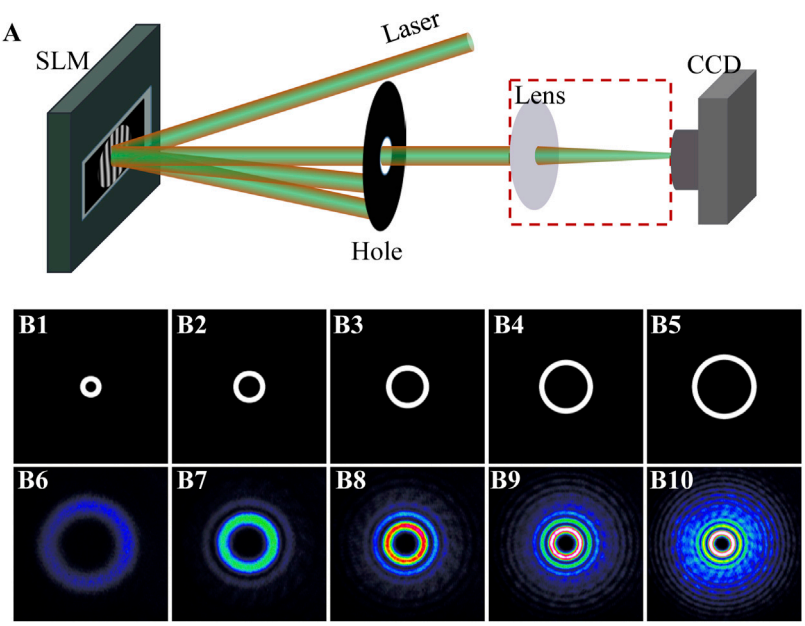

FIGURE 3 | Experimental setup and results for propagation and evolution of a vortex beam. **(A)** Schematic representation of the experimental setup. **(B1–B5)** Transmission rings with different outer radii of 0.86, 1.29, 1.72, 2.15, and 2.58 mm in the case of the same ring width of 0.43 mm, respectively. **(B6–B10)** Corresponding measured intensity distribution in the case of $l = 5$ and the propagation distance $z = 1$ m, respectively. All images have the same dimension of 6.2 mm × 6.2 mm.

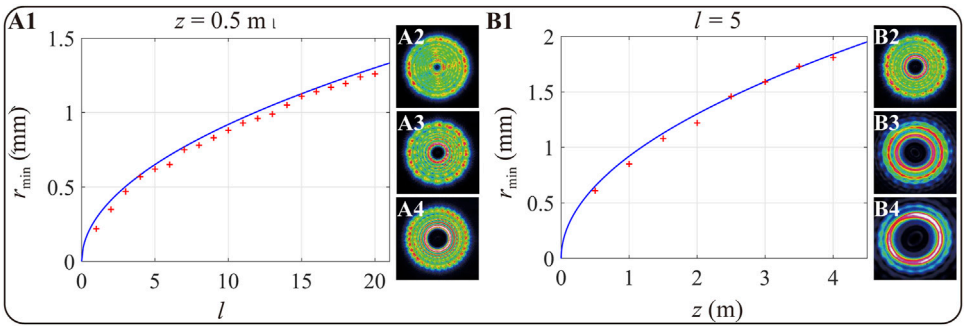

FIGURE 4 | Evolutionary process of the minimum radius of the dark ring of a vortex beam variation with *l* and *z* in the experiment. The relationship between r_{min} and **(A1)** the topological number *l* and **(B1)** the propagation distance *z*. The blue solid line is the simulation result, and the "+" marks are the experimental results. The measured intensity distributions for the vortex beam **(A2–A4)** at the propagation distance *z* = 0.5 m with the topological number *l* are 1, 4, and 8, and **(B2–B4)** the topological number *l* = 5 and the propagation distance *z* are 0.5, 1.5 and 2.5 m, respectively. All images have the same dimension of 6.2 mm × 6.2 mm.

selected diffraction order also have different radius but with the same width 0.43 mm). **Figures 3B6–B10** show the corresponding far-field intensity pattern at $z = 1$ m. We can see that the smaller the radius of the ring in the initial position ($z = 0$) is, the larger the radius of the vortex beam (main ring with the highest intensity) at a given propagation distance ($z = 1$ m) becomes, which are well in accord with the theoretical conclusions.

According to **Eq. 6**, we can get an inequation as follows:

$$r_z = \sqrt{l^2 z^2/(k^2 r_0^2) + r_0^2} \geq \sqrt{2lz/k} = r_{\min}, \tag{7}$$

where r_{min} is the radius of the dark spot of the vortex beam. According to **Eq. 7**, r_{min} is proportional to the root of *z* and *l*, which are shown by the blue solid line in **Figures 4A1, B1**, respectively. To prove the relationship between r_{min} and *l*, we measured the value of r_{min} with different topological charges *l*, which is from 0 to 20 in the experiment, and the results are marked by the red "+" in **Figure 4A1** and the measured intensity distributions for vortex beam with *l*=1,4,8 are shown in **Figures 4A2–A4**. We also measured the experimental results of r_{min} at different propagation distances (*z*), as shown by the red "+" in **Figure 4B1**. And **Figures 4B2–B4** are the measured intensity for *l*=5 at propagating distance z are 0.5,1.5 and 2.5 m. According to **Figure 4**, we can find that the experimental value of r_{min} is slightly smaller than the theoretical one, and the reason is that we do not consider the diffraction of vortex beams. However, the variation trend of r_{min} with *z* or *l* in the experiment agrees with the theoretical results.

According to **Eq. 4** and **Figure 1**, the rotation angle $\Delta\varphi_z$ of point P with respect to point A along the *z* axis can be written as follows:

$$\begin{aligned}\Delta\varphi_z &= \varphi_z - \varphi_0 = \tan^{-1}\frac{y_z/x_z - y_0/x_0}{1 + y_z y_0/(x_z x_0)} \\ &= -\tan^{-1}\frac{lz}{kr_0^2}.\end{aligned} \tag{8}$$

According to **Eq. 8**, the absolute value of $\Delta\varphi_z$ increases as the topological charge *l* increases, but it decreases as the initial radius r_0 increases. Point P rotates clockwise (or anticlockwise) with respect to the initial point A if *l* is positive (or negative), and $\Delta\varphi_z$ is equal to 90^0 as $z = +\infty$. The theoretical predictions and experimental confirmations are shown in **Figure 5**. In **Figure 5A**, we have shown the theoretical predictions of the rotation angles for vortex beams with different topological charges ($l = -20, -10, 0, 10$, and 20, respectively) at different propagation distances ($z = 0.5$ and 1 m, respectively) with $r_0 = 1.5$ mm. **Figures 5B1–B6** illustrates the corresponding experimental measured results of a_1-a_6 in **Figure 5A** by the truncated semicircular vortex beam. It is clear that the theoretical and the experimental results have some differences; however, the variation tendency is the same. For a specific radial position r_0 (white dotted circle in **Figure 5B**), the rotation angle of a semicircular beam located at the propagation distance $z = 1$ m is larger than that at $z = 0.5$ m in the case of the same topological number *l*, and the semicircular beam rotates clockwise (anticlockwise) in the case of $l > 0$ ($l < 0$), as shown in **Figures 5B1–B6**. To compare **Figure 5B1, B2**, we can see the rotation angle is larger if the topological charge is larger with the same propagation distance $z = 1$ m. In summary, we observed that the experimental results in **Figure 5** are in accordance with the theoretical results in **Eq. 8**.

3 FOCUSING PROPERTIES OF VORTEX BEAMS BASED ON LIGHT RAY TRACING

As is well known, the focusing properties of vortex beams can be calculated by diffraction integration. However, it is more intuitive to understand the focusing behavior of the vortex beam based on the ray-tracing method. As shown in **Figure 6**, we suppose that a light ray of the vortex beam propagates from the initial point A(x_0, y_0, 0) located in the plane of $z = 0$ to point P(x', y', z_0) located in the plane of $z = z_0$; then, it is deflected by the focusing lens located at $z = z_0$. The direction of light ray AP is the same as that of the wave-vector **k**, which can be written as follows:

$$\mathbf{k} = k_x\mathbf{e}_x + k_y\mathbf{e}_y + k_z\mathbf{e}_z, \tag{9}$$

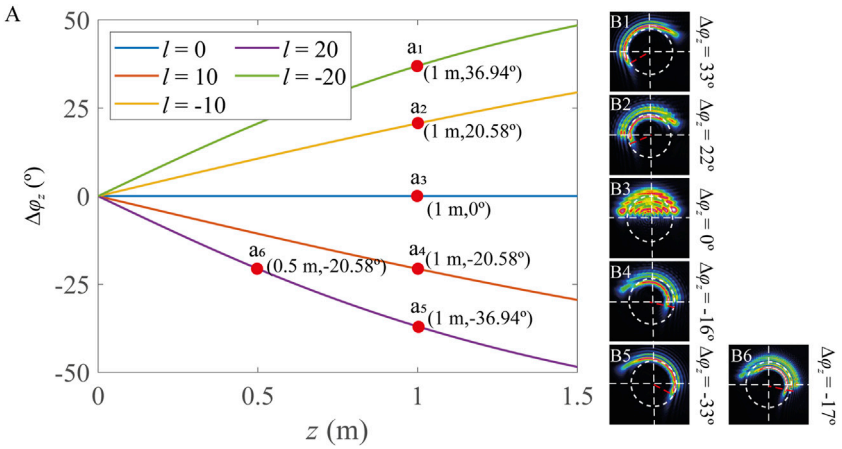

FIGURE 5 | Rotation angle predicted by theoretical derivations and the corresponding experimental results for vortex beams with different topological charges. **(A)** Rotation angle for vortex beams with different topological charges (*l* equal to 0, 10, −10, 20, and −20) at the propagation distance. **(B1–B6)** Corresponding measured intensity distributions and the rotation angles of (a1-a6) for truncated vortex beams. All images have the same dimension of 6.2 mm × 6.2 mm.

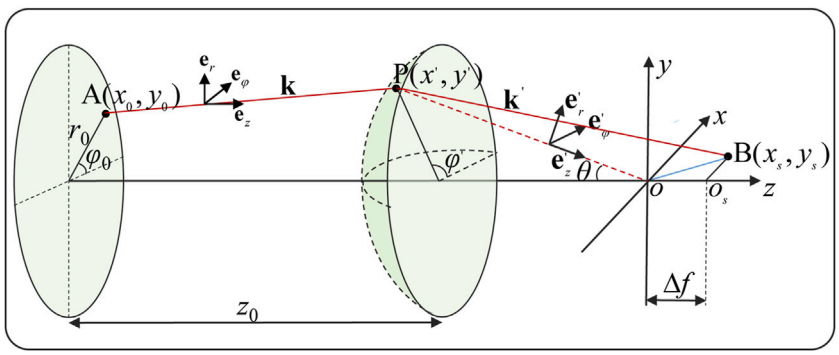

FIGURE 6 | Focusing sketch diagram of a light ray for a vortex beam. The light ray propagates from the initial point A to point P and is then deflected by lens and arrives at point B.

where

$$k_x = k(x' - x_0)\Big/\sqrt{(x' - x_0)^2 + (y' - y_0)^2 + z_0^2},$$
$$k_y = k(y' - y_0)\Big/\sqrt{(x' - x_0)^2 + (y' - y_0)^2 + z_0^2}, \quad (10)$$
$$k_z = kz_0\Big/\sqrt{(x' - x_0)^2 + (y' - y_0)^2 + z_0^2}.$$

In a cylindrical coordinate system, which has three unit vectors, i.e., $\mathbf{e}_r$, $\mathbf{e}_\varphi$, and $\mathbf{e}_z$, the coordinate of point P can be written as (r', φ', z_0). The transformation relationship between $\mathbf{e}_r$, $\mathbf{e}_\varphi$ and $\mathbf{e}_x$, $\mathbf{e}_y$ in the cartesian coordinate system can be written as follows:

$$\mathbf{e}_x = \cos\varphi'\mathbf{e}_r - \sin\varphi'\mathbf{e}_\varphi,$$
$$\mathbf{e}_y = \sin\varphi'\mathbf{e}_r + \cos\varphi'\mathbf{e}_\varphi. \quad (11)$$

When substituting **Eq. 11** into **Eq. 9**, **k** can be written as follows:

$$\mathbf{k} = \left(k_x\cos\varphi' + k_y\sin\varphi'\right)\mathbf{e}_r + \left(-k_x\sin\varphi' + k_y\cos\varphi'\right)\mathbf{e}_\varphi + k_z\mathbf{e}_z. \quad (12)$$

By replacing x_z, y_z, and z with x', y' , and z_0 in **Eq. 4**, we can get the following:

$$x' = ly_0z_0/(kr_0^2) + x_0,$$
$$y' = -lx_0z_0/(kr_0^2) + y_0. \quad (13)$$

When substituting **Eq. 13** into **Eq. 10**, we can get the following:

$$k_x = kly_0\Big/\left(r_0\sqrt{l^2 + r_0^2k^2}\right),$$
$$k_y = -klx_0\Big/\left(r_0\sqrt{l^2 + r_0^2k^2}\right), \quad (14)$$
$$k_z = k^2r_0\Big/\sqrt{l^2 + r_0^2k^2}.$$

According to **Eq. 13**, we can obtain

$$\cos\varphi' = x'\Big/\sqrt{(x')^2 + (y')^2} = \left(ly_0z_0/r_0 + x_0kr_0\right)\Big/\sqrt{l^2z_0^2 + k^2r_0^4},$$
$$\sin\varphi' = y'\Big/\sqrt{(x')^2 + (y')^2} = \left(-lx_0z_0/r_0 + y_0kr_0\right)\Big/\sqrt{l^2z_0^2 + k^2r_0^4}. \quad (15)$$

By further substituting **Eqs 14**, **15** into **Eq. 12**, we can obtain the following:

$$\mathbf{k} = \frac{k}{\sqrt{l^2 + r_0^2 k^2}}\left(\frac{l^2 z_0}{\sqrt{l^2 z_0^2 + k^2 r_0^4}}\mathbf{e}_r - \frac{k l r_0^2}{\sqrt{l^2 z_0^2 + k^2 r_0^4}}\mathbf{e}_\varphi + k r_0 \mathbf{e}_z\right). \tag{16}$$

As the light ray is deflected by the lens, its direction is then changed from $\mathbf{k}/k$ to $\mathbf{k}'/k$, and $\mathbf{e}_r$ and $\mathbf{e}_z$ are deflected by an angle of θ, with respect to the optical axis of the lens (which is coincided with the axis of the vortex beam). As a result, $\mathbf{e}_r$ and $\mathbf{e}_z$ were as follows: $\mathbf{e}_r'$ and $\mathbf{e}_z'$, respectively; then, $\mathbf{k}'$ can be written as follows:

$$\mathbf{k}' = \frac{k}{\sqrt{l^2 + r_0^2 k^2}}\left(\frac{l^2 z_0}{\sqrt{l^2 z_0^2 + k^2 r_0^4}}\mathbf{e}_r' - \frac{k l r_0^2}{\sqrt{l^2 z_0^2 + k^2 r_0^4}}\mathbf{e}_\varphi' + k r_0 \mathbf{e}_z'\right). \tag{17}$$

The light ray after deflection propagates to point B, and point B in the light ray PB is the nearest point to the z axis or the optical axis. The projection of the line segment PB at $\mathbf{e}_z'$ is the line segment PO, which is the focal length f of the focusing lens. According to **Eq. 17**, the projection of the line segment PB in the direction of $\mathbf{e}_r'$ and $\mathbf{e}_\varphi'$ can be written as follows:

$$\begin{aligned} s_r' &= f l^2 z_0 \Big/ \left(k r_0 \sqrt{l^2 z_0^2 + k^2 r_0^4}\right), \\ s_\varphi' &= -f k l r_0^2 \Big/ \left(k r_0 \sqrt{l^2 z_0^2 + k^2 r_0^4}\right). \end{aligned} \tag{18}$$

For the cylindrical system, the unit vector in the direction of the straight line OB can be represented as follows:

$$\mathbf{e}_{\mathrm{OB}} = \left(s_r' \mathbf{e}_r' + s_\varphi' \mathbf{e}_\varphi'\right) \Big/ s_{\mathrm{OB}}, \tag{19}$$

where s_{OB} is the length of the line segment OB and $s_{\mathrm{OB}} = \sqrt{(s_r')^2 + (s_\varphi')^2}$. By substituting $\mathbf{e}_r' = \cos\theta \mathbf{e}_r + \sin\theta \mathbf{e}_z$ into **Eq. 19**, we can get the following equation:

$$\mathbf{e}_{\mathrm{OB}} = \left(s_r' \cos\theta \mathbf{e}_r + s_r' \sin\theta \mathbf{e}_z + s_\varphi' \mathbf{e}_\varphi\right) \Big/ s_{\mathrm{OB}}. \tag{20}$$

According to **Eq. 11**, **Eq. 20** can be rewritten as follows:

$$\begin{aligned} \mathbf{e}_{\mathrm{OB}} \Big/ s_{\mathrm{OB}} = &\left(s_r' \cos\theta \cos\varphi' - s_\varphi' \sin\varphi'\right)\mathbf{e}_x \\ &+ \left(s_r' \cos\theta \sin\varphi' + s_\varphi' \cos\varphi'\right)\mathbf{e}_y + s_r' \sin\theta \mathbf{e}_z. \end{aligned} \tag{21}$$

According to **Eq. 21**, the coordinates of point B in the Cartesian coordinate system (with the origin O and the coordinate axes x, y, and z) can be written as follows:

$$\begin{aligned} x_s &= s_r' \cos\theta \cos\varphi' - s_\varphi' \sin\varphi', \\ y_s &= s_r' \cos\theta \sin\varphi' + s_\varphi' \cos\varphi'. \end{aligned} \tag{22}$$

Based on **Eq. 15** and **Eq. 18**, **Eq. 22** can be written as follows:

$$\begin{aligned} x_s &= \frac{f l^2 z_0 \cos\theta (l y_0 z_0 / r_0 + x_0 k r_0)}{k r_0 (l^2 z_0^2 + k^2 r_0^4)} + \frac{f l r_0 (-l x_0 z_0 / r_0 + y_0 k r_0)}{l^2 z_0^2 + k^2 r_0^4}, \\ y_s &= \frac{f l^2 z_0 \cos\theta (-l x_0 z_0 / r_0 + y_0 k r_0)}{k r_0 (l^2 z_0^2 + k^2 r_0^4)} - \frac{f l r_0 (l y_0 z_0 / r_0 + x_0 k r_0)}{l^2 z_0^2 + k^2 r_0^4}. \end{aligned} \tag{23}$$

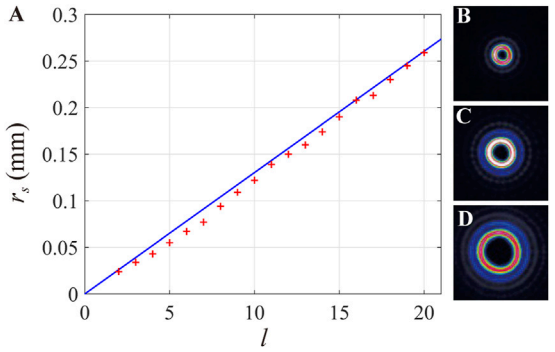

FIGURE 7 | Relationship between the radius r_s of the dark spot in the focal field and the topological charge of l. **(A)** Blue solid line is the simulation result, and the red "+" marks are the experimental results. **(B–D)** are, respectively, the intensity distributions in the focal field for vortex beams with the topological number l to be 4, 8, and 12. **(B–D)** have the same dimensions of 1 mm × 1 mm.

According to **Eq. 23**, the distance between point B and point O_s can be obtained as follows:

$$\begin{aligned} r_s &= \sqrt{(x_s)^2 + (y_s)^2} = \frac{|l|}{k \sin\theta}\sqrt{\frac{l^2 z_0^2 \cos^2\theta}{k^2 r_0^4} + 1} \\ &= \frac{|l| f}{k\sqrt{(l z_0 / k r_0)^2 + r_0^2}}\sqrt{\frac{l^2 z_0^2}{k^2 r_0^4}\left(1 - \frac{(l z_0 / k r_0)^2 + r_0^2}{f^2}\right) + 1}, \end{aligned} \tag{24}$$

where $\sin\theta = r'/f$, and $r' = \sqrt{(x')^2 + (y')^2}$ is the pupil radius of the focusing lens. According to **Eq. 24**, r_s decreases with the increase in r_0, which means that the maximum radius r_0 of the vortex beam in the plane $z = 0$ corresponds to the minimun ring radius r_s of the focal spot. The intensity near the center of the focal spot is zero, and the shape of focal spot is similar to a donut.

According to **Eq. 24**, we can see that the radius r_s of the dark spot in the focal plane is proportional to the topological charge l and the focal length f of the focusing lens but inversely proportional to the spot radius of the incident vortex beam.

In the experiment shown in **Figure 3**, we set the distance (z_0) between the lens and SLM to be 0.5 m, the maximum spot radius (r_0) of the vortex beam in the plane of SLM is 2.6 mm, and the focal length of the lens is equal to 400 mm. Based on **Eq. 24** and the aforementioned parameters, we derived the relationship between the radius of the dark focal spot and the topological charge l, as shown by the blue line of **Figure 7A**. Then, we measured the variation of the radius of the dark spot with the topological charge l, which changes from 2 to 20, and the results are marked by the red "+" in **Figure 7A**, and **Figures 7B–D** are the intensity distributions in the focal field for vortex beams with l=4,8,12. It can be seen that the experimental results are slightly smaller than the simulation results, which is because we do not take the diffraction into account; however, the experimental and simulation results have the same tendency.

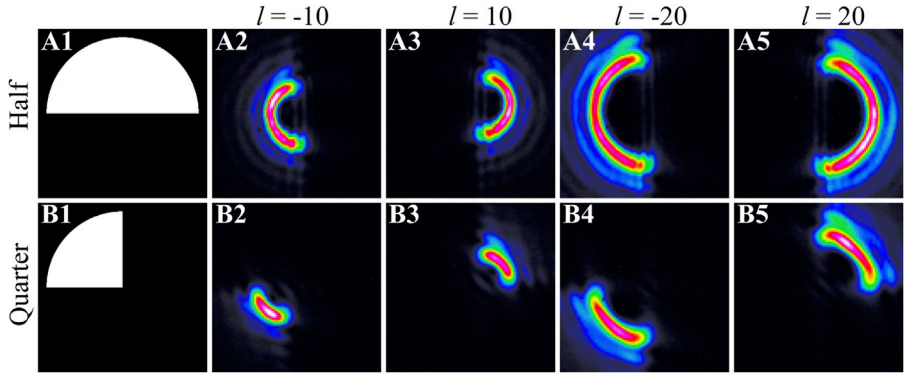

FIGURE 8 | Experimentally observed focusing property of vortex beams. **(A1)** and **(B1)** are the sketch diagrams of a half and a quarter circular pupil at $z = 0$ planes, respectively. **(A2–A5)** are the intensity distributions in the focal field for vortex beams with a half circular pupil in the case of the topological charge l to be −10, 10, −20, and 20, respectively, and **(B2–B5)** are the corresponding measured intensity distributions for the vortex beam with a quarter circular pupil. **(A)** and **(B)** have the same dimensions of 1 mm × 1 mm.

From **Eq. 21**, we can see that the position of the minimum focal spot for a vortex beam is not located in the focal plane of the focusing lens as $z_0 \neq 0$ but in the plane with a distance of Δf away from the focal plane. According to **Eq. 21**, we can get the expression of Δf as follows:

$$\Delta f = s_r' \sin\theta = l^2 z_0 \big/ \left(k^2 r_0^2\right). \tag{25}$$

According to **Eq. 25**, Δf is proportional to the square of l and z_0 but inversely proportional to the square of the initial radius r_0 of the light ray. If $z_0 = 0$, then $\Delta f = 0$, which means that the position of the minimum spot does not shift.

According to **Eq. 23**, when a vortex beam propagates from the initial plane at $z = 0$ to the plane which is away from the focal plane with a distance of Δf, we can get the rotation angle $\Delta\varphi_s$ of a certain point in the spot as follows:

$$\Delta\varphi_s = -\pi + \left(\varphi_s - \varphi_0\right) = -\pi + \tan^{-1}\left[\frac{\tan\varphi_s - \tan\varphi_0}{1 + \tan\varphi_s \tan\varphi_0}\right], \tag{26}$$

where $\tan\varphi_s = y_s/x_s$. Based on **Eq. 23**, we can get the following:

$$\Delta\varphi_s = \pi + \tan^{-1}\left[\frac{lz_0\cos\theta + k^2 r_0^4 \big/ \left(lz_0\right)}{kr_0^2\left(2 - \cos\theta\right)}\right]. \tag{27}$$

According to **Eq. 27**, we can see that the rotation angle $\Delta\varphi_s$ is equal to $-\pi/2$ (or $\pi/2$) for a negative (or positive) l. This result can be used to intuitively explain the results in [8].

For the given parameters $z_0 = 0.5$ m, $f = 400$ mm, and $r_0 = 2.6$ mm, we can calculate the value of $\Delta\varphi_s$, according to **Eq. 27**. The calculation result shows that the focal spot rotates clockwise about 93.6° (or 97.1°) with respect to the direction at the initial plane in the case of $l = 10$ (or $l = 20$), while for the negative l (e.g., $l = -10$ or $l = -20$), the rotation angle is opposite. To verify the theory analysis, we carried out the corresponding experiments. In the experiment, we just generated truncated half or quarter part of a vortex beam and then measured its intensity distribution in the focal plane; the results are shown in **Figure 8**. It is clear that for the negative or positive l, the rotation of the focal spot is slightly larger than 90°, and the direction is opposite. Meanwhile, the clockwise rotation angle (~ 95°) of the focal spot in the case of $l = 20$ is greater than that (~ 92°) in the case of $l = 10$. The experimental and theoretical results agree with each other very well, and it proves that the ray-tracing method is effective in predicting the evolution behavior of structured beams during the focusing process.

4 CONCLUSION

In conclusion, we derived analytically the propagation and focusing of vortex beams with top-hat intensity in the homogeneous medium by use of the light ray-tracing method, based on which some propagation behaviors and focusing characteristics of vortex beams can be understood intuitively. For example, the central dark spot of the vortex beam increases with the propagation distance and the topological number, and the relationship between the radius of the dark spot, the topological number, and the propagation distance can be derived. The experiment proves that vortex beams can rotate as it travels in the homogeneous medium, and the rotation angle is related to the propagation distance and the topological number. We can intuitively understand that the vortex beam can be focusing into a donut shape at the focal plane, and we can get the relationship between the radius of the dark spot at the center of the donut shape and the focal length of the lens, the topological charge, and the size of the incident vortex beam. In addition, the proposed method can be also applied to other specific vortex beams, and the results are helpful to understand the propagation and evolution of specific vortex beams.

DATA AVAILABILITY STATEMENT

The original contributions presented in the study are included in the article/supplementary material; further inquiries can be directed to the corresponding author.

AUTHOR CONTRIBUTIONS

M-QC and C-HT proposed the idea. M-QC completed the theory and experiment. QW organized the database. C-HT and Y-NL gave some suggestions in numerical simulations and experiments. M-QC, QW, and C-HT wrote the manuscript. All authors contributed to the final manuscript revision.

FUNDING

This work was supported by the National Key R&D Program of China (2017YFA0303800 and 2017YFA0303700) and the National Natural Science Foundation of China (12074196, 11774183, and 11904152).

REFERENCES

1. Allen L, Beijersbergen MW, Spreeuw RJC, Woerdman JP. Orbital Angular Momentum of Light and the Transformation of Laguerre-Gaussian Laser Modes. *Phys Rev A* (1992) 45:8185–9. doi:10.1103/PhysRevA.45.8185
2. Yao AM, Padgett MJ. Orbital Angular Momentum: Origins, Behavior and Applications. *Adv Opt Photon* (2011) 3:161–204. doi:10.1364/AOP.3.000161
3. Gieseler J, Gomez-Solano JR, Magazzù A, Pérez Castillo I, Pérez García L, Gironella-Torrent M, et al. Optical Tweezers - From Calibration to Applications: A Tutorial. *Adv Opt Photon* (2021) 13:74–241. doi:10.1364/AOP.394888
4. Grier DG. A Revolution in Optical Manipulation. *Nature* (2003) 424:810–6. doi:10.1038/nature01935
5. Dholakia K, Čižmár T. Shaping the Future of Manipulation. *Nat Photon* (2011) 5:335–42. doi:10.1038/nphoton.2011.80
6. Padgett M, Bowman R. Tweezers with a Twist. *Nat Photon* (2011) 5:343–8. doi:10.1038/NPHOTON.2011.81
7. Fu S, Zhai Y, Zhou H, Zhang J, Wang T, Liu X, et al. Experimental Demonstration of Free-Space Multi-State Orbital Angular Momentum Shift Keying. *Opt Express* (2019) 27:33111–9. doi:10.1364/OE.27.033111
8. Wang J, Yang J-Y, Fazal IM, Ahmed N, Yan Y, Huang H, et al. Terabit Free-Space Data Transmission Employing Orbital Angular Momentum Multiplexing. *Nat Photon* (2012) 6:488–96. doi:10.1038/NPHOTON.2012.138
9. Ambrosio A, Marrucci L, Borbone F, Roviello A, Maddalena P. Light-Induced Spiral Mass Transport in Azo-Polymer Films under Vortex-Beam Illumination. *Nat Commun* (2012) 3:1–9. doi:10.1038/ncomms1996
10. Toyoda K, Miyamoto K, Aoki N, Morita R, Omatsu T. Using Optical Vortex to Control the Chirality of Twisted Metal Nanostructures. *Nano Lett* (2012) 12:3645–9. doi:10.1021/nl301347j
11. Ni J, Wang C, Zhang C, Hu Y, Yang L, Lao Z, et al. Three-Dimensional Chiral Microstructures Fabricated by Structured Optical Vortices in Isotropic Material. *Light Sci Appl* (2017) 6:e17011. doi:10.1038/lsa.2017.11
12. Dorrah AH, Rosales-Guzmán C, Forbes A, Mojahedi M. Evolution of Orbital Angular Momentum in Three-Dimensional Structured Light. *Phys Rev A* (2018) 98:043846. doi:10.1103/PhysRevA.98.043846
13. Dorrah AH, Zamboni-Rached M, Mojahedi M. Controlling the Topological Charge of Twisted Light Beams with Propagation. *Phys Rev A* (2016) 93:063864. doi:10.1103/PhysRevA.93.063864
14. Schechner YY, Piestun R, Shamir J. Wave Propagation with Rotating Intensity Distributions. *Phys Rev E* (1996) 54:R50–R53. doi:10.1103/PhysRevE.54.R50
15. Srinivas P, Perumangatt C, Lal N, Singh RP, Srinivasan B. Investigation of Propagation Dynamics of Truncated Vector Vortex Beams. *Opt Lett* (2018) 43:2579–82. doi:10.1364/OL.43.002579
16. Wang X-L, Lou K, Chen J, Gu B, Li Y, Wang H-T. Unveiling Locally Linearly Polarized Vector Fields with Broken Axial Symmetry. *Phys Rev A* (2011) 83:063813. doi:10.1103/PhysRevA.83.063813
17. Shen D, Wang K, Zhao D. Generation and Propagation of a New Kind of Power-Exponent-Phase Vortex Beam. *Opt Express* (2019) 27:24642–53. doi:10.1364/OE.27.024642
18. Yan X, Guo L, Cheng M, Li J. Controlling Abruptly Autofocusing Vortex Beams to Mitigate Crosstalk and Vortex Splitting in Free-Space Optical Communication. *Opt Express* (2018) 26:12605–19. doi:10.1364/OE.26.012605
19. Davis JA, Cottrell DM, Sand D. Abruptly Autofocusing Vortex Beams. *Opt Express* (2012) 20:13302–10. doi:10.1364/oe.20.013302
20. Li X, Ma H, Yin C, Tang J, Li H, Tang M, et al. Controllable Mode Transformation in Perfect Optical Vortices. *Opt Express* (2018) 26:651–62. doi:10.1364/OE.26.000651
21. Zhang H, Li X, Ma H, Tang M, Li H, Tang J, et al. Grafted Optical Vortex with Controllable Orbital Angular Momentum Distribution. *Opt Express* (2019) 27:22930–8. doi:10.1364/OE.27.022930

Conflict of Interest: The authors declare that the research was conducted in the absence of any commercial or financial relationships that could be construed as a potential conflict of interest.

frontiers | Frontiers in Physics

TYPE Original Research
PUBLISHED 25 July 2022
DOI 10.3389/fphy.2022.898638

OPEN ACCESS

EDITED BY
Gianluca Ruffato,
University of Padua, Italy

REVIEWED BY
Siyuan Yu,
Sun Yat-sen University, China
Weiren Zhu,
Shanghai Jiao Tong University, China

*CORRESPONDENCE
Sheng Liu,
shengliu@nwpu.edu.cn
Peng Li,
pengli@nwpu.edu.cn

†These authors have contributed equally to this work and share first authorship

SPECIALTY SECTION
This article was submitted to Optics and Photonics,
a section of the journal
Frontiers in Physics

RECEIVED 17 March 2022
ACCEPTED 06 July 2022
PUBLISHED 25 July 2022

CITATION
Li Y, Xie Y, Liu S, Li P, Wei B and Zhao J (2022), Theoretical study of vortex beam generation based on geometric coordinate transformation.
Front. Phys. 10:898638.
doi: 10.3389/fphy.2022.898638

Theoretical study of vortex beam generation based on geometric coordinate transformation

Yanke Li†, Yuqing Xie†, Sheng Liu*, Peng Li*, Bingyan Wei and Jianlin Zhao

Key Laboratory of Light-field Manipulation and Information Acquisition, Ministry of Industry and Information Technology, Shaanxi Key Laboratory of Optical Information Technology, School of Physical Science and Technology, Northwestern Polytechnical University, Xi'an, China

By performing a conformal optical mapping of an input beam from Cartesian to log-polar coordinates, we propose a method to generate vortex beam. By tilting the incident beam, a phase gradient is attached and evolves into a vortex phase due to the optical transformation. Thus, the topological charge of the generated vortex beam is continuously adjustable. With this method, vortex beams with integer and fractional orders are generated. The purity of the generated vortex beam is theoretically analyzed, as well as the possible effects of phase misalignment on the output vortex. The continuously tunable vortex beam achieved by this method is expected to be used in information processing and optical routing in optical communications.

KEYWORDS

geometric coordinate transform, vortex beam, orbital angular momentum, fractional-order vortex, information codes

Introduction

In 1992, Allen proposed an light field with a helical wavefront exp ($i\ell\varphi$) carrying an orbital angular momentum (OAM) of $\ell\hbar$ per photon, which was later referred to as the vortex beam [1]. Vortex beams have attracted much attention due to their unique vortex phase as well as OAM [2, 3], and have a rich variety of promising applications in many fields such as optical tweezers [4], particle capture [5, 6], super-diffraction limit imaging [7], mode-division multiplexing [8] and quantum coding [9]. Especially for optical communication, the OAMs of vortex beams can be used as the information carrier to achieve novel communication modes different from that encoding by light intensity. Employing the orthogonal feature of OAMs, Wang et al. experimentally demonstrated the transmission of data in free space at the Tbit level [10]. Subsequently, they further investigated the transmission of OAM beam in optical fibres, greatly increasing the transmission distance and the capacity of optical communication [8]. These make the vortex beam play an important role in the development of optical communications.

The generation and manipulation of OAM modes have been extensively studied. Various methods for generating vortex beams have been proposed, including mode superposition [11] and transition with optical elements, such as spiral phase plates [12], computer generated holograms [13], liquid crystal plate [14], metasurface [15] et al.

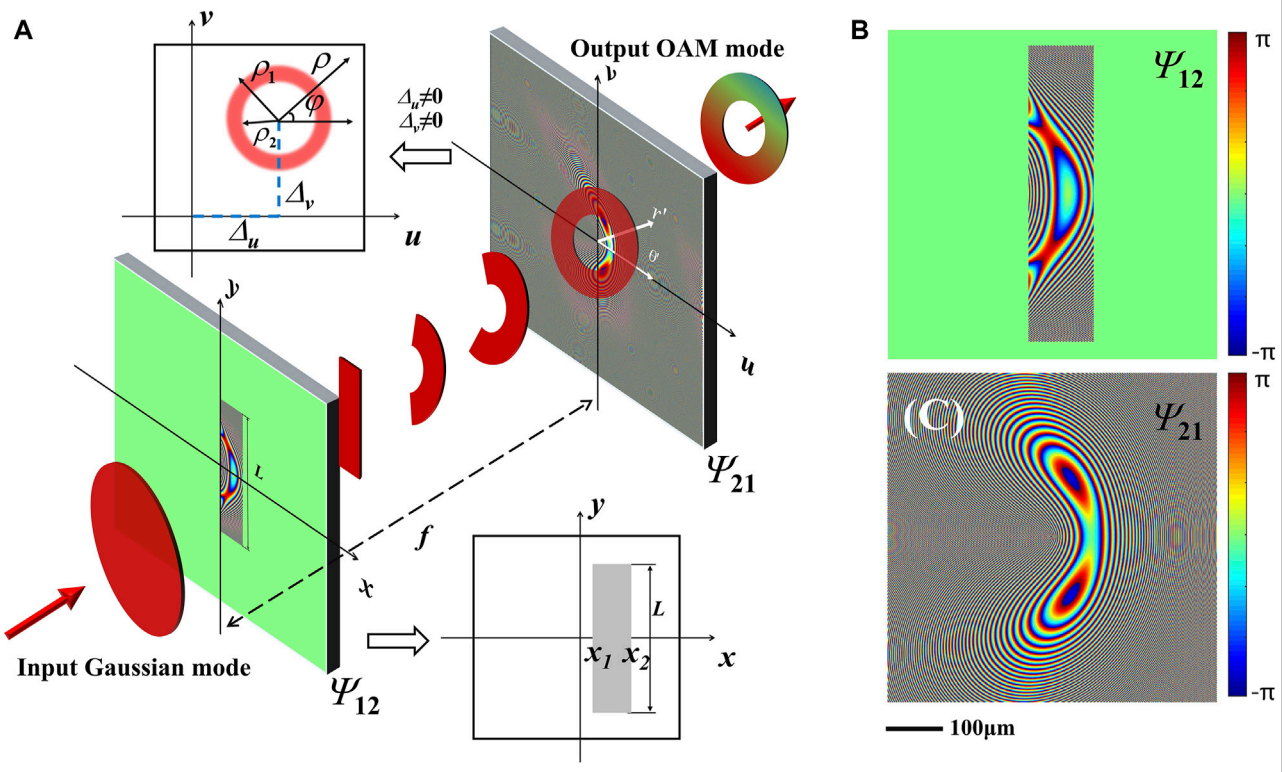

FIGURE 1
Vortex beam generation *via* geometric coordinate transformation (GCT). **(A)** Schematic of the coordinate transformation from a rectangular beam to a ring-shaped one. **(B,C)** Typical transforming (Ψ_{12}) and correcting (Ψ_{21}) phases.

Besides these fixed optical elements, adjustable schemes are also introduced to the generation of optical vortices. In 2008, Bernet et al. proposed spiral-phase moiré elements to generate vortex beams with variable helical phase, which can be continuously adjusted by rotating the phase-type elements [16].

As the most important parameter of vortex beams, the topological charge (TC) is closely related to the OAM and the relevant applications. Various methods have been proposed to modulate the TC of the optical vortex. One of the most widely used is the geometric coordinate transformation (GCT) [15–20]. The theory of the GCT was proposed in 1987 [17], which can realized a conformal transformation of a beam from one coordinate to another, by modulating and correcting the phases at the input and output planes, respectively. One practical application example of GCT is the mode detection of OAMs by using the Cartesian to log-polar coordinate transformation [18, 19]. Furthermore, a spiral coordinate transformation was proposed to realized the high-resolution and efficient sorting of the OAM modes [20]. In addition, different GCTs have been employed to manipulate the OAM of vortex beams, including the ring-to-fan mapping used to achieve multiplication and halving of the OAM modes [21], spiral coordinate transformation used to arbitrarily change the OAM modes [22]. These OAM modulations are of importance for optical switching and optical routing [23].

In this paper, a new method for generating vortex beams with continuously tunable TCs is proposed based on the principle of GCT. The method is inspired by the log-polar to Cartesian coordinate transformation [17]. The Cartesian to log-polar coordinate transformation is performed to achieve the conformal mapping from a rectangular beam to a ring-shaped one. On this basis, a phase gradient is attached to the rectangular beam by tilting the incident beam and evolves into a vortex phase gradually as the beam curls up into a ring. Then, we theoretically analyze the purity of the generated vortex beam and the possible effects of phase misalignment on the output. Our results are expected to be used in the information processing and the optical routing in optical communications.

Theory

To achieve the conformal mapping from a rectangular beam to a ring-shaped one, we employ a two-step coordinate transformation system proposed in Ref. 18. As shown in

Figure 1, the system consists of two phase elements (Ψ_{12} and Ψ_{21}). The first phase element Ψ_{12} is called "transforming phase", which achieves the conformal mapping of the beam. The incident beam in the rectangular region gradually curls up into a ring after being modulated by the transforming phase. The second phase element Ψ_{21} is called "correcting phase", which corrects the phase distortion caused by the beam curling at the output plane. It is important to note that the transforming and correcting phases are entirely unrelated to the input beam, thus the input parameters do not affect the transformation. This enables the conformal phase mapping without changing the output intensity distribution.

Assuming that the incident light field in the rectangular region in the input plane (x, y) would take part in the GTC, the rectangular function of this region can be expressed as:

$$\Theta(x,y) = \begin{cases} 1, \text{ if } x_1 \le x \le x_2, -\frac{L}{2} \le y \le \frac{L}{2} \\ 0, \text{ else} \end{cases}, (1)$$

where, x_1, x_2, L are to depict the range of the rectangular region.

After modulated by the transforming phase, the light field in the rectangular region curls up into an annular beam on the output plane (u, v). We suppose that the center of the annular beam is located at (Δ_u, Δ_v), and the outer and inner radii of the annular are $\underline{\rho}_1$, $\underline{\rho}_2$, respectively. Considering that the beam follows the paraxial propagation, and the coordinate transformation needs to satisfy a sufficient but not necessary condition if $\partial^2\Psi_{12}(x_1,y_1)/\partial x_1\partial y_1$ and $\partial^2\Psi_{12}(x_1,y_1)/\partial y_1\partial x_1$ exist and are continuous: $\partial u/\partial y = \partial v/\partial x$ and $\partial x/\partial v = \partial y/\partial u$ [17], the coordinate mapping relationship can be written as follows:

$$\begin{cases} u = bexp\left(-\frac{x}{a}\right)cos\frac{y}{a} + \Delta_u \\ v = bexp\left(-\frac{x}{a}\right)sin\frac{y}{a} + \Delta_v \end{cases}, (2)$$

$$\begin{cases} x = -aln\left(\frac{\rho}{b}\right) \\ y = a\varphi \end{cases}, (3)$$

where, $a = L/2\pi$ determines the length of the rectangular region; $b = x_{1,2}/\exp(-\rho_{1,2}/a)$, determines the ratio of the width of the rectangle and the ring width; Δ_u and Δ_v denote the offset distance of the annular beam in the direction of u and v axis, respectively; (ρ, φ) are the polar coordinates in the output plane with the origin set at (Δ_u, Δ_v), and meet

$$\begin{cases} \rho = \sqrt{(u-\Delta_u)^2 + (v-\Delta_v)^2} \\ \varphi = arctan\frac{v-\Delta_v}{u-\Delta_u} \end{cases}. (4)$$

As shown in Figure 1A, when Δ_u, Δ_v is not 0, the generated vortex beam will be shifted from the origin. The GTC must satisfy the following phase-solving conditions:

$$\begin{cases} \frac{\partial\Psi_{12}}{\partial x} = (u-x)\frac{k}{f}, \frac{\partial\Psi_{12}}{\partial y} = (v-y)\frac{k}{f} \\ \frac{\partial\Psi_{21}}{\partial u} = (x-u)\frac{k}{f}, \frac{\partial\Psi_{21}}{\partial y} = (y-v)\frac{k}{f} \end{cases}, (5)$$

where, $k = 2\pi/\lambda$ is the wavenumber, λ is the wavelength of the incident light, and f is the spacing between the two phase elements. By solving Eq. (5), the analytical expressions of the transforming and correcting phases are obtained as follows:

$$\begin{cases} \Psi_{12} = -\frac{k}{2f}\left[2abexp\left(-\frac{x}{a}\right)cos\left(\frac{y}{a}\right) - 2(\Delta_u x + \Delta_v y) + (x^2+y^2)\right] \\ \Psi_{21} = \frac{k}{2f}\left[2a(v-\Delta_v)\varphi - 2a(u-\Delta_u)ln\left(\frac{\rho}{b}\right) + 2a(u-\Delta_u) - (u^2+v^2)\right] \end{cases}. (6)$$

Figure 1B and Figure 1C represent the typical distributions of the transforming and correcting phases, respectively. Considering that only the incident light field in the rectangular region is needed, the transmission function of the incident plane should be restriced by a rectangular aperture function, expressed as t (x, y) = Θ(x, y)exp (iΨ12).

When an incident beam with a phase gradient in the y axis, expressed as $U(x,y)\exp(ik_y y)$, is input (Figure 1A), it will gradually curl up from a rectangle to a ring. To generate the ℓth-order spiral phase exp ($i\ell\varphi$), it is necessary to make the incident phase gradient satisfy $k_y = \ell/a$ according to Eq. (3). It can be concluded that by adjusting the phase gradient of the incident beam, a vortex beam with adjustable TC would be generated.

Results and analysis

We numerically simulate the above method of generating the vortex beam by choosing the following parameters: λ = 632.8nm, f = 175mm, $\Delta_u = \Delta_v = 0$, a = 1mm, b = 2 mm. The inner and outer radii of the annular beam to be generated are determined by taking ρ_2 = 0.5 mm and ρ_1 = 2mm, and then the rectangular function $\Theta(x, y)$ is calculated by substituting $L = 2\pi a$ and $x_{1,2} = b\exp(-\rho_{1,2}/a)$ into Eq. (1). To meet the experimental conditions, the incident light field is taken as a Gaussian beam, i.e., $U(x, y) = \exp[-(x^2+y^2)/w^2]$, with waist radius w = 8 mm. The incident field $U(x,y)\exp(ik_y y)$ is attached to the transforming phase Ψ_{12} and then propagates the distance f, where the diffraction field can be calculated by the Fresnel diffraction integral. Finally, the diffraction field is corrected by multiplying by the phase exp ($i\Psi_{21}$), and forms the output annular beam. The propagation process of the incident Gaussian beam is shown in Figure 2, where Figures 2A–F give the intensity distributions at different distances. The dashed line in Figure 2A marks the rectangular

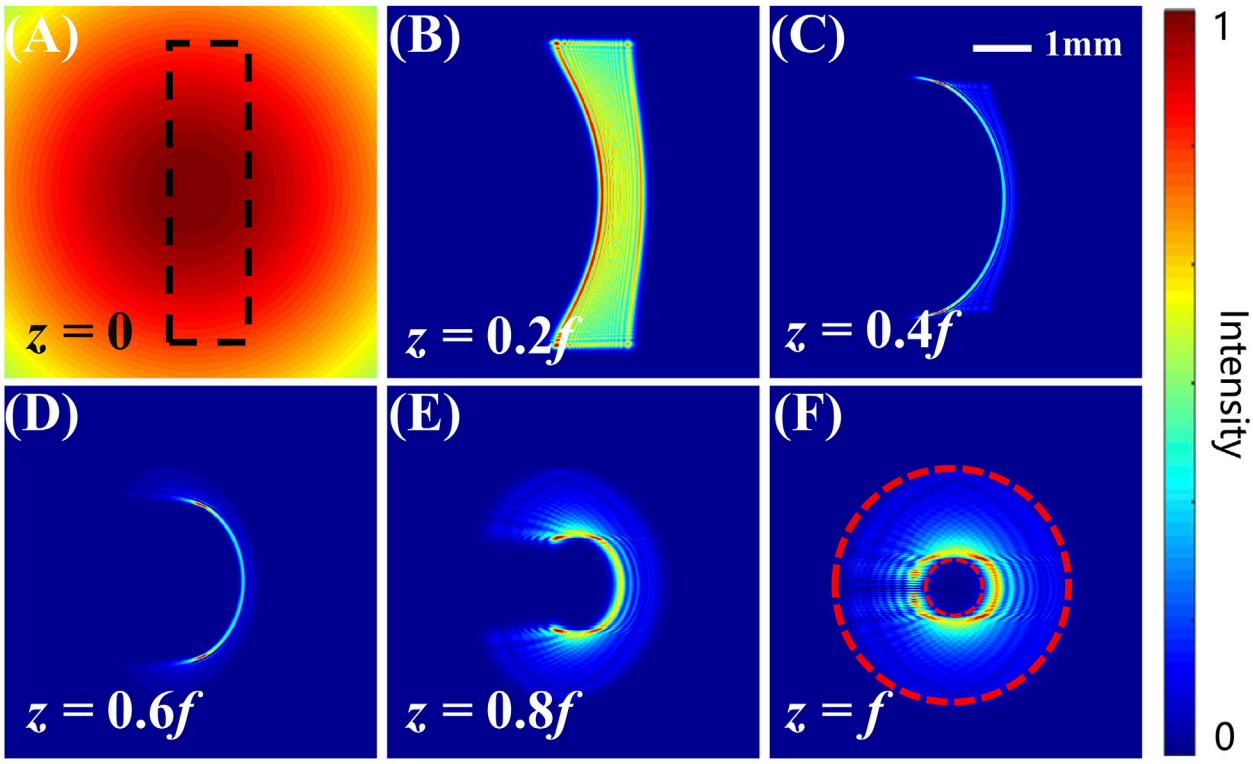

FIGURE 2
Propagation process for the GCT. **(A)** Input Gaussian beam, with the transmission area marked by the dashed rectangle. **(B–F)** Intensity distributions at different propagation distances.

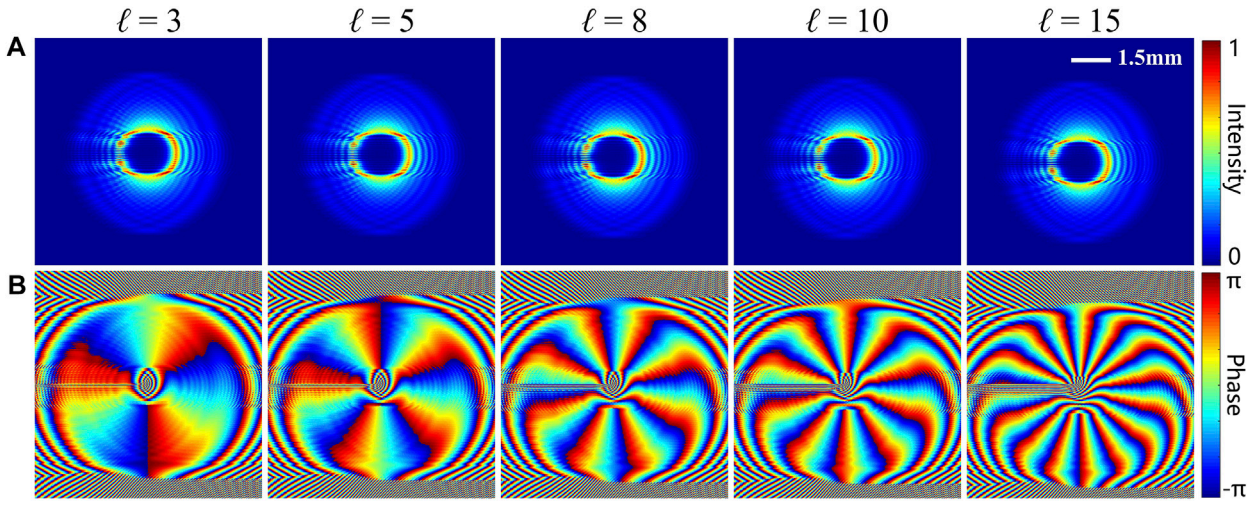

FIGURE 3
Intensity **(A)** and phase **(B)** distribution of the generated vortex beams by setting the topological charge ℓ = 3, 5, 8, 10, and 15.

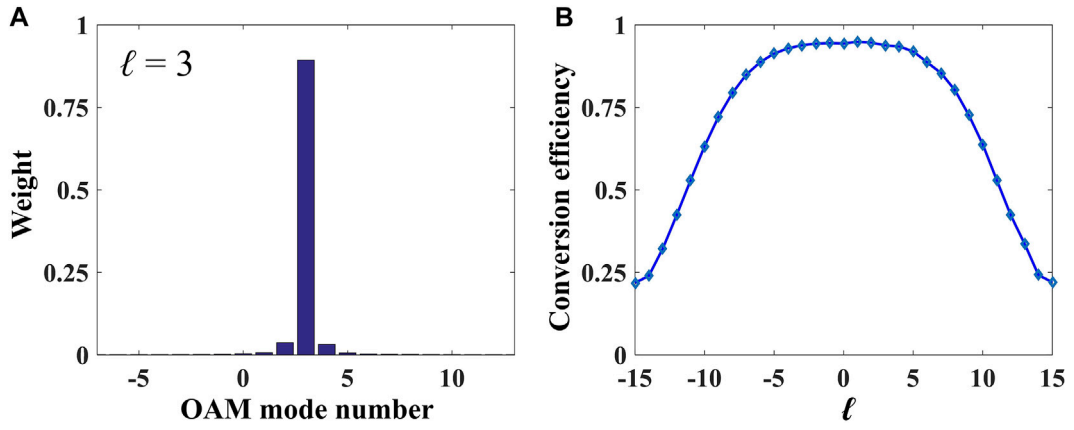

FIGURE 4
Purity of the generated vortex beams. **(A)** The OAM spectrum of output beam with ℓ = 3. **(B)** Conversion efficiency of vortex beam versus ℓ.

transmission area of the incident plane, and the dashed circles in Figure 2F mark the range of the predesigned output. From these results, we can clearly see: the rectangular beam gradually bends into an arc firstly, and tends to converge to a thin line (Figures 2B–D); thereafter, it bends further and gradually diverges to an annular beam (Figures 2E,F). The inner and outer radii of the resulting ring beam are basically in line with the preset values. It should be noted that, because the mapping of the coordinateis is nonlinear [$\rho_{1,2} = b\exp(-x_{1,2}/a)$], the intensity distribution of the resulting annular beam is not uniform, but declines as the radial location increases. Notablely, the nonuniform intensity distribution over the rectangular area would make the resulting annular beam axis-asymmetric. But hard-edge diffraction of the rectangular field has an even bigger effect. Thus, the input intensity distribution will not affect the purity of the OAM state too much.

By setting the TC ℓ = 3, 5, 8, 10, and 15, the phase gradient exp ($i\ell y/a$) is attached to the input beam, and the simulation results are shown in Figure 3, where Figure 3A and Figure 3B depict the intensity and phase distributions, resepectively. Notably, the intensity distributions of the resulting beams are almost identical, indicating that the phase variation of the incident beam has no significant effect on the GTC. While from the phase patterns, it can be clearly seen that the typical spiral phases are formed: the phases changes $2\pi\ell$ around the center. It indicates that vortex beams with TC of ℓ are generated.

The purity of the resulting integer-order vortex beam can be analyzsed with the Fourier relationship between the OAM spectrum [24]. For example, the OAM spectrum expansion is performed for the generated vortex beam with TC ℓ = 3, and the normalized percentage of each OAM component occupied is calculated. The result between the interval [-7, 13] is shown in Figure 4A. It can be seen that the OAM component with ℓ = 3 accounts for about 90% of the generated vortex beam, indicating the hight purity of the generated vortex beam and the high efficiency of the mode conversion. In order to analyse the purity of the resulting vortex beam with different TC, we calculate the OAM spectra by taking ℓ from -15 to 15, and extracting the corresponding OAM mode purity as shown in Figure 4B. It is obvious that the vortex conversion efficiency for the TC of $|\ell|$ becomes progressively lower as $|\ell|$ increases. This indicates that this method would be not so efficient for generating higher-order vortex beams. The conversion efficiency can be maintained at around 90% for ℓ between -5 and 5. However, as $|\ell|$ increases more, the conversion efficiency decreases significantly. Nevertheless, the efficiency can be guaranteed to be above 50% for the resulting beams with the absolute values of TCs less than 10.

For the phase gradient exp ($i\ell y/a$) attached to the input beam, ℓ can be chosen as not only an integer. When the phase gradient is changed continuously, ℓ is more likely to be a fraction. Thus, a fraction-order vortex beam can be generated for a non-integral ℓ. By changing ℓ as a fraction between 4 and 5, we generate the vortex beams with GCT, and the results are shown in Figure 5. Figures 5A–D show the phase distributions of the resulting beams. It is hardly to directly estimate the TC of these non-integer-order spiral phases. We extract the phase distributions at a circle of radius 1 mm in the phase patterns as shown in Figures 5A–D, and compare with the phases of the standard fractional-order vortex beams. The results are given in Figures 5E–H, where the blue and red curves correspond to the simulation and theoretical results, respectively. As can be seen, for an integral TC, the phase is continuous at -π and π (Figure 5E); while for a fractional TC, an obvious phase jump occurs at -π and π. More strikingly, the phases for the simulated results highly coincide with the theoretical ones except for some noisy points due to the edge diffraction of the light field (Figures 5F–H). Figures 5I–L show the corresponding comparations of the OAM spectra

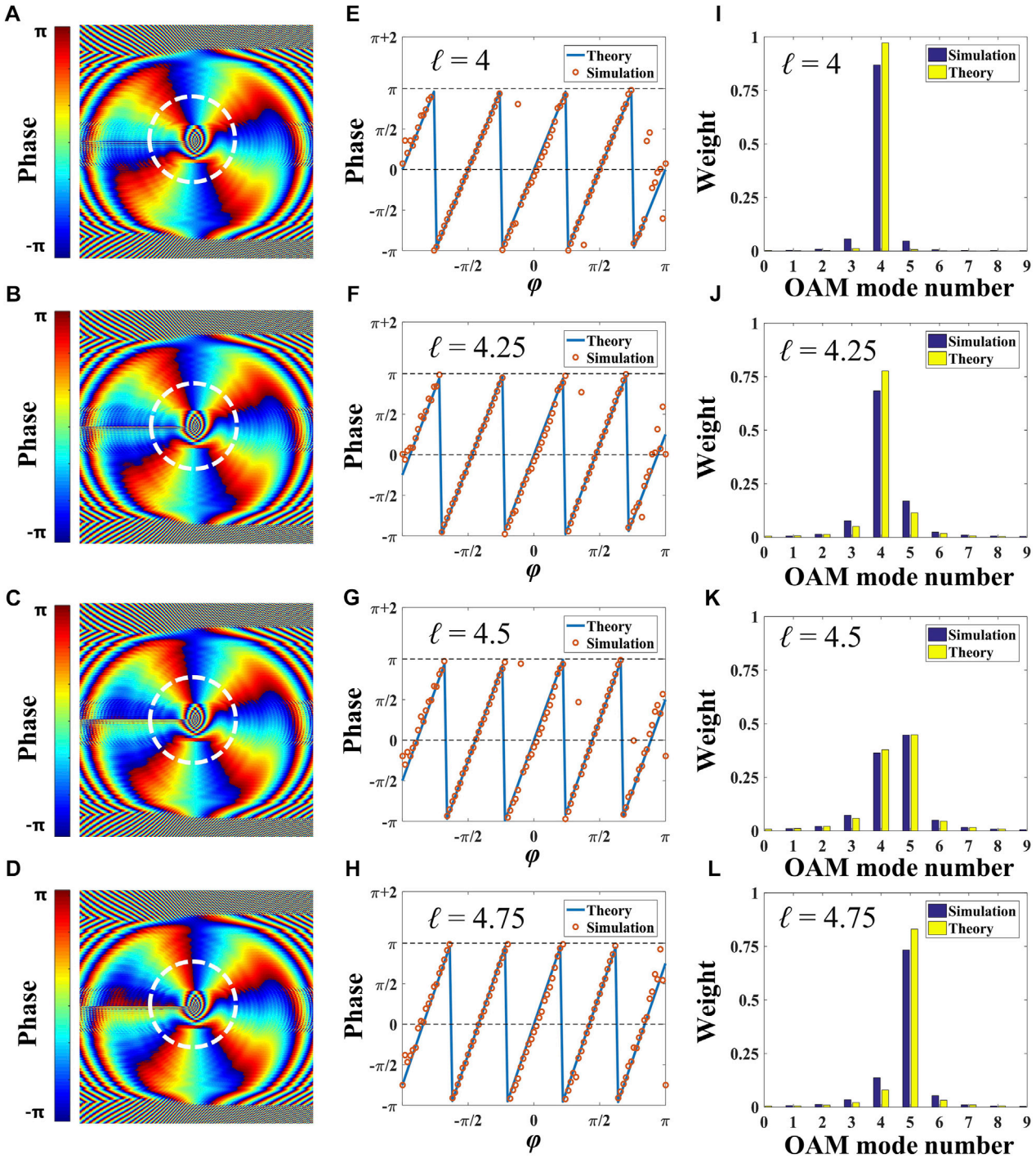

FIGURE 5
Properties of the generated fraction-order vortices. **(A–D)** Phase distributions. **(E–H)** Phase variations along with the circles in **(A–D)**. **(I–L)** OAM spectrum corresponding to **(A–D)**.

between the simulation and theoretical results. It can be seen that the fraction-order vortex beams no longer occupy a single OAM, but also has other OAM components. As ℓ approaches 4, the OAM modes with TC of 4 prevails; as ℓ approaches 5, the OAM modes with TC of 5 dominate the OAM spectrum. The simulation results are in general agreement with the

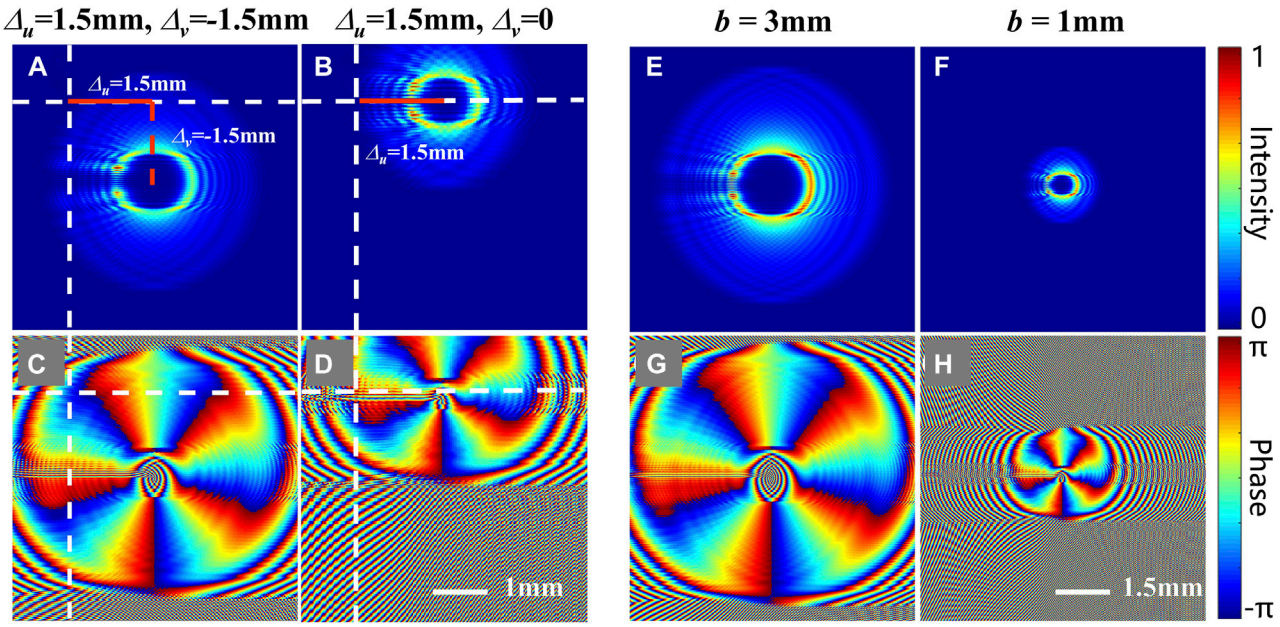

FIGURE 6
Control of the transverse position **(A–D)** and spot size **(E–H)** of the vortex beam. The top and bottom correspond to the intensity and phase distributions.

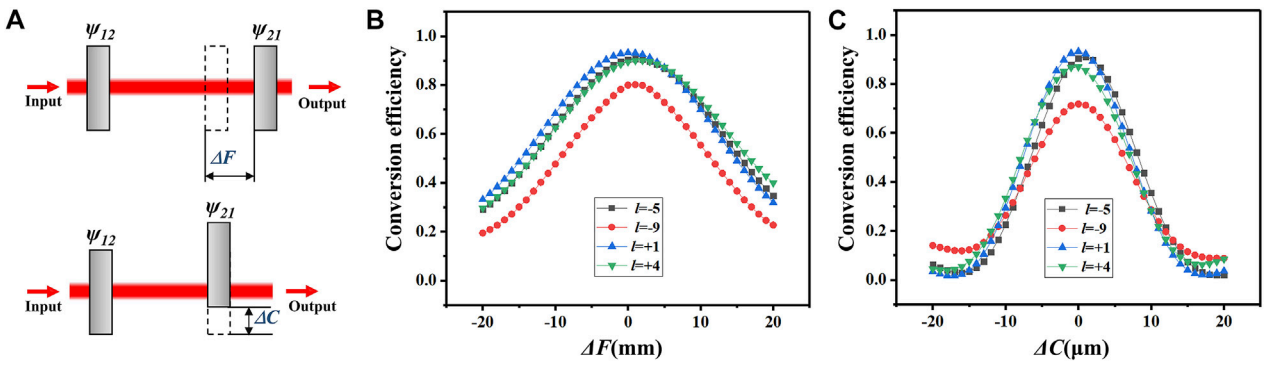

FIGURE 7
Effect of phase alignment. **(A)** Schematic of the axial and lateral offsets. **(B,C)** The conversion efficiency of the vortex beam vs. offset.

theoretical ones, except that the dominant OAM components are slightly lower because the conversion efficiency of the vortex beam in this method cannot be 100%.

The transverse position and spot size of the resulting vortex beam can be controlled by varying the parameters Δ_u, Δ_v, and b, as shown in Figure 6. By setting Δ_u = -Δ_v = 1.5mm, and Δ_u = 1.5mm, Δ_v = 0, the position control of the vortex beam is realized as shown in Figures 6A–D, where Figures 6A,B, and Figures 6C,D correspond to the intensity and phase distributions, respectively. Figures 6A,C, and Figures 6B,D obviously reveal that the resulting vortex beams are shifted along the vectors (1.5mm, -1.5 mm) and (1.5mm, 0), respectively. Here, the parameters Δ_u, Δ_v are taken into account in the coordinate mapping relationship, due to the consideration of the corresponding follow-up study under most experimental conditions. Since the phase modulation of an light field always has errors in experiments, the zero-order diffraction spot, which locates on the center of the coordinates, is hard to be eliminated. By attaching the parameters Δ_u, Δ_v to the phase, the resulting beam is moved far from the zero-order spot, which can be filtered out. Another consideration is the spot size.

A resulting beam with a large size might overlap with the zero-order spot, which would be adverse to the beam filtering. Thus, it is important to control the spot size in theoretical pre-research. Figures 6E–H represent the intensity and phase distributions of the vortex beams produced at different radii for $b = 3$ and 1mm, respectively. As can be seen, the size of the resulting vortex beam is adjustable by varying the parameter b.

In addition, considering that the phase alignment is also an unavoidable problem in the experiment, the influence of the misalignment of the phase elements is analyzed below. There are two main cases of phase misalignment as shown in Figure 7A: the axial offset (ΔF) and the lateral offset (ΔC). By choosing $\ell = -9, -5, 1$, and 4, we calculate the conversion efficiency of the OAM mode versus the axial and lateral offsets, as shown in Figure 7B and Figure 7C, respectively. From these results, it can be seen that the conversion efficiency of the OAM mode is basically normally distributed with the offsets. The position deviation of the correcting phase element, along with whether axial or lateral directions, would cause a rapid reduction of the efficiency of the resulting vortex beam. More importantly, the efficiency reduction is much more sensitive to the lateral offset. For the axial offset, the conversion efficiency of the 9 order vortex beam drops to about 50% when the offset is increased to10 mm. While for the lateral offset, the efficiency decreases rapidly to 20% once the offset exceeds 10 μm. In a word, the correcting phase needs more precise lateral alignment, while permitting the axial alignment in a larger tolerance range.

Conclusion

Based on the theory of GCTs, a method is proposed to generate the vortex beam, of which the TC can be adjusted by varying the phase gradient of the incident beam. The Cartesian to log-polar coordinate transformation is performed to achieve a conformal mapping from a rectangular beam to a ring-shaped one. By attached with a variable phase gradient, an input rectangular beam can curl up to an annular beam, and its phase eloves into a spiral one. In contrast to the previous research results, the advantage of this method is that the TC of the generated vortex beam is continuously tunable. Vortex beams with integer-order and fraction-order TCs are obtained by using this method. Based on the OAM spectrum, the purity of the generated vortex beam is analyzed, as well the possible effects of phase misalignment on the output vortex. The results show that the conversion efficiency would be gradually reduced with the increasing of TC of the generated vortex beam. In addition, it reveals that the correcting phase needs more precise lateral alignment, while permitting the axial alignment in a larger tolerance range. The proposed continuously tunable vortex beam is expected to be used in the information processing and the optical routing in optical communications.

Data availability statement

The original contributions presented in the study are included in the article/Supplementary Material, further inquiries can be directed to the corresponding authors.

Author contributions

SL, PL, BW, and JZ were responsible for the conceptualization of the study; Sheng Liu, Yanke Li, and YX wrote the draft. All authors were involved in the revision and agreed to be accountable for the content of the article.

Funding

National Key Research and Development Program of China (2017YFA0303800); National Natural Science Foundation of China (12074312, 11634010, 12174309, 12074313); Fundamental Research Funds for the Central Universities (3102019JC008).

Conflict of interest

The authors declare that the research was conducted in the absence of any commercial or financial relationships that could be construed as a potential conflict of interest.

Publisher's note

All claims expressed in this article are solely those of the authors and do not necessarily represent those of their affiliated organizations, or those of the publisher, the editors and the reviewers. Any product that may be evaluated in this article, or claim that may be made by its manufacturer, is not guaranteed or endorsed by the publisher.

References

1. Allen L, Beijersbergen MW, Spreeuw RJC, Woerdman JP. Orbital angular momentum of light and the transformation of Laguerre-Gaussian laser modes. *Phys Rev A* (1992) 45:8185–9. doi:10.1103/physreva.45.8185

2. Zhong J, Liu S, Guo X, Li P, Wei B, Han L, et al. Observation of optical vortex knots and links associated with topological charge. *Opt Express* (2021) 29:38849. doi:10.1364/OE.441263

3. Zhong J, Liu S, Wang K, Li P, Wei B, Guo X, et al. Poincaré sphere analogue for optical vortex knots. *Opt Lett* (2022) 47:313. doi:10.1364/OL.448783

4. Simpson NB, Allen L, Padgett MJ Optical tweezers and optical spanners with Laguerre-Gaussian modes. *J Mod Opt* (1996) 43:2485–91. doi:10.1080/09500349608230675

5. Paterson L, MacDonald MP, Arlt J, Sibbett W, Bryant PE, Dholakia K, et al. Controlled rotation of optically trapped microscopic particles. *Science* (2001) 292:912–4. doi:10.1126/science.1058591

6. MacDonald MP, Lynn P, Volke-Sepulveda K, Arlt J, Sibbett W, Dholakia K, et al. Creation and manipulation of three-dimensional optically trapped structures. *Science* (2002) 296:1101–3. doi:10.1126/science.1069571

7. Tamburini F, Anzolin G, Umbriaco G, Bianchini A, Barbieri C Overcoming the Rayleigh criterion limit with optical vortices. *Phys Rev Lett* (2006) 97:163903. doi:10.1103/PhysRevLett.97.163903

8. Bozinovic N, Yue Y, Ren Y, Tur M, Kristensen P, Huang H, et al. Terabit-scale orbital angular momentum mode division multiplexing in fibers. *Science* (2013) 340:1545–8. doi:10.1126/science.1237861

9. Mafu M, Angela D, Sandeep G, Daniel G, Melanie M, Miles JP, et al. Higher-dimensional orbital-angular-momentum-based quantum key distribution with mutually unbiased bases. *Phys Rev A* (2013) 88:032305. doi:10.1103/PhysRevA.88.032305

10. Wang J, Yang JY, Fazal IM, Ahmed N, Yan Y, Huang H, et al. Terabit free-space data transmission employing orbital angular momentum multiplexing. *Nat Photon* (2012) 6:488–96. doi:10.1038/nphoton.2012.138

11. Beijersbergen MW, Allen L, Veen HELOvan der, Woerdman JP Astigmatic laser mode converters and transfer of orbital angular momentum. *Opt Commun* (1993) 96:123–32. doi:10.1016/0030-4018(93)90535-D

12. Massari M, Ruffato G, Gintoli M, Ricci F, Romanato F Fabrication and characterization of high-quality spiral phase plates for optical applications. *Appl Opt* (2015) 54:4077. doi:10.1364/AO.54.004077

13. Heckenberg NR, McDuff R, Smith CP, White AG. Generation of optical phase singularities by computer-generated holograms. *Opt Lett* (1992) 17:221. doi:10.1364/OL.17.000221

14. Wei BY, Hu W, Ming Y, Xu F, Rubin S, Wang JG, et al. Generating switchable and reconfigurable optical vortices *via* photopatterning of liquid crystals. *Adv Mater* (2014) 26:1590–5. doi:10.1002/adma.201305198

15. Dorrah AH, Rubin NA, Tamagnone M, Zaidi A, Capasso F. Structuring total angular momentum of light along the propagation direction with polarization-controlled meta-optics. *Nat Commun* (2021) 12:6249. doi:10.1038/s41467-021-26253-4

16. Bernet S, Monika R. Adjustable refractive power from diffractive moire elements. *Appl Opt* (2008) 47:3722. doi:10.1364/AO.47.003722

17. Hossack WJ, Darling AM, Dahdouh A. Coordinate transformations with multiple computer-generated optical elements. *J Mod Opt* (1987) 34:1235–50. doi:10.1080/09500348714551121

18. Berkhout GCG, Lavery MPJ, Courtial J, BeijersbergenPadgett MWMJ. Efficient sorting of orbital angular momentum states of light. *Phys Rev Lett* (2010) 105:153601. doi:10.1103/PhysRevLett.105.153601

19. Mirhosseini M, Malik M, Shi Z, Boyd RW. Efficient separation of the orbital angular momentum eigenstates of light. *Nat Commun* (2013) 4:2781. doi:10.1038/ncomms3781

20. Wen Y, Chremmos I, Chen Y, Zhu J, Zhang Y, Yu S, et al. Spiral transformation for high-resolution and efficient sorting of optical vortex modes. *Phys Rev Lett* (2018) 120:193904. doi:10.1103/PhysRevLett.120.193904

21. Ruffato G, Massari M, Romanato F. Multiplication and division of the orbital angular momentum of light with diffractive transformation optics. *Light Sci Appl* (2019) 8:113. doi:10.1038/s41377-019-0222-2

22. Wen Y, Chremmos I, Chen Y, Zhang Y, Yu S. Arbitrary multiplication and division of the orbital angular momentum of light. *Phys Rev Lett* (2020) 124:213901. doi:10.1103/PhysRevLett.124.213901

23. Willner AE, Li L, Xie G, Ren Y, Huang H, Yue Y, et al. Orbital-angular-momentum-based reconfigurable optical switching and routing. *Photon Res* (2016) 4:5. doi:10.1364/prj.4.0000b5

24. Yao E, Franke-Arnold S, Courtial J, Barnett SM, Padgett M. Fourier relationship between angular position and optical orbital angular momentum. *Opt Express* (2006) 14:9071. doi:10.1364/OE.14.009071

frontiers | Frontiers in Physics

TYPE Original Research
PUBLISHED 17 August 2022
DOI 10.3389/fphy.2022.879826

OPEN ACCESS

EDITED BY
Gianluca Ruffato,
University of Padua, Italy

REVIEWED BY
Jietai Jing,
East China Normal University, China
Guoquan Zhou,
Zhejiang Agriculture and Forestry University, China
Yangjian Cai,
Soochow University, China

*CORRESPONDENCE
Shengmei Zhao,
zhaosm@njupt.edu.cn

SPECIALTY SECTION
This article was submitted to Optics and Photonics,
a section of the journal
Frontiers in Physics

RECEIVED 20 February 2022
ACCEPTED 18 July 2022
PUBLISHED 17 August 2022

CITATION
Zhao S, Qiao Q and Wang L (2022), Capturing the amplitude and phase profile of the vortex beam based on coherent detection.
Front. Phys. 10:879826.
doi: 10.3389/fphy.2022.879826

Capturing the amplitude and phase profile of the vortex beam based on coherent detection

Shengmei Zhao[1,2]*, Quanqing Qiao[1] and Le Wang[1]

[1]Institute of Signal Processing and Transmission, Nanjing University of Posts and Telecommunications (NUPT), Nanjing, China, [2]Key Lab of Broadband Wireless Communication and Sensor Network Technology, Ministry of Education, Nanjing University of Posts and Telecommunications, Nanjing, China

In this study, we propose a scheme to capture the amplitude and phase profile of the orbital angular momentum (OAM) beam based on coherent detection. In the scheme, the OAM beam to be measured is interfered with a local plain wave which is prepared at the receiver, and two charge-coupled devices (CCDs) are used to record the constructive and destructive interference patterns. By setting the phase of the plain wave to $\pi/2$ and π, one can extract the amplitude and phase profile of the OAM beam from the two interference patterns. We verify the feasibility of the scheme by simulation and experiments. The results show that both amplitude and phase profiles of single OAM and OAM superposition modes can be captured by using the proposed scheme, and the proposed scheme shows strong robustness even under the presence of atmospheric turbulence.

KEYWORDS

orbital angular momentum detection, coherent detection, amplitude and phase profile, superposition mode, atmospheric turbulence

1 Introduction

Orbital angular momentum (OAM) of light is an attractive degree of freedom for fundamental studies in classical communications [1, 2] and quantum information processing [3–5]. Since the first demonstration of that, an $e^{i\ell\theta}$ vortex phase structure of a circularly symmetric beam was found to have $\ell\hbar$ units of OAM in 1992, where $\hbar$ is Planck's constant [6], OAM has become a useful information carrier in a variety of applications [2, 7–9]. It is shown that OAM can be used together with polarization to increase the channel capacity of communication systems [10]. The usage of OAM multi-level encoding bases can increase the tolerance of quantum key distribution (QKD) systems against eavesdropping [11]. The multiplexing of OAM modes is also demonstrated to greatly increase the bandwidth efficiency both in free-space (FSO) and fiber optical communication systems [2, 12, 13].

Therefore, it is important to detect the OAM mode at the receiver end. Until now, there have been a lot of works focusing on this task [14–16]. The simplest way to detect an OAM beam is performing a projection measurement [2], where the OAM mode with ℓ topological charge is first transferred to a flat phase beam by being illuminated on a forked

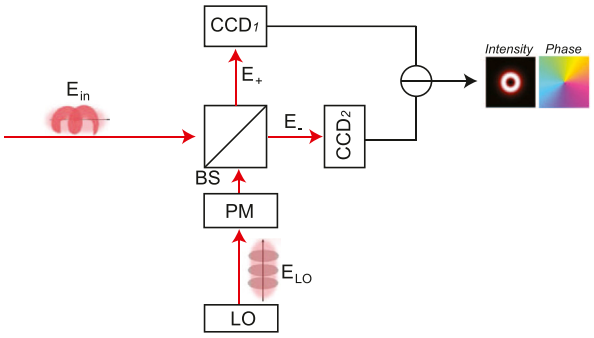

FIGURE 1
Scheme to capture the amplitude and phase profile of the OAM mode based on the coherent detection method. LO: local oscillator. PM: phase modulator. BS: beam splitter.

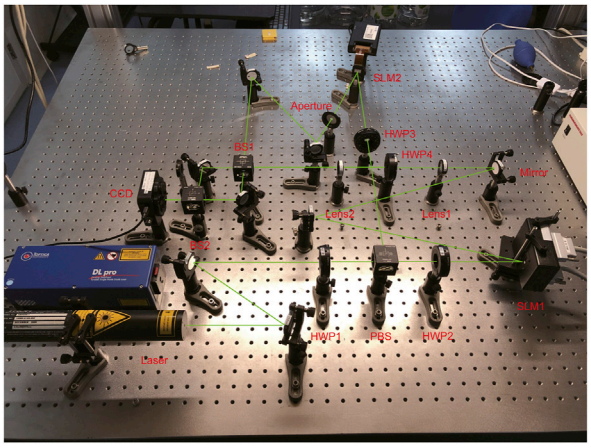

FIGURE 2
Experiment setup for the proposed scheme.

hologram with $-\ell$ and then detected by a power detector. Later, a technique for separating OAM modes by using a Mach–Zehdner interferometer at the single-photon level was presented [17]. To efficiently sort N OAM modes simultaneously, Berkhout *et al.* proposed a separating method based on the transformation from Cartesian to log-polar [18]. Also, the separation diffraction limitation was overcome by using the fan-out technique [19]. Simulations and experiments demonstrated that the separating method could distinguish the different OAM modes simultaneously with a detector array [20–22]. Thereafter, an efficient separating orbital angular momentum mode with radial varying phase was proposed [23]. Then, multiplane-light conversion, spiral transformation, and metasurfaces for combined OAM and SAM analysis were used to detect the OAM mode [24–28]. Recently, deep learning techniques were used to detect the OAM mode [29]. Also, the amplitude and phase quadratures of vortex beams are detected for testifying the quantum entanglement of vortex beams [30–34]. However, there are fewer studies carried out on capturing both the amplitude and phase profile of the OAM beam simultaneously.

In this study, we propose a scheme to capture the amplitude and phase profile of the OAM mode based on the coherent detection method. In the scheme, the receiver uses a beam splitter to integrate the OAM beam to be measured with a plain wave modulated with different phases to produce two interference patterns. Also, two charge-coupled devices (CCDs) are used to capture these patterns. By changing the phase of the plain wave with $\pi/2$ and π, one can obtain the amplitude and phase profiles of the OAM modes, including the single OAM mode and the superposition OAM mode, from the two CCD patterns.

There are some advantages of our scheme: 1) the proposed scheme could capture the amplitude and phase profile of the OAM mode simultaneously, 2) the proposed scheme can detect the single/superposition OAM modes, and 3) the scheme has strong robustness even under atmospheric turbulence.

2 Theory

Figure 1 shows the schematic diagram of the proposed scheme to capture the amplitude and phase profile of the orbital angular momentum mode based on the coherent detection method. The receiver uses a beam splitter to integrate the OAM beam to be measured E_{in} with a plain wave E_{LO} modulated with different phase φ_{PM} to produce the interference patterns. The plain wave E_{LO} is generated by a local oscillator and is then modulated by a phase modulator to obtain the phase φ_{PM}. The interference patterns E_+ and E_- are exported from the two outputs of the beam splitter. Two CCDs are used to capture the interference pattern from the two outputs of the beam splitter. By changing the phase φ_{PM} of the plain wave with $\pi/2$ and π, one can capture the amplitude and phase profile of the OAM beam E_{in} based on the interference pattern obtained from the CCDs.

The OAM mode to be measured E_{in} is assumed to be described as

$$E_{in}(r,\theta,t) = R(r)\exp(j\ell\theta)\exp(j\omega t), \tag{1}$$

where r and θ are the radial and azimuthal coordinates, respectively; $R(r)$ and $\exp(j\ell\theta)$ denote the amplitude and spatial phase of the beam, respectively; ℓ is the OAM topological charge, which is an integer; $R(r)$ could be different mode structures, such as Laguerre–Gaussian modes or Bessel–Gaussian modes; and ω is the frequency of the OAM beam.

A plain wave E_{LO} is generated by a local oscillator (LO) at first and is defined as

$$E_{LO}(r,\theta,t) = \exp(j\omega t). \tag{2}$$

Then, it is modulated a phase by a phase modulator (PM),

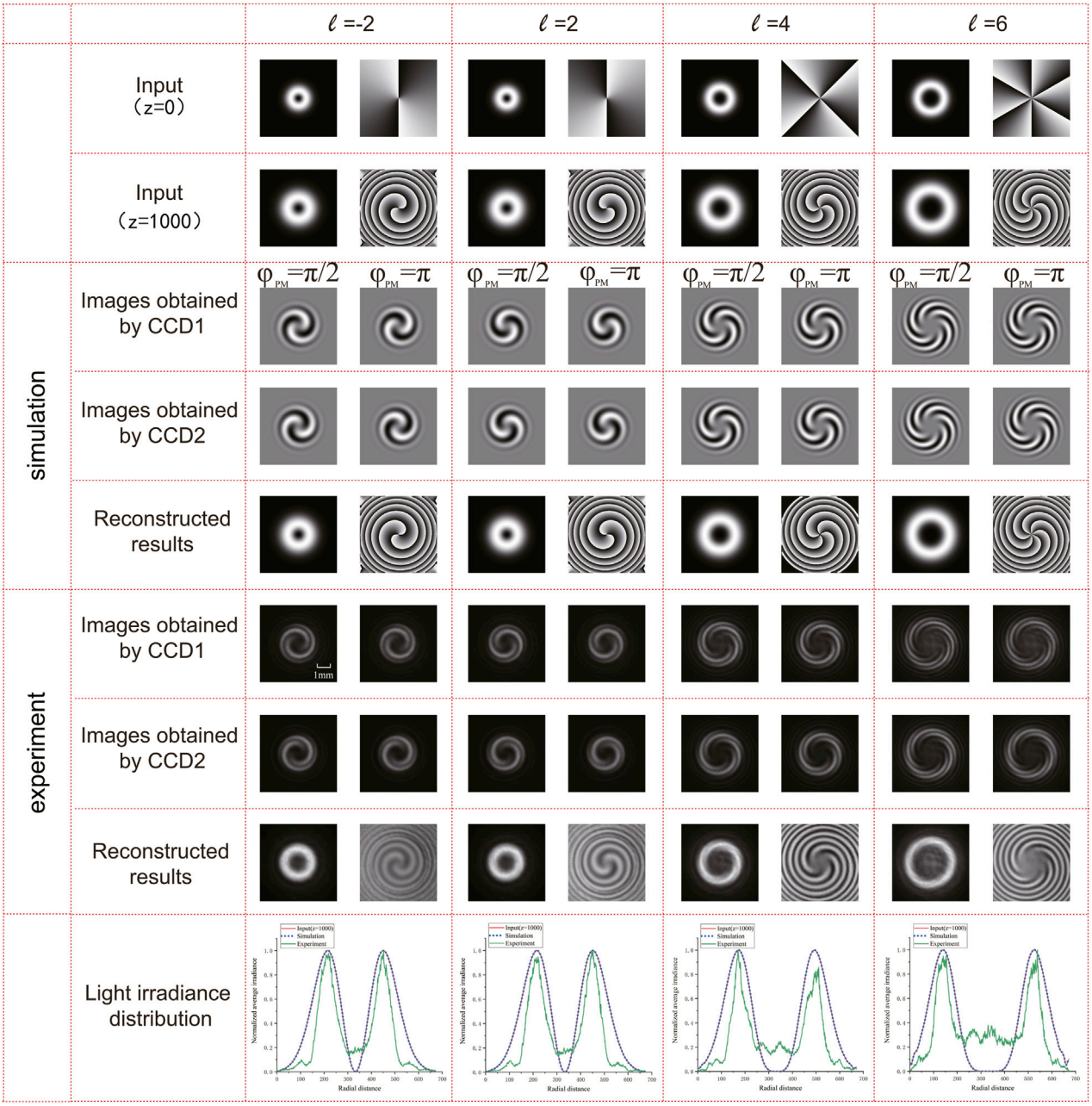

FIGURE 3
Simulation and experimental results of the proposed scheme to capture the amplitude and phase profile of single OAM beam E_{in}.

$$E_{LO}(r,\theta,t) = \exp\left(j\left(\omega t + \varphi_{PM}\right)\right), \tag{3}$$

where φ_{PM} is the phase modulated by the phase modulator.

After that, a beam splitter is used to combine the received OAM beam E_{in} and the plain wave E_{LO} to produce interference patterns. The interference patterns E_+ and E_- are exported from the beam splitter, i.e.,

$$E_+(r,\theta,t) = jE_{in}(r,\theta,t) + E_{LO}(r,\theta,t), \tag{4}$$

and

$$E_-(r,\theta,t) = E_{in}(r,\theta,t) + jE_{LO}(r,\theta,t). \tag{5}$$

Two CCDs are used to detect the interference patterns. The interference pattern obtained by CCD1 should be $|E_+(r, \theta, t)|^2$, and the interference pattern obtained by CCD2 should be $|E_-(r, \theta, t)|^2$. One can obtain the difference between $|E_+(r, \theta, t)|^2$ and $|E_-(r, \theta, t)|^2$ as

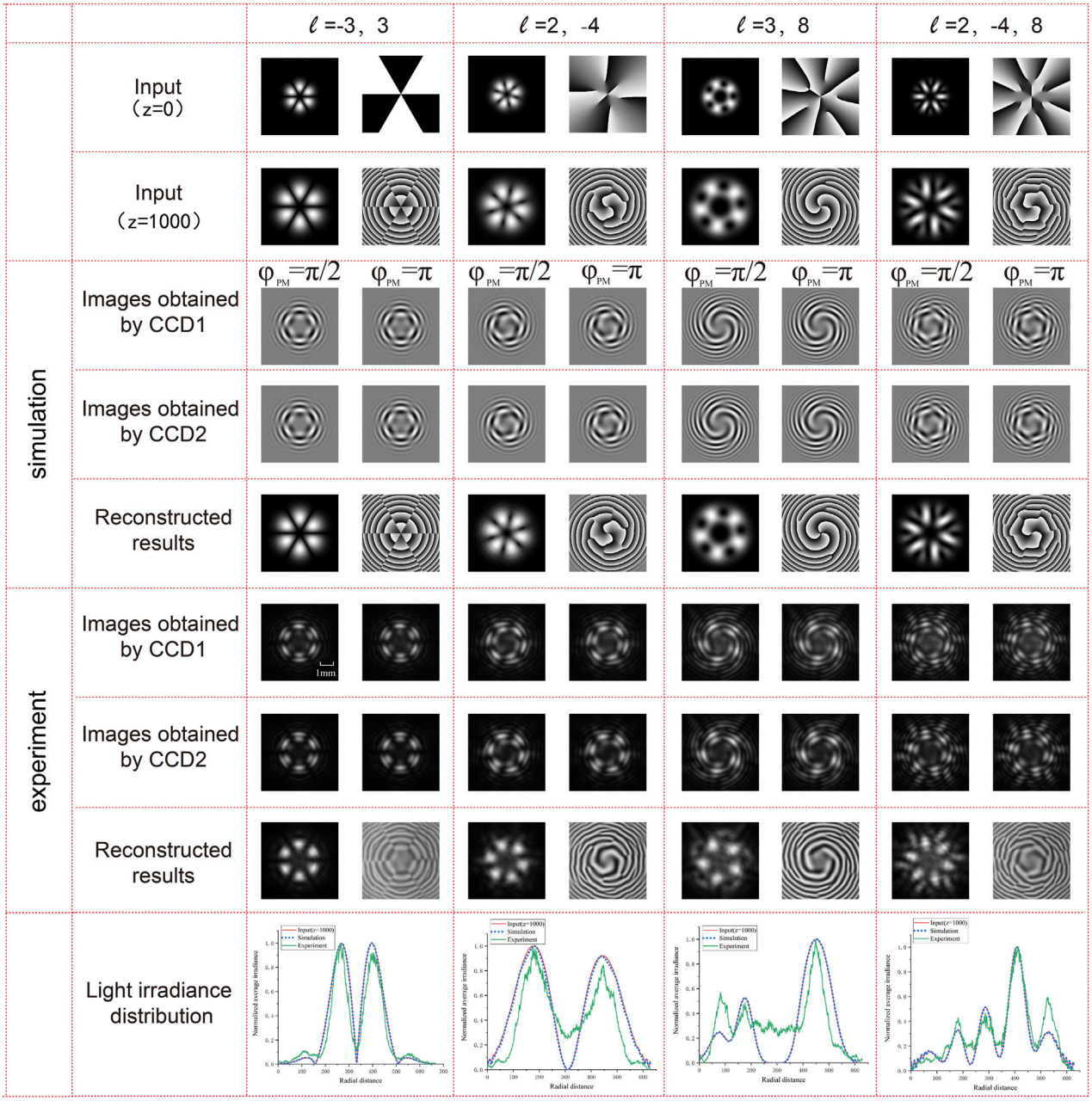

FIGURE 4
Simulation and experimental results of the proposed scheme to capture the amplitude and phase profile of OAM superposition beam E_{in}.

$$\begin{aligned}&|E_+(r,\theta,t)|^2-|E_-(r,\theta,t)|^2\\&\quad=|jE_{in}(r,\theta,t)+E_{LO}(r,\theta,t)|^2-|E_{in}(r,\theta,t)+jE_{LO}(r,\theta,t)|^2\\&\quad=2jR(r)\left[\exp\left(j\ell\theta-j\varphi_{PM}\right)-\exp\left(j\varphi_{PM}-j\ell\theta\right)\right].\end{aligned}\tag{6}$$

During detection, φ_{PM} is given two values for two measurements. For the first time, the modulated phase φ_{PM} is set to $\pi/2$. For the second time, the modulated phase φ_{PM} is set to π. Since Eq. 6 is related with φ_{PM}, we define the difference $|E_+(r, \theta, t)|^2 - |E_-(r, \theta, t)|^2$ as a function $f(\varphi_{PM})$, i.e.,

$$\begin{aligned}f\left(\varphi_{PM}\right)&=|E_+(r,\theta,t)|^2-|E_-(r,\theta,t)|^2\\&=2jR(r)\left[\exp\left(j\ell\theta-j\varphi_{PM}\right)-\exp\left(j\varphi_{PM}-j\ell\theta\right)\right].\end{aligned}\tag{7}$$

By setting the phase φ_{PM} of the plain wave to $\pi/2$ and π individually, we can obtain the light field distribution of the OAM beam E_{in} based on the interference pattern obtained from the two CCDs, that is,

$$\begin{aligned}f\left(\pi/2\right)&=2jR(r)\left[\exp\left(j\ell\theta-j\pi/2\right)-\exp\left(j\pi/2-j\ell\theta\right)\right]\\&=4R(r)\cos\left(j\ell\theta\right),\end{aligned}\tag{8}$$

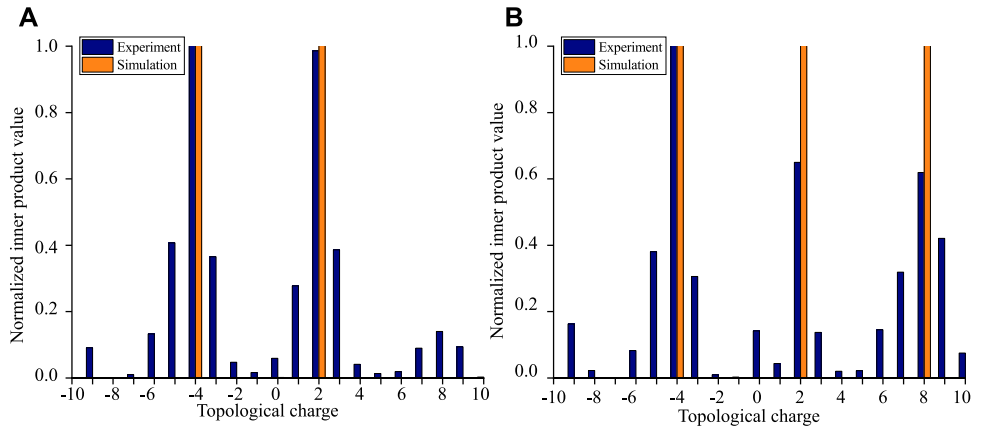

FIGURE 5
Inner product results of OAM superposition beams with **(A)**ℓ = 2, − 4 and **(B)**ℓ = 2, − 4, 8.

$$f(\pi) = 2jR(r)\left[\exp(j\ell\theta - j\pi) - \exp(j\pi - j\ell\theta)\right] = 4R(r)\sin(j\ell\theta), \quad (9)$$

and

$$E_{in}(r,\theta) = R(r)\exp(j\ell\theta) = \frac{1}{4}\left[f(\pi/2) + jf(\pi)\right]. \quad (10)$$

Therefore, the amplitude profile should be

$$Amplitude\{E_{in}\} = R(r) = abs\left\{\frac{1}{4}\left[f(\pi/2) + jf(\pi)\right]\right\}, \quad (11)$$

and the phase profile should be

$$Phase\{E_{in}\} = \ell\theta = angle\left\{\frac{1}{4}\left[f(\pi/2) + jf(\pi)\right]\right\}. \quad (12)$$

3 Results and discussion

In this section, we discuss the performance of the proposed scheme. The experimental setup for the proposed scheme is shown in Figure 2. A linear fundamental mode Gaussian beam (waist radius $\omega_0 = 0.8mm$) at a wavelength of 633 nm is generated by a He–Ne laser (Thorlabs, Model HRP020-1). After being reflected by two mirrors, the beam passes through a half-wave plate (HWP1) to adjust the intensity ratio of the two Gaussian beams after splitting. A polarization beam splitter (PBS) is used to separate and polarize the incident Gaussian beam to two beams. Then, each Gaussian beam passes through a half-wave plate (HWP1 and HWP2) to match the polarization direction of the Spatial Light Modulator (SLM1, Hamamatsu, Model X10468-07, SLM2, Holoeye, Model PLOTO-VIS-006-A). After that, each Gaussian beam is diffracted by a computer-controlled SLM. SLM1 carries a phase hologram of $\pi/2$ or π (the same function as the phase modulator), and SLM2 carries a special phase hologram for the LG mode of different topological charges ℓ. The Gaussian beam needs to pass through another half-wave plate (HWP3) to equalize the polarization of the two beams so as to satisfy with the superposition conditions. At the same time, one aperture is used to filter out the first-order diffracted light from the diffracted beam, and two convex lenses (focal length f1 = 100 mm, f2 = 200 mm) are used to amplify the Gaussian beam. Thereafter, the two outcoming beams interfere at a beam splitter (BS1). For simultaneous measurement, two mirrors and beam splitter (BS2) are used to focus the two output beams of BS1 on a plane so that the two output beams can be captured by one CCD (Thorlabs, Model BC106N-VIS/M, 989 × 745 pixels of 8.8 mm × 6.6 mm size) at one time.

Then, we demonstrate the proposed scheme for the single OAM mode in Figure 3. The upper part is the simulation results, and the lower part is the experimental results. The topological charges ℓ for the measured OAM mode are setup to $\ell = -2$, $\ell = 2$, $\ell = 4$, and $\ell = 6$. In order to compare the performance, we also list the intensity and phase distribution of the input OAM beam (z = 0) and the input OAM beam (z = 1000 m) at the first two rows, where z is the propagation distance. It is can observed that the intensity and phase distribution are diverged with the propagation distance in comparison with for the input OAM beam (z = 0). *Images obtained by CCD1* and *Images obtained by CCD2* are the interference patterns obtained by CCD1 and CCD2, respectively, representing the constructive and destructive interference patterns, and *Reconstructed results* are the amplitude and phase profile of the OAM beam recovered by the proposed scheme. The simulation and experimental results show that our scheme has the ability to capture the amplitude and phase profile of the input OAM beam E_{in} accurately. For example, the interference patterns formed by the input OAM beam with $\ell = 2$ is a "pinwheel-shaped" pattern with two stripes

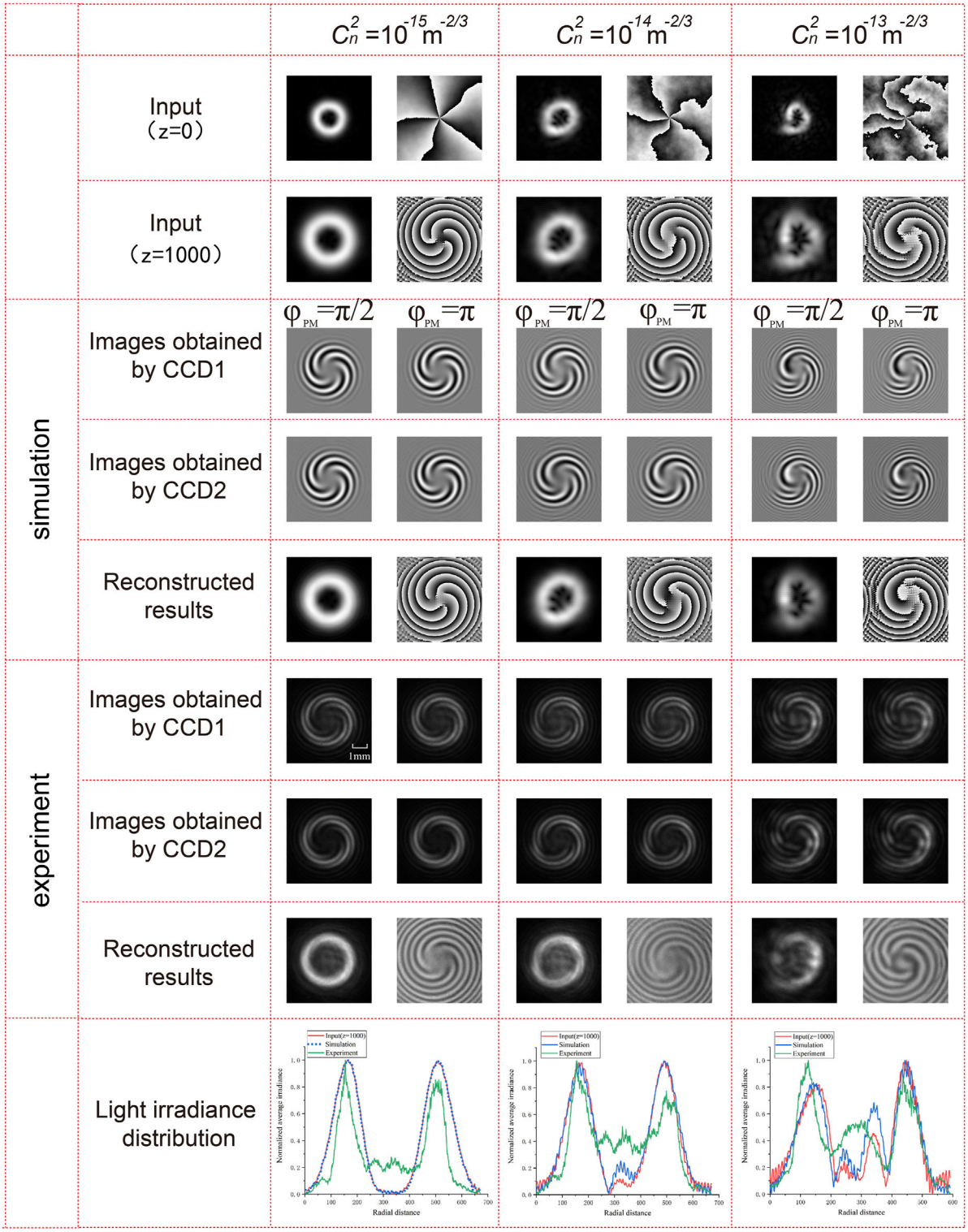

FIGURE 6
Simulation and experimental results of the proposed scheme to capture the amplitude and phase profile of the OAM beam (ℓ = 5) under the presence of atmospheric turbulence.

TABLE 1 Peak signal-to-noise ratio of simulation and experimental results.

PSNR	ℓ								C_n^2		
	−2	2	4	6	−3, 3	2, −4	3, 8	2, −4, 8	10^{-15}	10^{-14}	10^{-13}
Amplitude	19.4	19.07	16.26	14.71	17.78	18.97	18.29	18.37	15.72	16.69	17.08
Phase	13.04	12.5	8.95	9.37	11.07	12.97	9.44	10.76	9.96	10.88	9.5

and clockwise rotation both in simulation and experiment, while they are "pinwheel-shaped" pattern with two stripes and counterclockwise rotation for the input OAM beam with $\ell = -2$. Comparing with the simulation results, the experimental results show the same characteristic distribution of the interference patterns and phase patterns, including the rotation direction and number of "pinwheel-shaped" stripes, but with some blurring in the patterns, which is caused by the noise in experiment. *Light irradiance distribution* further demonstrates the consistency among the input OAM beams, the simulation results, and the experimental results. Here, the input OAM beams are those OAM beams with propagation distance (z = 1000 m). Since there always exists the propagation of the beams in experiment, we use the input OAM beams with propagation distance for comparison.

Then, we further verify the case when the incident beam is an OAM superposition beam in Figure 4. Here, the selected OAM superposition beams are composed by two or three OAM modes, such as $\ell = -3, 3$, $\ell = 2, -4$, $\ell = 3, 8$, and $\ell = 2, -4, 8$. Also, the intensity and phase profile of the superposition OAM beams are demonstrated in the first and the second row, followed by the interference patterns obtained at CCD1 and CCD2, and the last row is the recovered results by using the proposed scheme. Different from the single OAM mode, the intensity profile of the superposition OAM modes becomes bright and dark petal patterns, and the singular points in the phase profile are more complex, especially for the superposition mode composed by more OAM modes. The upper part is the simulation results, and the lower part is the experimental results. The simulation and experimental results show that both interference patterns and captured amplitude and phase patterns have the same distribution, including the number and shape of petals. It is indicated that our proposed scheme also has the ability to capture the amplitude and phase profile of the OAM superposition beam E_{in} accurately. *Light irradiance distribution* also demonstrates the similarity among the input OAM beams, the simulation results, and the experimental results.

Based on the mutual orthogonality of OAM beams with different topological charges, we can obtain the topological charge composition of OAM superposition beams according to the reconstructed amplitude and phase profile. Firstly, the amplitude and phase profile are combined into an OAM beam, and then the topological charge composition of OAM superposition beams can be obtained by inner product with OAM beams with different topological charges ($\ell = 10, -9, \ldots, 9, 10$). Figure 5 shows the inner product results of OAM superposition beams with $\ell = 2, -4$ and $\ell = 2, -4, 8$. It can be seen from the figure that we can detect the topological charge of OAM superposition beams based on the reconstructed amplitude and phase profile. There are some differences between the simulation and experiment detection results. The reason is that it is hard to locate the center of the experimental "reconstructed result", and an insignificant misalignment will cause mode crosstalk. However, one can still judge the topological charge composition according to the experimental intensity distribution.

Next, we discuss the robustness of the proposed scheme when the OAM beam is propagated under atmospheric turbulence (AT) in Figure 6. Here, we use random phase screen model simulating atmospheric turbulence [35, 36]. The simulated parameters for the random phase screen are set as follows. The wavelength λ is $633nm$, the space Δz between the two random phase screen is $200m$, the beam waist ω_0 is $0.1m$, the outer scale is $L_0 = 50m$, and the inner scale is $l_0 = 0.001m$. The topological charge of the input OAM beam is $\ell = 5$. The atmospheric refractive index structure constant C_n^2 (usually used to describe the intensity of atmospheric turbulence) is set to 10^{-15}, 10^{-14}, and $10^{-13} m^{-2/3}$. Here, one random phase screen is used for simplicity. In the experiment, the random phase screen representing atmospheric turbulence is superimposed on the OAM generating phase mask so that the input OAM mode contaminated by atmospheric turbulence is obtained when the Gaussian beam is illuminated on the SLM2 loaded by the superimposed phase distribution. It can be seen from Figure 6 that the amplitude and phase of the measured OAM beam are distorted by AT, and the stronger AT is, the larger distortion the measured OAM beam has. However, our scheme has the ability to capture the amplitude and phase profile of the OAM beam E_{in} even in this case. The simulation and experimental results show that our proposed scheme has strong robustness even under the presence of atmospheric turbulence.

The peak signal-to-noise ratio (PSNR) is often used to quantitatively estimate the recovered image quality [37], which is defined as

$$\mathrm{PSNR} = 10\lg\left(\frac{\mathrm{MAX}_\mathrm{I}^2}{\mathrm{MSE}}\right), \tag{13}$$

where MAX_I is the maximum possible pixel value of the image. MSE is the mean square error of the image, which is defined as

$$\mathrm{MSE} = \frac{1}{M \times N}\sum_{i=0}^{M-1}\sum_{j=0}^{N-1}\left\|f\left(x_i, y_j\right) - g\left(x_i, y_j\right)\right\|^2, \tag{14}$$

where $g(x_i, y_j)$ and $f(x_i, y_j)$ are gray-values in (x_i, y_j) for the original and reconstructed images, respectively. $M \times N$ is the pixel of the image. Generally, the higher PSNR is, the better quality of reconstructed image is.

Finally, we calculated the peak signal-to-noise ratio (PSNR) of amplitude and phase profile captured by simulation and experiment results mentioned above to illustrate the similarity between simulation and experiment results. Table 1 shows the peak signal-to-noise ratio of the simulation and experiment results. "Amplitude" denotes the PSNR for recovered amplitude part, and "phase" denotes the PSNR for the recovered phase part. C_n^2 represents the strength of the atmosphere turbulence. The results show that the simulation and experimental results have a high degree of similarity.

4 Conclusion

In this study, we have proposed a scheme to capture the amplitude and phase profile of the incident OAM beam based on the coherent detection. With the interference between the measured OAM beam and a local plain wave, the amplitude and phase profile of the measured OAM beam could be captured by the calculation on the detection results in CCDs. The simulation and experimental results have showed that both amplitude and phase profiles can be detected by using the proposed scheme not only for the single OAM mode but also for the OAM superposition mode. Furthermore, the amplitude and phase profiles of the measured OAM beam can even be detected under the presence of atmospheric turbulence. Our method can capture the amplitude and phase profile of the input OAM beam, regardless of whether the input beam passes through atmospheric turbulence or not. At the same time, compared with the previous method which can only obtain the amplitude profile, our method can obtain amplitude and phase profile simultaneously, that is, our method can obtain more information about the beam, so it will be more conducive for detecting topological charges in strong atmospheric turbulence environment.

Data availability statement

The original contributions presented in the study are included in the article/Supplementary Material; further inquiries can be directed to the corresponding author.

Author contributions

SZ, QQ, and LW contributed to conception and design of the study. LW performed the simulation analysis and QQ performed the experimental verification. SZ and QQ wrote the first draft of the manuscript. SZ and LW presented the revision of the manuscript. All authors contributed to manuscript revision, read, and approved the submitted version.

Funding

National Natural Science Foundation of China (NSFC) (61871234, 62001249). This work was supported in part by Open Research Fund Program of the State Key Laboratory of Low-Dimensional Quantum Physics, Tsinghua University under Grant KF201909.

Conflict of interest

The authors declare that the research was conducted in the absence of any commercial or financial relationships that could be construed as a potential conflict of interest.

Publisher's note

All claims expressed in this article are solely those of the authors and do not necessarily represent those of their affiliated organizations, or those of the publisher, the editors, and the reviewers. Any product that may be evaluated in this article, or claim that may be made by its manufacturer, is not guaranteed or endorsed by the publisher.

References

1. Willner AE, Huang H, Yan Y, Ren Y, Ahmed N, Xie G, et al. Optical communications using orbital angular momentum beams. *Adv Opt Photon* (2015) 7:66–106. doi:10.1364/AOP.7.000066

2. Wang J, Yang JY, Fazal IM, Ahmed N, Yan Y, Huang H, et al. Terabit free-space data transmission employing orbital angular momentum multiplexing. *Nat Photon* (2012) 6:488–96. doi:10.1038/nphoton.2012.138

3. Malik M, Erhard M, Huber M, Krenn M, Fickler R, Zeilinger A. Multi-photon entanglement in high dimensions. *Nat Photon* (2016) 10:248–52. doi:10.1038/nphoton.2016.12

4. Wang XL, Cai XD, Su ZE, Chen MC, Wu D, Li L, et al. Quantum teleportation of multiple degrees of freedom of a single photon. *Nature* (2015) 518:516–9. doi:10.1038/nature14246

5. Zhang W, Ding DS, Dong MX, Shi S, Wang K, Liu SL, et al. Experimental realization of entanglement in multiple degrees of freedom between two quantum memories. *Nat Commun* (2016) 7:13514. doi:10.1038/ncomms13514

6. Allen L, Beijersbergen MW, Spreeuw RJC, Woerdman JP. Orbital angular momentum of light and the transformation of Laguerre-Gaussian laser modes. *Phys Rev A* (1992) 45:8185–9. doi:10.1103/PhysRevA.45.8185

7. Mair A, Vaziri A, Weihs G, Zeilinger A. Entanglement of the orbital angular momentum states of photons. *Nature* (2001) 412:313–6. doi:10.1038/35085529

8. Molina-Terriza G, Torres JP, Torner L. Twisted photons. *Nat Phys* (2007) 3:305–10. doi:10.1038/nphys607

9. Barreiro JT, Wei TC, Kwiat PG. Beating the channel capacity limit for linear photonic superdense coding. *Nat Phys* (2008) 4:282–6. doi:10.1038/nphys919

10. Malik M, O'Sullivan M, Rodenburg B, Mirhosseini M, Leach J, Lavery MPJ, et al. Influence of atmospheric turbulence on optical communications using orbital angular momentum for encoding. *Opt Express* (2012) 20:13195–200. doi:10.1364/OE.20.013195

11. Bourennane M, Karlsson A, Björk G. Quantum key distribution using multilevel encoding. *Phys Rev A* (2001) 64:012306. doi:10.1103/PhysRevA.64.012306

12. Bozinovic N, Yue Y, Ren Y, Tur M, Kristensen P, Huang H, et al. Terabit-scale orbital angular momentum mode division multiplexing in fibers. *Science* (2013) 340:1545–8. doi:10.1126/science.1237861

13. Boffi P, Martelli P, Gatto A, Martinelli M. Mode-division multiplexing in fibre-optic communications based on orbital angular momentum. *J Opt* (2013) 15:075403. doi:10.1088/2040-8978/15/7/075403

14. Leach J, Padgett MJ, Barnett SM, Franke-Arnold S, Courtial J. Measuring the orbital angular momentum of a single photon. *Phys Rev Lett* (2002) 88:257901. doi:10.1103/PhysRevLett.88.257901

15. Gibson G, Courtial J, Padgett MJ, Vasnetsov M, Pas'ko V, Barnett SM, et al. Free-space information transfer using light beams carrying orbital angular momentum. *Opt Express* (2004) 12:5448–56. doi:10.1364/OPEX.12.005448

16. Krenn M, Fickler R, Fink M, Handsteiner J, Malik M, Scheidl T, et al. Communication with spatially modulated light through turbulent air across Vienna. *New J Phys* (2014) 16:113028. doi:10.1088/1367-2630/16/11/113028

17. Leach J, Courtial J, Skeldon K, Barnett SM, Franke-Arnold S, Padgett MJ. Interferometric methods to measure orbital and spin, or the total angular momentum of a single photon. *Phys Rev Lett* (2004) 92:013601. doi:10.1103/PhysRevLett.92.013601

18. Berkhout GCG, Lavery MPJ, Courtial J, Beijersbergen MW, Padgett MJ. Efficient sorting of orbital angular momentum states of light. *Phys Rev Lett* (2010) 105:153601. doi:10.1103/PhysRevLett.105.153601

19. Mirhosseini M, Malik M, Shi Z, Boyd RW. Efficient separation of the orbital angular momentum eigenstates of light. *Nat Commun* (2013) 4:2781. doi:10.1038/ncomms3781

20. Li C, Jiang R, Wang L, Zhao SM. Simulations of high efficient separation of orbital-angular-momentum of light. *J Nanjing Univ Post Telecommun* (2016) 36:47–52. doi:10.14132/j.cnki.1673-5439.2016.03.007

21. Huang H, Milione G, Lavery MPJ, Xie G, Ren Y, Cao Y, et al. Mode division multiplexing using an orbital angular momentum mode sorter and MIMO-DSP over a graded-index few-mode optical fibre. *Sci Rep* (2015) 5:14931. doi:10.1038/srep14931

22. Huang H, Ren Y, Xie G, Yan Y, Yue Y, Ahmed N, et al. Tunable orbital angular momentum mode filter based on optical geometric transformation. *Opt Lett* (2014) 39:1689–92. doi:10.1364/OL.39.001689

23. Li C, Zhao SM. Efficient separating orbital angular momentum mode with radial varying phase. *Photon Res* (2017) 5:267–70. doi:10.1364/PRJ.5.000267

24. Fontaine NK, Ryf R, Chen H, Neilson DT, Kim K, Carpenter J. Laguerre-Gaussian mode sorter. *Nat Commun* (2019) 10:1865. doi:10.1038/s41467-019-09840-4

25. Wen YH, Chremmos I, Chen YJ, Zhu JB, Zhang YF, Yu SY. Spiral transformation for high-resolution and efficient sorting of optical vortex modes. *Phys Rev Lett* (2018) 120:193904. doi:10.1103/PhysRevLett.120.193904

26. Lei T, Fang JC, Xie ZW, Yuan XC. High-resolution cylindrical vector beams sorting based on spin-dependent fan-out optical geometric transformation. *Opt Express* (2019) 27:20901–9. doi:10.1364/OE.27.020901

27. Ruffato G, Capaldo P, Massari M, Mafakheri E, Romanato F. Total angular momentum sorting in the telecom infrared with silicon Pancharatnam-Berry transformation optics. *Opt Express* (2019) 27:15750–64. doi:10.1364/OE.27.015750

28. Wang BM, Wen YH, Zhu JB, Chen YJ, Yu SY. Sorting full angular momentum states with Pancharatnam-Berry metasurfaces based on spiral transformation. *Opt Express* (2020) 28:16342–51. doi:10.1364/OE.393859

29. Cox MA, Celik T, Genga Y, Drozdov AV. Interferometric orbital angular momentum mode detection in turbulence with deep learning. *Appl Opt* (2022) 61:D1–D6. doi:10.1364/AO.444954

30. Pan XZ, Yu S, Zhou YF, Zhang K, Zhang K, Lv SC, et al. Orbital-angular-momentum multiplexed continuous-variable entanglement from four-wave mixing in hot atomic vapor. *Phys Rev Lett* (2019) 123:070506. doi:10.1103/PhysRevLett.123.070506

31. Li SJ, Pan XZ, Ren Y, Liu HZ, Yu S, Jing JT. Deterministic generation of orbital-angular-momentum multiplexed tripartite entanglement. *Phys Rev Lett* (2020) 124:083605. doi:10.1103/PhysRevLett.124.083605

32. Wang W, Zhang K, Jing JT. Large-scale quantum network over 66 orbital angular momentum optical modes. *Phys Rev Lett* (2020) 125:140501. doi:10.1103/PhysRevLett.125.140501

33. Liu SS, Lou YB, Jing JT. Orbital angular momentum multiplexed deterministic all-optical quantum teleportation. *Nat Commun* (2020) 11:3875. doi:10.1038/s41467-020-17616-4

34. Chen YX, Liu SS, Lou YB, Jing JT. Orbital angular momentum multiplexed quantum dense coding. *Phys Rev Lett* (2021) 127:093601. doi:10.1103/PhysRevLett.127.093601

35. Zhao SM, Wang L, Zou L, Gong LY, Cheng WW, Zheng BY, et al. Both channel coding and wavefront correction on the turbulence mitigation of optical communications using orbital angular momentum multiplexing. *Opt Commun* (2016) 376:92–8. doi:10.1016/j.optcom.2016.04.075

36. Zhao SM, Leach J, Gong LY, Ding J, Zheng BY. Aberration corrections for free-space optical communications in atmosphere turbulence using orbital angular momentum states. *Opt Express* (2012) 20:452–61. doi:10.1364/OE.20.000452

37. Horé A, Ziou D. Image quality metrics: PSNR vs. SSIM. In: 2010 20th International Conference on Pattern Recognition. Istanbul, Turkey: IEEE (2010). p. 2366–9. doi:10.1109/ICPR.2010.579

Advantages of publishing in Frontiers

OPEN ACCESS
Articles are free to read for greatest visibility and readership

FAST PUBLICATION
Around 90 days from submission to decision

HIGH QUALITY PEER-REVIEW
Rigorous, collaborative, and constructive peer-review

TRANSPARENT PEER-REVIEW
Editors and reviewers acknowledged by name on published articles

Frontiers
Avenue du Tribunal-Fédéral 34
1005 Lausanne | Switzerland

Visit us: www.frontiersin.org
Contact us: frontiersin.org/about/contact

REPRODUCIBILITY OF RESEARCH
Support open data and methods to enhance research reproducibility

DIGITAL PUBLISHING
Articles designed for optimal readership across devices

FOLLOW US
@frontiersin

IMPACT METRICS
Advanced article metrics track visibility across digital media

EXTENSIVE PROMOTION
Marketing and promotion of impactful research

LOOP RESEARCH NETWORK
Our network increases your article's readership